Jan Lichtenberg

A Microchip-based Ion Analysis System

Incorporating Electrophoretic Separation, Conductivity Detection, and Sample Pretreatment

Institute of Microtechnology
University of Neuchâtel
Neuchâtel, Switzerland

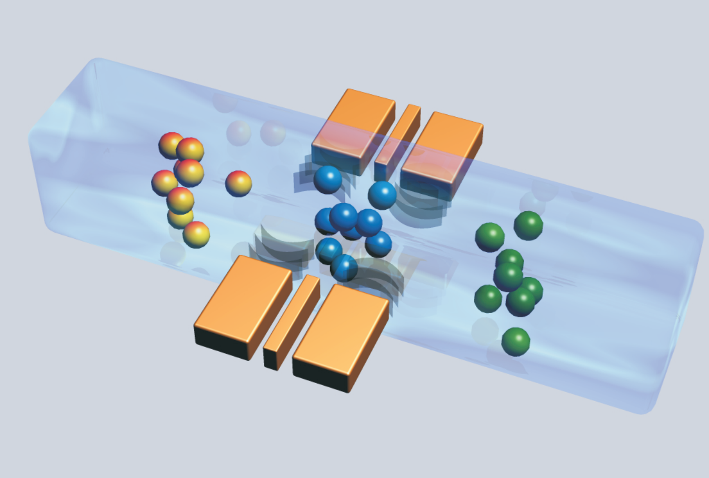

Dissertation
submitted to the Faculty of Sciences of the University of Neuchâtel
in fulfillment of the requirements for the degree of "Docteur ès Sciences"

A Microchip-based Ion Analysis System Incorporating Electrophoretic Separation, Conductivity Detection, and Sample Pretreatment

by

Jan Lichtenberg

Electronics Engineer (Dipl.-Ing.)

Institute of Microtechnology
University of Neuchâtel
Rue Jaquet-Droz 1
CH-2007 Neuchâtel
Switzerland

IMPRIMATUR POUR LA THESE

A microchip-based ion analysis system incorporating electrophoretic separation, conductivity detection and sample preconcentration

de M. Jan Lichtenberg

UNIVERSITE DE NEUCHATEL

FACULTE DES SCIENCES

La Faculté des sciences de l'Université de Neuchâtel sur le rapport des membres du jury,

Mme S. Verpoorte,
MM. N. de Rooij (directeur de thèse),
P.-A. Farine et A. Manz (Londres)

autorise l'impression de la présente thèse.

Neuchâtel, le 5 décembre 2002

Le doyen:

F. Zwahlen

“The human mind is like an umbrella – it works best when open”

Walter Gropius, Architect, in The Observer, 1956

Table of Contents

Summary

With the goal of small ion analysis in mind, a prototype of a microchip capillary electrophoresis (CE) device has been developed based on a new, integrated, in-plane, contactless conductivity detector (CCD). The device allows fast separation of inorganic anions and cations in the range of 20 s. The microfabrication process developed in the context of this thesis makes it possible to easily integrate CCDs with standard glass and polymer micromachining. It also allows to place the electrodes close to the separation channel independent of the substrate type, which is a requirement for good detector sensitivity and spatial (i.e. separation) resolution.

As CCD methods generally have a ~10-fold lower sensitivity than their contact-mode counterparts, field-amplified sample stacking (FASS) was implemented on microfluidic devices for sample preconcentration. In order to visualize the microfluidic phenomena involved in stacking, the technique was performed using fluorescently labeled amino acids as analyte. These studies gave important insight into the effect of pressure-driven flow in particular that is generated during the stacking process. Signal enhancements due to the preconcentration of up to 95-fold could be obtained by a new sweeping technique, while the, technically less complex, stacking of 400-µm-long sample plugs showed a 20-fold increase in peak height. FASS was then deployed in a microchip containing a CCD and achieved a 4-fold signal enhancement by stacking of a 150-µm-long sample plug. It is assumed that longer sample plugs containing a larger amount of the analyte increase the enhancement factor further.

As an alternative to CCD, a new potential-gradient detector (PGD) was developed. Though this device also discriminates analyte zones based on their conductivity, it requires direct electrolyte-contact to detect the potential difference between two closely spaced platinum electrodes. Although the detector lifetime will be reduced when compared to a CCD due to electrochemical degradation of the electrodes, preliminary results indicated a very high sensitivity of the device. For the indirect conductivity detection, the microchip CE-PGD device can even compete with more complex methods such as indirect laser-induced fluorescence detection.

Chapter 1

Introduction

1.1 Does Moore's Law apply to down-scaling of chemical systems?

The rapid development of microelectronic devices has changed our lives tremendously since the invention of the transistor in 1947 by Brattain and Bardeen and the development of the first integrated circuit (IC) by Kilby and Noyce in 1958. A major key to this revolution is the constant miniaturization of the IC base elements, which allows the integration of more functionality at lower cost into a single chip. Furthermore, shrinking device dimensions generally reduces electrical power consumption – an important factor for portable devices.

Gordon E. Moore, at the time director of R&D at Fairchild Semiconductor, observed in his 1965 paper "Cramming more components onto integrated circuits", that the density of transistors in integrated circuits doubled every year. Moreover, he predicted a similar development for the future [1]. This statement was given only four years after the development of the first planar semiconductor device and it turned out that the development pace slowed down somewhat. In the following years, a doubling of component density after every 18-month period was noted, which basically holds true until today. Based on his original statement, the term "Moore's Law" was coined for this relationship, named after the man who went on to co-found Intel Corp. in 1968 and remained the company's chairman until 1997. Figure 1-1 shows the development in terms of numbers of transistors per chip for the Intel microprocessors since 1971. It should be noted, however, that major road blocks to conventional CMOS technology (complementary metal-oxide-semiconductor) are expected around 2010 to 2015 as the transistor gate length will show quantum confinement due to dimensions below 30 nm [2].

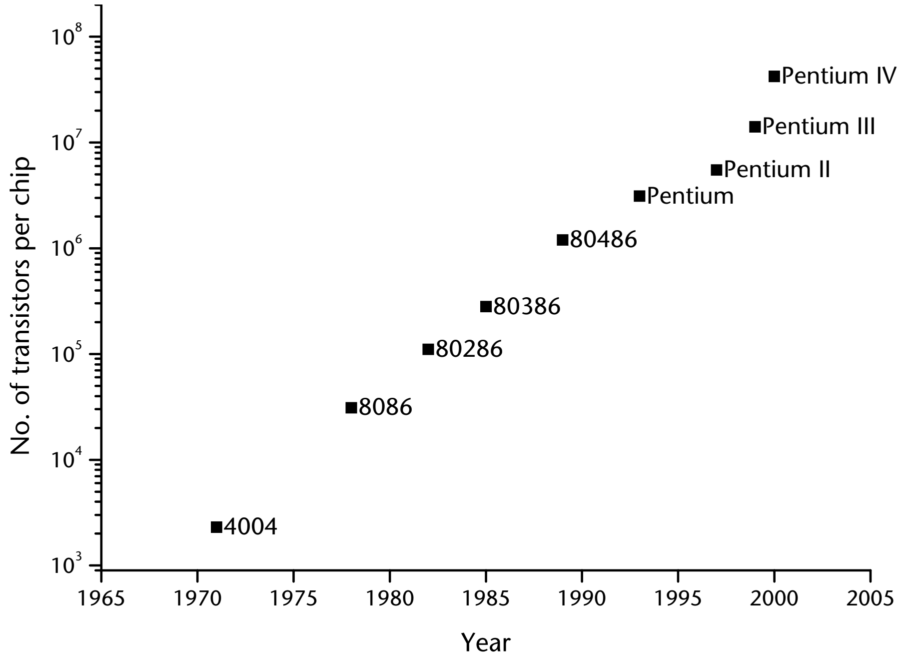

***Figure 1-1**: Number of transistors per microprocessor for the Intel product line (chart based on data available on Intel's world wide web site www.intel.com).*

Microfluidic devices do not only share a large part of the fabrication technology with their microelectronic counterparts. Also here, a constant thrive to increase functionality per unit area pushes researchers to more and more refined prototypes. If we enlarge the scope of Moore's Law to functionality and number of parallel operations, we observe similar trends in the world of microfluidics. In the case of DNA separation and sequencing by electrophoresis for example, Figure 1-2 shows the increase in the number of parallel separations integrated on a single device. Similar observations can also be made for analysis times, which shrink down to the sub-millisecond regime [3], for sample volumes or numbers of molecules needed for detection. Again, similar to the electronics world, miniaturization is limited physically, although it is more difficult to estimate miniaturization limits than for CMOS devices. For one thing the conduits of the microfluidic system must be large enough to let analyte molecules pass. This may present a constraint when designing devices for large protein or other large biomolecule analysis or chemistry. A reduction in sample size also brings up the question of whether the minute amount of substance analyzed properly represents the chemical composition of the macroscopic volume being tested.

However, as microelectronics and microfluidics address different applications, the scientists and engineers involved face different challenges. For instance, while microelectronic components do not necessarily interact physically with the environment, microfluidic structures do when samples are loaded onto the device. Issues like material compatibility, contamination and product lifetime in general also appear in a different light if the device is to be disposable.

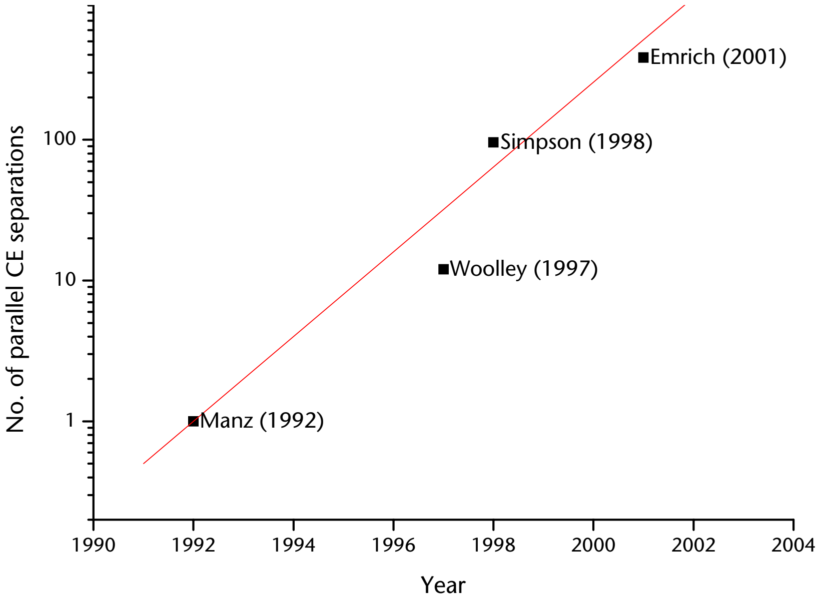

Figure 1-2*: Exponential increase of the number of parallel electrophoresis separations on microfabricated analysis devices. Data taken from publications [4-7].*

It therefore remains questionable, whether integration densities comparable to microprocessors will ever be achieved for microfluidics – and whether this is desirable at all. However, similar conservative statements were made before for the computer market and the originators were proved to be dramatically wrong[1].

1.2 Microfluidic devices for chemical analysis

The broadness of the field of chemical analysis as well as the importance of the resulting information to our personal well-being makes it desirable to have chemical analysis instrumentation available on a wide and distributed basis. By bringing the analysis instrument close to the source of the sample, the information sought is acquired faster, allowing transient processes to be recorded. A larger number of analysis systems allows better and more detailed monitoring and could reveal lo-

---

[1] "I think there is a world market for maybe five computers." – Thomas Watson, chairman of IBM, 1943

cal changes across a large system, an important feature for instance for environmental monitoring.

However, chemical analysis generally requires fairly complex processes to separate the analyte (the species about which information is required) from the actual sample taken, and to retrieve information about the amount and type of analyte. The analyte may be reacted with a specific reagent to form a colored compound, which can then be optically detected. Alternatively, the sample mixture could be separated into single analyte zones in a chromatographic column. In most cases, the analysis requires a fairly large amount of manual labor and specialized laboratory equipment. While automated (sometimes even robotic) instruments are available for routine analysis, these devices are generally very complex, expensive and high-maintenance. As a result, most chemical analysis, independent of the application area, is performed in large, centralized and specialized laboratories.

The concept of the total analysis system, or TAS, proposed by H. Michael Widmer, was a first attempt to de-centralize chemical analysis and to turn it into a real-time technology [8]. The main focus was industrial process control, which would benefit from fast feedback for closed-loop process control. A TAS was meant to contain all components necessary to perform an integrated chemical analysis from sampling to sample pretreatment to the analysis and finally data processing. In a complex factory, a multitude of TAS could be installed directly at the respective fabrication sites and transmit the acquired information to a central location from which the production process is controlled. A drawback of the concept is the complex construction required, comprising tubing, pumps, valves, and a certain amount of control electronics. Furthermore, these components have fairly large volumes, at least compared to their microfluidic counterparts described later in this section. Large volumes mean that large amounts of sample and reagents are necessary during the operation, which in turn requires large storage tanks for the latter to allow continuous operation over a given time. Chemical reactions are also affected by the volumes used, in the sense that smaller volumes often decrease the response time of an analysis as diffusion times are shortened, mixing is improved and reaction conditions can be better controlled.

Reduction of sample volumes, i.e. miniaturization, was identified as a key to a new technology, which was baptized µTAS by its originators Andreas Manz and H. Michael Widmer [9]. Here, all components of the analysis system are assembled into a small device, which performs the whole analysis process in an autonomous fashion. However, instead of assembling the system from discreet components, it is integrated onto a planar, microchip-like platform [4, 10-14]. Interconnected tubes are replaced by networks of microchannels with dimensions in the range from hundreds down to a few micrometers, which are fabricated in the substrate. To manipulate reagents on a chip, mechanically active pumps and valves may be integrated, or alternatively, non-mechanical pumping concepts applied [15]. Especially the latter class of pumping techniques, namely electro-osmotic pumping, was adopted rapidly during the first years of µTAS activities, as it allows precise and valve-less flow control [16].

Although the µTAS concept has initiated an exponentially growing field of research, truly integrated devices are seldom presented today. This is partly due to the complexity of the task for this still rather young field, and partly because full integration is not necessarily the best option in terms of value for money. This is especially true for disposable devices, which are favored for critical applications like medical diagnostics [17]. In this case, it is much more cost-efficient to keep certain elements (like optical detectors) as part of the external instrument within which the chip is operated. It is up to the developer to decide which components are better integrated onto the chip and which should remain part of the external setup. This decision depends basically on the benefits obtained by miniaturization of the component, potential complications in its fabrication posed by integration, and by its fabrication cost.

In order to avoid the impression that all miniaturized analysis systems are “total”, the general term “microfluidic device” will be adopted for this thesis. This class of chips comprises both fairly simple systems containing only a single functional element and also complex devices, with a number of parallel and sequential chemical processes.

1.3 Technology platforms for microfluidic devices

The majority of microfluidic devices presented to date rely on planar fabrication technology, which comprises all techniques that create patterns of multiple layers on a thin, flat substrate. In the stricter sense of microelectronics fabrication, planar technology is based on three processes: layer formation, pattern definition and layer removal. At the beginning of microfluidic research in the early 1990s, these techniques were readily available in the field of microfabrication, and were therefore directly adopted for the fabrication of microchannels.

Substrates of choice were the well-known mono-crystalline silicon [18-23], low-alkali glass [10-14] and fused silica [24-26] in the form of polished wafers. The wafer surface is covered with an inert material layer, which is subsequently patterned by photolithography. The underlying bulk material can then be etched to form minute channels, reaction chambers, filters and the like [27]. After removal of the protective coating used during etching, the still-open microchannels are sealed with a cover plate to form a closed channel network. In most cases, the cover plate has access holes that match up with the ends of the channels to allow filling of the network with reagents.

Silicon was the substrate of choice for a true µTAS example which was way ahead of its time. In 1975, Terry *et al.* integrated a complete gas chromatograph onto a silicon wafer, including injector, separation column, and a thermal conductivity detector [18][2]. However, as silicon is electrically conductive and easily corroded by basic solutions [28], it needs to be protected for most chemical applications. Protective coatings, such as silicon dioxide or silicon nitride, only offer limited insulation for high-voltage applications like CE [20]. For these reasons, inert, insulating and additionally optically transparent materials like glass and quartz became the favorite of the microfluidics community. Examples of technology platforms in several substrate materials are shown in Figure 1-3.

However, since the mid-90s, polymer microfluidic devices have received increasing attention, both because of their low cost and simple fabrication. The devel-

---

[2] This reference dates back to 1979, but in fact S. C. Terry finished his thesis at Stanford in 1975.

opment has been driven on the high-volume end by the need for inexpensive, disposable microchips for mass markets. On the research end, the quest for rapid-prototyping techniques for laboratory experiments has driven this development. Polymer microfabrication by hot embossing or injection molding covers the first requirement and allows mass production using a variety of materials with highest precision [29]. Casting and molding of elastomers, especially poly(dimethyl siloxane) (PDMS), has been welcomed by the research community, as it allows rapid access to microfluidic devices without the requirement of a semiconductor-style cleanroom and hazardous chemistry [30, 31].

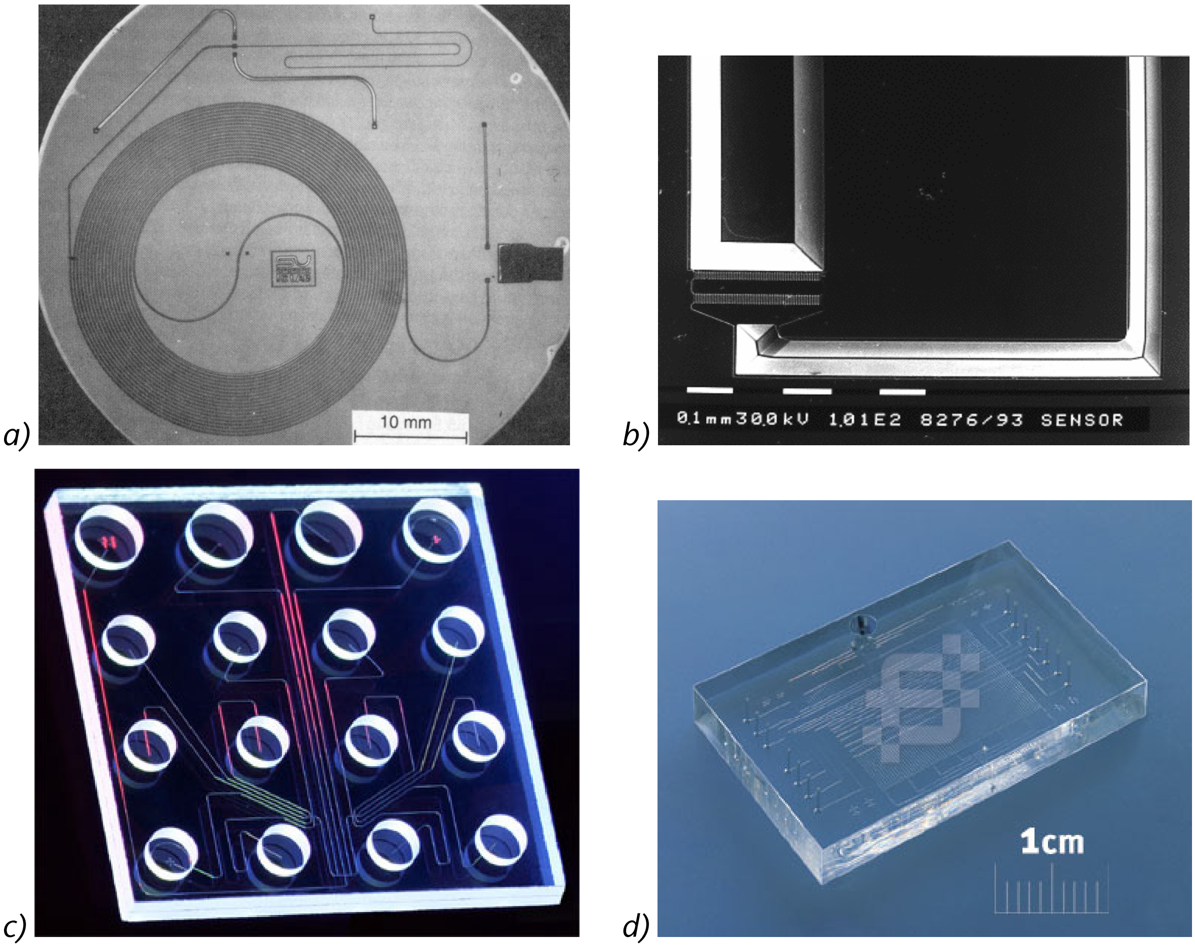

***Figure 1-3**: Examples of planar microanalysis devices: a) Integrated gas chromatograph in silicon [18]; b) Integrated liquid chromatograph [23]; c) Glass-based CE chip (from Agilent, www.agilent.com); d) Microfluidic device made in PDMS (from Fluidigm, www.fluidigm.com)*

1.4 Capillary electrophoresis CE

CE is the third major instrumental separation technique after the introduction of gas chromatography in the 1960s and high-performance liquid chromatography in the 1970s. The basic theory of the electrophoretic migration of ions was already formulated more than a century ago [32]. Although early ion separations in solution under the influence of a direct electrical field were studied in the late 1930s, it took until 1981 that CE in the stricter sense was introduced by Jorgenson and Lukacs [33-35]. He was the first to deploy narrow bore (75 µm inner diameter or smaller) glass capillaries for electrophoresis, which is the form of CE most widely used today. Previously, researchers only had larger glass and Teflon tubes available (Hjertén used millimeter-bore capillaries in [36], which was reduced to 200 µm diameter by Virtanen [37] and Mikkers [38]). Jorgenson's narrow capillaries reduced the electrical current flowing during the separation and thereby electrolyte heating (Joule heating). The latter was a major drawback in large tubes, affecting the separation efficiency by convective dispersion.

Separation in CE is based on the mobility of the analyte ions under the influence of an electric field in a capillary filled with an electrolyte (Figure 1-4). Once the electric field is applied, ions of type *i* migrate at a velocity v_i, at which the Coulomb force acting on the charge is equal to the viscous forces the moving ions experience [39-41][3]. The mobility, denoted μ_{ep}. therefore depends largely on the charge of the ion and its size (see Equation 9 on page 58). Ions with different μ_{ep} contained in a small sample plug can therefore be separated into distinct zones when migrating over a long enough distance through the capillary.

In parallel to the ion-specific, electrophoretic migration, a bulk flow is generated by the electrical field applied to the capillary. This electro-osmotic flow (EOF) is due to the Coulomb force on the mobile part of the electrolyte double layer, which forms on the capillary wall. Under regular conditions, this layer consists of positive ions which are attracted to the negatively charged capillary wall. The flow

---

[3] The first two references give a good, solid introduction to CE, which goes far beyond the short outline presented in this section. The third reference is recommended as an extensive knowledge base for CE and related techniques.

of these cations towards the negative electrode causes the whole capillary volume to migrate as a consequence of the viscous drag caused by the movement of the mobile layer. The electro-osmotic mobility, μ_{eo}, depends on a number of factors, such as buffer pH, ionic strength, and the capillary wall material.

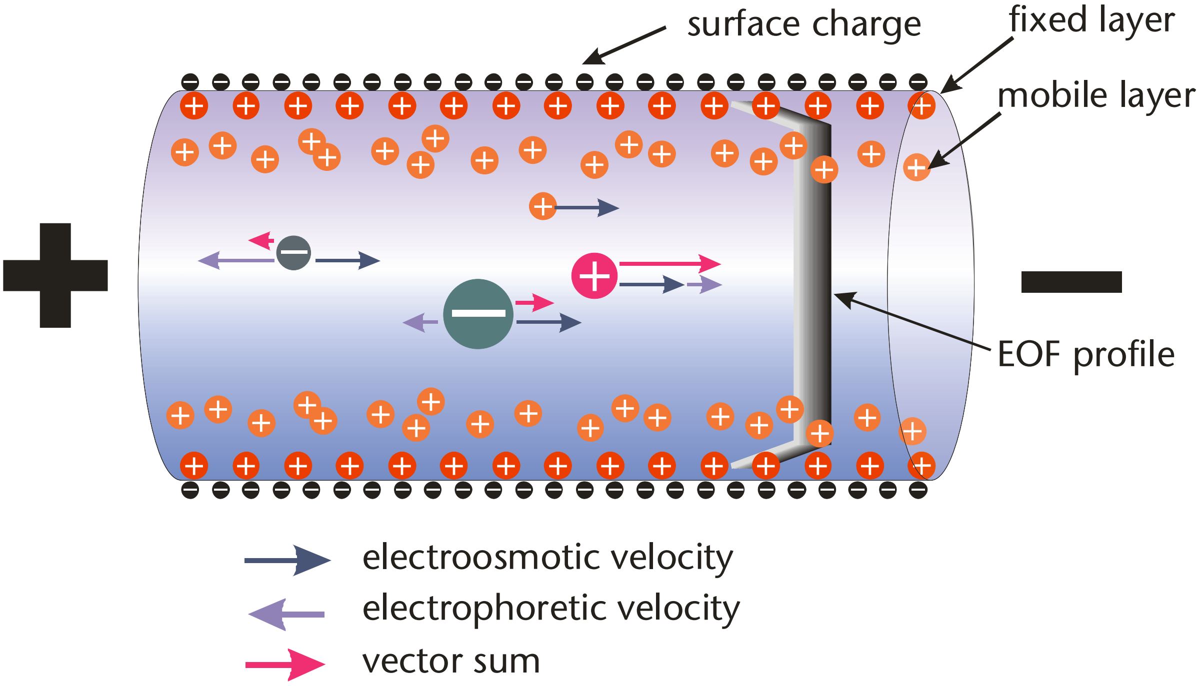

Figure 1-4: *Schematic representation of the sources for ion transport in a glass or fused silica capillary filled with an electrolyte.*

In practice, CE is performed by filling a 20-to-80-cm-long capillary (15 to 75 µm inner diameter) with the separation buffer (Figure 1-5). Then, a short plug (generally < 1% of the capillary length) of the sample solution is injected into one end of the capillary. Both ends are then placed into two buffer reservoirs, which are connected to a high-voltage power supply (~ 10 to 30 kV). Upon application of the separation voltage, the migration starts and the separated analyte zones can be recorded by a suitable detector at the outlet side of the capillary. A variety of detector types is available depending on the chosen analyte, including visible and UV absorbance, laser-induced fluorescence (LIF), conductivity, amperometry and voltammetry.

Its capability of rapidly separating charged analyte molecules made CE an interesting option for the analysis of small inorganic and organic ions, which is the focus of this thesis. CE equipped with a conductivity detector was used for ion detection in environmental chemistry [42, 43], CE in conjunction with indirect UV absorbance detection was used for quality control of osmotically treated water [44], and various techniques were applied to metal ions and their complexes [45]. Haber *et al.* improved CE with conductivity detection by including an internal standard and were able to obtain quantitative measurements at low-to-sub-ppb detection limits [46].

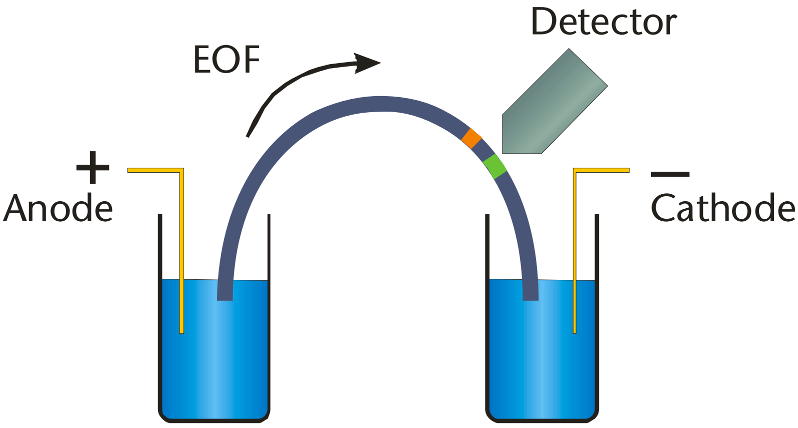

Figure 1-5: *Cartoon of a typical CE setup. The separation capillary is placed in two reservoirs filled with buffer. Upon application of the separation voltage, the sample plug (here introduced on the left side) migrates towards the cathode and the analyte ions separate into distinct zones. These are then recorded by a suitable detector.*

1.5 Microchip CE: Better separations through miniaturization

Miniaturizing a CE device and implementing it on a planar substrate has tremendous advantages, as recognized by the first commercial chip-CE instruments that appeared on the market. Shorter separation channels reduce the analysis time considerably, while smaller channel cross-sections allow higher separation fields without degenerating the efficiency due to Joule heating. At the same time, lower separation voltages are required for a given field strength, which makes instrumentation simpler.

Most important, however, is the fact that complex, dead-volume-free networks of microfluidic channels can be integrated on these chips. The remarkable impact of this feature has been illustrated since the early days of microchip CE in the form of volume-defined sample plug formation (or injection) [13, 47, 48]. By using two or three intersecting channels (the latter type is shown in Figure 1-6), sample plugs of a geometrically defined volume can be formed in the separation channel in a highly reproducible manner. If a counterflow is applied from both sides of the separation channel to confine the plug further and to reduce diffusion-related effects, unmatched injection reproducibility can be achieved (Figure 1-6 on the left).

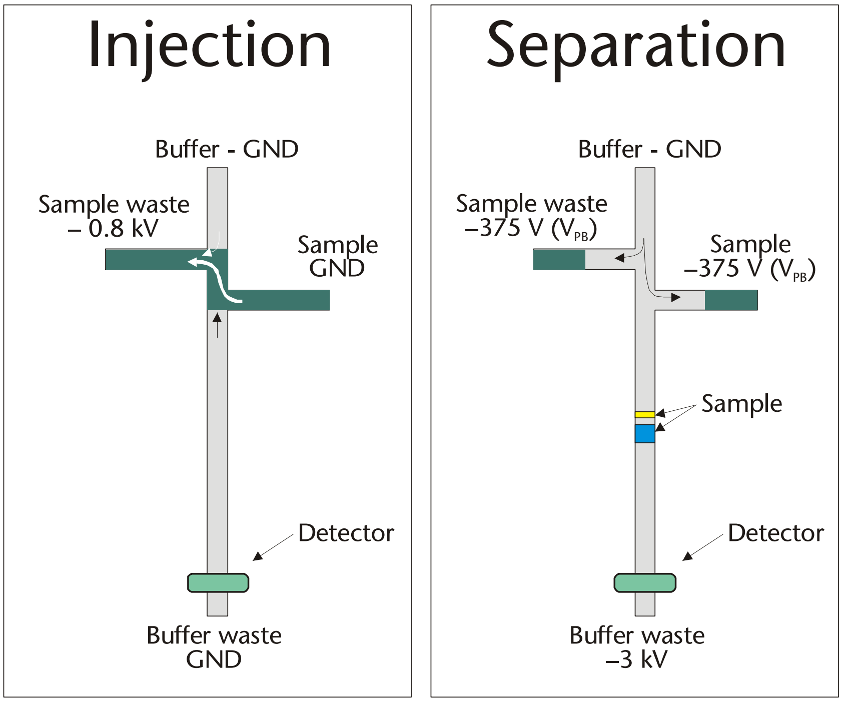

***Figure 1-6**: A typical microchip CE separation with volume-defined sample plug formation in a double-T element. Voltages are indicated as an example.*

Another advantage, relying again on the availability of channel networks, are the integration of pre- and post-column derivatization procedures (see [49] for an overview). These allow analytes to be tagged with a fluorescent label before [50] or after separation [25, 51]. Similar designs were used for post-column complexation of metals [52] and proteins [53].

1.6 Microchip CE: Integration of sample pretreatment steps

The labeling examples above underline the unique feature of microfluidic devices, namely that several steps of an analytical procedure can be integrated and combined in one chip to yield faster, less laborious instrumentation. While the actual separation techniques were in the focus of research during the early stage of µTAS development, the integration of sample pretreatment techniques has gained increasing attention recently [49].

Sample pretreatment is an important part of every chemical analysis procedure. Once a representative sample is obtained from its original source, a number of processing steps are necessary to transform it in order to conform with the requirements of the analysis technique chosen without losing the chemical information contained in it. The general term "sample pretreatment" comprises many different methods, ranging from filtering to remove particles to analyte labeling for detection purposes.

Examples of integrated sample pretreatment are on-chip particle filters [54, 55], DNA amplification by PCR [56-59], enzymatic digestion [60], sample preconcentration [61-64] and many more. For a full review see [49].

1.7 Research goal of this thesis: A miniaturized ion analysis system

This thesis follows the idea of pushing integration further to achieve a higher-functionality device by adding of complementary components into the system. While miniaturization and highly parallel processing are not the main focus of this thesis, it will be illustrated how the integration of metal electrodes on-chip can add new capabilities for chemical analysis. The application area is the analysis of small inorganic ions, such as sodium, potassium, lithium, chloride and nitrate. Samples can be drinking water, process water from an industrial environment, surface water from lakes or rivers, or waste water. The envisaged instrument should be small, eventually portable, but most of all should deliver rapid measurement results (interval < 5 min) and work independently over an extended period of time (> 6 months).

Miniaturizing an analysis system has a number of interesting prospects for this particular application, generally centered around real-time, autonomous chemical monitoring. As will be discussed in more detail later, miniaturized chemical analysis systems have shorter measurement times than most macroscopic counter parts. This allows analysis in the range of minutes, where the conventional method needs one or two orders of magnitude more time to deliver results. At the same time, miniaturization reduces the amounts of sample and reagents necessary for the analysis. While the sample is generally available in abundance in the case of water analysis, reagent consumption directly dictates the autonomy of the instrument (the time over which an analysis can be repeatedly performed until the reagent containers of the instrument are empty).

The analysis will be done by separation of the analytes contained in the sample by microchip-based capillary electrophoresis (CE) (Figure 1-7). Separation techniques in general have the advantage of delivering simultaneously qualitative and quantitative information about all separable species in the sample. This characteristic makes separations more advantageous for this broad, multi-analyte analysis than specific methods like colorimetric speciation, which has also been implemented on microchips [65, 66].

All separation devices consist of the actual separation column and a detector close to or at its end that identifies the separated analyte zones. While direct laser-induced fluorescence detection is the prevailing method for microchip-based analysis due to its sensitivity and ease of implementation, it is not adapted to the detection of the analytes mentioned above[4]. These ions are not inherently fluorescent and also difficult to label or to complex for fluorescence detection. However, their common characteristic is their high ionic mobility, which leads to a high molar conductivity of the ions. It is therefore possible to detect these ions by monitoring the local change of conductivity at the end of the separation column by so-called conductivity detection. As the lifetime of our device is supposed to be fairly long, a contactless, impedimetric method was chosen for implementation

---

[4] An exception is indirect fluorescence detection, which allows the detection of non-fluorescent analyte molecules separated in a fluorescent background buffer [136]. Despite being a versatile technique, the sensitivity of indirect methods is generally lower than that of their direct counterparts.

on chip, which features a high long-term stability. The development and characterization is presented in Chapter 5 with some application examples given in Chapter 6. Chapter 7 describes the instrumentation involved in contactless detection and presents a new, sensitive detection mode based on synchronous demodulation.

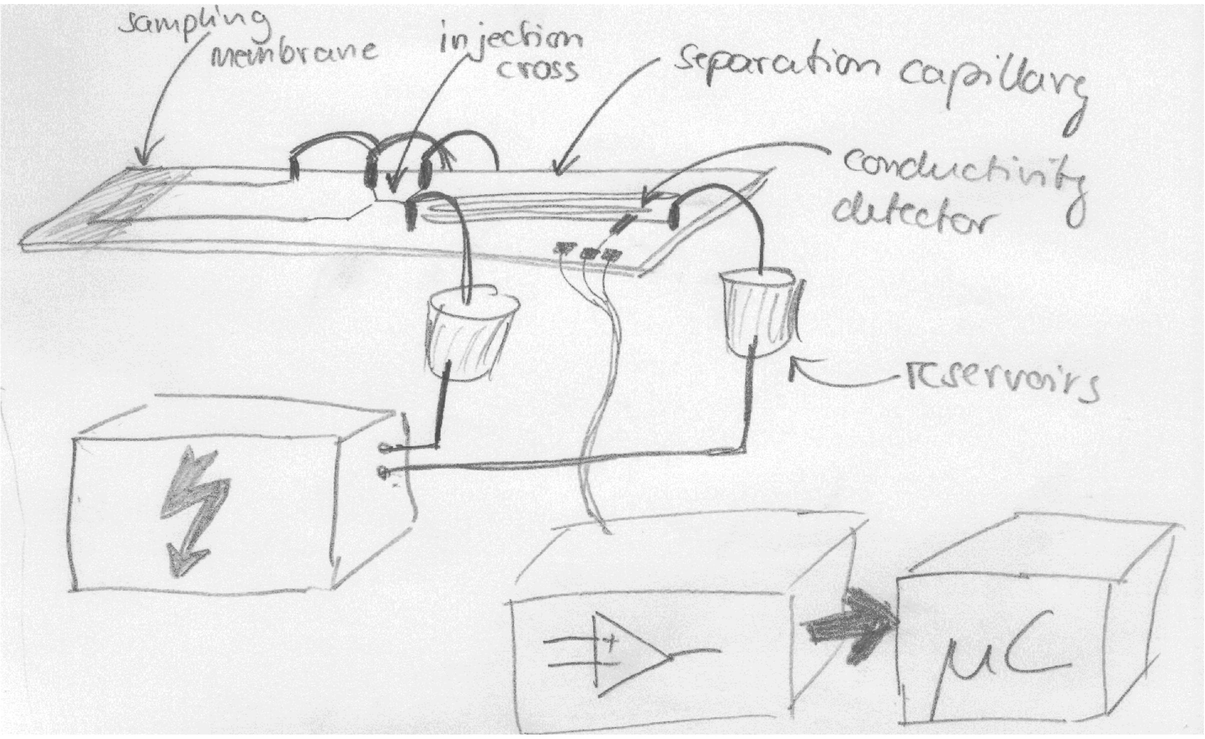

Figure 1-7*: Early sketch of the microchip analysis device for water analysis. Above, the microfluidic chip for CE with conductivity detection. Below, the external instrumentation including high-voltage power supply, detector electronics and computer. At this stage of the project, sampling via a dialysis membrane was proposed, to be able to draw samples directly from the environment. However, time did not permit the implementation of this step.*

A drawback of the contactless conductivity detection method is the sensitivity, which is about a factor of 10 lower compared to alternative conductivity detection techniques. This might pose problems for samples with low analyte content. To overcome this problem, the integration of sample preconcentration techniques into microfluidic analysis systems was studied. Here, the analyte contained in a comparatively large sample volume is concentrated into a narrow zone, which is subsequently analyzed by CE. As the intermediate concentration is many times higher than the original in the sample, less stringent requirements are imposed on the detector. The technique chosen is field-amplified sample stacking (FASS), which only requires that the sample matrix is of lower electrical conductivity than the running buffer used for separation. The stacking process has been implemented, optimized and further developed for stacking of particularly large sample volumes, as presented in Chapter 4.

Also, a different detection method, potential gradient detection (PGD), also based on the analyte conductivity, has been developed. The technique is known since the early days of electrophoretic separations, but has in our opinion gained in attractiveness. This is due to the availability of new external instrumentation which makes the conductivity monitoring task easier and more precise. The detector is presented in Chapter 8.

Finally, the early chapters focus on the technological basis of the research done in the context of this thesis. Chapter 2 describes all instrumentation necessary for microchip CE (excluding conductivity detection, which has a chapter exclusively devoted to this). The fabrication of microfluidic devices in glass is outlined in Chapter 3.

1.8 Conclusion

More than a decade after the first examples of microchip-based analysis systems, the field continues to grow and the annual number of related publications to increase. Worldwide efforts to commercialize various microfluidic devices, paired with the successful examples already available on the market, are a second indicator of this technology's impact in the field of chemical analysis.

The research efforts presented in this thesis were made in order to develop two major building blocks, namely a FASS preconcentrator and a conductivity detector, which can be used in a variety of microanalysis systems in the future.

Chapter 2

Instrumentation for Chip-Based Analysis Systems using Laser-Induced Fluorescence and Electro-Osmotic Pumping

Instruments specially adapted to the requirements of microfluidic devices are a key element for research in the field. This chapter describes the development of two types of high-voltage power supplies for microchip CE, one for the use as a standard laboratory instrument, the other conceived for portable, battery-powered operation. These supplies allow rapid voltage control for up to eight fluid reservoirs for precise and reproducible electro-osmotic (EO) pumping and separation processes. Additional circuitry for voltage and current monitoring is discussed, as well as electronic filtering methods to improve the instrument's signal-to-noise ratio. Finally, an optical setup for laser-induced fluorescence (LIF) detection for microchip CE is presented.

2.1 Introduction

Microchip-based analysis systems generally require external instrumentation for their operation. There is on the one hand a high-voltage power supply, which is necessary to provide the driving electric fields for electro-osmotic (EO) pumping and/or electrophoretic separation. Because of the fast fluid transport in microchannel networks, the supply has to be capable of rapidly[5] (at least 200 ms, but faster is desirable) switching potentials and providing voltage control for a num-

---

[5] In order to achieve a good separation resolution, it is important to start the separation with a narrow, spatially confined sample plug (see Section 8.1.4 for a more detailed discussion). A molecule like an amino acid diffuses on average over a distance of ~10 µm in 200 ms, assuming a diffusion coefficient of $2.5 \cdot 10^{-6}$ cm^2/s. A sample plug initially 100 µm long therefore lengthens to 120 µm in this time frame.

ber of electrodes (at least four for most applications, see Figure 1-6). As these requirements are generally not fulfilled by commercial CE power supplies, a new type of control system for chip-based CE and electro-osmotic fluid handling in general will be described in this section.

The second main function that instrumentation for chip-based analysis systems must fulfill is the detection of the analyte. Laser-induced fluorescence (LIF) setups are widely used because of their high sensitivity. This mode of detection does not require extra components like electrodes to be integrated on-chip, though integrated optical elements in microfluidic devices have been reported for improved performance [67-69]. This chapter will briefly describe the LIF detection used, and focus on noise reduction and electronic filtering for improved limits of detection (LOD).

2.2 Laboratory high-voltage power supplies for microchip-based separation systems

To assure reliable operation of chip-based microfluidic devices, it is advisable to control the potential at all reservoirs during device operation. A good example is given in Figure 1-6, showing a typical microchip CE separation with volume-defined plug formation using two pinching flows from the separation channel. In the second step, during separation, a push-back voltage is applied to the side channels to avoid leakage into the separation channel. Leaking may arise from unbalanced filling of the reservoirs, electro-osmotically induced pressure effects in the channel (e.g. see Section 4.2.4), and the like. Apart from the requirement of controlling multiple electrodes simultaneously, potentials need also to be switched rapidly and with precise timing. This is crucial to achieve good reproducibility of solution delivery, and hence of the analysis. It requires not only computer control for both high-voltage programming as well as data acquisition, but also special circuitry on the high-voltage side to assure fast charge transfer when potentials are switched. Table 1 summarizes a number of requirements we believe are necessary for a power supply for microfluidics research.

Based on these requirements, a power supply was designed for research and development of microfluidic devices. Special care has been taken to render the system as flexible as possible and to give the user full control over all system parameters at any time. The result of these efforts is a power supply with the properties listed in Table 2. This supply is the standard instrument used for almost all experiments presented in this thesis.

Although this power supply is relatively compact, flexibility, reliability and safety require a certain footprint. Miniaturized, portable high-voltage power supplies are also possible, however; one example is presented in Section 2.3. This device has been used for microchip CE in conjunction with potential-gradient detection as described in Chapter 8.

General Safety Remark

The high-voltage instruments presented in this thesis operate at voltages presenting a lethal risk. Therefore, proper electrical insulation, warning signs and safety mechanisms such as interlocks should be used to minimize the danger of coming into contact with high voltages, particularly when manipulating the electrodes. None of the above, however, can replace the operator's carefulness and prudence.

Output voltage range	*100 – 5,000 V DC* This value corresponds to a field strength of 20 to 1,000 V/cm for a 5-cm channel. Generally, the supply polarity does not matter; however, for special applications like coupling to a mass spectrometer, the situation might be different.
Max. output current	*200 µA* Due to the small channel cross-sections, currents surpassing the 50-µA mark are rare, except in cases of improper sealing of devices. Typical separation currents are in the range of 10–25 µA. The polarity has to be chosen according to the application: for some, ground potential at the injection end might be necessary, for others, ground is required at the detector end (e. g. for most electrochemical detectors).
Power supplies	*2 independent voltage sources* During the CE separation, it is often necessary to bias the side channels at a medium potential to avoid leakage out of those arms. Therefore, at least two different supplies are necessary. However, Jacobson et al. presented an alternative using only one supply [70].
Number of controllable electrodes	*At least 4, desirable 6 or 8* As it is often desirable to permanently control the potential at each chip reservoir, the number of electrodes should match the number of reservoirs used for the chip.
Operation modes	*Constant voltage or constant current* Constant current operation is typically used for isotachophoresis separations or potential-gradient detection (see Chapter 8). Constant voltage operation is the standard for capillary electrophoresis and electro-osmotic pumping applications, although recently also constant current schemes have been used in order to avoid thermal runaway and better control of microfluidic networks.
Programming	*Real-time programming and read-out for voltages/currents, digital programming for relays* Real-time access to the supply allows for complex processes, where the software can react on measurement data received from the supply (e.g. a voltage can be applied until a certain threshold current is reached, see Section 4.6 for an example).

Table 1*: Requirements for a flexible, laboratory-type high-voltage power supply for microfluidic applications.*

Output voltage range	*100 – 10,000 V DC (negative polarity)*
Max. output current	*1 mA*
Power supplies	*2 independent DC/DC converters*
Number of controllable electrodes	*8*
Electrode states	*High-voltage, ground or floating*
Operation modes	*Constant voltage or constant current*
Switching technique	*Electromechanical high-voltage relays with discharge resistor for fast switching*
Programming	*Real-time, analog programming for voltages/currents, digital programming for relays*
Computer interface	*National Instruments boards:* *AT-MIO-16XE-50: 16-bit analog input and output* *PC-DIO-24: digital input and output*

***Table 2**: Technical specifications of the high-voltage power supply constructed.*

2.2.1 General power supply structure

The HV power supply consists of three distinct building blocks: the HV sources, the relay network and the computer control (see Figure 2-1) . Except for the computer interface cards, all electronic and electromechanical components are mounted in a grounded 3HE-19”-case.

For the generation of high voltages, two independent switched-mode DC/DC converters (PSM 10-103N, Hitek Power, Bognor Regis, UK) were used. They convert the 24-V supply voltage into an output voltage between 100 and 10,000 V. The sources can be operated in constant current or constant voltage mode, the setpoint being defined by an analog control voltage ranging from 0 to 10 V. Both supplies operate independently of each other for increased flexibility and are connected such that four HV connectors are driven by supply 1 while the other four are connected to supply 2.

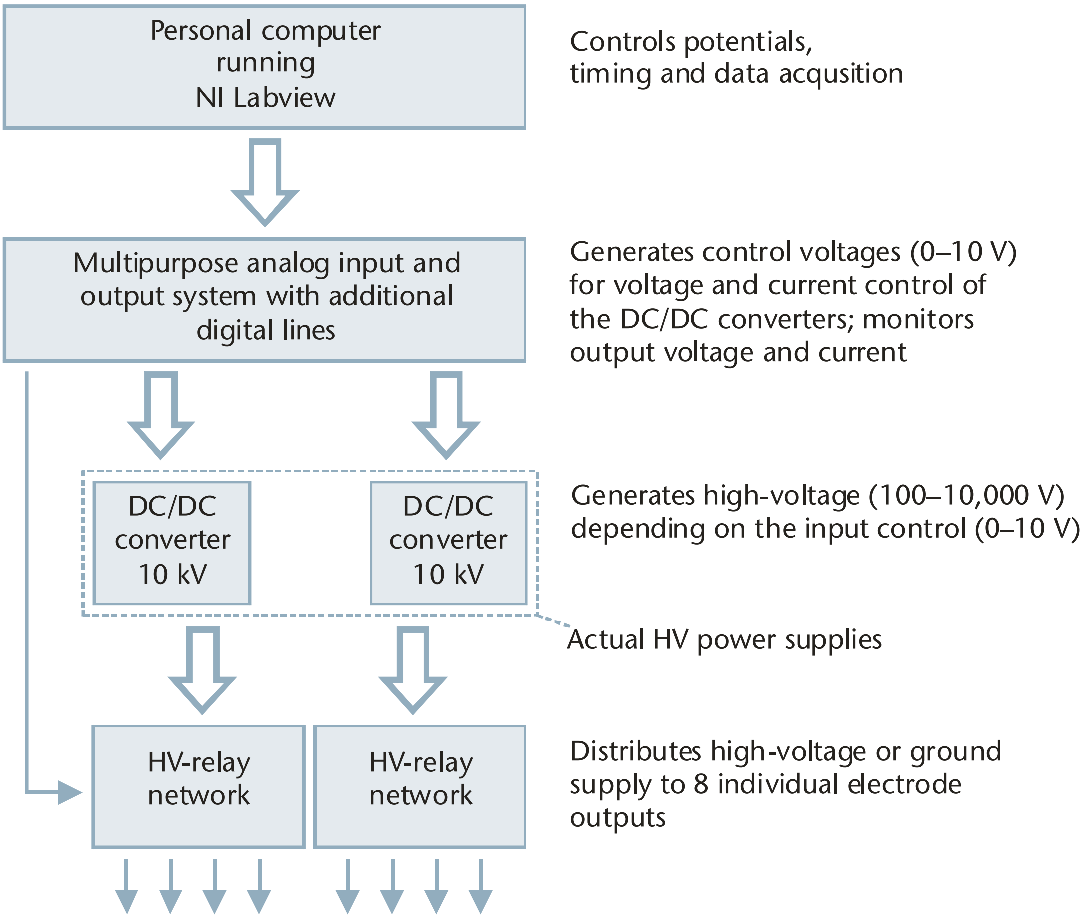

Controls potentials, timing and data acqusition

Generates control voltages (0–10 V) for voltage and current control of the DC/DC converters; monitors output voltage and current

Generates high-voltage (100–10,000 V) depending on the input control (0–10 V)

Actual HV power supplies

Distributes high-voltage or ground supply to 8 individual electrode outputs

Figure 2-1*: Schematic block diagram of the computer-controlled high-voltage power supply.*

The connection between the HV supplies and the HV connectors (which finally are wired to the CE electrodes) is established via a computer-controlled relay network. Each connector is wired to two HV-compatible relays, which connect the respective electrode either to one of the two supplies or to ground. If both relays are in open state, the HV connector is electrically floating. The construction of the relay network, especially of its optocoupled computer interface, is described in more detail in Section 2.2.2.

For control of the power supply, the computer has to be capable of generating analog signals (to define the setpoints for the two DC/DC converters), reading analog signals (to monitor voltages and currents) and to generate digital outputs (to switch the relays). This is achieved by two interface cards from National Instruments. The analog card has the additional purpose of acquiring additional analog signals, like the output of a laser-induced fluorescence detector or the like.

All signal inputs are filtered electronically using an active first-order low-pass filter.

2.2.2 Optocoupled relay control

To be able to electrically control microfluidic systems with as many as eight different reservoirs (and electrodes), a computer-controlled network of high-voltage-compatible relays (type 33921290246, Günther GmbH, Nürnberg, Germany) is used to distribute the various potentials to the electrodes. As mentioned above, two relays are necessary to achieve full control at each electrode, including high-voltage, ground and floating states. Relays are switched by an optocoupled driver stage as described later in this section. Although galvanic isolation by optocoupling is not required per se for this application, it suppresses transient voltage spikes. These appear under certain switching conditions and perturb the computer controlling the power supply. Optocoupled relay control is also described later in conjunction with potential-gradient detection (Section 8.1.2). However, the optocoupler design presented here was developed with a different motivation than the floating computer interface presented for potential-gradient detection.

Figure 2-2 schematically depicts the connections made between one of the two DC/DC-converters and an electrode. Both relays are controlled by the PC using a digital card and the optocoupling circuitry described below. Relay 1 is used to connect the HV output of the supply to the electrode (upper left in Figure 2-3), while relay 2 is used to create a ground connection. If both relays are open, the electrode remains in an unconnected, floating state and no current flows. The fourth state, in which both relays are closed, is forbidden, as it short-circuits the DC/DC converter.

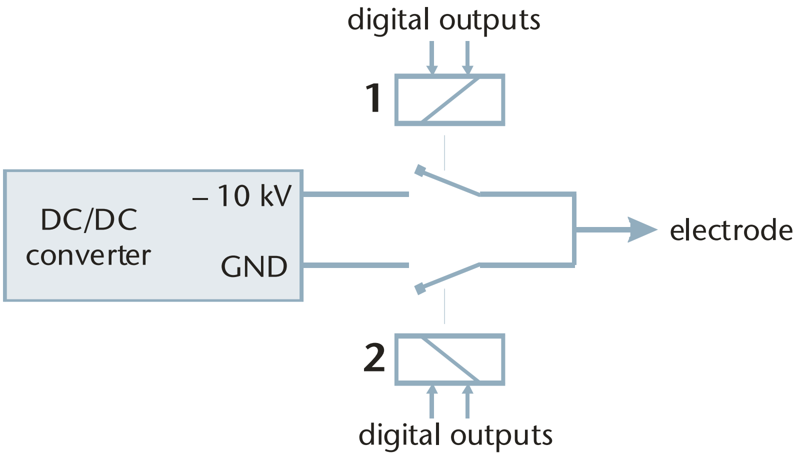

***Figure 2-2**: Two relays make either HV (relay 1), ground (relay 2) or floating connection with the electrode. Relay control is achieved by the PC via an optocoupled interface circuit.*

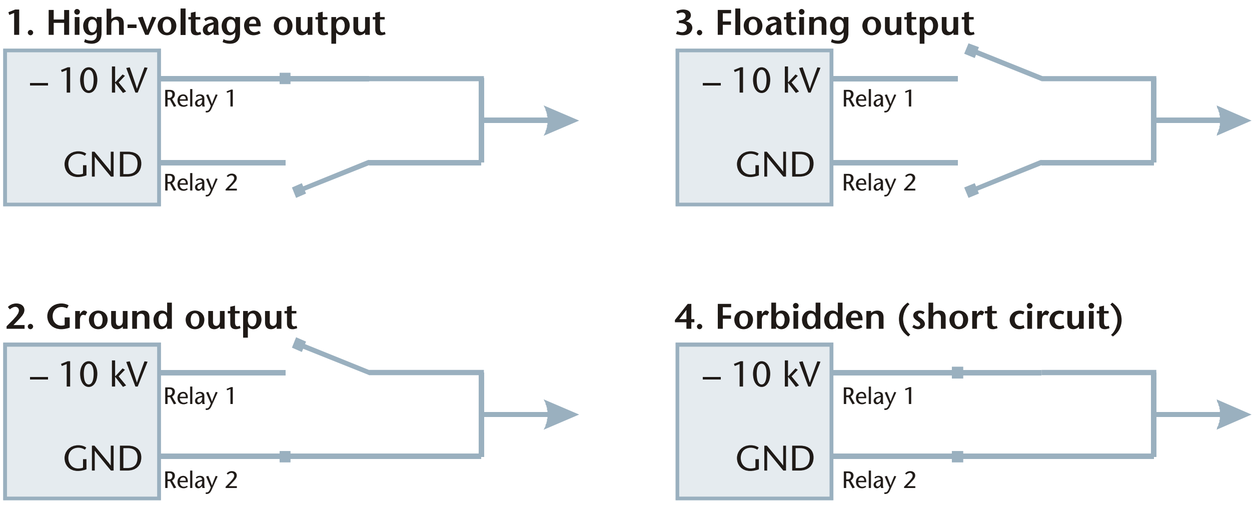

***Figure 2-3**: The three operating states of the relays are: 1) HV output, 2) ground output and 3) floating output. The fourth case, where both relays are closed, is forbidden, as it causes a short circuit.*

Although the components used for the relay network are compatible with the voltages used, closing and especially opening relays under high voltage conditions causes electrical transients that make operation difficult. When the high-voltage supply is galvanically connected to a sensitive system like a personal computer, switching transients may even cause the computer to lock up, making a reboot necessary.

In order to reduce this kind of problem, the driving circuit for the HV relays was galvanically separated from the computer and its digital control hardware. Galvanic separation is generally achieved by optocouplers which convert an electrical signal into light by a light-emitting diode (LED) and back into an electrical current using a photo-transistor. Information-carrying signals can thus be transmitted from one device to another without the requirement for a common, galvanic contact.

Figure 2-4 presents the complete driving circuit for one electrode, including two relays. The digital input required from the computer has TTL level (off = 0 V, on = 5 V) and is buffered by an inverting standard logic gate (IC1 and IC3, 74LS241). This gate drives the optocoupler LED (part of IC2 and IC4, ILQ74) via the series resistors R1 and R3 (330 Ω). The light signal switches the photo transistor part of the optocouplers, which causes the signal to be transmitted via the galvanic barrier into the gates of field-effect transistors T1 and T2 (BS170). These are needed to provide the current necessary to drive the electromagnetic coils of the HV relays Rel1 and Rel2 (24 V, 70 mA). Resistors R2 and R4 (39 kΩ) act as pull-downs to keep T1 and T2 switched off while the optocoupler transistor is off.

As mentioned above, it is important to assure that Rel1 and Rel2 are not activated simultaneously, as this will short circuit the DC/DC converter. Although this issue is mostly related to the control software, a very simple protection circuit can be implemented to avoid problems. The two standard silicon diodes D3 and D4 (1N4148) are connected to the outputs of the buffer stage IC1/IC3 in an exclusive-or connection, which allows at most one relay to be switched on. To understand the operation, we assume that the upper TTL line is active in order to switch on Rel1. The 5-V level is inverted to 0 V by IC1 and drives the optocoupler LED, which in turn activates the circuitry on the right side of the coupler. At the same time, diode D4 is forward-biased and pulls the potential at the node between R3 and IC3 to roughly 0.7 V. As this voltage is not enough for the LED of IC3 to work, the second relay cannot be activated. As the circuit works the same way in the other direction, both relays will be off and the electrode floating, if the control software tries to activate them both simultaneously.

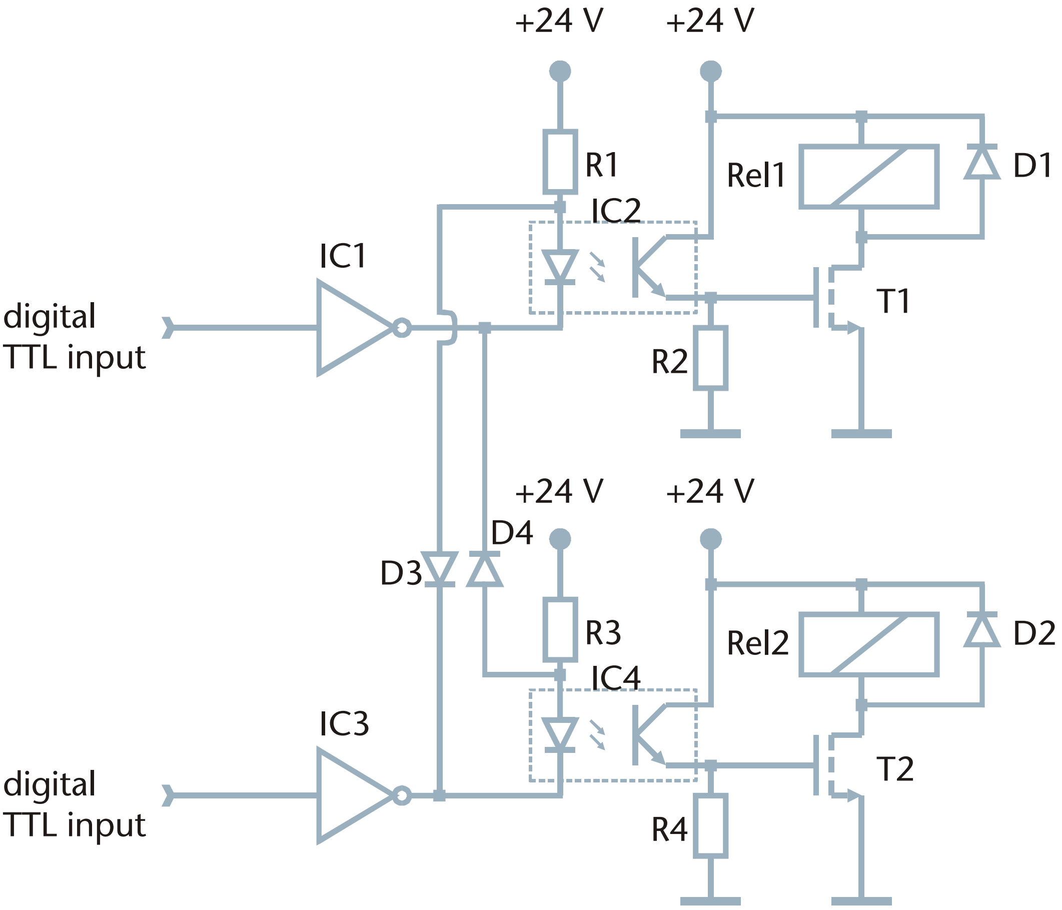

***Figure 2-4**: Optocoupler-based driving circuit for two HV relays, including a wired exclusive-or gate to avoid both relays being activated at the same time (causing a short-circuit).*

2.2.3 Rapid voltage switching by an additional discharge resistor

Precise flow handling in electrokinetically driven microfluidic systems requires rapid (<200 ms) and reproducible control over voltage changes. While it is easy to provide the required low-voltage control signals using a PC and analog interface cards, the high-voltage DC/DC converters react with a certain delay. This delay is especially long, if the voltage change is negative (i.e. from a higher to a lower voltage), as the output capacitance of the supply has to be discharged. In the case of microfluidic systems, the resistive load imposed on the supply – that is the electrolyte-filled microchannel – is generally very low and has a resistance in the order of 10s to 100s of MΩ. This causes extremely long discharge times, which are close to the open-circuit values for the respective DC/DC converters.

To illustrate the problem, Figure 2-5 shows the discharge curve over time for the PSM10-DC/DC converter used in the standard power supply when connected to a

44-mm-long microchannel (50 µm wide, 12 µm deep) filled with 10 mM MES/His buffer[6]. It takes nearly 5 s for the voltage to drop below 10% of its original value of 2 kV. As the electro-osmotic flow continues during this time and as the discharge time varies with buffer conductivity, precise flow control is difficult to obtain.

The solid line in the same figure represents the resulting voltage profiles with a 50-MΩ discharge resistor connected in parallel to the output of the DC/DC converter. As a result, the settling time is reduced from 5 s to 160 ms. It should be noted that the resistor does not influence the rise time (charging) of the power supply, while considerably reducing the discharge time. It is therefore always recommended to use a discharge resistor, as it contributes to better voltage control in general.

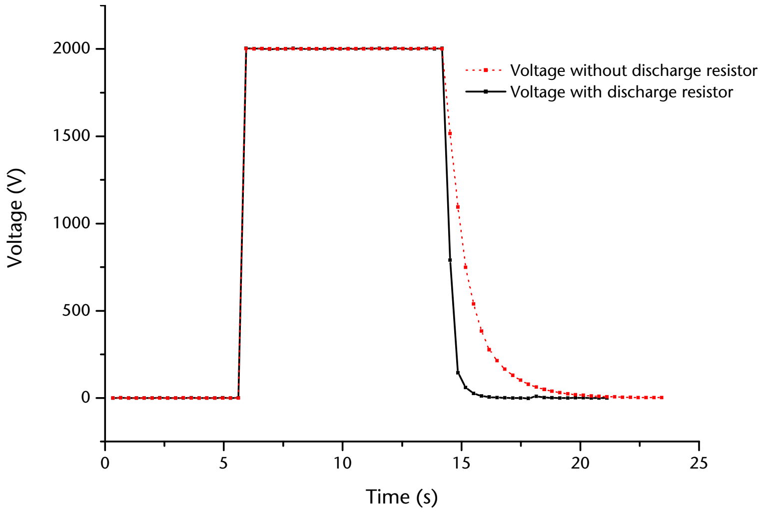

***Figure 2-5**: Measured voltage profiles for a power supply equipped with a 50-MΩ discharge resistor compared to one without. Note that the discharge time is considerably reduced, while the charge time remains unaltered.*

To understand the effect of the discharge resistor better, the voltage V across a capacitance C during discharge over a parallel resistor R can be calculated mathematically as:

$$V(t) = V_0 e^{-\frac{t}{RC}} \tag{1}$$

with V_0: voltage at time 0

t: time

---

[6] The buffer preparation is described in detail in Section 5.7.1.

The PSM10 DC/DC converters used in this work have a maximum stored charge of about 15 µC, which gives a capacitance of 1.5 nF for 10 kV ($C=Q/V$). Assuming a typical microchannel resistance of 250 MΩ, the time constant RC becomes 0.375 s and it takes about 900 ms for the output voltage to drop below 10% of its original value (see dashed line in Figure 2-6).

As pointed out above, a solution to this problem is an additional resistor between the high-voltage and ground output of the DC/DC converter, which assures a quiescent current of about 20% of the maximum output current of the converter module. During regular operation, the additional current does not harm the experiment going on, although current measurements have to be corrected for it if used to monitor device operation. If the voltage is changed, this resistor allows a rapid discharge of the internal capacitances. The calculated result for a discharge resistor value of 50 MΩ in parallel to the 250 MΩ of the microchannel (load resistance is 42 MΩ and $RC = 0.0625$ s) is depicted in Figure 2-6 as a solid line. The discharge time needed to drop below 10% of the original voltage is reduced from 900 ms down to 140 ms, which is in good agreement with the measured data in Figure 2-5.

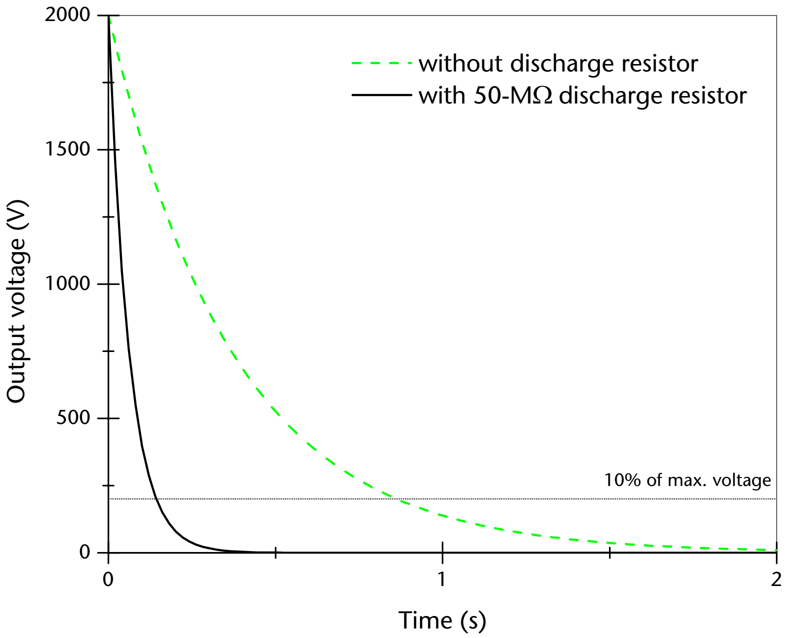

***Figure 2-6**: Calculated output voltage drop from 2 kV to 0 V with and without an additional discharge resistor. A stored charge of 15 µC and a resistive load of 250 MΩ is assumed.*

The time until the output voltage drops below 10% of its original value is 900 ms without and 140 ms with the discharge resistor.

2.2.4 Current and voltage monitoring

Current monitoring is one of the most powerful and essential diagnostic tools for measuring fluid flow in microfluidic devices. First of all, it allows verification of whether the microchannel is filled properly and not obstructed by air bubbles or particles. In an even broader sense, it indicates whether all electrical connections have been properly made and electrodes are correctly positioned in their respective reservoirs.

Another important application of this technique is the measurement of the electro-osmotic flow velocity v_{eo} as proposed by Huang et al. [71]. Initially, the channel is filled entirely with a buffer solution of a given conductivity. To perform the measurement, the inlet reservoir is filled with a slightly diluted (~95%) version of the buffer in the channel and a voltage is applied to both ends of the channel. During the process, the current is plotted versus time, leading to a diagram like the one depicted in Figure 2-7. While the buffer in the channel is being replaced with the dilute solution from the reservoir, the current drops linearly as a function of displaced channel volume.

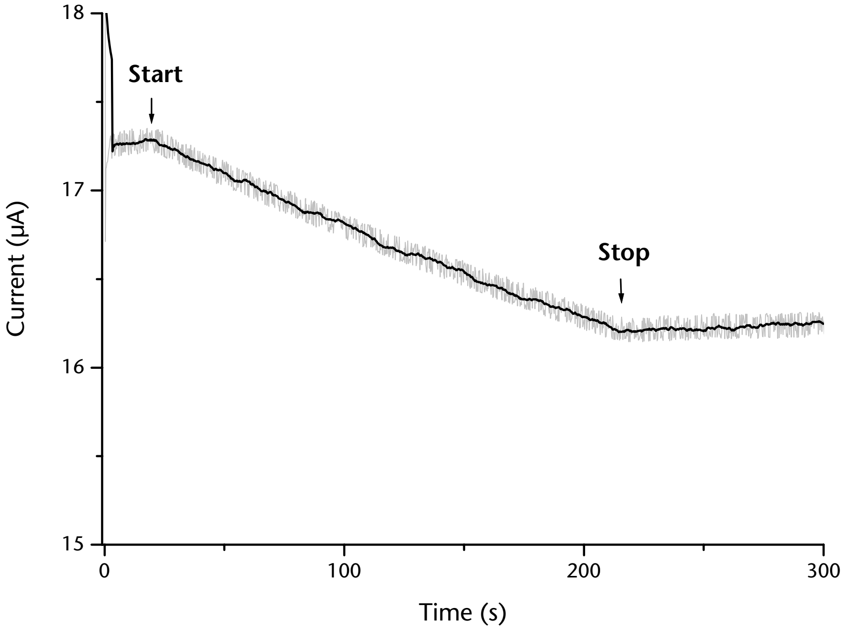

Figure 2-7: Measurement of electro-osmotic flow velocity in a 145-mm-long microchannel using current monitoring. Initially, the channel was filled with carbonate buffer (32 mM, pH 9.6), which was subsequently replaced by 95% dilution of the same buffer. The dark trace shows the signal after low-pass filtering, the gray trace is the unfiltered signal.

Once the whole channel is filled with the 95% buffer, the current should stabilize. v_{eo} can then be calculated as:

$$v_{eo} = \frac{L}{\Delta t} \tag{2}$$

with L: length of the channel

Δt: time between the start of filling and complete filling of the channel with low-conductivity buffer

Although many HV power supplies have a current monitor output, precise measurements generally require an alternative circuit. The main reason for this is the large current range most supplies provide (1 mA for the PSM10), which makes it difficult to detect current changes in the low-µA range. However, current monitoring can be easily performed using a simple series resistor at the grounded end of the microchannel as depicted in Figure 2-8. This sensing resistor converts the electric current through the microchannel into a voltage which can be monitored using a standard voltmeter or data-acquisition card. The resistor can be chosen by defining the conversion factor (e.g. 1 µA should cause a voltage drop of 1 V) following Ohm's law ($R=V/i$, e.g. 1 MΩ). It is important to make sure that the resistor value is much smaller than the electrical resistance of the filled microchannel as this would influence the effective electrical field in the channel otherwise. Also, the internal resistance of the voltmeter (load resistance) has to be much higher than that of the sensing resistor to reduce current division between the two resistances in parallel.

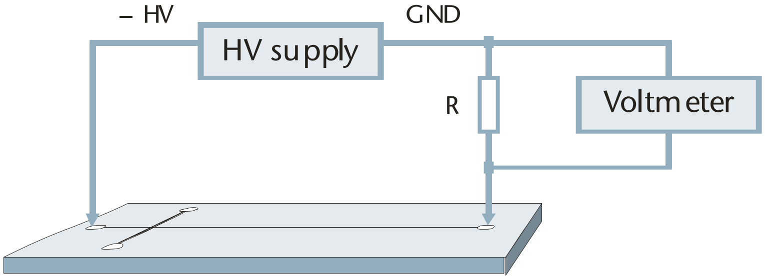

***Figure 2-8**: A simple current monitoring setup measuring the voltage drop across a sensing resistor connected to the grounded end of the microchannel.*

In practice, it is advised to add filtering and protection circuitry to the simple setup depicted in Figure 2-8 in order to improve both precision and reliability of the system. Filtering can be achieved by a simple, passive low-pass filter based on an RC group as depicted in Figure 2-9a. The filter cut-off frequency f_c (defined as the frequency at which the output voltage is $1/\sqrt{2}$ or –3 dB of the input voltage) is equal to:

$$f_c = \frac{1}{2\pi RC} \tag{3}$$

After Laplace transformation, the filter transfer function (the ratio between output and input voltage) in the frequency domain can be written for the complex Laplace variable s as:

$$\begin{aligned} A_v(s) &= V_{out}/V_{in} \\ &= \frac{1}{sRC+1} \end{aligned} \tag{4}$$

The frequency response of this 1st order filter is depicted as a Bode plot in Figure 2-10 as a result of a simulation (Electronics Workbench 5.0, Electronics Workbench Ltd., Toronto, Canada) using the component values indicated in Figure 2-9. For frequencies higher than f_c, the gain drops by a roll-off of -20 dB/decade[7], which causes a suppression of higher frequency components.

Better filtering can be achieved by using higher order filters, which have a stronger roll-off. Figure 2-10 compares the frequency response of 1st and 2nd order filters, the latter having a roll-off of – 40 dB/decade. The frequency response depicted in the diagram was obtained from a simulation of the active Butterworth circuit shown in Figure 2-9b. As an active filter, it has the advantage of a low-impedance output driven by the op-amp, so that more filters can be cascaded for improved filtering performance without interfering with each other.

---

[7] dB=20log$_{10}$(V$_2$/V$_1$) where V$_1$ and V$_2$ are the two signal amplitudes. At gain of –20 dB the output amplitude is only 10% of the input amplitude.

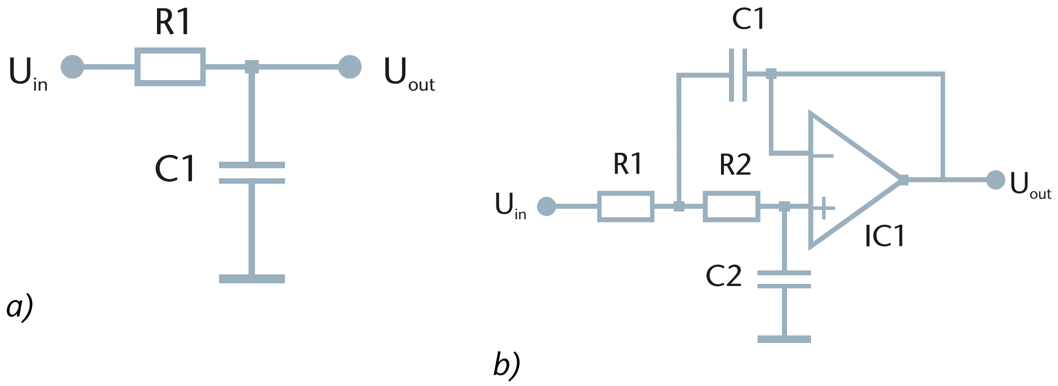

***Figure 2-9**: a) 1st order, passive low-pass filter (example for f_c = 15 Hz: R1 = 39 kΩ, C1 = 270 nF); b) 2nd order, active, Butterworth low-pass filter (example for f_c = 15 Hz: R1 = R2 = 39 kΩ, C1 = 380 nF, C2 = 190 nF, IC1 is a standard operational amplifier, e.g. AD711)*

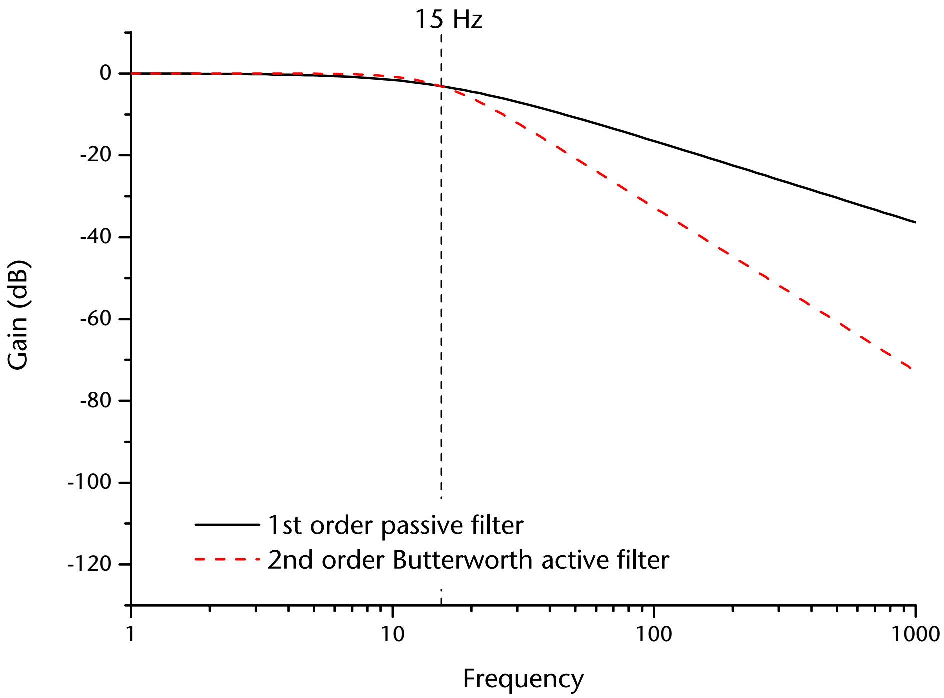

***Figure 2-10**: Bode plot of the gain for a 1st order, passive low-pass filter and a 2nd order, active version. Both have a cut-off frequency of 15 Hz. It is obvious that the damping of unwanted higher frequency components is much more efficient for the 2nd order filter.*

To protect the filter and voltmeter from overvoltage across the resistor due to high peak currents, a high-conductance, low-leakage diode (e.g. FDH333 from Fairchild Semiconductor, South Portland, ME, USA) can be added to short-circuit transient over-voltage peaks between the filter input and the negative supply voltage of the electronics.

As almost no commercial meters for high-voltage monitoring are available, a custom solution was developed for this application as well. Generally, standard voltmeters can be adapted to a higher voltage range by combining with a voltage divider, as depicted in Figure 2-11. The measurement voltage V_m can be calculated by:

$$V_m = V_{HV} \frac{R_2}{R_1 + R_2} \tag{5}$$

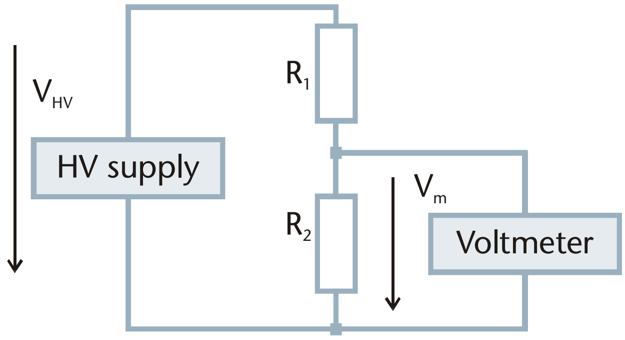

***Figure 2-11**: A resistive voltage divider allows the measurement of high voltages using a standard voltmeter.*

For a conversion ratio of 1 kV to 1 V, the fractional term needs to become 1/1000, which leads to $R_1 = 999R_2$. A reasonable combination to measure voltages up to 10 kV would be R_1 = 100 MΩ and R2 = 100.1 kΩ. Note that the high-ohmic resistors have to be HV compatible to avoid electrical breakdown (resistors used in this work were obtained from Nircom Electronic, Novazzano, Switzerland).

2.3 Portable, battery-power high-voltage supplies

An important focus of miniaturized analysis systems is their application as autonomous, portable instruments for field-based environmental monitoring or point-of-care diagnostics at the patient bedside. However, despite efforts in miniaturization of the fluidic device, the external instrumentation required for operation generally still compromises portability in terms of volume, weight and power consumption.

In the framework of this thesis, a small, portable control system for microchip-based capillary electrophoresis, or µCE controller, has been developed[8]. The instrument features are summarized in Table 3 and a block diagram is given in Figure 2-12. Different from the power supply described in 2.2, this device features one miniature DC/DC converter (GP50, EMCO Highvoltage, Sutter Creek, CA, USA) per electrode, thereby avoiding bulky HV relays and related electronics. At the same time, the flexibility is improved as potentials at all four electrodes can be controlled independently. Center piece of the instrument is a microcontroller, type 386EX (Intel, Santa Clara, CA, USA), which consists of an Intel-PC-compatible microprocessor core enhanced by a large number of in- and output interfaces. These allow direct interaction between the microcontroller and external components like keyboards, LCD displays and the HV power supply.

The system is controlled by an embedded software application written in Borland TurboPascal 6 (Borland, Scotts Valley, CA, USA) and translated for the 386EX-environment using the GMC368.8 locator (GMC GmbH, Berlin, Germany). The software is used to set separation parameters (separation/injection voltage and time, floating or pinched injection, etc.). At the same time it has the capability to acquire an analog signal from a detector and store the data for later processing. As an example, an opto-electronically decoupled potential-gradient detector was implemented in the instrument (see Chapter 8). Archived electropherograms can later be transferred to a regular PC via a serial RS232 interface for analysis. For this purpose, a small Windows-based application has been developed in Delphi 3 (Borland) to receive the data files from the µCE controller.

---

[8] The µCE controller was mainly developed by Olivier Scherler (HV control and microcontroller programming) and Stephan Beer (potential gradient conductivity detector), who worked on this device during their semester projects at IMT, Neuchâtel. Their help is gratefully acknowledged.

Output voltage range	*50 – 5,000 V DC (negative polarity)*
Max. output current	*200 µA*
Power supplies	*4 independent DC/DC converters (EMCO GP50)*
Number of controllable electrodes	*4*
Electrode states	*High-voltage or floating (a ground connection is made by setting the output voltage to zero)*
Operation modes	*Constant voltage*
Switching technique	*Electrodes are directly driven by the DC/DC converters*
Programming	*Microcontroller-based instrument for HV control and timing as well as detector data acquisition (GMC386.8 microcontroller development system, GMC GmbH, Berlin, D)*
Computer interface	*Serial RS232-interface*
Size	*14 x 23 x 3 cm^3*

***Table 3**: Technical specifications of the portable µCE control system*

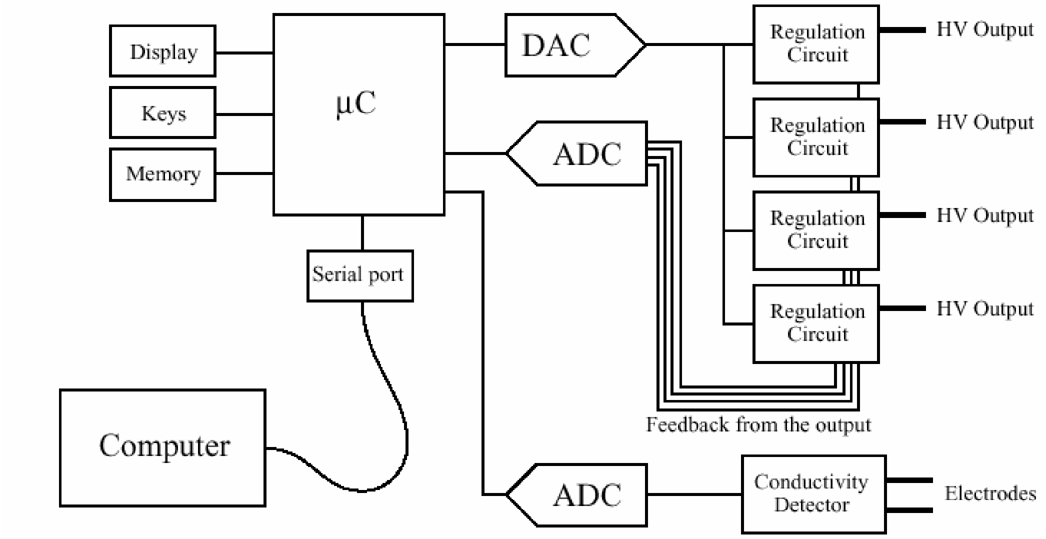

***Figure 2-12**: Block diagram of the portable µCE controller. Four HV outputs are driven by independent regulators, which are in turn controlled by a microcontroller (µC). Interfacing is achieved via a four-channel digital-analog converter (DAC) and eight-channel analog-digital converter (ADC). An analog signal from an external detector (here a potential gradient conductivity detector) can be acquired during the process. An LCD display and four keys serve as the user interface for the stand-alone controller. For data processing, archived electropherograms can be downloaded onto a PC via an RS232 serial interface.*

The miniature DC/DC converters operate from a 5 V supply at a maximum current of 150 mA and are therefore perfectly adapted for battery-driven operation. As the output is proportional to the input voltage, but not precisely regulated, an external control circuit, as depicted in Figure 2-13 for a single channel, was conceived to assure accurate voltage application. The control voltage generated by the microcontroller is applied as set-value to the input of the operational amplifier U2 (OP07C), which is used as a proportional controller of the output voltage. The output of U2 drives the DC/DC converter U3 via the bipolar power transistor T2 (BD237). The actual HV output is monitored using a resistive voltage divider as described in Section 2.2.4 and fed back into the inverting input of the regulator U2. The capacitor C1 is necessary to prevent oscillations at high output voltages and the low-voltage relay Rel1 allows deactivation of the DC/DC converter which sets the HV output into a floating state. Different from the standard instrument described in Section 2.2, no additional relays are integrated for an electrode ground connection to save space. Instead, the miniature DC/DC converters is set to its lowest voltage (~ 2 V, as a small, residual voltage remains), which is close enough to ground potential. Finally, for monitoring purposes, the voltage feedback signal is also made available for the microcontroller via the buffer amplifier U1 (OP07C).

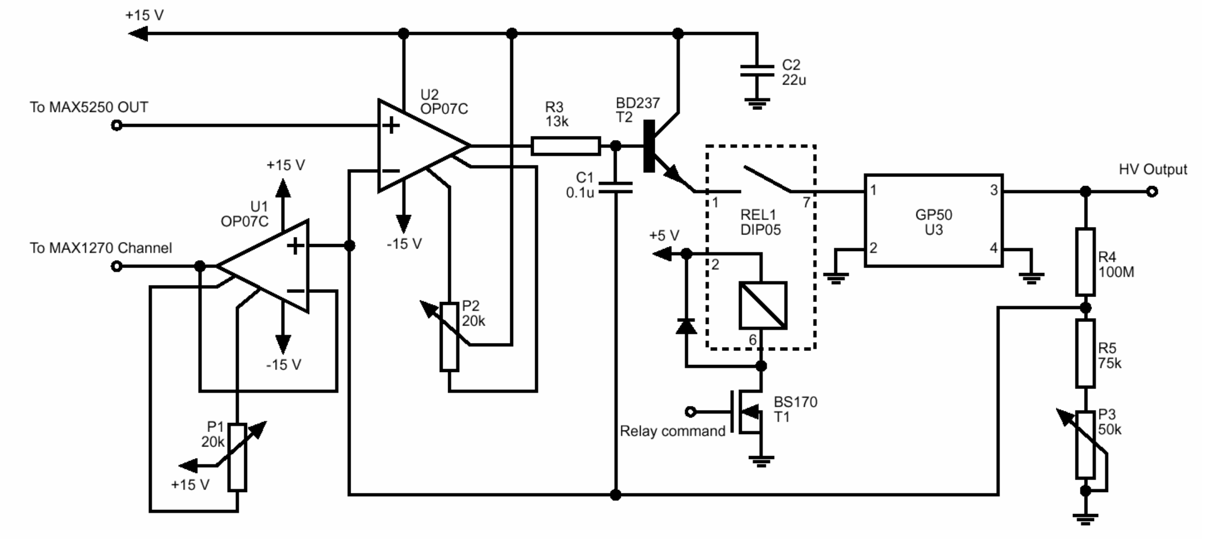

Figure 2-13: Control circuit for one electrode. See text for explanation.

2.4 Laser-induced fluorescence detection

Laser-induced fluorescence (LIF) is the dominant detection method for microchip-based analysis devices. Its outstanding sensitivity and an increasingly wide choice of fluorescent markers for non-fluorescent biomolecules make this technique very attractive. Also, as a non-contact detection technique, no extra components have to be integrated on-chip and all detector instrumentation remains external for most cases. This is especially interesting for disposable chips that require low-cost fabrication procedures, as expensive detector components are reused. It should be noted, however, that integrated, optical elements can be an interesting solution to improve detection limits [67, 72].

Although the LIF setup presented in this section is not entirely new, it is nevertheless worth describing in more detail. The target fluorophore for the experiments was fluorescein, which uses 488 nm as an excitation wavelength and emits at 514 nm.

2.4.1 Excitation

As they are perfectly adapted to the fluorescein absorption spectrum, a 10 mW argon-ion laser (Ion Laser Technology, Salt Lake City, USA) is used for fluorescence excitation (see Figure 2-14). A 125-µm-core-diameter optical fiber with FC-connectors (GMP SA, Renens, Switzerland) connects the laser output to the focusing optics. The latter consists of two lenses, the first having a focal length of 60 mm, the second, 80 mm. Lenses, fiber holders and related components were obtained from Linos AG (formerly Spindler & Hoyer, Göttingen, Germany) and mounted into Linos' Microbench system for optical setups. An off-axis excitation scheme was chosen that projects a ~40-µm-wide spot onto the plane of the microchannels impinging at an angle of 45°. The laser focusing system was mounted on a manual x-y stage for precise alignment of the laser spot with the microchip.

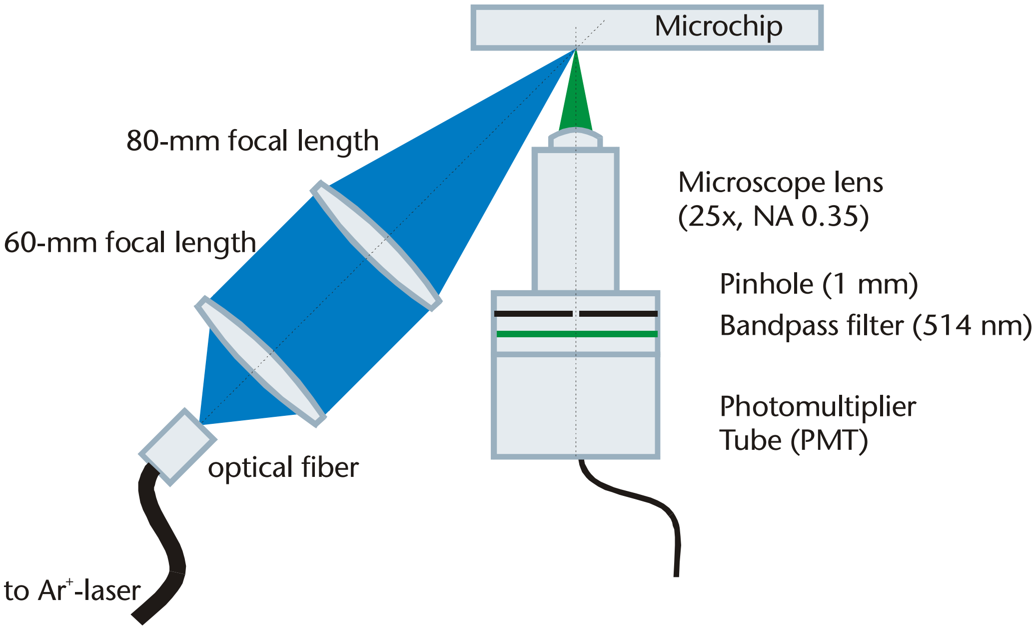

***Figure 2-14**: Laser-induced fluorescence setup for microchip-based CE. Off-axis illumination was used.*

2.4.2 Fluorescence measurement

The subsystem for fluorescence measurement is based on an inverted microscope, which is placed vertically under the chip holder. All components are mounted onto an X95 rail (Linos) and can be moved vertically for focusing of the microscope. The chip or wafer holder is additionally mounted on an x-y-stage to allow precise alignment of the microchannels with the microscope.

The fluorescence signal is collected by a microscope objective (NPL FL, 25×, NA 0.35, Leica, Glattbrugg, Switzerland) with a long working distance, which is necessary to avoid interference with the incident laser beam. Also, the use of long-working-distance microscope lenses prevents electrical arcs between chip and lens body when working from the top side of the chip, close to the biasing electrodes. To select only the fluorescent light, an interference-type 514-nm band-pass filter (Melles-Griot 03FIL004, 10 nm full-width-at-half-maximum, Irvine, CA, USA) is used. This filter is mounted in a custom-made housing together with a 1-mm pinhole, which spatially selects a 40-µm-diameter area from the microscope image for detection. Both wavelength and spatial filtering reduce noise caused by stray light from either the excitation source or ambient light.

The filtered light is finally converted into an electrical signal by a photomultiplier tube, model H5701-50 (Hamamatsu, Schüpfen, Switzerland). To remove high-frequency noise, the acquired signal is analog low-pass filtered either by a simple R-C filter (cut-off at 15 Hz, as presented in Section 2.2.4) or by a more advanced higher-order filter as presented in the next section. After analog-to-digital conversion at 12 bit, a numerical fifth-order algorithm (cut-off at 25 Hz) was applied within the Labview program used for data acquisition. The limit of detection for the optical setup was found to be 5 nM for fluorescein-isothiocyanate-labeled amino acids at a signal-to-noise ratio of 3 using the higher-order filter.

2.4.3 Enhanced analog filter for LIF detection

To improve detection limits, enhanced noise reduction is an important issue. While the filtering strategies presented in Section 2.2.4 are sufficient for current measurements, the detector response should always be acquired with the best noise rejection possible. For this purpose, an enhanced analog filter was conceived for LIF detection. Different from the purely analog filters described above, this filter uses a commercial integrated circuit based on the switched-capacitor (SC) technique. SC-filters show excellent performance and require only few external components for higher-order filter architectures. One drawback, however, is the influence of the internal switching clock (200 kHz) on the output signal (clock feed-through), which raises the noise floor.

The central component of the circuit, depicted in Figure 2-15, is the integrated circuit LT1063[9] (Linear Technology, Milpitas, CA, USA), an integrated, DC-accurate, 5th-order Butterworth low-pass filter with an internal wide-band noise of 95 μV_{RMS}. The interesting feature of this device is that the cut-off frequency is selected by a built-in oscillator. By changing the external RC group of the oscillator (Rclk and Cclk in Figure 2-15), the cut-off frequency can be tuned to:

$$f_c = \frac{1.07}{100RC} \tag{6}$$

---

[9] Datasheet available at www.linear.com

Figure 2-16 shows the measured filter performance as a function of frequency taking into account internal noise sources of the filter.

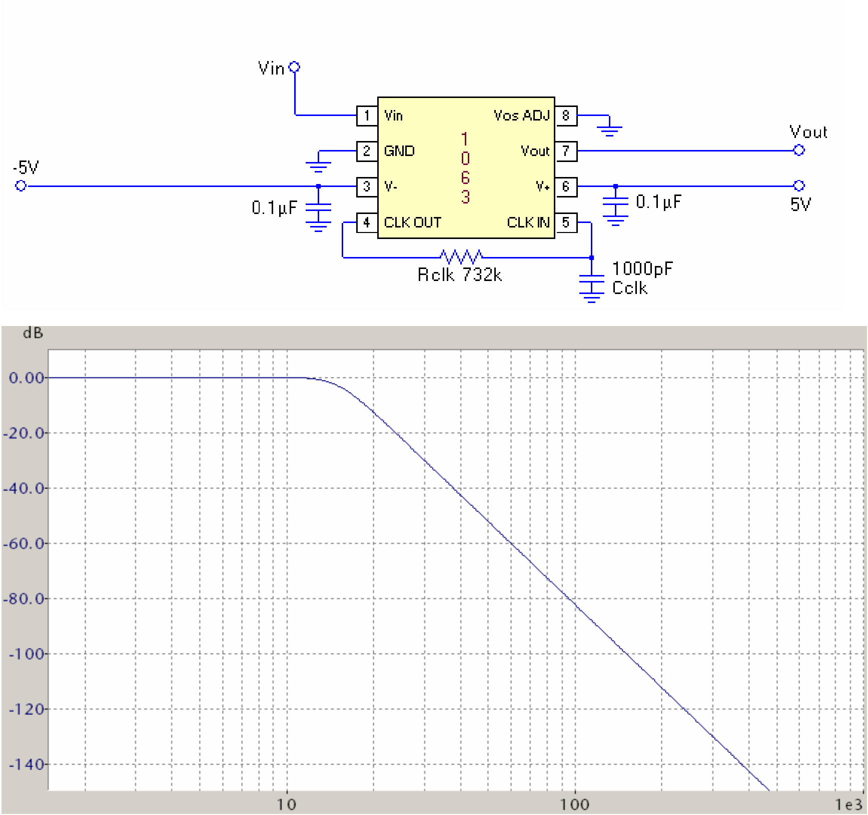

***Figure 2-15*:**

a) Schematic circuit of the 5th-order low-pass filter with a cut-off frequency of 15 Hz and a roll-off of -100 dB per decade.

b) Theoretical frequency response of the filter. In reality, suppression of high-frequency signals is limited to 75-80 dB due noise sources of the filter itself.

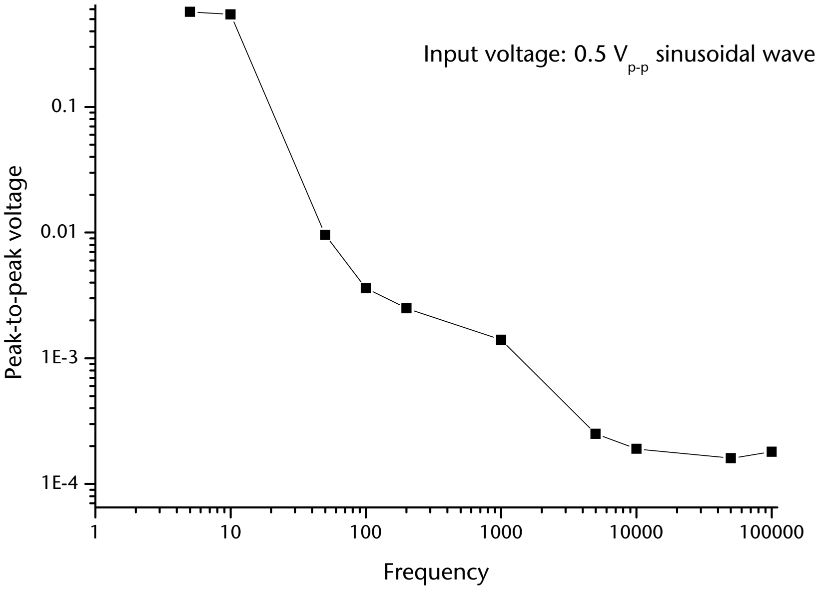

***Figure 2-16*:** *Signal at filter output as a function of frequency. The input signal was a sinusoidal wave with 0.5 V_{p-p}. As mentioned in the text, the filter reaches the noise floor caused by internal noise sources such as Johnson noise or clock feed-through, which limit the maximum high-frequency suppression.*

The impact of this excellent filter on the signal noise is presented in Figure 2-17 for the background signal of the LIF detector presented earlier. Using a cut-off frequency of 12 Hz, the noise floor is reduced by 12.5 from around 1 mV to 80 µV.

This is only one order of magnitude higher than the limiting resolution of the analog-to-digital converter used in the setup (6.1 µV for the 200 mV measurement range).

The design presented here can be used as a standard building block for data acquisition systems in general. However, especially for filters with a steep roll-off like the one presented here, care must be taken when choosing the cut-off frequency. Lowering f_c reduces the noise as the detector bandwidth is limited. However, if it is too low, peak distortion or even suppression may occur, depending on the rise time of the signal. This is particular important for microchip separations, where peaks are generally much sharper than in conventional devices. For the LIF-CE of amino acids using the setup presented earlier with the chip layout described in Section 4.4.1, it was found that the peak maximum was visibly reduced for cut-off frequencies below 10 Hz.

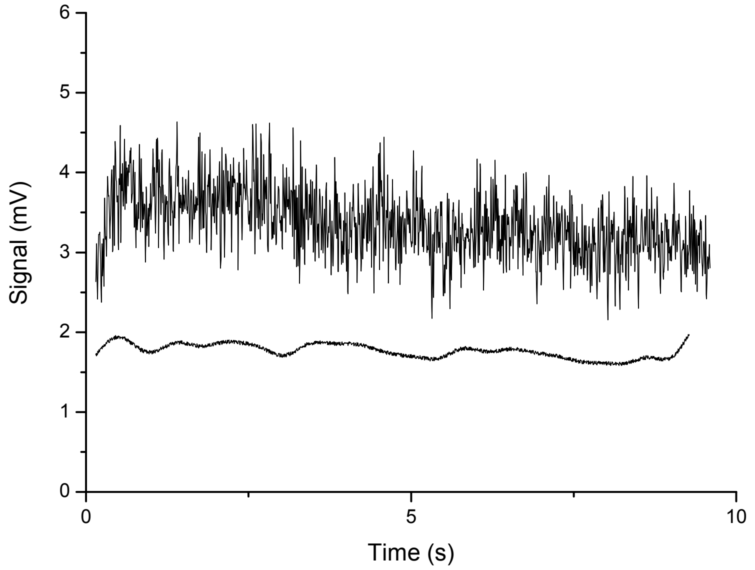

***Figure 2-17**: Background signal obtain from the photomultiplier in the LIF setup depicted in Figure 2-14. The upper trace shows the signal after analog filtering using the simple RC combination in Figure 2-9a (noise ~1 mV_{p-p}). Below, the result for the 5^{th}-order filter in Figure 2-15a, leading to a noise floor around 80 μV_{p-p} corresponding to a 12.5-fold improvement.*

2.5 Conclusion

For successful microfluidic device operation, specialized instrumentation is recommended. This applies to both power supplies as well as detector setups and related data acquisition electronics. The circuits and devices presented in this chapter have proven to be useful in the framework of this thesis and might also be a good basis for other experiments in the field – either as entire circuits or as building blocks for other circuits.

Chapter 3

Fabrication of Microfluidic Devices in Glass Substrates

Glass and fused silica have a number of interesting material properties that make them a popular choice for the fabrication of microfluidic devices. Although polymer-based microchips have a high potential as low-cost and disposable devices, glass has chemical stability and a long history of use by chemists generally. All microfluidic devices presented in this thesis are based on Pyrex 7740 glass. The basic fabrication procedure for a sealed microchannel network is presented here. The use of polysilicon as masking material for wet etching in hydrofluoric acid differentiates this process from that used by most groups, and makes it very short and efficient.

3.1 Introduction

Glass is one of the most inert materials used for the fabrication of labware, withstanding most acids, bases, and solvents. It is therefore no wonder that glass is also one of the preferred substrates for the fabrication of microfluidic devices. Its chemical stability is paired with physical strength and good optical characteristics, which are only insufficient for operation in the UV range. For fluorescence-based applications, the low auto-fluorescence of most glass types is a relevant feature. For electrokinetic separation systems such as capillary electrophoresis (CE) and electrochromatography (CEC), glass is interesting because of its electrical insulating property, which makes the application of high voltages possible. The glass surface is also one of the best characterized interfaces in chemistry, with a vast variety of chemistries at hand for surface modification and functionalization. This know-how allows to reduce the drift in migration times in CE due to surface changes [73, 74], for example, or to improve separations by dynamic coatings [75-

79]. Last but not least, glass is available in the form of polished wafers compatible with microelectronic fabrication equipment, and can therefore be easily worked with in standard cleanroom environments.

It should be noted that all of the points mentioned above as well as most of the fabrication technology described in the following sections do not only apply to glass but also to fused silica or quartz wafers. These are especially interesting for applications with optical detection in the UV range. However, this comes at the cost of higher annealing and softening points. Therefore, fusion bonding for sealing the microfluidic network becomes more difficult.

This chapter covers our preferred fabrication procedure for microfluidic devices in Pyrex 7740 glass in detail. This technology is used for most devices throughout this thesis. All other chapters will only mention differences to the basic procedure explained here.

3.2 Glass micromachining

Microchannel structures were designed using the layout software CleWin (WieWeb Software, Hengelo, The Netherlands). Standard glass/chrome masks with a 1.2-µm resolution were fabricated on the basis of the layout files by Deltamask (Enschede, The Netherlands) using a DWL200 Laser Beam Pattern Generator (Heidelberg Instruments, Heidelberg, Germany). Alternatively, transparency masks may be used for rapid prototyping. These were ordered from DIP-Repro (Lausanne, Switzerland) and were generated by an Agfa Avantra imagesetter at 3,600 dots-per-inch (7.5 µm dot size)[10]. For compatibility reasons, the CIF-layout file produced by CleWin had to be converted into Postscript using the PostCIF conversion software (now sold by LinkCAD, Aptos, USA). To be able to load the transparency mask into an commercial wafer aligner, the film was cut to a square 115 mm on a side

---

[10] To avoid rastering artifacts, only linewidths matching multiples of the actual grid size (1 inch/3600 dpi =7.05 µm) were used for all designs made for transparency masks (e. g. 7 µm, 14 µm, 21 µm, etc.). Arbitrary linewidths are printed either thicker or thinner than desired, causing discrepancies in chip layouts with thin lines. For highly repetitive structures (e. g., arrays of posts), a general 7-µm-grid should be used for the layout and an additional correction factor of 1.0071 can be deployed in PostCIF to correct for the difference between this grid and the physical 7.05-µm raster of the imagesetter.

and fixed on a clear 5″-glass blank using adhesive Kapton tape (3M, Rüschlikon, Switzerland).

Most chips used during this thesis were fabricated in glass using conventional microfabrication techniques (outlined in Figure 3-1) [80]. As a substrate, double-side polished, 100-mm-diameter, 500-µm-thick wafers of low-alkali Pyrex 7740 glass were used (for its chemical composition, see Table 4). This glass is originally manufactured by Corning, but cutting and polishing of the wafers is performed by different manufacturers, such as Schott-Guinchard (Yverdon-les-Bains, Switzerland), Bullen Ultrasonics (Eaton, OH, USA) and Sensorprep Services (Elburn, IL, USA).

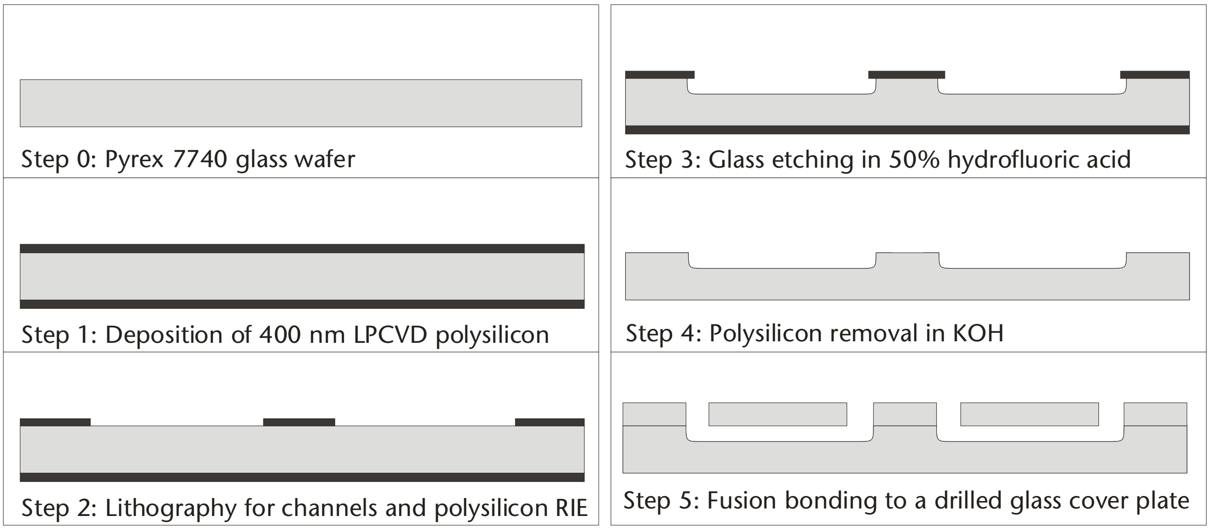

Step 0: Pyrex 7740 glass wafer

Step 1: Deposition of 400 nm LPCVD polysilicon

Step 2: Lithography for channels and polysilicon RIE

Step 3: Glass etching in 50% hydrofluoric acid

Step 4: Polysilicon removal in KOH

Step 5: Fusion bonding to a drilled glass cover plate

***Figure 3-1**: Schematic process sequence for micromachining of a microfluidic network in glass.*

To protect the wafers during the hydrofluoric acid (HF) etching procedure, a 400-nm layer of low-temperature, low-pressure, chemical-vapor deposited (LPCVD) polysilicon is deposited on both sides of the wafers. As the annealing point of Pyrex 7740 is around 560 °C (see Table 5), the deposition temperature has to be limited to a value lower than the usual process parameters (600 °C) to avoid bending and deformation (“warping”) of the wafer. A deposition temperature of 570 °C was chosen as a compromise between thermal compatibility with the glass and deposition rate, which is a function of temperature itself[11].

Compound	*Concentration*
SiO_2	80.5 %
B_2O_3	12.9 %
Na_2O	3.8 %
Al_2O_3	2.2 %
K_2O	0.4 %
CaO	0.10 %
Cl	0.10 %
MgO	0.05 %
Fe_2O_3	0.04 %

***Table 4**: Chemical composition of Pyrex 7740*[12]

LPCVD polysilicon proved to be a very good mask material for HF etching, as it adheres perfectly to the glass surface and has a very low etch rate in HF. An equally important factor, however, is the pinhole density. Pinholes can result in pitting of the glass surface during etching, though the mask generally remains intact. It turns out that 400 nm is sufficient for regular channel fabrication down to depths of 100 to 150 µm at an acceptable defect density. Deeper etching, for instance for the fabrication of through holes (i.e. 250 µm etching simultaneously from both sides), requires a thicker layer of polysilicon. For these applications, glass wafers with 800 nm polysilicon were used, with the layer being deposited in two runs of 400 nm each to reduce the risk of wafer deformation.

---

[11] Further process parameters: pressure ~220 mtorr, silane SiH_4 flowrate ~20 cm^3/min, deposition rate ~35 Å/min.

[12] Information taken from www.corning.com.

Property	*Value*[13]
Density	*2.23 g/cm^3*
Strain Pt. (10^{14} poises)	*510 °C*
Annealing Pt. (10^{13} poises)	*560 °C*
Softening Pt. (10$^{7.6}$ poises)	*821 °C*
Coefficient of expansion (0-300 °C)	*32.5·10^{-7}/°C*
Specific heat @ 25 °C	*0.18 cal/g-°C*
Thermal conductivity @ 25 °C	*0.0027 cal-cm/sec-cm^2-°C*
Transmittance @ 440 nm	*91.0% for 1.0 mm*
Refractive index @ 589 nm	*1.474*
Volume resistivity @ 250 °C	*10$^{8.1}$ Ω·cm*
Dielectric constant @ 20 °C and 1 MHz	*4.6*

***Table 5**: Material properties of Pyrex 7740 glass*[13]

Pattern transfer into the polysilicon mask is achieved by standard photolithography followed by reactive-ion etching (RIE). To increase resist adhesion, the wafer is first dehydrated in an oven under air at 200 °C for 30 min to desorb water molecules attached to the silicon surface (Figure 3-2a). Then, the surface is reacted with gaseous hexamethyldisilazane (HMDS, from Laporte Electronic Chemicals, Riddings, United Kingdom), which attaches to the silicon via the silazane groups to form a monolayer (Figure 3-2b and c). The six methyl groups of the HMDS improves organic resist adhesion. Layer deposition is achieved in 15 min at room temperature from the gas phase by flowing nitrogen through a bottle of HMDS.

The positive di-azo resist AZ1518 (Clariant, Muttenz, Switzerland) is used for lithography. A 1.8-µm thick layer is spin-coated onto the wafer by pipetting ca. 2 mL of resist on the wafer. The wafer is then spun at 500 rpm for 10 sec to distribute the liquid, followed by a spin at 4000 rpm for 30 sec to achieve the final layer thickness. A pre-bake step at 100 °C for 1 min on a hotplate serves to remove solvents from the thin resist layer and render it mechanically more stable.

---

[13] Information taken from Pyrex 7740 product datasheet, issued by Corning Germany in 1999.

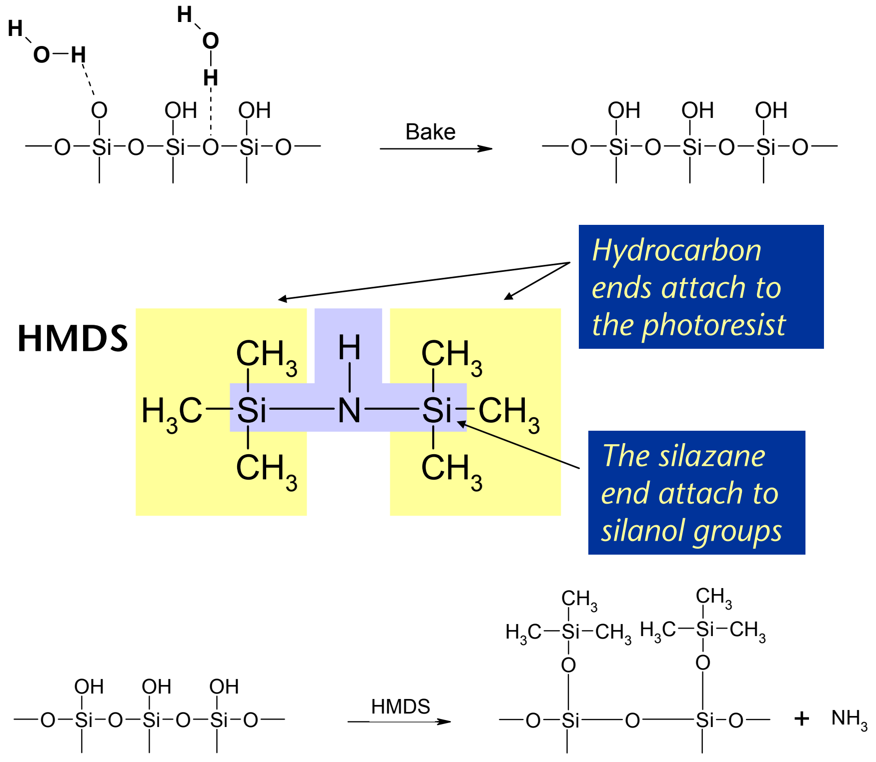

Hydrocarbon ends attach to the photoresist

The silazane end attach to silanol groups

Figure 3-2:

a) Water is desorbed from a silicon surface during the dehydration bake.

b) The HMDS molecule has six methyl groups which interact with the photoresist via hydrophibic forces. The two silane groups react with surface silanol groups to form covalent Si-O bonds.

c) An HMDS monolayer is formed on the substrate during the vapor phase reaction.

The wafer is exposed using an AL6-2 aligner (Electronics Visions Group, Schaerding, Austria) equipped with a mercury arc lamp operating at a wavelength of 365 nm. For a resist thickness of 1.8 µm and a glass/chromium photomask, an exposure dose of 55 mJ/cm^2 is used for low-reflective substrates such as polysilicon (highly reflective metal surfaces are exposed with 35 mJ/cm^2). If transparency masks are used, the exposure dose is increased by 10% to compensate for the reduced optical transmission through the polymer sheet. Except for very large structures (>250 µm), contact mode exposure at a contact force of 0.5 N is used. Especially for transparency masks, which are difficult to fix flatly onto the glass carrier, contact mode exposure increases the reproducibility of the obtained structural dimensions, as the transparency sheet is pressed onto the wafer.

After exposure, the resist layer is developed in a 1:4 (v/v) mixture of AZ351B developer (Clariant AG, Muttenz, Switzerland) and de-ionized water (DI water, 18 MΩ-cm) for 1 min with manual agitation. After rinsing in DI water, the wafer is dried under nitrogen flow and postbaked at 100 °C for 1.5 min on a hotplate to further strengthen the stability of the resist layer.

The structured photoresist layer then serves as an etching mask for RIE of the underlying polysilicon layer (Alcatel Vacuum Technology, Annecy, France). After RIE, the resist is removed by dissolution in acetone for at least 2 min, followed by a rinse in acetone, then isopropanol, and finally DI water. Sometimes, the resist hardens during longer RIE processes and cannot be fully removed using organic solvents. In this case, a 15-min etch in an oxygen plasma (Plasmaline from Tegal, Petaluma, CA, USA)[14] generally removes all remaining resist residues from the surface.

For the actual glass etching, 50% hydrofluoric acid (Rockwood Electronic Materials, Saint Fromond, France) is used at room temperature (typical etch rate for Pyrex 7740 varies between 9 and 11 µm/min). As the etch rate fluctuates considerably from day to day, it is monitored during the initial part of the process to adjust etching times accordingly. To do so, the first wafer is etched for 1 min, rinsed in DI water and then surface-profiled using an AlphaStep stylus profiler (Tencor, San Jose, USA). Once the measured etching depth is corrected for the polysilicon mask layer thickness, the etch rate is known. Further etching is then precisely timed. When the desired etch depth is reached, the wafer is rinsed in DI water and the polysilicon mask is subsequently removed in 40% KOH at 60°C (5 min).

3.3 Thermal fusion bonding

To seal the channel network, the etched wafer is fusion-bonded to a second Pyrex 7740 wafer (the so-called coverplate) containing access holes which line up with the channel ends. There are several ways to machine these access holes (0.8–1.5 mm diameter) into the coverplate wafer. In the framework of this thesis, either sequential (hole by hole) diamond-drilling (Stecher AG, Thun, Switzerland), simultaneous ultrasonic drilling of a grid of holes (Sensorprep Services, Elburn, USA) or HF-etching using a 800-nm-thick polysilicon mask (in-house) were used.

---

[14] Further process parameters: pressure ~0.1 mtorr, microwave power ~270 W, temperature 100 °C.

As fusion bonding is not based on attractive forces like the widely used anodic bonding technique, special care has to be taken to avoid particle contamination on the wafer surface. Each particle causes an un-bonded region (void), its size depending on the particle diameter. A thorough cleaning procedure which includes a surface activation step is therefore carried out prior to bonding. First, MOS-grade acetone and isopropanol are used to remove organic residue followed by a rinse in DI water. The dried wafer is then submersed in 100% (fuming) nitric acid for 10 min, which activates the surface and improves the bonding yield. After rinsing in DI water, a DI water pistol at high pressure is directed onto the wafer for at least 2 min to remove any remaining particles from the surface. Finally, the wafer is again rinsed and dried in a commercial spin-rinse-drier (Semitool, Kalispell, USA). Alternatively, a high-pressure cleaning system like the Micro-Automation 2006 (now part of Ultra T Equipment, Fremont, CA, USA) can be employed to remove particles. This machine uses a high-pressure (200 bar) spray of 0.2-µm-filtered DI water to clean the wafer, which rotates on a vacuum chuck.

Once both channel and cover wafers are clean, they are visually aligned so that holes line up with the ends of channels. They are then fixed with a drop of MOS-grade isopropanol, which wicks in between the two wafer surfaces. The assembled wafers are then placed in a muffle furnace (model M110, Heraeus Instruments, Hanau, Germany) between two Al_2O_3-ceramic plates (Haldemann et Porret, Le Locle, Switzerland). A round steel weight of about 1 kg mass is used to provide pressure during the bonding process (Figure 3-3a). The wafer stack is then submitted to the temperature profile shown in Figure 3-3b, with a maximum temperature of 650 °C and a total time of ~18 hours.

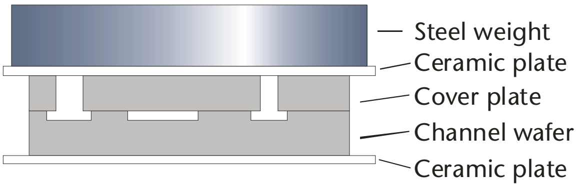

a)

***Figure 3-3**: a) Setup of the wafer stack in the muffle furnace. Both glass wafers are sandwiched between the ceramic plates and held under pressure using a steel weight. b) The temperature program used for fusion bonding.*

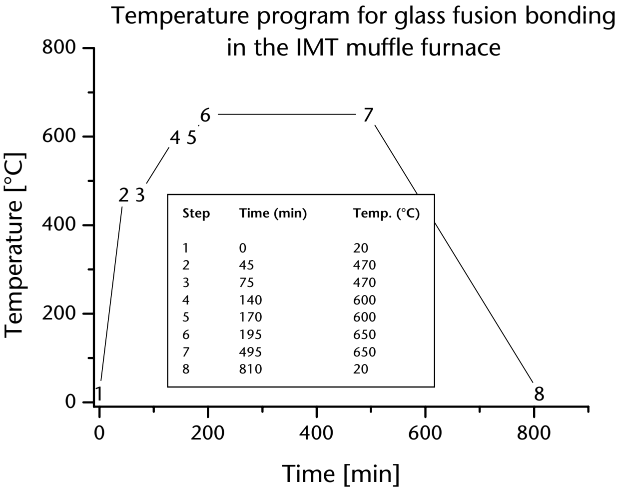

Step	Time (min)	Temp. (°C)
1	0	20
2	45	470
3	75	470
4	140	600
5	170	600
6	195	650
7	495	650
8	810	20

b)

3.4 Chip holder

The diced chips were mounted in a specially constructed holder consisting of a bottom and top plate, which were held together by eight stainless steel M3-screws (see Figure 3-4). The bottom plate was either made from 10-mm-thick poly(methyl methacrylate) (PMMA) for earlier designs or from 2-mm-thick, eloxated aluminum. The aluminum is stiffer and reduces warping of the chip holder when the screws are tightened too strongly. To accommodate the microfluidic chip, a recess of the same depth as the chip thickness was milled into the top side of the bottom plate. If fluorescence detection from below with an inverted setup had to be performed, a small part of the bottom plate was removed by milling to let the light beam pass unhindered.

The top plate, made from 4-mm-thick PMMA serves to fix the chip on the holder and also provides the reagent reservoirs. These comprise a volume of 50 µL and are formed by 4-mm-diameter holes in the PMMA, which were sealed to the chip surface by Viton O-rings (shore hardness 75A, 4 mm inner diameter, 1 mm width, obtained from NTKD, Hombrechtikon, Switzerland). Although Viton is compatible with a wide range of solutions, the O-rings can be replaced with Teflon or Kalrez counterparts if necessary. The O-rings are placed in 0.7-mm deep recesses around the reservoir holes on the bottom face of the top plate to receive the recommended degree of compression for good sealing when the holder is closed. Figure 3-5 shows a photograph of a chip holder made from two PMMA plates.

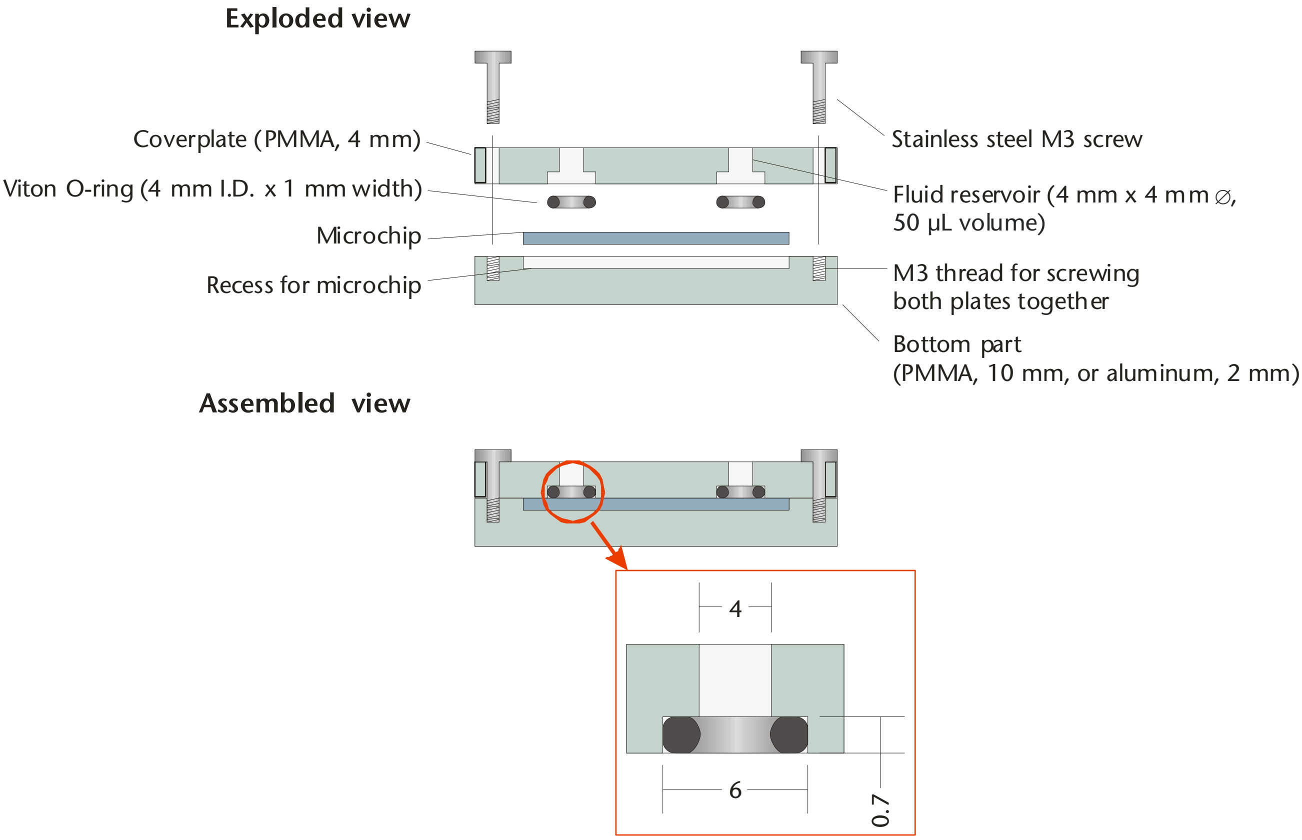

Figure 3-4*: Cross-sectional view of the chip holder for microfluidic devices. Fluid reservoirs are made by holes in the cover plate and an O-ring seal with the chip surface (see inset at the bottom). Dimension in the inset are in mm.*

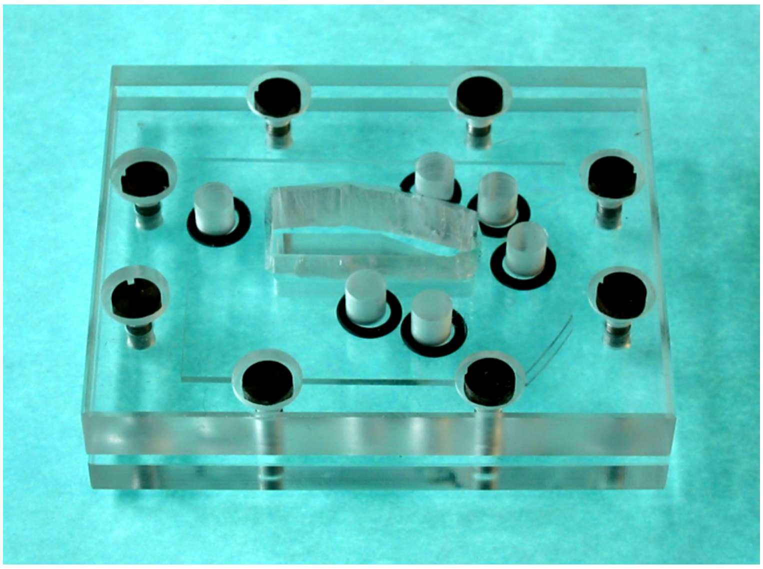

Figure 3-5*: A chip holder with a PMMA top and bottom plate. Six reservoirs drilled into the cover are sealed by O-rings to the chip. For improved laser-induced fluorescence detection and optical inspection, openings were milled in both cover and bottom plates.*

The reservoirs proved to be very reliable and no leakage problems occurred during the extensive use of the holder for various projects. Due to the softness of the O-rings and the protective recess for the device, chips could not be broken in the holder. Also, the holder could be mounted with a precision of 50 µm onto the clamping stage of our LIF detector system. This facilitated channel alignment especially in cases of low sample concentration, where visual alignment was not possible.

3.5 Conclusion

The glass micromachining procedure based on HF etching with a polysilicon mask has a few advantages over the metal mask techniques (chromium/gold) typically used by other research groups:

1. As polysilicon is deposited by chemical vapor deposition, both faces of the wafers are directly protected without a second deposition run being necessary.

2. Polysilicon is easily etched by reactive ion etching machines using photoresist as masking material, while chromium/gold layers need two consecutive wet etching steps, which are not necessarily compatible with local clean-room standards.

3. After HF etching, the remaining polysilicon is easily removed by wet etching in KOH, while chromium/gold layers again need two etching steps.

It should be noted, however, that LPCVD deposition on glass needs special care due to the low softening point of the substrate. Therefore, it is not compatible with all glass types, but rather limited to high-softening-point glasses like Pyrex 7740.

Chapter 4

Integrated Field-Amplification Sample Stacking

A variety of sample preconcentration techniques have been shown to improve limits of detection in microchip-based analysis systems. Of these, sample stacking by field amplification (FASS) in a low-conductivity sample matrix may be the most easily implemented from the point of view of chip fabrication, as it does not require channels to be coated or packed. The fact that signal gains of 1 to 3 orders of magnitude have been demonstrated in conventional systems certainly means that the incorporation of this type of preconcentration onto chips warrants some additional study[15]*.*

A microchip structure for FASS was developed, which allowed the formation of comparatively long, volumetrically defined sample plugs with a minimal electrophoretic bias. Signal gains of up to 20-fold were achieved by injection and separation of 400 µm long plugs in a 7.5 cm long channel. Fluidic effects arising when solutions with mismatched ionic strengths are electrokinetically handled on microchips were studied.

To further improve the signal gain, a new chip layout was developed for full-column stacking with subsequent sample matrix removal by polarity switching. The design features a coupled-column structure with separate stacking and CE-channels, showing signal enhancements of up to 65-fold for a 69 mm long stacking channel.

---

[15] Major parts of this chapter have been published in: J. Lichtenberg, E. Verpoorte, N.F. de Rooij, "*Sample preconcentration by field amplification stacking for microchip-based capillary electrophoresis*", Electrophoresis, vol. 22, pp. 258–271, 2001. Amongst the previously unpublished material are the general introduction including stacking theory, the study of stacking efficiency versus stacking channel length for the column-coupled design, and the section on current monitoring.

4.1 Introduction

In the field of analytical separation technology, most instrumentation developers face the problem that particular applications require a lower limit-of-detection (LOD) than what can be achieved using the available detector. Physiological samples present a particular challenge, since analytes are often present at sub-mM levels. The analysis of hormones in serum by liquid chromatography is one such example, where concentrations of analyte range from nM to pM, but fluorescent labeling is rather difficult to achieve [81]. Though UV absorbance may be used, it exhibits detection limits of at best 10^{-7} M. In the domain of microchip-based analysis systems, this issue is further complicated by the fact that only minute amounts of sample are available for detection due to the small dimensions of the fluidic structures.

For these reasons, sample preconcentration is a very interesting technique to be integrated with microchip-based analysis systems [49]. Here, analyte molecules from a comparatively large sample volume are concentrated (or “stacked”) into a much smaller volume, which is subsequently analyzed using an appropriate technique (e.g. electrophoresis or an immunoassay). The analyte concentration that the actual analysis process has to deal with is therefore much higher (5- to 10^6-fold, depending on the preconcentration method) than the original concentration in the sample. This can alleviate the high performance requirements imposed on the detector instrumentation and widen the choice of suitable detector types for a particular application.

Fortunately, combining an additional sample preconcentration step with the actual analysis is comparatively trouble-free if done on planar, microfluidic devices, as the microchip format lends itself perfectly to the dead-volume-free integration of complex microfluidic networks at comparatively low cost.

In the context of the work presented here, field-amplified sample stacking (FASS) was studied in detail for the integration with on-chip capillary electrophoresis (CE). FASS allows the preconcentration of charged molecules at electric-field gradients caused by local changes in buffer concentration. Sample dissolved in a low-conductivity matrix can thereby by enriched at the interface to a high-conductivity CE buffer.

4.2 Theory of field-gradient stacking

4.2.1 Creating electrokinetic velocity gradients

FASS depends on an electrokinetic velocity gradient as the key element of the preconcentration process. Independent of whether its position in the microchannel network is stationary or not, molecules that travel through the gradient will experience a change in velocity that leads to preconcentration (slowing down) or dilution (speeding up). To understand the nature of these gradients, we will review the underlying principles of electro-osmotic and electrophoretic flow components in this section before the actual stacking process is considered.

For simplicity, the general discussion of molecular transport at an electrokinetic velocity gradient will be focused on a straight, buffer-filled, fused-silica capillary. Consider an analyte, *i,* migrating under the influence of an electric field, *E*. The migration velocity of the analyte is the sum of the electrophoretic velocity of the ion itself and the electro-osmotic velocity of the bulk solution. The latter is caused by the electric field acting on the charged, mobile portion of the double layer causing a plug-type flow of the bulk solution by viscous drag (for a more detailed discussion, see references [39-41] or Chapter 1.4). The migration velocity is proportional to the sum of its electrophoretic mobility, μ_{ep}, and the electro-osmotic mobility of the buffer, μ_{eo}:

$$v_i = E\underbrace{(\mu_{ep} + \mu_{eo})}_{\mu_i} \tag{7}$$

The observed migration direction of the ion depends on the sign of the sum of μ_{ep} and μ_{eo}, which is therefore also called observed mobility μ_i.

Approximating the ion with its surrounding hydration shell as a particle, the electrophoretic mobility of an ion can be expressed by the Stokes-Einstein relation [82]:

$$\mu_{ep} = \frac{q}{6\pi r\eta} \tag{8}$$

with q: charge of the particle with its ionic cloud
r: its effective radius due to the hydration shell of H_2O molecules
η: buffer viscosity

The electro-osmotic mobility, μ_{eo}, on the other hand, is a function of buffer and capillary surface parameters, as the double layer is the major reason for the development of electro-osmotic flow:

$$\mu_{eo} = \frac{\varepsilon\zeta}{\eta} \tag{9}$$

with ε: dielectric constant of the buffer
ζ: potential at the plane of shear between the stagnant and mobile layers of the double layer

Regarding the adjustable parameters in equations 7 to 9, a number of possibilities arise to create electrokinetic velocity gradients. In order to increase v_i, one could locally:

a) increase the electrical field strength E,

b) reduce the buffer viscosity η,

c) increase the dielectric constant of the buffer ε, or

d) increase the zeta potential ζ (by modification of the channel wall or changing the solution pH).

Of these options, no reports for c) can be found in the literature, but all other techniques have been used to create velocity gradients [79, 83-86]. Today's dominating technique, FASS, relies on changing the electrical field strength in a small portion of the channel by locally adjusting the concentration of buffer ions. Hence, the relation between buffer ion concentration, solution conductivity, σ, and the electric field strength, E, is the key for FASS:

$$E = \frac{i}{A\sigma} \tag{10}$$

with i: current in the capillary
A: cross-section of the capillary
σ: buffer conductivity

While i is constant in a uniform capillary (having a constant A) due to Kirchhoff's law, the electric field depends on σ, which in turn is a function of the buffer concentration:

$$\sigma = F\sum_n z_n \cdot \mu_{ep,n} \cdot c_n \tag{11}$$

with F: Faraday's constant (96,495 C/mol)
z_n: valence of species n
$\mu_{ep,n}$: μ_{ep} of species n

Therefore, the channel section filled with a high concentration of buffer shows a lower electrical field-strength (lower migration velocity) than the low-conductivity portion (higher migration velocity).

An alternative method for creating electrokinetic velocity gradients is based on a thermal effect. A voluntarily induced, localized temperature change can be deployed to achieve a gradient in the conductivity which in turn gives rise to an electric field gradient in the capillary [84]. In contrast to the method mentioned above, the position of the field gradient remains constant as it is defined by the external or internal heat source. Therefore, this technique is better controllable than most others for very high preconcentration factors (>10,000) where analyte needs to be collected for long times (>5 min).

4.2.2 Molecular transport in systems with a field gradient

In order to understand the molecular transport across a velocity gradient, consider a fixed electric field gradient in the capillary at zero electro-osmotic flow as depicted in Figure 4-1, caused for example by a sudden change in electrical buffer conductivity. For the following discussion, it is convenient to define γ as the ratio between the high and low field strengths (E_H and E_L) in the system:

$$\gamma = \frac{E_H}{E_L} \tag{12}$$

As the field strengths are proportional to the buffer resistivities (inversely proportional to the buffer conductivities), γ is called *relative conductivity* [83]. Note, that while E_H is larger than E_L, the picture is turned around for conductivities. Conductivity in the high field-strength region, σ_{EH}, is lower than conductivity in the low field-strength region, σ_{EL} (i.e. $\sigma_{EH}<\sigma_{EL}$). γ than becomes σ_{EL}/σ_{EH}.

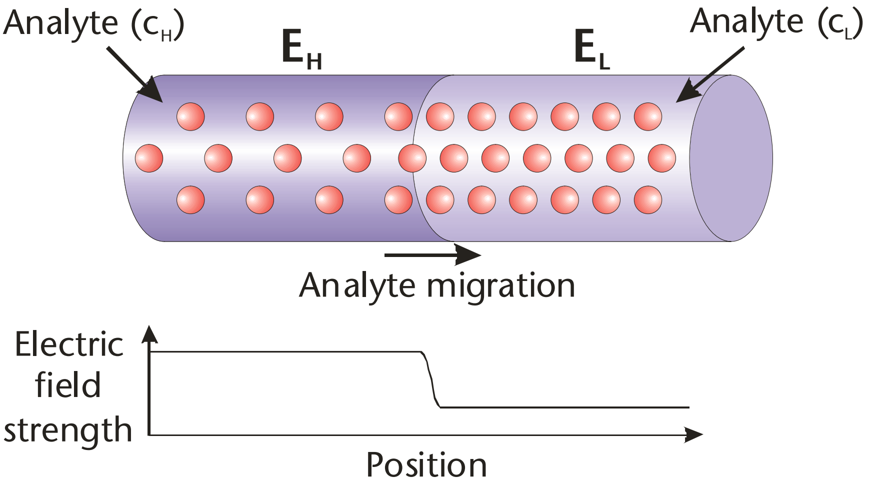

***Figure 4-1**: Analyte stacking at an electric field strength gradient: The analyte migrates from the high field - strength region (E_H) into the low field strength, E_L, thereby slowing down and increasing in concentration. De-stacking (loss of analyte concentration) occurs if the migration direction is reversed.*

Under an applied electric field, ions migrate from one side of the gradient to the other, the direction being dependent on the apparent velocity, v_i. For each species, *i*, the ionic flow, F_i, through the cross-section of the channel (in molecules per second) can be described as:

$$F_i = N_i \cdot v_i \cdot A \tag{13}$$

with N_i: concentration of species *i* (molecules/m^3)

A: channel cross-section (m^2)

In order to fulfill the mass-balance requirement, F_i has to be constant on both sides of the gradient. We can therefore write for the flows in the low and high field-strength regions, F_{iEH} and F_{iEL} respectively, after eliminating the constant capillary cross-section, A, and the constant observed mobility, μ_i:

$$\begin{aligned} F_{iEH} &= F_{iEL} \\ c_{iEH} \cdot v_{iEH} \cdot A &= c_{iEL} \cdot v_{iEL} \cdot A \\ c_{iEH} \cdot E_H \cdot \mu_i &= c_{iEL} \cdot E_L \cdot \mu_i \\ \frac{c_{iEL}}{c_{iEH}} &= \frac{E_H}{E_L} = \gamma \end{aligned} \tag{14}$$

The concentrations of each ionic species therefore adjusts instantly when ions pass from one side of the gradient to the other. Consequently, the concentration is increased or decreased (depending on the migration direction) by the factor, γ; in the former case, γ, is thus also called the preconcentration factor. In a practical implementation of the configuration in Figure 4-1, the sample is dissolved in a low-conductivity buffer, creating a high field strength in this region, while the separation buffer has a high conductivity leading to a low field strength.

4.2.3 Field-amplified sample stacking

To understand the FASS technique better, let us consider the field-amplified sample stacking situation depicted in Figure 4-2. Contrary to the example in Figure 4-1, the high and low field-strength zones do not extend infinitely. Instead, a small sample plug of length L_{iEH}, containing analyte cations dissolved in a low-conductivity buffer, is injected into a capillary filled with a high-conductivity separation buffer. We assume that the electro-osmotic flow is in its normal direction towards the cathode. Preconcentration takes place rapidly after the separation voltage is applied, because a high electric field is generated within the low-conductivity sample plug. This rapidly drives anions to one end and cations to the other end of the plug. As soon as they reach the respective gradient at the end of the sample matrix plug, they are subject to a sudden drop in field strength, and therefore slow down and stack.

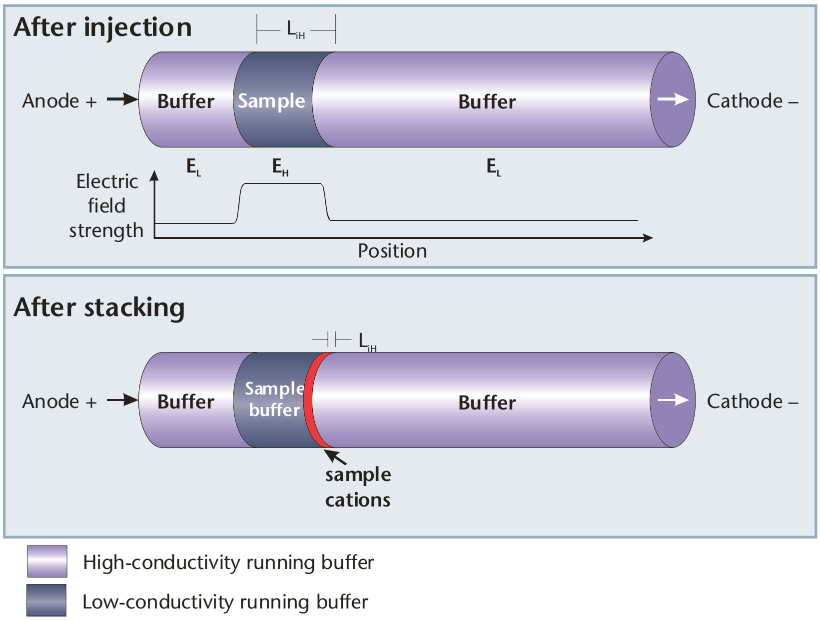

Figure 4-2: *Mechanism of FASS. The electric field strength is concentrated in the low conductivity buffer plug and drives ions to the ends of the plug. Once they reach the high conductivity running buffer, they slow down and stack due to the lower field strength.*

The field strength distribution in a capillary of length *L*, which is filled with low-concentration running buffer to a length of *xL* (*x* ranging between 0 and 1), can be written as follows [83]:

$$\begin{aligned} E_H &= \frac{\gamma E_0}{\gamma x + (1 - x)} \\ E_L &= \frac{E_0}{\gamma x + (1 - x)} \end{aligned} \qquad (15)$$

with E_0: average electric field over the capillary

The average electric field strength, E_0, is equal to the field strength in the same capillary assuming it is filled with only one buffer. Hence, $E_0 = V/L$, where *V* is the separation voltage.

Due to the adverse effects of the hydrodynamic pressure generated when a potential difference is applied (see Section 4.2.4), *x* is limited to 0.01–0.05 for most practical cases, which leads to field strengths as listed as an example in Table 6.

A second reason for limiting the sample plug length is illustrated in Figure 4-3. For very long plugs, the field strength in the high-conductivity buffer, E_L, is reduced so much that the quality of the CE separation degrades both in terms of separation time and resolution. At the same time, the field strength in the low-conductivity buffer (sample matrix), E_H, is reduced as well, which increases the time necessary to complete the stacking process.

Zone	*Normalized field strength for x=0.01*	*Field strength for x=0.01 and E_0=500 V/cm*	*Normalized field strength for x=0.05*	*Field strength for x=0.05 and E_0=500 V/cm*
E_H	$9.17 \cdot E_0$	*4.59 kV/cm*	$6.90 \cdot E_0$	*3.45 kV/cm*
E_L	$0.92 \cdot E_0$	*0.46 kV/cm*	$0.69 \cdot E_0$	*0.35 kV/cm*

***Table 6**: Example for field strengths in a capillary under stacking conditions when filling 1% and 5% of the total capillary length with the low-conductivity sample buffer. The relative conductivity, γ, is assumed to be 10.*

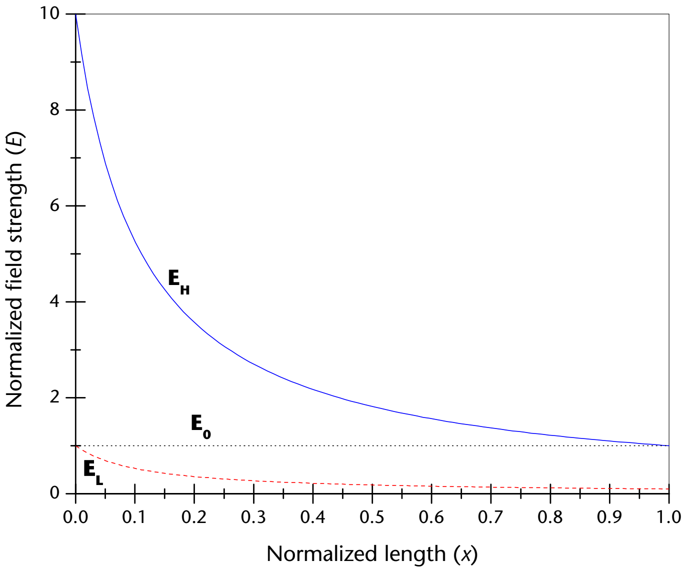

***Figure 4-3**: Field strengths E_H and E_L as a function of filled capillary length. Field strength is normalized with respect to E_0, the average field applied across the capillary. The filled length is normalized with respect to the total capillary length L. The relative conductivity, γ, is assumed to be 10.*

In the extreme case of $x \to 0$, E_L spans across the full capillary and becomes equal to E_0. Inversely, if $x \to 1$, E_H equals E_0.

4.2.4 Effects of mismatched electro-osmotic flow due to a conductivity discontinuity

The difference in buffer concentrations changes not only the buffer conductivity in the two zones of the capillary, but has also great impact on the electro-osmotic flow, something that has been neglected so far. The first change in EOF is induced by the difference in electric field strength in both zones of the capillary. This is because the electro-osmotic flow velocity, v_{eo}, depends linearly on E:

$$v_{eo} = \mu_{eo} E \qquad (16)$$

The low-conductivity buffer zone with the high electric field, E_H, will therefore exhibit an increased electro-osmotic flow velocity. Simultaneously, this tendency is aggravated by the fact that μ_{eo} itself is dependent on the ionic strength of the buffer via the Debye-Hückel parameter:

$$\mu_{eo} = -\frac{\sigma_s}{\eta\kappa} \tag{17}$$

with σ_s: capillary surface charge

κ: Debye-Hückel parameter, see Equation (18)

$$\kappa = \sqrt{\frac{2000F^2}{\varepsilon RT} I} \tag{18}$$

with R: universal gas constant (8.31 J/kmol)

T: temperature

I: ionic strength of the buffer, see Equation (19)

$$I = \frac{1}{2}\sum_j z_j^2 c_j \tag{19}$$

The value of v_{eo} increases with decreasing buffer concentration due to I, leading to a mismatch in electro-osmotic flow in a capillary with zones of different conductivity.

Figure 4-4 shows a capillary section with two regions of different electro-osmotic flow velocity. To maintain flow continuity in such a system, the difference in EOF velocity is compensated by a pressure-induced flow component [85]. The superposition of the flat EOF profile and of the parabolic Poiseuille profile give rise to increased dispersion of a well-defined sample plug, ultimately leading to sample dilution and reduced separation efficiency (Figure 4-5) [87, 88]. These flow profiles have been observed both in capillaries [85] and in microfluidic devices during the research done for this thesis [62] (see also Section 4.4.4).

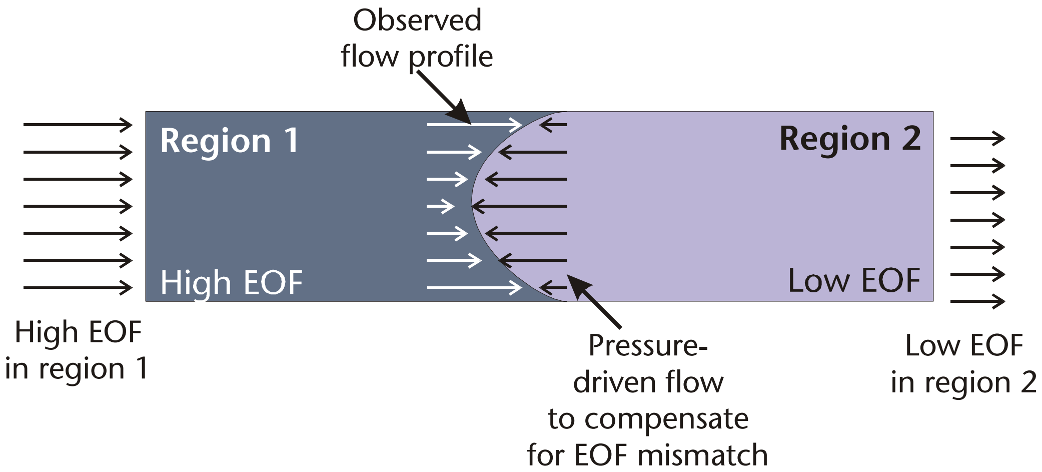

Figure 4-4*: Microchannel section with two regions of different EOF velocity. A pressure-driven flow is induced in order to maintain flow continuity, which leads to a parabolic flow profile. The observed flow profile is the sum of the high EOF and the pressure-driven flow directed against it.*

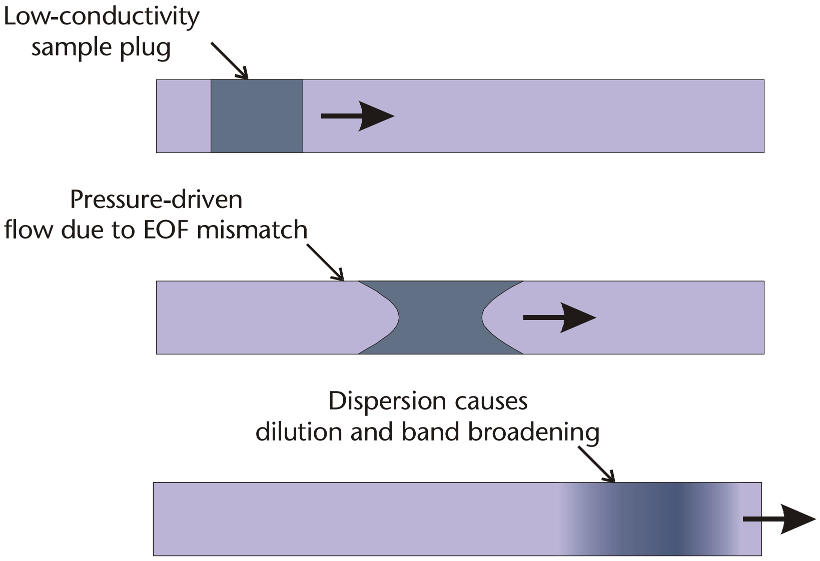

Figure 4-5*: Dispersion due to pressure-driven flow causes sample plug dilution and band broadening.*

It should be noted that Burgi and Chien have developed a mathematical model to optimize FASS by balancing the effects of analyte preconcentration (and peak narrowing) and of peak broadening due to laminar Poiseuille flow [88]. To do so, the impact of the Poiseuille flow in a circular capillary is modeled by introducing an enhanced diffusivity term, D_a, as known from chromatography [38]:

$$D_a = \frac{r_0^2 v_a}{48 D_i} \tag{20}$$

where r_o: radius of the capillary

v_a: average laminar flow velocity

D_i: diffusion coefficient of analyte *i*

The contribution to the variance of the peak due to Poiseuille flow after a time *t* is then:

$$\begin{aligned}\sigma_a^2 &= 2D_a t \\ &= \frac{r_0^2 v_a t}{24 D_i}\end{aligned} \tag{21}$$

For the optimization of the stacking process, Burgi and Chien have developed a global equation combining the various, stacking-related sources of the peak variance. The minimum variance can be determined by taking the derivative of this expression with respect to γ to zero. For the development of the complete theory, the authors' excellent paper is recommended [88].

From Equation (21), it is clear that reducing capillary diameters decreases the variance due to Poiseuille flow. As the flow resistance to pressure-driven flow increases with shrinking capillary diameter, the Poiseuille flow is reduced and thereby also band-broadening. At the same time, Taylor flow theory predicts reduced dispersion due to increased radial diffusion in a small narrow-bore capillary. As a consequence of both arguments, higher relative conductivities, γ, are acceptable in narrow capillaries and therefore higher preconcentration factors are achievable. This relationship makes microchip-based CE devices even more interesting for FASS applications, as comparatively small channel cross-sections are easily realized.

4.2.5 Field-amplified stacking in conventional systems

As mentioned above, the electric field gradient in FASS is generated by dissolving the sample in a buffer that has a much lower conductivity than the surrounding running buffer used for separation. Once a short sample plug is injected into the separation capillary, preconcentration is achieved by generating a high electrical field within the low-conductivity sample plug. Since v_{ep} is increased when E increases, anions rapidly migrate to one end of the plug, while cations move rapidly to the other (see Figure 4-2). Here, the ions experience a sudden drop in field strength and abruptly slow down, which causes stacking of the ions at an increased concentration.

Because electric field strengths are inversely proportional to solution conductivities (directly proportional to solution resistivities), a linear relationship between the stacking efficiency and the relative conductivity γ is expected. However, a pressure-driven flow component as outlined in the previous section (4.2.4) causes band-broadening due to the Poiseuille profile generated, thus precluding infinitely improving performance. FASS was first mentioned by Mikkers *et al.* [38] and was intensively studied by Chien, Burgi *et al.* [87-89]. The latter proposed a model described above to predict buffer conductivities and injection lengths for an optimum compromise between signal gain and separation performance [88].

In general, FASS of hydrodynamically injected, short sample plugs can yield a signal gain of up to 20-fold.

4.2.6 Field-amplified injection in conventional systems

In a defined plug of low-conductivity buffer surrounded by high-conductivity separation buffer, stacking at both field gradients at the two ends of the plug occurs. In field-amplified injection (FAI), the low-conductivity matrix is confined to one end (the injection end) of the capillary and only one gradient is present (see Figure 4-6). While FASS works for both negatively and positively charged ions, field-amplified injection (FAI) has an electrophoretic bias depending on the direction of EOF, and therefore only stacks one type of ions. The advantage of FAI over FASS is that analyte ions from a large sample volume (i.e. the whole sample vial) may be preconcentrated, while the volume in FASS is limited by the tolerable length of the sample plug. Although larger amounts can be injected in full-column FASS as described in the next section, an additional step for sample matrix removal has to be included in the procedure.

In the capillary format, FAI has been successfully implemented as *head-column stacking*, by first introducing a short plug of de-ionized water and then electrokinetically injecting the sample [90-92]. This method is especially robust as it does not rely on the sample matrix conductivity itself, but deploys de-ionized water as an independent stacking medium. Preconcentration factors of up to 1000-fold could be achieved with this technique.

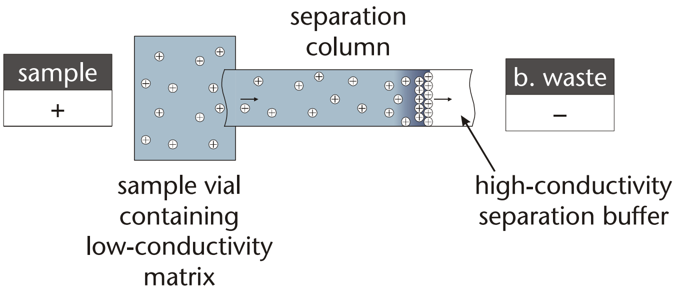

Figure 4-6*: FAI from a vial containing sample in a low-conductivity matrix. Under the conditions depicted here, sample cations are preconcentrated at the field gradient created at the interface between sample and separation buffer. Note that anions are not preconcentrated.*

4.2.7 Full-column stacking

A major obstacle for increased signal enhancement by stacking for CE is the low sample volumes typically used. A way around to this problem is preconcentration of the analyte contained in a whole column's worth of sample [93, 94]. Figure 4-7 presents the general scheme: the column is filled entirely with the sample contained in a low-conductivity matrix, which is then driven back to the inlet side by the separation buffer. The field gradient zone thereby travels back to the injection end and the – potentially separation-compromising – length of the low-conductivity zone is reduced while holding on to the preconcentrated analyte.

While Figure 4-7 shows sample matrix removal by electrokinetic pumping, other removal schemes like hydrodynamic counterbalancing [95] or electro-osmotic flow modifiers [96, 97] have been reported for the capillary format.

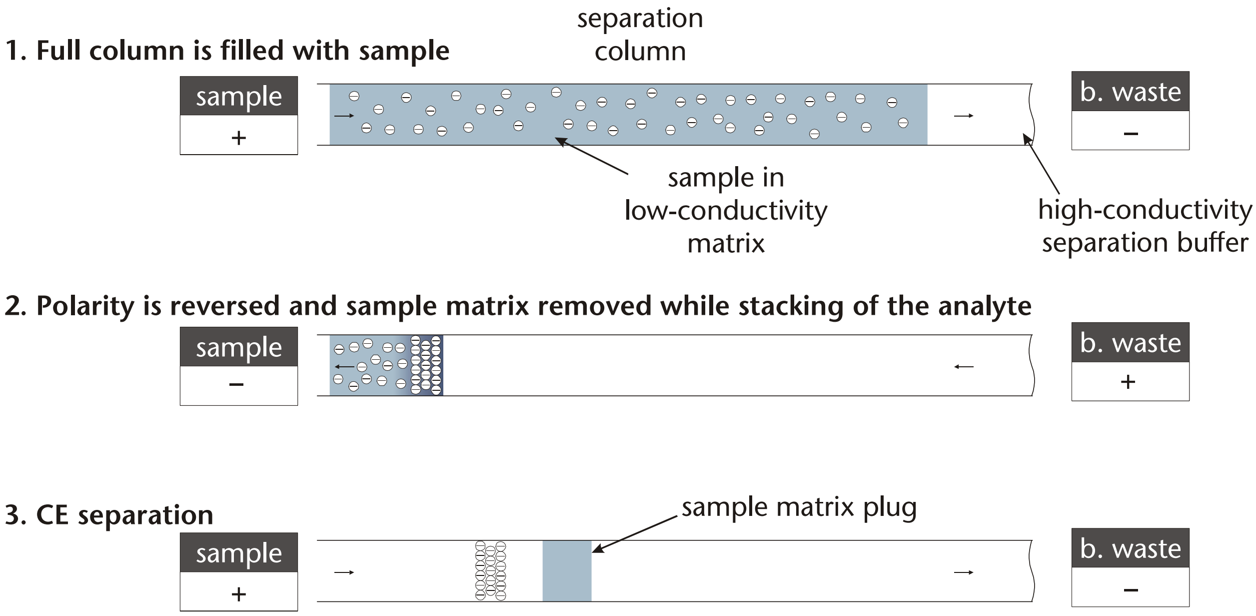

Figure 4-7: *Full-column stacking requires a three-step procedure. First, the full column is filled with the sample dissolved in a low-conductivity sample matrix. Then, the polarity of the applied voltage is reversed, which causes removal of the sample matrix by electro-osmosis. At the same time, analyte ions having an electrophoretic mobility high enough to overcome the EOF stack and concentrate at the interface between sample matrix and high-conductivity running buffer. Finally, the voltage is reversed again and CE separation starts. Timing is crucial for this type of stacking as the third step can only start when the column is largely cleared of the sample matrix. At the same time, loss of analyte has to be avoided.*

4.3 Implementations of chip-based preconcentration devices

First applications of sample stacking on microfabricated devices were FAI by Ramsey's group, followed by full-column sweeping in Harrison's group and our team (see Section 4.6). Simultaneously to the latter, stacking of large, volumetrically defined sample plugs was reported by our group, as will be described in Section 4.4.

Field-amplified injection (FAI)

FAI has been applied to microchip-based analysis by Jacobson *et al.* [98] and Kutter *et al.* [52] using gated injection into the separation channel to form long injection plugs for large anion and metal cation analysis, respectively. FAI is achieved using a low-conductivity sample matrix and a time-based, gated injection technique [47]. Gated injection as presented in the comparison in Figure 4-8, has an inherent electrophoretic bias, which can be exploited for stacking if a field gradient is present.

FAI yielded a concentration enhancement for dansylated amino acids of up to 13.8-fold at a γ of 970 [98]. The efficiency was also investigated. Separations using stacked injection had efficiencies of 22,000 to 29,000 theoretical plates, which made them only 60 to 70% as efficient as CE on the same devices using a volume-defined, pinched injection scheme.

However, use of the head-column injection technique has not been reported in the literature so far. This could lead to better concentration gains than observed above, given the experience with this method in conventional techniques [90-92].

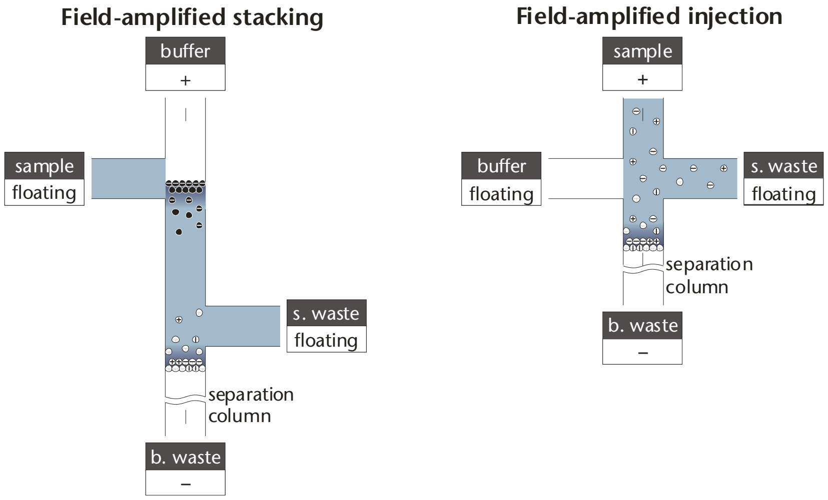

***Figure 4-8**: Comparison of FASS and FAI in the microchip format. While on-chip FASS allows preconcentration of both anions and cations in volumetrically defined plugs, field-amplified injection enriches only one ionic species at the front boundary of the injection plug.*

Field-amplified sample stacking

Aside from the work presented in this thesis, FASS of volumetrically defined sample plugs on microchips has not been reported per se.

Full-column sweeping

Li *et al.* used stacking of long protein-containing sample zones for sample preconcentration prior to injection into a mass spectrometer, with enrichment factors of up to 50-fold [61]. The sample matrix was removed by polarity reversal prior to injection into the mass spectrometer. A somewhat different approach employing separated preconcentration and separation channels is presented in this thesis.

Other techniques

It should be noted that a number of other sample preconcentration methods has been implemented for microchip devices recently. Amongst those are:

Isotachophoresis (ITP)

In ITP, the sample plug is sandwiched between two different background buffers. Upon application of the separation voltage, the sample constituents separate over a given time into distinct zones located between leading and terminating electrolyte in order of descending mobilities. In terms of sample preconcentration, ITP has the interesting property that the sample zones always adjust to the concentration of the leading buffer, which therefore determines the preconcentration factor. ITP was successfully applied to the preconcentration of fluorescent marker molecules with signal enhancements of more than 400-fold [99]. Kaniansky *et al.* applied ITP as a combined sample preconcentration and sample clean-up step for water analysis prior to CE [100].

Stacking of neutral analytes

In contrast to the methods mentioned so far, this technique allows preconcentration of neutral analytes in micellar CE. The analyte is swept by the micelle phase, which is driven electro-osmotically. Micelles then stack and preconcentrate at an electric-field gradient induced by a stepwise change in sodium chloride concentration in the buffer [64]. Signal gains of up to 20-fold could be achieved for BODIPY as a model analyte.

Preconcentration at porous membranes

Recently, a new way of DNA sample preconcentration was introduced in the form of integrated porous membrane structures, which allowed DNA fragments to be concentrated up to 100-fold before separation [101, 102]. A thin layer of porous potassium or sodium silicate acts as a semipermeable membrane between a side channel and the main channel in the region of the injection junction. Ionic current can flow over the junction thus carrying analyte molecules towards the mem-

membrane, which retains molecules above a certain size. However, recent research indicates that mass transport in channels with dimensions close to the thickness of the electrolyte double-layer might also have to be taken into consideration to explain this process [103, 104].

Preconcentration at integrated metal electrodes

A similar structure replacing the porous membrane mentioned above by a metal electrode was also applied to the preconcentration of DNA molecules on PMMA chips [105].

Solid-phase extraction

Finally, also solid-phase extraction allows sample preconcentration, as was shown on channel surfaces by Kutter *et al.* (80-fold preconcentration of a neutral coumarin dye [106]) and by Oleschuk *et al.* on functionalized silica beads packed into a microchannel (80-to-500-fold preconcentration of BODIPY [107]). Other implementations of solid-phase extraction can be found in [61, 108].

4.4 Stacking of 400-µm-long, volume-defined sample plugs

In order to take advantage of the peak-narrowing property of FASS, a microchip CE device was developed having new sample plug formation element that allowed the injection of volumetrically defined, 400-µm-long sample plugs. Using this device, the influence of pressure-driven flow on stacking in the plugs, caused by the local mismatch of electro-osmotic velocities, was studied.

4.4.1 Chip layout and fabrication

The basic chip layout incorporates a separation channel which is 45 µm wide across the top, 12 µm deep and 7.5 cm long (Figure 4-9a) with overall chip dimensions being $44 \times 32\ \text{mm}^2$. To accommodate the comparatively long separation channel in a microchip format, a serpentine structure was chosen. Hence, the analyte zones pass a number of turns before they reach the detector region, which induces a certain amount of band-broadening [47, 109, 110]. The injection element of the chip allowed a number of volume-defined injection modes to be tested, examples of which are presented in Figure 4-9b and c. The latter plug formation scheme is a new approach developed in this thesis, which allows the formation of comparatively long (400 µm) sample plugs between the two sample channels of the modified double-T configuration without dilution of the plug by the running buffer used for spatial confinement. This is a key prerequisite for successful implementation of FASS in microdevices. A more detailed discussion of this subject is reported in Section 4.5.

For a discussion about the fabrication of these glass-based microdevices, the reader is referred to Chapter 3.

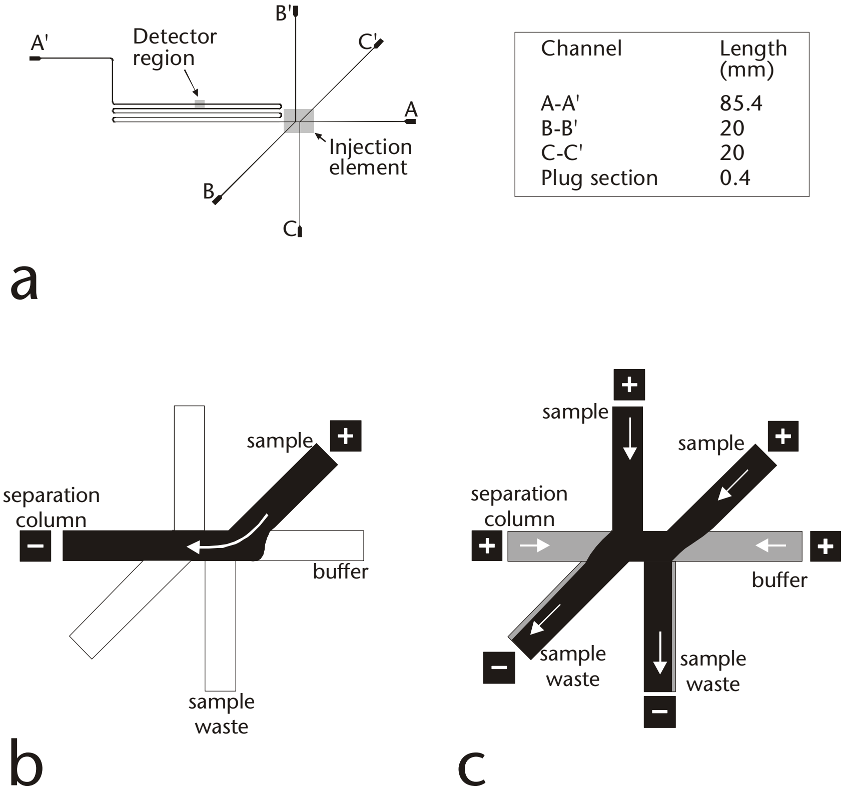

Channel	Length (mm)
A-A'	85.4
B-B'	20
C-C'	20
Plug section	0.4

Figure 4-9:

a) Standard stacking chip layout with 45-µm-wide channels and a multiport injection element.

b) Standard gated (time-based) injection.

c) Volume-defined filling of the double-T section without diluting the sample plug with running buffer.

4.4.2 Experimental

The experimental setup comprised computer-controlled high-voltage power supplies and an optical system for laser-induced fluorescence (LIF) detection of analytes labeled with fluorescein-isothiocyanate (FITC), as described in Chapter 2.

Two different sample and buffer systems were used in this study: a medium-conductivity buffer with 100 mM Tris and 20 mM boric acid at pH 9.1

(σ=0.75 mS/cm) and a high-conductivity buffer with 32 mM carbonate at pH 9.6 (σ=6.76 mS/cm). A mixture of two amino acids, serine (Ser) and glycine (Gly), was used to measure the preconcentration efficiency for carbonate and Tris / boric acid buffers. For the examination of different relative conductivity situations, the sample buffer was diluted with de-ionized water.

Amino acids were bought from Sigma (St. Louis, MO), tris(hydroxymethyl)-aminomethane (Tris) from Fluka (Buchs, Switzerland) and sodium carbonate and bicarbonate from Merck (Darmstadt, Germany). All solutions were made using de-ionized water. Labeling procedures and electrophoretic mobility data for labeled amino acids can be found in [13].

4.4.3 Stacking efficiency versus relative conductivity

Different sample buffer concentrations were tested, from matching conductivities (γ=1) down to heavily diluted sample buffer (γ=700). A medium conductivity buffer (Tris / boric acid) and a high conductivity buffer (carbonate) were compared at different concentrations. Sample plugs were formed using the fully pinched technique depicted described later (Section 4.5.2) for optimum performance (the different injection techniques are discussed later).

Stacking of 400-µm-long, volume-defined sample plugs resulted in a signal gain of up to 20.3-fold for carbonate buffer, and up to 15.7-fold for Tris/boric acid (Figure 4-10). Signal gain refers to the increase in peak height obtained under stacking conditions with respect to separations done using the same plug formation technique at γ=1. The detection limit of the optical setup used here was 1.4 µM for FITC-labeled Ser. Figure 4-11 relates signal enhancement in terms of peak height to the relative conductivities used in the experiments. Although the reason for the differences between the two buffer types was not clear initially, it is probably related to the separation efficiency and/or different migration times observed in the buffers. It was found when comparing peak widths for both buffer systems that separations in Tris/boric buffer showed wider peaks than in carbonate buffer (by a factor of 12% for FITC and 17% for Gly). This might be partly due to the longer migration times in Tris/boric buffer, which lead to an increase in peak width and a reduction in height due to diffusion. For the channel layout and solutions used in this work, dilution of the sample to γ-values above 350 does not seem to further improve the preconcentration. This is in agreement with the theoretical prediction of reduced stacking performance at high γ due to induced hydrodynamic flow effects leading to increased dispersion, and with values for stacking found in the literature [52, 98].

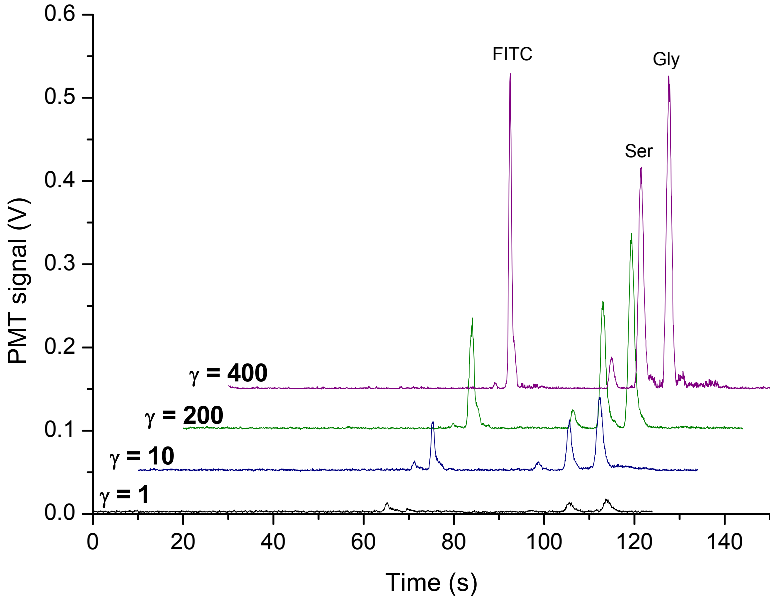

Figure 4-10: Comparison between a CE separation of two amino acids (10 µM of FITC-labeled Ser and Gly) with sample stacking and without (sample dissolved in running buffer, γ=1). Separation conditions: capillary length: 7.5 cm, field strength: 460 V/cm, running buffer: 32 mM carbonate at pH 9.6, volume-defined injection without dilution.

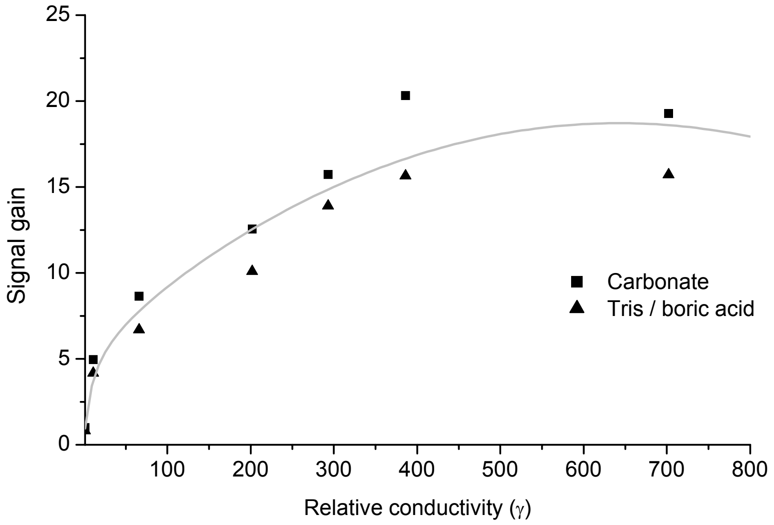

Figure 4-11: Signal gain as a function of relative conductivity for a high conductivity (32 mM carbonate at pH 9.6) and a medium conductivity (100 mM Tris / 20 mM boric acid at pH 9.1) buffer. Other separation conditions and sample composition as in Figure 4-10. Each data point is the average of data for Gly peaks obtained from 10 separations. Line represents empirical data fit for the sake of clarity. Signal gain is defined as the increase in peak height compared to that at γ=1.

4.4.4 Visualization of hydrodynamic pressure effects during stacking

To evaluate the importance of hydrodynamic pressure effects during the stacking process, video sequences were recorded upon application of the separation voltage. Still frames from a video of an injection sample under the condition γ=10 are presented in Figure 4-13, with a schematic explanation of the different processes going on given in Figure 4-12. The plug was formed using the volumetrically defined formation mode without dilution of the sample plug. The sequence starts at the moment when an electric field of 460 V/cm is applied to the separation channel with all other reservoirs floating (potentials are kept constant for all images). Prior to this, the double-T was filled with sample, with flow from B to C'. At t=80 ms, three effects can be observed. First, the FITC-labeled amino acids (negatively charged) migrate against the EOF and begin to concentrate into a narrow band at the rear of the plug. Second, at the front end of the injection element, low-conductivity buffer, cleared of the analyte, moves at a high velocity to the left into the separation channel, which is filled with the high-conductivity running buffer moving at a lower velocity. This generates an electro-osmotic pressure that pushes the sample buffer into the field-free short side channels B and B', due to their low fluidic resistance. This is in agreement with the natural push-back that has been observed in separations with matching conductivities for particular injector designs [48]. An inverse parabolic flow profile is generated at the front end of the contracting zone containing sample, most likely also an effect of the electro-osmotic pressure creating hydrodynamic backflow in the sample plug [88]. Third, a parabolic flow profile appears at the end of the plug, as a result of the different local electro-osmotic velocities, v_{eo}, in the sample and the running buffer. To maintain the overall mass balance of fluid flow, the sample plug can be viewed as drawing in high-conductivity running buffer from channel A [85]. Due to the induced shear forces of Poiseuille flow, the rear interface between sample and running buffer assumes a parabolic profile. As can be seen at t=320 ms, the inverse parabolic profile at the front of the plug is reduced with time. This is probably due to the increasing distance between sample buffer plug and the analyte, as well as to the fact that a considerable amount of sample buffer is actually removed from the separation column through the side channels.

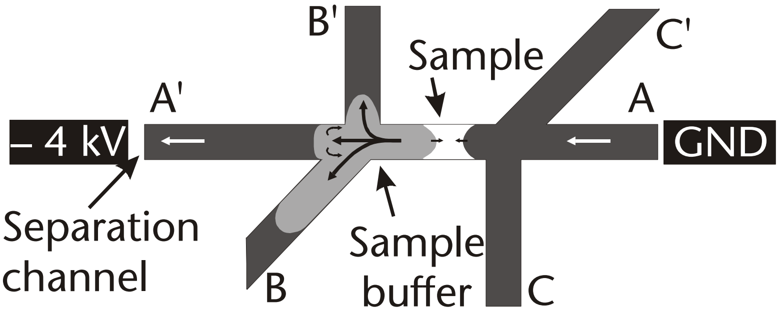

Figure 4-12*: Illustration of the different effects during sample stacking in the microchip structure used here. Black: running buffer, gray: sample buffer with no analyte, white: sample buffer with analyte. Sample: B; sample waste: C'; buffer: A; buffer waste and separation channel: A'; channels B' and C unused, but reservoirs filled with the same level of buffer as found in other reservoirs. Electric field applied between A and A', with all other reservoirs left floating.*

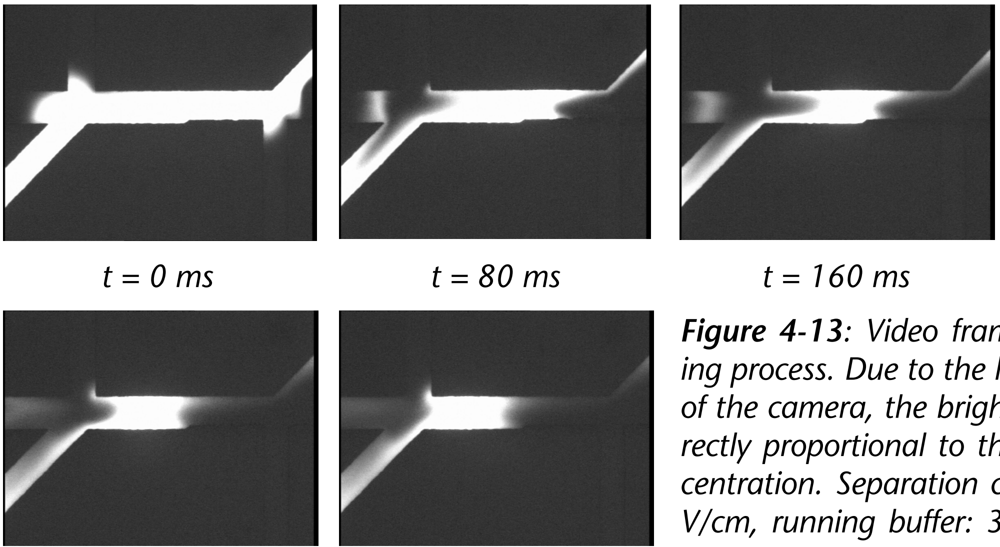

t = 0 ms *t = 80 ms* *t = 160 ms*

t = 240 ms *t = 320 ms*

Figure 4-13*: Video frames of a stacking process. Due to the limited contrast of the camera, the brightness is not directly proportional to the analyte concentration. Separation conditions: 560 V/cm, running buffer: 32 mM carbonate at pH 9.6, sample: 20 µM FITC-labeled Arg and Gly in 3.2 mM carbonate buffer (γ=10).*

The size of the preconcentrated analyte zones was measured directly on digitized video frames, choosing the minimum size found during the experiments. For γ=10, the initially 400-µm-long plug was reduced to 130 µm (size ratio: 3.1), for γ=100 a length of 100 µm could be observed (size ratio: 4). If a triangular concentration profile is assumed for the stacked segment, a peak concentration of 6.2-fold (γ=10) or 8-fold (γ=100) can be expected, which is in good agreement with the measurements presented in Figure 4-11. It is clear from these images, then, that a substantial amount of stacking takes place before the plug actually exits the injection intersection. It was decided, therefore, to examine more closely the influence of sample plug formation on FASS performance.

4.5 Sample plug formation for FASS

A major advantage of planar, miniaturized CE systems over their conventional counterparts is the ability to perform volumetrically-defined sample injections without electrophoretic bias. This assures both reproducibility and robustness of the analysis. It turns out that these features become especially important if a mismatch in conductivity is apparent between sample matrix and separation buffer, and hydrodynamic pressure effects have to be controlled. At the same time, a new injection element developed in the framework of this thesis allows not only to maintain the volumetric control but also assures that the low-conductivity sample matrix remains unchanged during the plug formation.

4.5.1 Plug shaping in microchip CE

Two designs to perform volumetrically defined sample injections without electrophoretic bias, the simple injection cross and the more advanced double-T injector [4, 13], are widely used. To avoid the spreading of sample into the separation channel, which deteriorates the volumetric definition of the sample plug, plug shaping, or pinching, has been used widely [47, 48]. Recently, Shultz-Lockyear *et al.* studied injection effects for different injection schemes where conductivity mismatches between running and sample buffer were present [48].

4.5.2 Plug formation for sample matrices with a conductivity mismatch

The generation of hydrodynamic pressure at a buffer concentration boundary was already discussed in Section 4.2.4. Video observations revealed the important effect that electro-osmotically-generated pressure due to the mismatch in ionic strength plays, especially during formation of the sample plug. The appearance of electro-osmotic pressure in a microfluidic system is caused by a difference in fluid flow velocity in two adjacent channel zones. Assuming constant channel cross-sections, this difference may be caused by:

a) difference in electrical conductivity in two regions of the channel, which produces a change of electric field strength in each zone,

b) dissimilar ionic strength in two parts of the channel, which changes the double layer thickness, the ζ-potential and thereby the electro-osmotic mobility [111, 112],

c) change in ζ-potential due to surface properties, e. g. by application of coatings [85].

In our experiments, no changes to the surface chemistry on the channel walls were made, and therefore only the first two cases are important for this discussion. Figure 4-14 illustrates the impact that differences in electro-osmotic flow velocity have when a low-conductivity sample must displace a more highly concentrated form of the same buffer in order to fill the injection element on a microchip. Initially, the injection element with all side channels was completely filled with running buffer. Then, an electric field of 340 V/cm was applied to inject a low-conductivity sample (γ=100) from the top left to the bottom right channel, while the other channels were kept floating. When the sample stream reached the intersection with the separation channel (at t=0.8 s), the sample spread with nearly equal flow velocity into all side channels, independent of the electric field configuration (see Figure 4-15 for a schematic representation). Only the separation channel A' was less affected, most likely as a consequence of its long length and high flow resistance. While the sample stream continued to fill the sample waste channel C, the electro-osmotic pressure decreased and the flow in the floating side channels stopped.

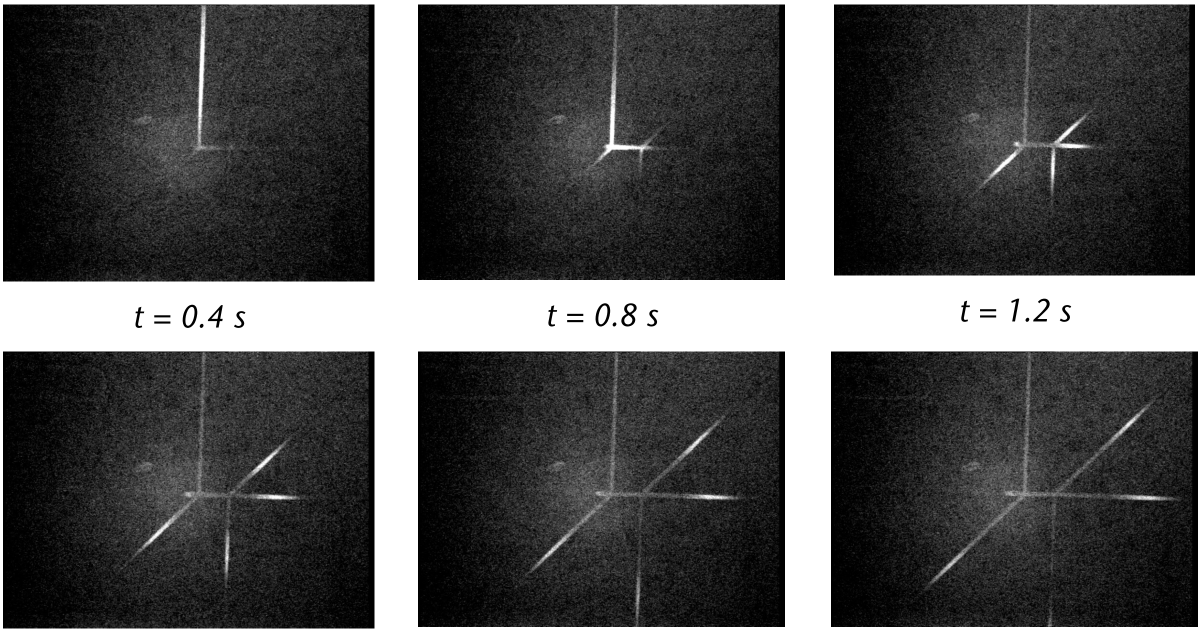

t = 0.4 s *t = 0.8 s* *t = 1.2 s*

t = 1.6 s *t = 2.0 s* *t = 2.4 s*

***Figure 4-14**: Effects of hydrodynamic pressure during a floating injection process of a low-conductivity sample (γ=100) into a microchip. The electric field for sample injection (340 V/cm) was applied between reservoirs at channel B′ and C. However, the positive pressure created due to the higher electro-osmotic velocity in the sample matrix region pushed the liquid into all side channels at velocities nearly independent of the electric field applied. Running buffer was 32 mM carbonate at pH 9.6 and sample consists of 20 μM FITC-Arg and -Gly.*

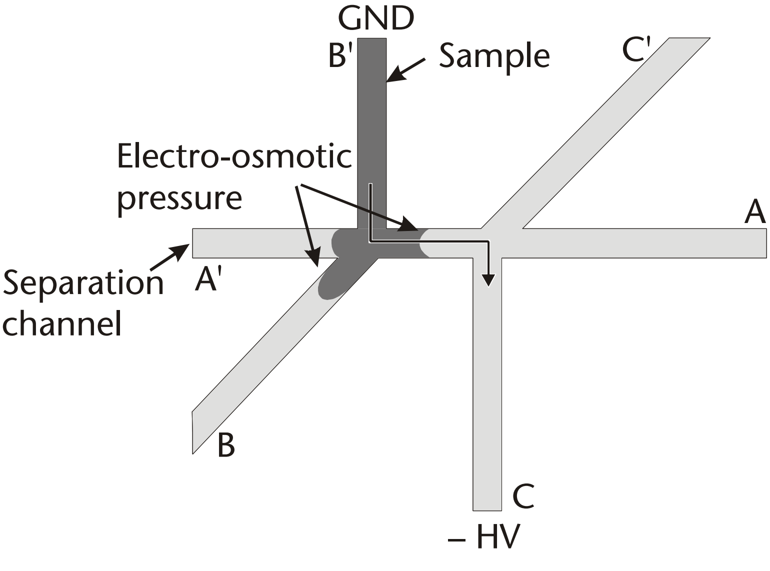

***Figure 4-15**: Schematic representation of the injection and the generation of electro-osmotic pressure in the injection element.*

If a pinched injection mode is used, it takes between 10 and 20 seconds, depending on injection field strength and relative conductivity, to remove the excess sample from the buffer inlet channel. Floating side channels containing buffer will also be cleaned to a large extent if the injection voltage is applied for a long enough time. It is assumed that this effect is due to a combination of viscous drag and Bernoulli forces caused by the electro-osmotic flow in the sample channel sections dragging solution out of the other stationary side channels. Assuming no height differences, Bernoulli's equation can be considered to be a statement of conservation of energy:

$$P_1 + \frac{1}{2}\rho v_1^2 = P_2 + \frac{1}{2}\rho v_2^2 \tag{22}$$

where ρ: mass density of the fluid,
v_i: velocity at point i,
P_i: pressure at point i.

Hence, the electro-osmotically driven liquid causes a pressure drop in the channel that aspirates liquid from the field-free side channels with v=0.

Figure 4-16a shows video images of five different injection schemes using carbonate buffer and a sample with a relative conductivity γ of 100. Figure 4-16a(i) depicts the situation of a floating injection 20 seconds after the application of the injection voltage of 1 kV (injection field strength: 490 V/cm). Sample is initially transported significantly into all side channels, as described above. Figure 4-16a(ii) and (iii) show two arrangements employing pinching, which will be referred to as "upstream" injection, because the sample is injected from the side channel closer to the detector to the side channel further away (for instance B' to C (Figure 4-16a(ii)) and B to C' (Figure 4-16a(iii))). The sample plug is well shaped in both cases, although qualitative differences can be observed between an injection from the perpendicular side channels and via the two diagonal ones. Sample is pushed back into the intersection at the back end of the plug by an auxiliary buffer flow from either A to C (Figure 4-16a(ii)) or A to C′ (Figure 4-16a(iii)). This flow of buffer serves to sharpen the plug boundary and therefore does not contribute significantly to sample dilution. However, in order to obtain a sample plug with sharp edges whose volume is well defined, a small but perceptible buffer flow from the separation channel A' is required.

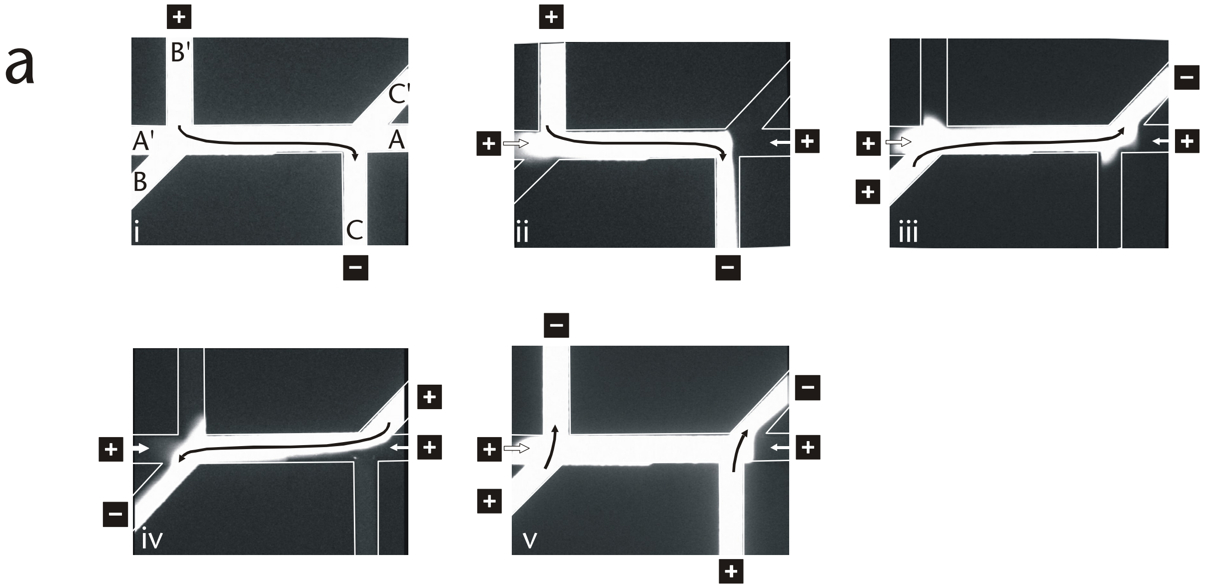

***Figure 4-16**: a) Different schemes of injection plug formation (dark arrows: sample flow, white arrows: pinching buffer flow): i) floating injection, ii) fully pinched injection in upstream direction, iii) fully pinched injection via diagonal channel, iv) fully pinched injection in downstream direction, v) fully pinched injection via two sample inlets. The long separation channel is A'. The injection voltage is –1 kV, indicated by a – at the corresponding channel; the resulting electrical field is 490 V/cm. All other reservoirs are grounded (+) or floating. A mixture of 20 µM FITC-labeled Arg and Gly was used as sample at γ=100, running buffer was 32 mM carbonate buffer at pH 9.6.*

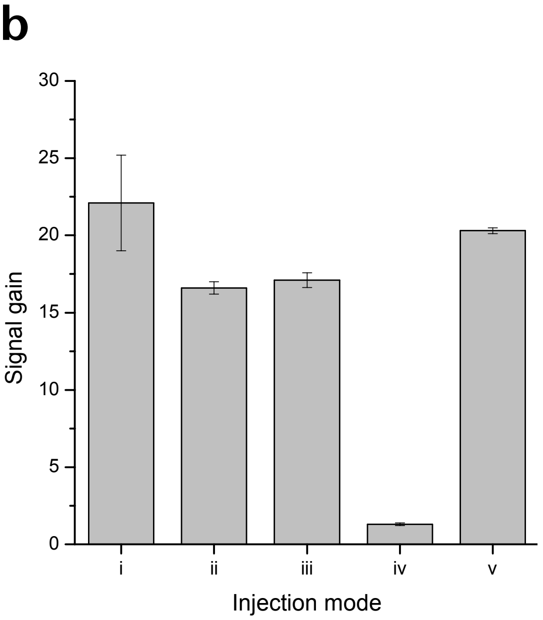

b) Maximum signal gain achieved for each scheme of injection plug formation at γ=390 for Gly using 32 mM carbonate buffer at pH 9.6. Separation conditions as in Figure 4-10. Signal gain is the ratio of peak height at γ=390 to that obtained at γ=1 for each plug formation method.

To maintain the simplicity of the voltage application configuration, three of the four channels involved in plug formation are maintained at ground. However, this means that buffer from A′ must traverse the sample as it moves into the sample waste reservoir C (Figure 4-16a(ii)) or C' (Figure 4-16a(iii)), which causes a dilution of the sample plug with running buffer. Under conditions of matching conductivities, this does not affect separation performance much. However, the stacking performance of a low-conductivity sample is reduced considerably, as Figure 4-16b shows. This is because dilution of the low conductivity sample with a high conductivity buffer results in a reduction of γ. The detector signal is 18 % lower than the maximum achieved by a plug formation scheme that avoids this kind of dilution with running buffer.

A more severe situation is created if the sample injection is performed in a "downstream" manner, with the sample flowing towards the detector into the double-T injection element. Due to the similar lengths of the sample channel from C′ and buffer channel from A, and the fact that both reservoirs are set at the same potential (Gnd), the electric fields in these channels are also similar. Hence, a strong flow of running buffer is generated that runs parallel with the actual sample stream in the formed plug (Figure 4-16a(iv)). In this case, the conductivity mismatch seems to be compensated for by dilution in a very efficient way, thereby suppressing FASS. This is evident in Figure 4-16b, where a signal gain of only 2 or so was obtained at a γ of 350. This effect could prove useful in applications not involving stacking, as is pointed out in a later section.

Finally, to resolve the adverse effects of pinching on sample plug purity, a new injection scheme is proposed, as was presented in Figure 4-9c and shown here in Figure 4-16a(v). Sample is transported via two channels from both sides into the injection element, fills the intersection and leaves the network via two sample waste channels. Consequently, the pinching streams from up- and downstream flow into different channels without passing and diluting the sample plug. Furthermore, complete and rapid loading of the channel segment between the intersections is assured by the fact that the potentials at A and A' are not exactly the same so that flow stagnation in this segment is prevented. The potential difference is due to ground being applied at both A and A', while distances between the injector and the electrodes A (buffer reservoir) and A' (separation channel) are different. Other realizations of this method for plug formation, involving a single sample channel in the middle of the injector delivering to both exit channels simultaneously, are also possible, but were not fully evaluated. This injection mode achieved the best signal gain by FASS of all tested in this study, without compromising the advantages of volumetrically controlled and bias-free injection. Although floating injection (Figure 4-16a(i)) showed a better signal gain due to the large amount of sample that is injected by diffusion/electro-osmotic pressure into the separation channel, it was also the least reproducible method.

Repeated experiments underlined the high repeatability of sample stacking in conjunction with volume-defined injection. FASS of a 5 µM FITC-sample at γ=10 could be performed with a reproducibility of 1.1% RSD (N=35) for the peak height, which is three times better than the results that were obtained by conventional gated injection (Figure 4-9b). In this case, the signal gain compared to non-stacking CE was 5.2, using the plug formation method mode in Figure 4-9c/Figure 4-16a(v).

As a conclusion of this experiment, it is obvious that only pinched injection schemes are appropriate if working with low-conductivity samples (or mismatched buffers in general).

4.5.3 Compensation for buffer mismatch by pinched injection

It was shown above that the choice of plug formation method has a strong influence on the stacking efficiency. Any method encouraging dilution of the sample plug with running buffer, thus reducing γ, will decrease FASS efficiency. This is particularly true of the downstream mode, where a strong pinching flow from the buffer to sample waste reservoir is observed, due to the short distance and the resulting high field strength between the two reservoirs and the injection volume (Figure 4-17).

If a very robust separation method rather than stacking is required, this effect could be exploited to compensate for changes in the sample buffer conductivity. Figure 4-18 shows three separations of the same sample of FITC-labeled amino acids dissolved in 100 mM, 50 mM and 10 mM Tris/boric acid buffer (pH 9.1). All three electropherograms are similar, as stacking is suppressed by the dilution effect. The video images in Figure 4-17 show that the degree of dilution is less with reduced sample buffer concentration, which is probably due to the stronger electro-osmotic flow of the low ionic strength solution. It is precisely this effect, in fact, that makes controlled, predictable mixing of solutions at a T- or Y-junction in an electrokinetically driven chip difficult when solution compositions vary substantially [16].

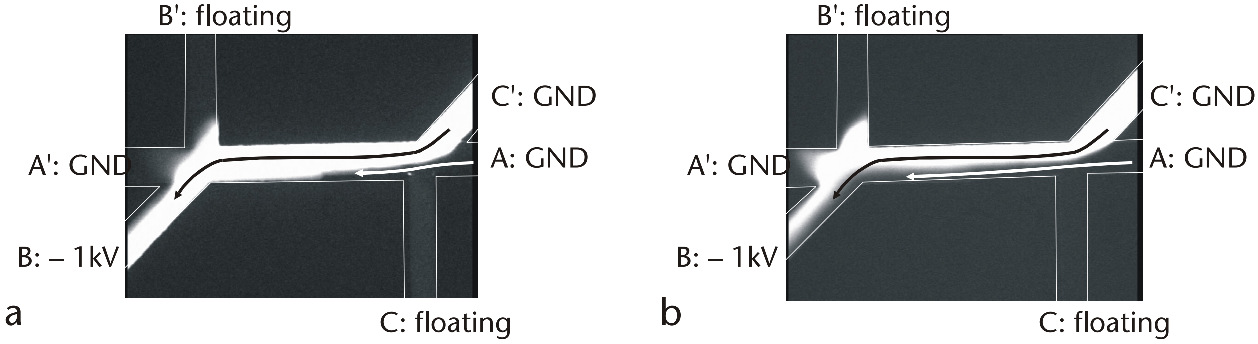

***Figure 4-17**: Dilution of a sample stream (black arrow) with running buffer (white arrow) during pinched sample plug formation in the downstream direction for a) γ=100 and b) γ=1 (sample: C'; sample waste: B; buffer: A; buffer waste and separation channel: A'). Conditions: injection voltage: 1 kV (field strength: 490 V/cm); other reservoirs grounded or floating; running buffer: 32 mM carbonate at pH 9.6; sample: 20 µM FITC-Arg and -Gly.*

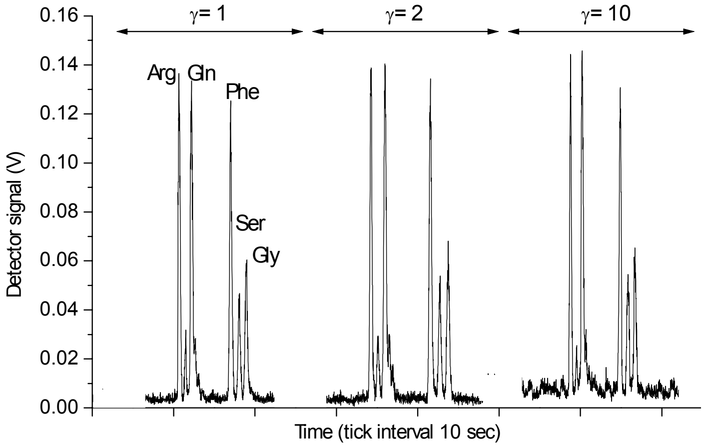

***Figure 4-18**: The pinched injection mode appears to compensate for changes in the sample matrix by diluting the sample plug with running buffer. The plot shows three CE separations with different sample matrices (relative conductivities 1, 2 and 10). Separation at 450 V/cm, running buffer 100 mM Tris and 20 mM boric acid at pH 9.1 (σ=0.75 mS/cm). Sample: 10 µM each of FITC-labeled Arg, Ser, Gly, Phe (phenylalanine) and Gln (glutamine).*

4.6 Full-column stacking

The method of sample stacking investigated above is based on the principle of injecting a volume of sample dissolved in low-conductivity buffer into a stream containing a higher concentration of the same buffer. As pointed out, signal enhancement is in theory directly proportional to the relative conductivity. However, induced pressure-driven flow effects limit the injected plug length and γ if optimal performance is to be obtained [88]. In fact, a plug length of 400 µm for a total separation length of 7.5 cm was chosen for the chip in an effort to minimize band broadening. To further increase the signal gain by FASS, different groups have proposed ways of increasing the injected sample volume available for stacking. The largest amount of sample which may be injected is in these cases determined only by column volume. Often, the whole separation column is filled with sample, which then undergoes stacking and removal of the sample buffer. Buffer elimination may be accomplished by applied back pressure [95], modification of electro-osmotic flow by dynamic wall coating [96] and polarity switching, both off- [93] and on-chip [61, 113].

Li *et al.* [61] have recently used polarity switching to preconcentrate trace level protein digests on a microchip prior to injection into a time-of-flight mass spectrometer. The separation channel on the chip was first filled with sample. This was followed by a flow reversal (i.e. polarity switching) as higher ionic strength buffer pushed sample back up the column away from the outlet, resulting in stacking of sample ions from a 10-nL initial volume to a final volume of 0.2 to 0.5 nL. The structure studied in this work for full-column stacking on planar substrates differs from the cited literature example, in that the layout consists of a stacking column coupled to a shorter separation capillary, as shown in Figure 4-19.

4.6.1 Chip design

Zero dead-volume fluidic interconnections – a task very difficult to achieve in the macroscopic world – are one of the main qualities of microfluidic systems. This chip design takes advantage of this feature by combining a separate stacking channel and a shorter separation channel, which have a 9-mm-long intersection (3.9 nL volume) in common.

In the version depicted in Figure 4-19, the preconcentration column is 69 mm long, comprising a maximum sample volume of 30 nL. Other designs feature preconcentration columns of 54, 134 and 174 mm with volumes of 23.5, 58 and 75.5 nL. The preconcentration column has two terminating reservoirs on either side of the intersection with the separation channel. One serves as stacking (or sample) waste, the other as a stacking buffer reservoir. This allow true volumetric definition of the stacked sample, as the sweeping procedure is always executed with fresh stacking buffer from the dedicated reservoir while the stacking waste is constantly contaminated with sample aliquots during filling.

Another advantage of this design is that preconcentration column and separation channel length can be chosen independently of each other. This is especially important as the preconcentration column is generally long (for a high sample loading capability), while the separation channel is comparatively short (for fast separations at low voltages). The separation channel (measured from the end of the intersection) is 38 mm for all designs.

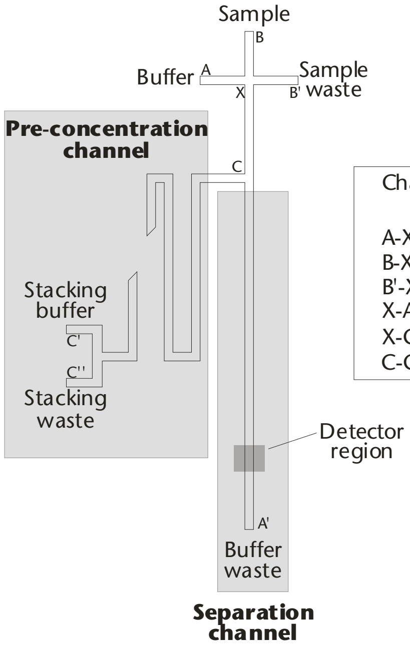

Channel	Length (mm)
A-X	9
B-X	7.2
B'-X	9
X-A'	38
X-C	9
C-C' and C-C''	69

***Figure 4-19**: Schematic chip layout of a column-coupled system with a long preconcentration channel (left) and a shorter separation channel (right). Both sections are connected via a 9-mm-long common channel region.*

4.6.2 Chip operation

As shown in Figure 4-20, the stacking and separation procedure requires three steps. First, the preconcentration column is completely filled with the sample by applying a potential between the sample and stacking waste reservoirs. Current monitoring is used to determine when the column is filled. Then, the electric field is reversed by applying ground to the stacking buffer reservoir and a negative voltage to the sample waste. High conductivity running buffer is dragged into the capillary and sweeps the analyte anions back, thereby increasing their concentration. Finally, the stacked sample plug reaches the 9-mm-long intersection of the preconcentration and CE channels, and can be separated rapidly by applying an electrical field between buffer and buffer waste reservoir. Again, the moment of switching between sample matrix push-out to CE separation is determined by current monitoring of the stacking channel. Depending on γ and analyte composition, switching was performed as soon as the current reached around 75 to 80% of its final value, which was measured prior to the separation.

The use of two separate reservoirs at the end of the preconcentration channel assures that sample does not mix with the running buffer during the first filling step, as might occur in other designs for long column stacking. This design provides a high degree of flexibility, as stacking and separation parameters may be defined nearly independently of each other. The stacking efficiency is assumed to be proportional to the preconcentration channel length, which could be increased to gain higher sensitivity without affecting the CE channel.

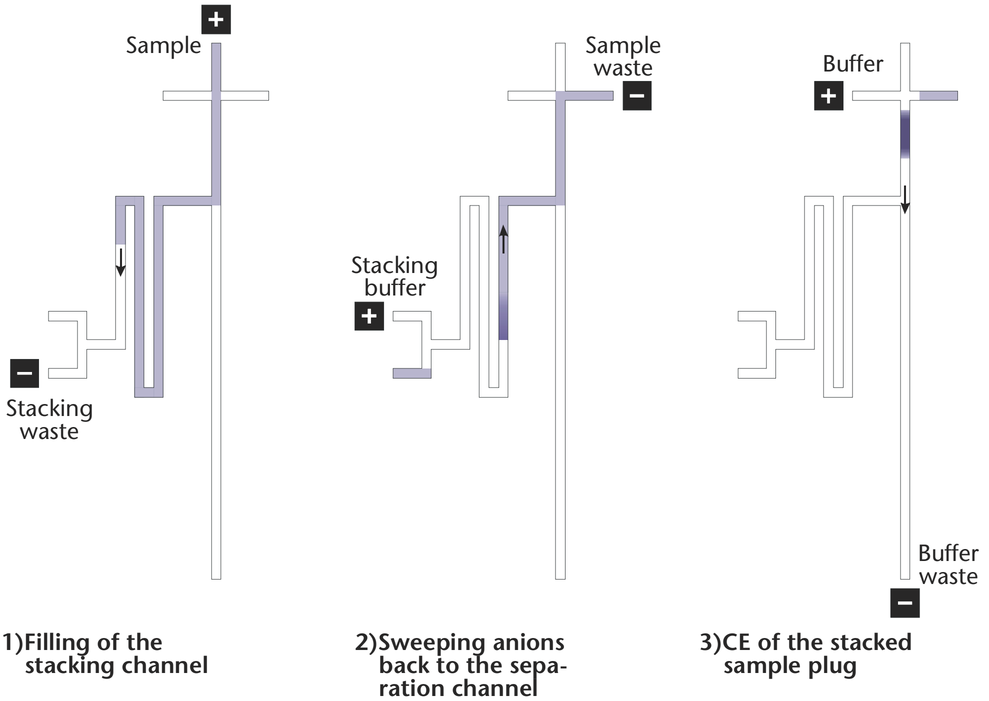

Figure 4-20: *The three process steps for full column stacking in a coupled column configuration (for details see text).*

4.6.3 Stacking efficiency versus stacking channel length

Filling of the stacking channel was performed at high field strengths of up to 520 V/cm for 45 seconds (for the 54-mm stacking channel), to assure an unbiased composition of the sample in the column. The electric field strength and time required for filling were dependent on the stacking channel length. Then, the voltage was reversed and stacking was performed at the same field strength until the endpoint current was reached. A short cleaning step which involved pumping buffer into the sample waste reservoir followed, in order to remove sample from the buffer channel that might have been introduced due to hydraulic pressure as discussed earlier. The absence of small satellite peaks at the detector preceding those due to the stacked sample indicates that no sample solution was pushed into the separation channel during the filling process, which is in agreement with the observations in Figure 4-21. Finally, the preconcentrated sample plug was separated in the CE channel at 460 V/cm. Figure 4-21 shows results for this stacking method, yielding a 65-fold preconcentration of a sample containing 100 nM of FITC-Arg and FITC-Gly at γ=160, with 32 mM carbonate as running buffer. The experimental result obtained at γ=1 is shown for comparison, and was carried out by simply filling the 9 mm long injector with sample in the running buffer, and separating as above.

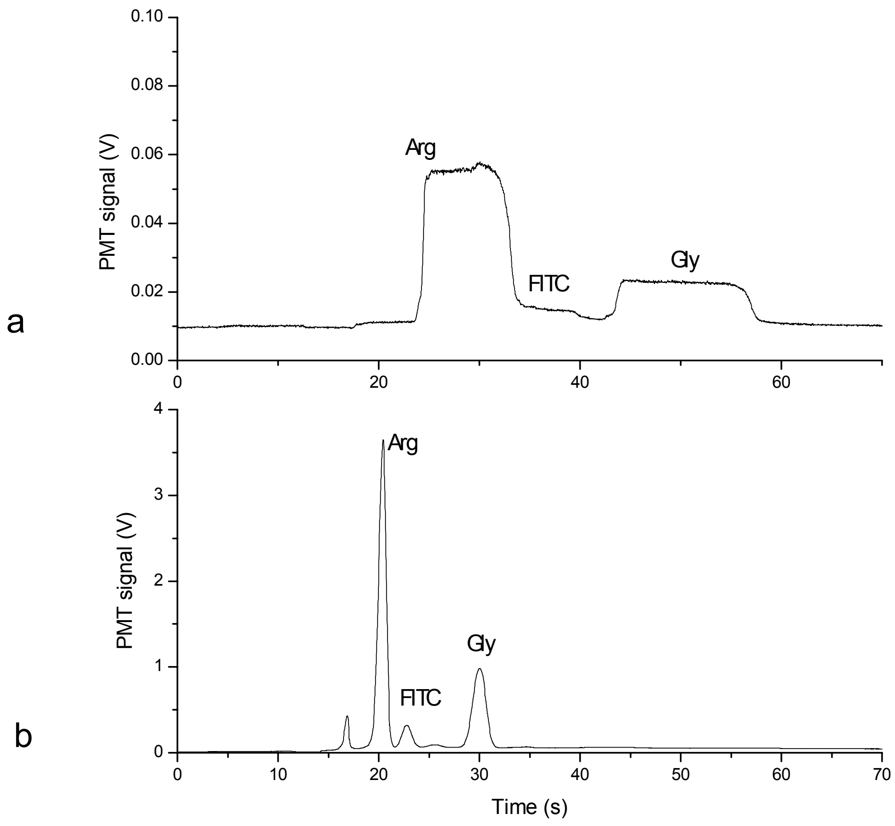

***Figure 4-21**: Separation of 100 nM FITC-labeled Arg and Gly in 32 mM carbonate buffer in the coupled-column structure depicted in Figure 4-19.*

a) Reference experiment under non-stacking conditions at γ=1 for comparison with the mode in b). To create a long sample plug, a pinched injection of the sample into the 9-mm-long channel segment X-C using channel B as sample and C as sample waste, was performed. Pinching was accomplished by small, auxiliary flows from A and A'. Separation conditions: 460 V/cm from A to A', running buffer 32 mM carbonate at pH 9.6, effective separation length: 33 mm.

b) CE using FASS in 200 µM carbonate buffer in the completely filled stacking channel (γ=160, procedure see text). Other separation conditions as a).

Measured theoretical plate numbers are 3280 for Arg and 2344 for Gly. From the measured efficiency, and taking into account diffusive dispersion, the length of the stacked sample plug that was injected into the separation channel is estimated to be 1.8 mm [13]. Going to sample buffers of a lower conductivity should improve the sharpness of the stacked analyte zone and increase the separation resolution. Another possibility under investigation is the injection of an additional low-conductivity buffer plug behind the preconcentrated sample zone to perform a second stacking step during the CE separation.

From the separation in Figure 4-21, limits of detection were found to be 80 pM for Arg and 300 pM for Gly. The limit of detection for the improved optical setup used in this experiment (described in Section 2.4) for γ=1 is 20 nM FITC-labeled Gly at a signal-to-noise ratio of 3 (noise: 1 mV peak-to-peak).

Figure 4-22 shows the relationship between the length of the preconcentration column (and therefore sample loading capacity) and the achievable signal enhancement. Over the range from 54 to 174 mm, the function is nearly linear, which indicates that the preconcentration efficiency can be tailored by choosing an appropriate channel length. As an effect of the longer preconcentration column length compared to the experiment in Figure 4-22, the separation in Figure 4-22a reduced the limit of detection further to 55 pM for Arg and 220 pM for Gly.

It is noteworthy that the achievable signal gain also depends on the applied electric field during the preconcentration step. Comparatively low field strengths (150 to 250 V/cm) have been chosen for the preconcentration step to reduce dispersion due to the parabolic plug profile caused by the mismatched buffers. For higher fields, the signal gain is reduced, which was experimentally verified for 400 V/cm. The signal gain obtained for the 54-mm channels was 24% less than in the low-field-strength case and 21% less for the 69-mm channel (longer channels could not be examined due to limitations of the absolute voltage applicable with our setup).

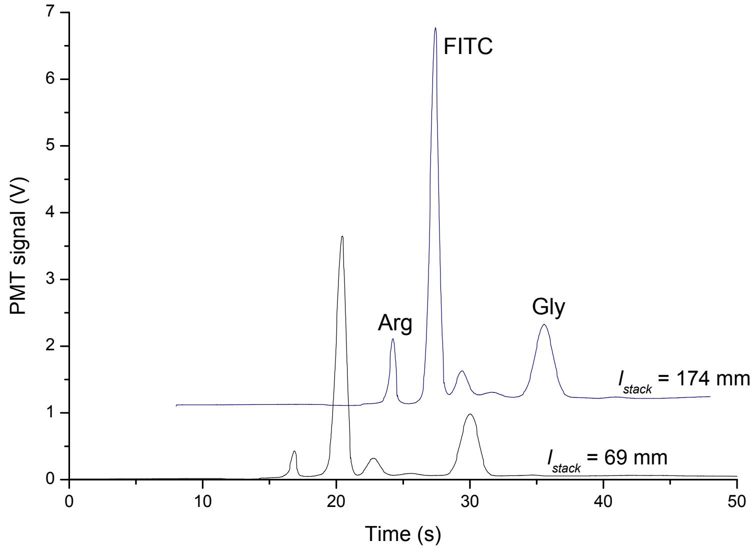

Figure 4-22:

a) CE separation with sample preconcentration using full-column sweeping for two different preconcentration column lengths (69 and 174 mm). The signal enhancement for the 69-mm channel is 65, while it is 95 for the 174-mm-long channel.

Sample: 100 nM FITC-Arg and -Gly, γ=160

Separation cond.: E=460 V/cm, running buffer: 32 mM carbonate at pH 9.6

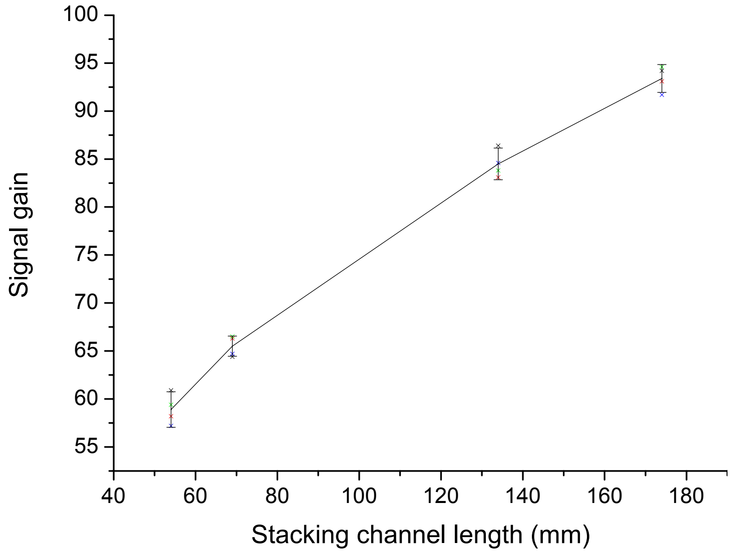

b) Signal enhancement as a function of preconcentration column length. A linear relationship between the length (and therefore loaded sample volume) and yield is visible.

4.6.4 Current monitoring as a diagnostic tool

As the discussion about electro-osmotic flow in the earlier sections has shown, a good understanding of the various, simultaneous flow effects going on in a microfluidic network is essential for successfully deploying these kind of devices. As long as fluorescently labeled molecules or markers are used, optical inspection under a fluorescence microscope is a useful tool to look locally at plug formation, channel filling and other fluidic operations. However, it is often desirable to obtain a rather macroscopic view of the situation in the microfluidic channel network. In this case, if the various liquids used differ in electrical conductivity, monitoring the DC current in the different branches of the device is a good source of information about flow rates. It is also a good way to ascertain how much liquid has entered certain branches. Current monitoring has already been used to measure electro-osmotic flow rates in capillaries [71], or as a diagnostic tool for microchannel surface coating techniques and chip operation for heterogeneous immunoassay application [114].

Two examples are presented in this section to illustrate the usefulness of this technique within the context of this work. First, current monitoring was used to verify successful sample introduction and plug formation in the integrated CE device; second, current monitoring was used as an active part of the control software to precisely position the preconcentrated sample zone after sweeping into the separation channel.

Assuming that a fraction of x ($0 \leq x \leq 1$) of a capillary of length L is filled with a low-conductivity buffer, we can derive the electrical resistance of the two channel regions as follows (to remain consistent with the previous sections, the subscript EH is used for the low-conductivity, high-field strength region):

$$\begin{aligned} R_{EH} &= \rho_{EH} \frac{xL}{A} \\ R_{EL} &= \rho_{EL} \frac{(1-x)L}{A} \end{aligned} \tag{23}$$

The current is then simply obtained by dividing the applied voltage by the total resistance $R_{EH}+R_{EL}$ (neglecting heating effects and the like). For a typical microfluidic channel etched isotropically into the substrate, the cross-section A is (assuming a semicircular shape with a flat bottom):

$$A = \frac{1}{2}\pi d^2 + wd \tag{24}$$

with d: etching depth

w: mask linewidth

For a typical separation channel 45 µm wide at the top, 15 µm deep and 85 mm long, R_{total} becomes 122 MΩ if filled entirely with 32 mM carbonate buffer at pH 9.6 (σ=6.76 mS/cm). Currents are therefore around 20 µA if a voltage of 2.5 kV is applied to the channel. As the noise of the current monitor provided by the DC/DC-converters (see Chapter 2) is in the order of 1 µA, a more sensitive measurement setup was used (described in detail in Section 2.2.4). Briefly, it consists of an ohmic resistor in series with the separation channel, which converts the current passing through the channel into a voltage. This in turn is buffered using an high-ohmic voltage follower based on an operational amplifier, providing a current sensitivity in the order of 10 nA.

Figure 4-23 shows the measured current versus time for a CE separation with FASS of a low-conductivity sample (10 µM of FITC-labeled serine and glycine, conditions as in Figure 4-10). After plug formation and at the start of the separation, the current is low as the sample plug increases the total resistance of the channel. The current level serves as a measure for the sample plug length and provides verification of whether the plug shaping conditions (pinching flows) work properly. During the separation, current monitoring indicates if sample is leaking from the side channels into the main channel, which causes a further reduction in current. If the push back voltages are chosen correctly and the liquid levels in the reservoirs are equilibrated, the current should stay approximately constant during the separation. Once the sample matrix plug leaves the separation channel and enters the buffer waste reservoir, the current rises back to its normal (separation buffer) level. The migration time of the sample buffer plug could potentially be used as an internal marker for migration time compensation.

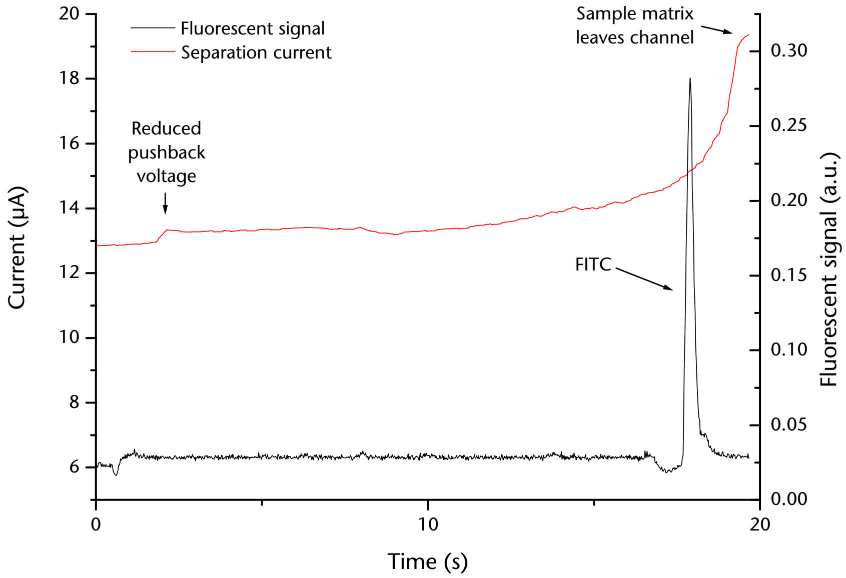

Figure 4-23: Current monitoring allows the assessment of plug formation, sample leakage and sample matrix migration time in FASS.

Clearly, the diagnostic aspects of current monitoring are very useful both for laboratory as well as commercial applications. However, the technique can be taken even a step further. The full column stacking technique presented in this section relies on current monitoring to switch from sample matrix removal to separation mode at the exact moment that the preconcentrated sample plug enters the intersection. As the high-concentration buffer flows into the capillary from the reservoir, the current continuously increases. At a value of 95% of the original value (stacking channel entirely filled with separation buffer), voltages are switched and the CE separation starts.

4.7 Conclusion and outlook

The design of a modified double-T injector with a comparatively long plug allowed the formation of volumetrically controlled injections for FASS which were free of electrophoretic bias. Video observations indicated that full pinching during plug formation is necessary to avoid uncontrolled spreading of the sample into the adjacent channels due to diffusion and, in particular, electro-osmotic pressure.

Several methods for sample zone formation, using auxiliary buffer flows to shape the plugs, were investigated. Of these, the mode yielding best results employed two adjacent side channels to introduce sample to the injection element. Two adjacent channels on the other side, positioned directly opposite the sample inlets, carried excess sample to two waste reservoirs. The use of two parallel sample waste outlets from the injection element avoided dilution of the low-conductivity sample by the high-conductivity running buffer used for pinching. The lower signal gain observed for plugs made using a single inlet and outlet for filling the injection element was due to such a dilution effect.

Using the new, dual-inlet injection technique, preconcentration efficiencies of 20-fold for carbonate buffer and 16-fold for Tris/boric acid buffer could be achieved by stacking 400-µm-long sample plugs followed by CE. The reproducibility was found to be 1.1% RSD for peak height, for repeated injections of an FITC-labeled sample. The signal gain was found to increase with decreasing sample buffer conductivity, as predicted by theory. Relative conductivities higher than 350 did not improve the detector signal. This was most likely due to increasing band-broadening caused by induced Poiseuille flow as a consequence of the buffer mismatch.

It was found that on-line dilution of the sample plug could be used to improve CE separations if no FASS was required. Over a relative conductivity range of one decade, the peak height was maintained quite constant if a downstream injection mode was used. Hence, discrepancies in sample matrices with respect to the running buffer may be corrected to some extent through design of an injector that allows dispersion-free dilution of the volume-defined plug.

However, handling of an extremely low-conductivity sample required careful control of push-back and pinching voltages. As the overall resistance in the separation column changed drastically in the course of the separation, generating push-back using voltage sources seemed not to be the best option. Constant current sources at the sample and sample waste reservoir facilitated the application of a constant push-back independent of the chemical situation in the separation channel. It is also envisaged to use a constant current mode of control for the CE separation. This is because it allows a constant electrical field strength to be maintained in the running buffer, thereby improving migration time reproducibility when different sample buffer conductivities are present.

To further improve the efficiency of FASS, a new channel structure was introduced, combining a long stacking channel and a short separation channel in a column-coupling configuration. Preliminary results indicate preconcentration factors of about 95-fold on a time scale of a few minutes. However, the separation resolution needs to be improved to turn this technique into a useful tool for microscale separations of trace analytes. Since the length of the stacked plug injected appears to be too long, different stacking channel lengths and geometries will be investigated to optimize not only stacking, but also injected plug length.

Microchip-based fluidic systems have the potential to dramatically simplify the instrumentation used for separations. This is especially true for techniques requiring the sequential addition of several different solutions to a separation column, or for many column-coupling techniques. To take advantage of the added complexity of micromachined systems, however, a more fundamental insight must be obtained of the various effects that, either singly or combined, determine the fluid dynamic situation at channel intersections and segments. A thorough theoretical analysis and modeling of the effects buffer mismatch has on the performance of FASS in integrated fluidic structures is required to optimize this type of preconcentration on chips.

As a future direction of research, the new injection method proposed in this chapter (Figure 4-24a) could be further simplified by using only one sample inlet while keeping the two sample waste side channels (Figure 4-24b). The resulting injection performance and the overall benefit should be basically the same as the dual-inlet design (Figure 4-24a), while the single inlet channel reduces the complexity of the microfluidic network. However, this injection mode was not evaluated in this work, as the layout was not compatible with the chip available (depicted in Figure 4-9). A device based on this three-port plug-formation element has recently been discussed in the literature [115].

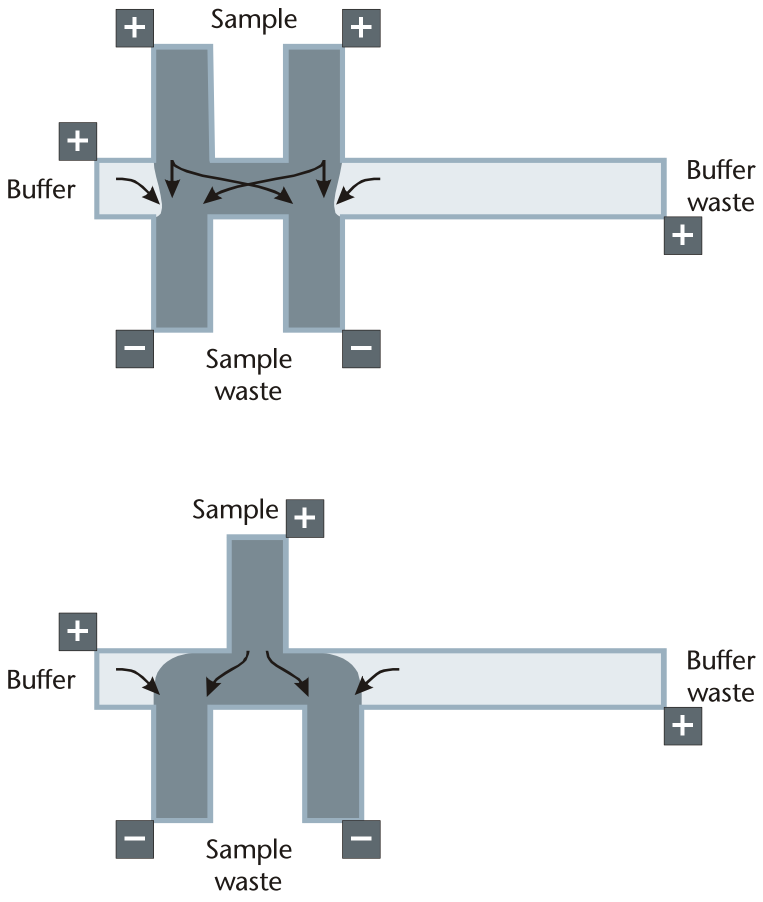

Figure 4-24:

a) New design for creating volumetrically defined sample plugs, while avoiding the buffer dilution problem. Here, the pinching flows from the buffer and buffer waste reservoirs are directed into the sample waste by two channels at both ends of the sample plug. Buffer flow through the plug does not occur.

b) A simplified version of the plug-formation element depicted in Figure 4-9c with only one sample inlet channel. The benefit is the same with a somewhat reduced design complexity.

Chapter 5

Contactless Conductivity Detection

A new, integrated, in-plane, contactless conductivity detector (CCD[16]) was developed for the analysis of small ions by capillary electrophoresis (CE). The device allows fast separation of inorganic anions and cations in the order of 20 s. The microfabrication process developed in the context of this thesis makes it possible to easily integrate CCDs with standard glass and polymer micromachining. It also allows the placement of the electrodes close to the separation channel, independent of the substrate type, which is a requirement for good detector sensitivity and spatial (i.e. separation) resolution. The device is characterized in terms of sensitivity and linearity, and a procedure for optimizing the operational parameters of the detector is proposed. Finally, an improved electrode layout is presented, which shows higher sensitivity and better spatial resolution.

5.1 Introduction

As outlined in Chapter 1, microfabrication has proven to be an excellent tool for the development of miniaturized total chemical analysis systems (µTAS). Outnumbering all other analytical techniques implemented on chip to date is capillary electrophoresis (CE), which benefits from miniaturization both in terms of separation time and efficiency [11, 13, 14, 116-119]. During the past decade, the main research focus of the field was the development and understanding of microfluidic components necessary for the actual separation, i.e. the fabrication of channel systems and plug formation elements, or the study of electro-osmotic and pressure-driven flow in microstructures. However, at least two other key components are necessary for the successful implementation of true miniaturized separa-

---

[16] Although the abbreviation CCD also stands for charge-coupled device in the field of opto-electronics, it was adopted here in accordance with terminology in the recent literature on this subject.

tion systems: 1) specially adapted high-voltage control systems and 2) miniaturized detectors, which record the separated analyte zones at the end of the separation channel. The first topic was already covered in detail in Chapter 2, describing the development of both laboratory-type and portable power supplies for microfluidic applications. This chapter focuses on the development of a new detector system for microchip-based separation devices, which distinguishes analyte zones on the basis of their different electrical conductivities[17].

Most reports on microchip CE devices rely on laser-induced fluorescence (LIF) to detect the analytes at some point towards the end of the separation channel, as described in [13, 120, 121]. LIF is fairly easy to implement with many biochemical analytes, though most of these require labeling with a fluorescent marker, an extra step in the analysis process. Its sensitivity is unparalleled, with detection down to single molecule levels possible on chip [120-123]. Detection sensitivity is especially important, as the detector volume is very small in microchip CE devices (from tens of pL to a few nL), reducing the number of molecules available for detection as well.

Despite its advantages, LIF detection is not universally applicable for chip-based systems. Many species, besides not being intrinsically fluorescent, cannot be made to fluoresce. Small inorganic ions fall into this category. Though addition of a fluorescent marker to the background buffer for indirect detection of the ions is an option [124-126], sensitivity is generally compromised somewhat in this detection mode. With LIF detection, it is also usual that the chip is the smallest component in the entire analysis system, with the peripheral optical system depending on larger, conventional components. Often the laser dwarfs all of the other detection elements put together. It is therefore difficult to realize robust, portable microanalytical systems using fluorescence detection, making LIF-based µTAS less accessible for field-based environmental or point-of-care applications.

---

[17] Major parts of this chapter have been published in: J. Lichtenberg, N.F. de Rooij, E. Verpoorte, "*A microchip electrophoresis system with integrated in-plane electrodes for contactless conductivity detection*", Electrophoresis 23 (2002) 3769-3780. Amongst the previously unpublished material are the general introduction including theory and conventional conductivity detectors, numerical modeling and the comparison of different electrode layouts.

To enhance the versatility of microfabricated analysis systems, research efforts have recently been directed increasingly towards the development of new integrated detection systems in the optical as well as in the electrochemical domain. With respect to optical detection, the integration of microlenses and aperture layers onto sealed glass microfluidic devices for LIF detection has been reported recently by Roulet *et al.* [67, 72]. Webster *et al.* integrated a photodiode for fluorescence detection into a silicon substrate also incorporating microchannels for CE [68], while Chabinyc *et al.* embedded a microavalanche photodiode into a poly(dimethylsiloxane) microfluidic device [69]. Refractive index detection using a holographic element was carried out by Burggraf *et al.* to detect the separation of sugars on a microchip CE device [127].

Electrochemical detection, which includes amperometric, potentiometric and conductometric detection, scales better upon miniaturization than absorbance or fluorescence detection, and so is the subject of an increasing number of research papers looking at its integration into microfluidic chips [128, 129]. For the analysis of small inorganic and organic ions, conductivity detection is particularly promising, with potential applications in environmental and food analysis [130]. This detection method monitors local changes of solution conductivity in the detector volume, and is well suited to small ions having high equivalent conductivities. Since the application in this study focused on the analysis of small inorganic ions in water, conductivity detection was viewed as an appropriate choice for on-chip detection.

5.2 Theory

5.2.1 Electrical conductivity and electrolyte composition

Liquids exhibit the property of electrical conductivity if they contain charged particles, generally ions, that are free to move through the liquid. When an electric field is applied across a volume of liquid, the ions travel along the field lines, carrying an electrical charge that gives rise to an electrical current. A material's ability to transport charges is called its electrical conductivity [82, 131].

All ionic species in a solution (denoted as *i*) contribute to the electrical conductivity. The magnitude of each contribution is proportional to electrophoretic mobility, $\mu_{ep,i}$ (cm^2/V·s) (in general electrochemistry also called ion mobility [131]), charge, q_i (C) and the number of ions per cm^3 (N_i). Conductivity, σ, (S/cm) is therefore defined as[18]:

$$\sigma = \sum_{i=1}^{n} N_i |q_i| \mu_{ep,i} \tag{25}$$

An electrical field, *E*, applied across the conducting liquid exerts a Coulomb force on the charged ions, which accelerates them to a velocity of v_i[19]:

$$v_i = \mu_{ep,i} E \tag{26}$$

Once v_i is reached, frictional forces due to ion movement are in equilibrium with the Coulomb force acting on it. Note that the migration direction is defined by the sign of $\mu_{ep,i}$, with cation mobility being positive and anion mobility negative.

The resulting net motion of charges gives rise to an electric current, expressed here as a current density, *J*, per surface area (A/cm^2):

$$J = E \cdot \sum_{i=1}^{n} N_i |q_i| \mu_{ep,i} \tag{27}$$

As it is more convenient in chemistry to work in terms of concentration than in ions per cm^3, we can use the following relation[20]:

$$c_i = 1000 \frac{N_i}{N_{AV}} \tag{28}$$

where N_{AV}: Avogadro's constant ($6.02 \cdot 10^{23}$)

---

[18] Note that σ depends basically on q_i^2, as the charge is already included in the ionic mobility. While the migration velocity depends linearly on q_i, every molecule contributes additionally in proportion to its charge to the electrical conductivity.

[19] The effect of electroosmotic flow on the ion migration and the resulting current is not included here, as the general case does not necessarily include EOF.

[20] The factor 1000 converts from cm^3 to dm^3 or L for the concentration unit.

Thus, J and σ become:

$$J = E \cdot \underbrace{F \sum_{i=1}^{n} c_i \cdot z_i \cdot \mu_{ep,i}}_{\sigma} \qquad (29)$$

where F: Faraday's constant (96,495 C/mol)
z_i: valence of species i

To derive a measure of conductivity independent of the solution concentration, a molar conductivity Λ can be derived as:

$$\Lambda = \frac{\sigma}{c} \qquad (30)$$

However, due to intra-molecular interactions, Λ does vary with concentration [131]. For strong electrolytes, Λ decreases only slightly with increasing concentration, but for weak electrolytes the dependence is much stronger. For strong electrolytes, the actual molar conductivity can be modeled according to Kohlrausch's law originating from the 19th century:

$$\Lambda(c) = \Lambda_0 - \alpha\sqrt{c} \qquad (31)$$

where Λ_0: limiting molar conductivity for $c \to 0$
α: a positive constant

A comprehensive list of limiting molar conductivities for various ions can be found in [132].

5.2.2 Conductivity detection in conventional systems

Prior to its application to CE by Mikkers *et al.* [38], conductivity detection had been used very successfully in ion chromatography [133]. Signal response in conductivity detection arises directly from the relative difference in conductivity of the background buffer electrolyte (BGE) and the separated analyte zones. Therefore, to maximize concentration sensitivity, a BGE has to be selected that differs strongly from the analyte in terms of conductivity [130, 134]:

$$\Delta\sigma = \left|\sigma_{analyte} - \sigma_{BGE}\right| \overset{!}{=} \max \tag{32}$$

Generally, we can distinguish between direct and indirect conductivity detection techniques. Direct detection applies to highly conducting (i.e. highly mobile) analytes, which can be well distinguished from a low-conductivity BGE. This technique is by far the more common one in the literature and is especially suited for the analysis of small inorganic or organic ions, like alkali metals [38, 42, 134, 135], halogens [42] or organic acids [136, 137]. Detection limits as low as 1 ppb for common alkali metals (~100 nM) have been achieved in capillary systems [134].

Indirect detection on the other hand targets medium- and low-conductivity analytes which show negative conductivity peaks when separated in a highly conductive BGE. This technique has been used for the separation of cationic and anionic surfactants [138, 139]. For example, sodium with triethanolamine (TEA) was used as a highly conducting BGE for the analysis of alkylammonium salts in the latter reference. This combination of BGE and analyte allowed limits of detection (LODs) below 10^{-5} M. It is observed that indirect detection methods are generally less sensitive than their direct counterparts, which also holds true not only for conductivity detection. This is mainly due to the unfavorable measurement situation, where minor perturbations in a high background signal have to be detected [140]. Hence, a high dynamic range of the detector system is required for sensitive, indirect operation.

The role of the background electrolyte

Independent of whether direct or indirect detection is used, the conductivity of the BGE is the major parameter affecting the sensitivity of the conductivity detection scheme. For low LODs, the conductivity of the BGE has to be as different as possible from that of the analyte as shown in equation 32. As we focus on the direct detection technique for small ions in this section, we note that the BGE conductivity has to be as low as possible.

One way to achieve this is by reducing the BGE concentration, which affects the buffer conductivity nearly linearly over a wide range [83]. Huang *et al.* have found for instance that a 4-fold reduction of the buffer electrolyte concentration resulted in a 12-fold improvement of the detector LOD [141]. However, dilution of the buffer is a somewhat limited solution, as the buffer capacity should not be compromised for a reliable separation procedure.

As an alternative, the BGE molar conductivity can be reduced by choosing a suitable composition. In ion chromatography, buffers based on low-mobility benzoate or complex borate-gluconate anions have been used, whose conductivity differs strongly from that of solutions containing small analyte ions [142]. While these BGE ions do not affect the separation efficiency of chromatographic methods, the large difference in electrophoretic mobility does severely reduce separation performance in CE. For optimum separation performance, the buffer co-ion's mobility should be equal to that of the analyte to obtain maximum peak symmetry [130]. If it is faster, analyte peaks exhibit tailing, or if slower, a leading peak shape.

A good choice of buffers for conductivity detection are therefore amphoteric electrolytes with a low equivalent molar conductivity, also known as Good's buffers [143, 144]. These buffers are based on zwitterionic amino acids and can be used at comparatively high ionic strengths without compromising the detection sensitivity too severely. An amphoteric compound in solution tends to adjust the pH to its isoelectric point, and isoelectric buffer constituents have only a few charged groups [145-147]. Therefore, they do not show a high molar conductivity, although the electrophoretic mobility of the buffer ions is comparatively high[21]. For anion separations, the most well-known buffers for CE with conductivity detection are based on either 2-[N-morpholino]-ethanesulphonic acid (MES) or 2-[N-cyclohexylamino]-ethanesulphonic acid (CHES). For cations, MES is used in combination with L-histidine (His) or a-hydroxyisobutyric acid (HIBA) to provide a suitable counter-ion.

A different approach to reduce the influence of the BGE is suppressed conductivity detection [148, 149], which has also been adapted from ion chromatography [133]. Here, BGE ions are removed or neutralized at the end of the separation column just before the detector by an ion exchange column (suppressor). In the case of an anion separation in borate buffer, for example, the suppressor consists of a strong cation exchange membrane. This replaces sodium ions in the running buffer by protons, which interact with the borate to form weakly acidic species. As weak acids are generally much less dissociated than their salts, the background conductivity is reduced. It could be shown that the BGE conductivity at the output of the suppressor was reduced 100-fold, leading to LODs of 1-10 ppb for common organic and inorganic ions [149].

Sample preconcentration combined with conductivity detection

Independent of the choice of BGE, the analyte sensitivity can be further improved by integrating sample preconcentration steps into the analysis. Quantification of anions at sub-ppb levels was achieved by Haber *et al.* by including a transient isotachophoresis (t-ITP) step prior to the actual CE separation [46].

5.2.3 Contact-mode detection in conventional systems

Generally, in order to measure the conductivity of a sample, a measurement current, *i*, is applied across a defined volume of the sample, while the voltage, *V*, required to establish the current is monitored. As an alternative, a fixed measurement voltage can be applied while monitoring the current; both schemes are equivalent. Electrical contact between the measurement instrument and the sample is generally achieved by metallic contacts. The conductance *G* (in S), which is the inverse of the resistance *R* (in Ω) can then be calculated by:

$$G = \frac{1}{R} = \frac{i}{V} \qquad (33)$$

---

[21] The morpholine ion has a μ_{ep} of $4.13 \cdot 10^{-4}$ cm^2/V-s, which is close to the μ_{ep} of lithium ($4.01 \cdot 10^{-4}$ cm^2/V-s) for example. Values taken from the software package PeakMaster 4.0 (by Boruslav Gaš, www.natur.cuni.cz/~gas/)

The material property of specific conductivity σ (in S/cm) can then be found by taking the sample volume dimensions into consideration:

$$\sigma = G\frac{L}{A} \tag{34}$$

where A: sample cross-section (perpendicular to the direction of i)
L: sample length (parallel to i)

Although direct-current (DC) techniques are widely used for conductivity measurements of solid material samples [82, 150, 151], they do not work equally well with liquids, i.e. electrolyte solutions. As the electrical current in electrolytes is not carried by electrons and holes as in solid-state conductors, but by ions, conversion from electronic to ionic conduction and back has to be performed. This conversion happens at the electrode surface in the form of electrochemical reduction or oxidation. This process in turn causes several phenomena [152]:

- **Electrode polarization**: The metal electrodes used to convert the ionic current in the solution to electronic current are polarized by a layer of solution ions that forms on the surface to compensate for charge transferred at this interface. This gives rise to a potential which interferes with the actual measurement.

- **Electrolysis**: As the measurement current is converted from an electronic to an ionic current, electrons are exchanged between the metal and the solution ions, which carry the charge through the liquid. As one possible charge carrier in aqueous solutions, water molecules react on the electrodes to form gaseous oxygen and hydrogen. The gas bubbles which result can severely perturb both the conductivity measurement as well as the electrophoretic separation as a whole by interrupting the applied electric currents.

- **Material deposition on the electrodes**: In parallel with the electrolysis reaction, sample, buffer or contaminant ions can oxidize or reduce at the electrode and form a more or less insoluble coating on the surface. Although these coatings can sometimes be removed electrochemically [153], they are better prevented if possible.

These effects are reduced but not completely prevented by reducing electrode currents to minute amounts as is done for the potential gradient detection described in Chapter 8. Another elegant way of circumventing these problems is the replacement of the DC source of *i* by an alternating current (AC) source, generally operating at frequencies in the range from 1 to 10 kHz. As the average charge transfer of such a source is zero, the above-mentioned effects are cancelled out assuming that a) all the processes occurring are reversible and b) the AC frequency is high enough to prevent accumulation of species at electrode surfaces (e.g. gas molecules which leads to formation of gas bubbles).

Apart from the external instrumentation, a galvanic contact has to be established between the AC source and the electrolyte to be interrogated. Due to the small dimensions in CE compared to ion chromatography, the construction of a conductivity detection cell is a major challenge. An on-column detector cell integrated into a fused-silica capillary was presented by Huang *et al.* [136]. A computer-controlled CO_2 laser was used to drill two opposing 40-µm-inner-diameter holes into fused silica capillaries of 50- and 75-µm diameter. Then, two electrodes were formed by placing 25-µm platinum wire into the holes, which were subsequently sealed. Apart from the fact that the detector fabrication was quite laborious, this type of on-column detection also suffers from interference from the high separation voltage in the capillary.

As an alternative, an end-column configuration was proposed by the same group, whereby detector electrodes are placed at the grounded outlet of the separation capillary [134, 137]. While this concept solves problems associated with the separation voltage, peak broadening as the analyte zones leave the capillary reduces the separation resolution.

Together with the AC-type current or voltage source, AC conductivity detectors also have special circuitry to demodulate the acquired signal into a DC form that directly represents the solution conductivity. As a detailed description of this type of contact-mode detector is surely worth a book on its own, it is not discussed further here. However, a number of papers [134-136, 154] and book chapters [41, 142, 152, 155] cover the subject well.

5.2.4 Contactless detection in conventional systems

As mentioned in the previous section, a galvanic contact between the measurement instrument and the electrolyte causes a number of problems. Some can be reduced and controlled by adopting an AC measurement scheme, while others remain. Amongst those still persisting is for instance electrode degradation due to the constant contact between the metal and the electrolyte. Also important is the interference of the high potential in the separation column with the conductivity measurement during CE separation, which requires special protection electronics [154].

These remaining issues can be solved by the use of external electrodes that are coupled capacitively to the electrolyte (contactless or oscillometric mode, briefly CCD for contactless conductivity detection) instead of relying on a galvanic contact. The electrodes are thus spatially separated and electrically insulated from the electrolyte in the detector volume by an insulating dielectric, e.g. the glass wall of the separation capillary. At frequencies high enough to overcome the impedance of the capacitors formed by each of the measurement electrodes with the electrolyte, an AC current can flow through the arrangement.

CCD was invented as early as 1980 as a detector technique for ITP in large-bore capillaries applied to ion analysis [156-158]. However, it took until 1998 for the technique to be adapted to capillary-based CE [159, 160]. This was accomplished by placing two ring electrodes side-by-side around the outer polyimide coating of the fused-silica capillary, and measuring the conductivity of the solution in the section of capillary between them. The electrodes essentially form cylindrical capacitors with the electrolyte, so that the fused-silica wall is the dielectric. They are characterized by an impedance, X_c, also known as capacitive reactance in this case. X_c is inversely dependent on the capacitance, C, given by [161]:

$$X_c = \frac{1}{\omega \cdot C} \tag{35}$$

where C: capacitance

ω: angular frequency ($2\pi \cdot$ frequency in Hz)

By applying a sinusoidal radio-frequency (30 kHz to 500 kHz) voltage to one electrode, an alternating current can be capacitively coupled into the electrolyte and picked up at the second measurement electrode. The higher the frequency, the less reactance or impedance a capacitor offers to the flow of charge.

To achieve contactless conductivity detection, it is essential to bring the electrodes as close as possible to the electrolyte channel to assure good capacitive coupling. As shown in Equation (36), C is dependent on the distance, d, between the two conductive plates of a parallel plate capacitor, where d is equivalent to the thickness of the insulator layer [161] (see Figure 5-1):

$$C = \frac{\varepsilon_0 \cdot \varepsilon_r \cdot A}{d} \tag{36}$$

where ε_0: permittivity of free space ($8.854 \cdot 10^{-12}$ Fm^{-1}),

ε_r: dielectric constant of the medium between the two plates,

A: plate surface area.

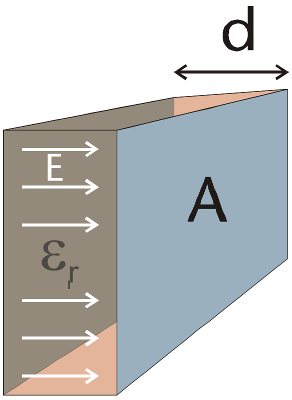

***Figure 5-1**: A parallel plate capacitor with two electrodes of area A and spaced at distance d. The space between the two plates is filled with an insulator having a dielectric constant of ε_r. E indicates the electric field between the plates.*

Substituting this expression for C into Equation (35) yields:

$$X_c = \frac{d}{\omega \cdot \varepsilon_0 \cdot \varepsilon_r \cdot A} \tag{37}$$

This equation clearly shows that X_c is directly dependent on insulator thickness, and that higher signal frequencies must be used for thicker insulating layers, ultimately limiting the application of the technique from a technical point of view. Generally, thinner insulating layers make for more efficient capacitive coupling of signal into the electrolyte. This condition can be very well met by microfabrication techniques as presented in Section 5.3.

For capillary-based CC detectors utilizing syringe needles or metal rings as electrodes, a cylindrical capacitor model can be employed, which is more accurate than the parallel plate approximation given in Equation (35). In this case, C is given by the capacitance of two concentric cylinder electrodes [162] (see Figure 5-2):

$$C = \frac{2\pi\varepsilon_0\varepsilon_r}{\ln(b/a)} L \tag{38}$$

where a: inner radius of the separation capillary,
b: inner radius of the electrode,
L: length of the electrode

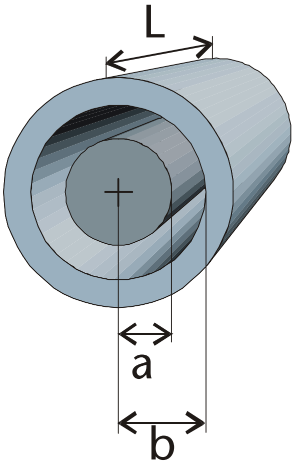

Figure 5-2*: A cylindrical capacitor with two concentric electrodes of radii a and b and a common length of L. The space between the two cylinders is filled again with a dielectric having* ε_r.

5.3 State of the art

The analytical and instrumental advantages of conductivity detection have led to increasing research efforts over the last years. This has resulted in improvements of detection instrumentation, new applications and integration into microfluidic platforms. Though the latter is the focus of this chapter, we will begin by briefly reviewing recent developments in the field of capillary-based systems.

5.3.1 CCD in capillary-based CE

After the original reports by Zemann [159] and da Silva [160], CCD became increasingly interesting for ion analysis applications in capillary-based CE. As these reports are also of great interest to the development of a microchip-based version of this technique, they are briefly reviewed here.

Mayrhofer *et al.* [163] studied CE-CCD in narrow bore capillaries (inner diameter between 5 and 100 µm) using the setup described in [159]. Da Silva *et al.* applied their detector for the analysis of aliphatic alcohols by micellar electrochromatography [164]. In 2002, the same group proposed a number of hardware improvements and a strategy for finding optimum operational parameters for CCD [165]. Other instrumental improvements were proposed by Tanyanyiwa *et al.* [166] (higher excitation voltages of up to 200 $V_{p\text{-}p}$) and Baltussen [167] (lock-in amplifier based detection for improved signal-to-noise ratio). Furthermore, two approaches for simultaneous separation of anions and cations using CCD were proposed, involving dual-opposite end injection by Kuban *et al.* [168], and a movable detector by Unterholzner *et al.* [169].

5.3.2 Contact-mode conductivity detection in microfabricated devices

As alluded to in Sections 5.2.3 and 5.2.4, microfabrication for this type of application is quite attractive, since electrodes can be relatively easily integrated into microfluidic channels for conductivity detection of electrophoretic separations. Recently, contact-mode conductivity detection has been used for several microchip-based analysis methods, such as isotachophoretic (ITP) separations [170, 171], combined ITP and CE separations of inorganic ions [100], CE and micellar electrokinetic chromatography of various biomolecules [172], CE separations in powder-blasted channels [173] and monitoring of mixing in microchannels [174]. Glass microchannels containing integrated gold electrodes have also been reported for electric impedance spectroscopy in femtoliter volumes [175].

5.3.3 In-channel electrodes with insulating coating

As the reduction of the coupling capacitance is the major goal when optimizing a CCD design, it is desirable to separate electrodes and electrolyte by very thin dielectric layers. These can be easily deposited in a variety of materials using standard microelectronics fabrication technology. Laugere *et al.* proposed a chip-based system with thin-layer platinum electrodes directly placed into the channel in the direction of flow [176]. Electrical insulation was achieved by covering the 106 × 25 μm^2 electrodes with a 30-nm-thick layer of silicon carbide. This detector exhibited good performance, with capacitive coupling of 7 to 10 pF and a range of operating frequencies extending below 10 kHz. However, the fabrication process is fairly complex compared with microfluidic systems containing simple channels only. The high-temperature processes for dielectric layer deposition also exclude the use of polymers as substrate material. Another disadvantage is the low electrical breakdown strength of the thin insulation layers, which requires specially developed high-voltage power supplies or detector electronics to assure proper device operation during the CE run [177].

5.3.4 Electrodes outside the separation channel

A technologically much simpler approach is the fabrication of measurement electrodes outside the separation channel. This can be in-plane with the channels as proposed in this work [178-180] or – even further separated – on one of the outer surfaces of the chip.

The latter design was recently proposed by Pumera *et al.* [181]. They mounted two 800-µm-wide aluminum electrodes, made from 10-µm-thick foil, directly onto the top of a CE chip fabricated in poly(methyl methacrylate) (PMMA). The electrodes were positioned perpendicular to the channel and separated by 700 µm, over which distance the conductivity of the electrolyte was monitored. The top polymer layer of the chip was 125 µm thick, which allowed for good capacitive coupling between electrodes and electrolyte. Detection limits were in the range of 5 µM for common anions and cations, for an excitation frequency of 200 kHz.

5.4 Device concept

The device design presented in this thesis uses a new approach to integrate multiple, spatially well-defined electrodes into microfluidic systems. In contrast to the work described in the previous section, the electrodes are placed in-plane with and adjacent to the microchannels, as depicted in Figure 5-3. The microchip CE system consists of a lower glass wafer with interconnecting channels and adjacent recesses in which the platinum electrodes are formed. A cover wafer with drilled access holes seals the system. Placement of electrodes very close to the detection volume becomes possible using the chosen fabrication method, which is described in detail in Section 5.6. For contactless operation, the electrodes are electrically separated by a thin, 10- to 15-µm-wide glass wall from the electrolyte in the channel. The proximity of the emitting and receiving electrode to the separation channel should allow good spatial resolution and high sensitivity of the detector.

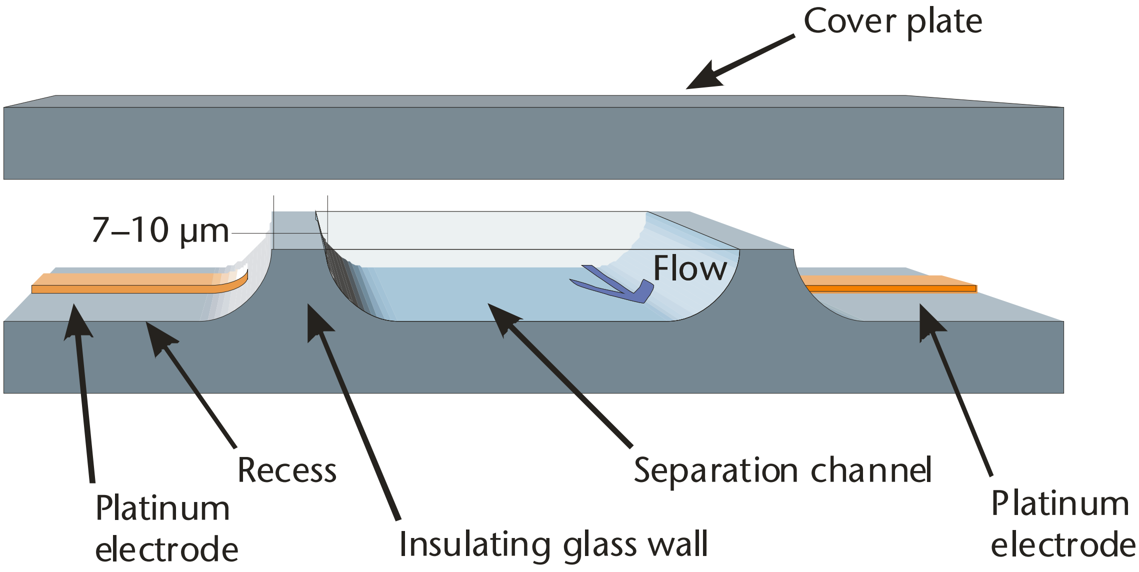

***Figure 5-3**: Sketch of the contactless conductivity detector in a cross-section perpendicular to the flow direction in the separation channel. The two platinum electrodes are separated from the electrolyte (and the high potential) in the channel by two glass walls. As these electrodes are deposited in recesses etched into the lower substrate, they do not interfere with the fusion-bonding procedure used to seal the channels with the cover-plate.*

Integrated electrodes for microfluidic devices are most easily fabricated by depositing and patterning a metal layer (< 1 µm) on a wafer surface. The resulting structures protrude slightly from the surface, so that the wafer is no longer completely flat. Microfluidic channels made in an elastomeric substrate like poly(dimethylsiloxane) (PDMS) can be easily sealed to such patterned surfaces, since this material conforms well to surfaces containing a topography. This approach has therefore been employed by a number of researchers to create hybrid PDMS/glass devices with integrated electrodes for contact-mode conductivity and amperometric detection [171, 182-184]. However, we have chosen to work with wholly glass devices in Pyrex 7740, because of the good chemical stability and insulating properties of this material. Critical to the success of glass-to-glass bonding is absolute planarity of the contacting surfaces. Electrodes protruding from one surface would thus interfere with bonding, and undesirable voids between wafers leading to imperfect sealing of microchannels would result. To circumvent this problem, it was decided to deposit all metal structures into recesses formed in the substrate to maintain wafer planarity. To simplify the fabrication process, the recesses are fabricated together with the microfluidic channel structures (described in Section 5.6 in detail).

This device concept has a number of advantages compared to approaches reported by other groups [173, 176, 181]. The method allows full integration of electrode designs ranging from simple metal lines to complex structures including electrical shielding systems, as the available area for electrode placement is larger than in the in-channel design [173, 176]. Especially for the fabrication of low-cost, disposable analysis devices, it is important that the fabrication procedure presented here is not only compatible with typical glass processes (see Chapter 3). Because only low-temperature and gentle structuring processes are used for the electrode fabrication, the device design is also amenable to a wide range of polymer techniques [29].

5.5 Design tools

Given the small magnitudes of capacitive coupling feasible in a miniaturized conductivity detector, special care has to be taken when designing the electrode geometry. The most important aspect of detector design is to maximize the coupling capacitance between electrodes and electrolyte with respect to the parasitic stray capacitance between the electrodes.

Analytical models allow sufficiently precise modeling of coupling capacitance and first-order frequency behavior [151, 162]. At the same time, they provide insight into the role that the different parameters play. To achieve a higher degree of accuracy, complex lumped-element models can be derived, including additional components such as capacitances induced by connection cables or the read-out circuitry. As a closed, analytical solution to these models is difficult to achieve, numerical simulation tools for microelectronic circuits are deployed for model analysis [185, 186].

5.5.1 Analytical models

The detector cell is depicted in Figure 5-4, together with the lumped-element equivalent circuit proposed to model it. The electrolyte solution within the detector volume is described by a resistance, R_{el}, and a capacitance, C_{el}, in parallel [160]. The capacitance of the electrolyte double-layer at the wall is represented as C_{dl}, and C_w is the capacitance defined by the glass wall between the measurement electrodes and the solution. For a typical conductivity measurement, an alternating voltage between 30 kHz and 500 kHz is applied between the two electrodes, and the resulting AC current induced through the electrolyte is monitored. At these measurement frequencies, the impedance of the double layer is negligible when compared to that of the bulk solution, and can be ignored [160]. For the detector structure presented here, the double layer capacitance is in the order of 100 to 200 pF, assuming a typical value of 10 $\mu F/cm^2$ [187]. However, part of the current induced will flow directly from one electrode to the other through the surrounding glass substrate, bypassing the actual detector volume. This signal is characterized as a parasitic stray capacitance, C_s, and is due to capacitive cross talk between the electrodes on the chip, and between the connection wires used for the chip holder. C_s can significantly influence the measured impedance at high frequency. Hence, experimental conditions should be carefully chosen.

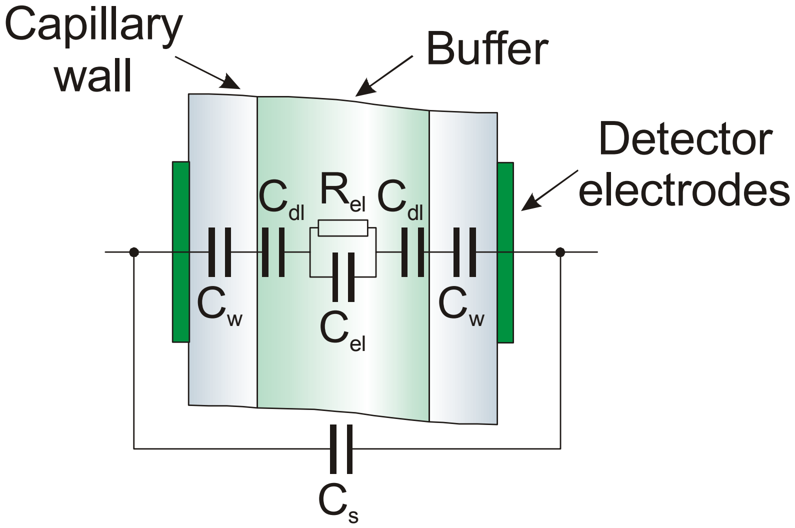

Figure 5-4*: Schematic of detector cell, showing the orientation of the electrodes with respect to the electrolyte-filled channel. A lumped-element equivalent circuit of the contactless conductivity detector is also presented.* R_{el} *and* C_{el}*: parallel resistance and capacitance of the electrolyte solution within the detector volume;* C_{dl}*: capacitance of the electrolyte double-layer at the wall;* C_w*: capacitance between the measurement electrodes and the solution via the glass wall;* C_s*: parasitic stray capacitance.*

For the electrode design reported here, the coupling efficiency between one electrode and the channel can be approximated by the following formula for two parallel strip conductors above a ground plane [162] (see Figure 5-5):

$$C = \frac{\pi \varepsilon_0 \varepsilon_r w}{\ln\left(\frac{\pi d}{L+t}+1\right)} \tag{39}$$

with: ε_0: electric permittivity of vacuum ($8.85 \cdot 10^{-12}$ $\mathrm{Fm^{-1}}$)

ε_r: relative electric permittivity of Pyrex 7740 glass (4.6 (see www.corning.com))

w: electrode width

d: glass wall thickness

L: electrode width perpendicular to the channel

t: vertical distance to the ground plane

Assuming w = 400 µm, d = 10 µm, L = 500 µm, and a wafer thickness of 500 µm for t, the resulting capacitance is 1.65 pF. As the detector has two electrode-solution capacitors, the total impedance (neglecting the solution resistance) is the series combination of the two, resulting in 825 fF. If an AC voltage of 10 V peak-to-peak at 100 kHz is applied to a capacitance of this value, the resulting current is of the order of 5.2 µA peak-to-peak.

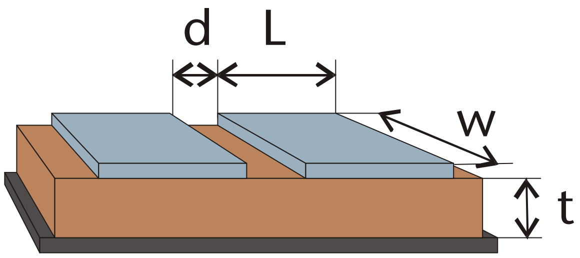

***Figure 5-5**: A capacitor model for two strips and a plane. The electrode strips have the dimensions w·L and distance d. The dielectric thickness above the ground plane is t.*

5.5.2 Lumped-element models solved by circuit simulators

Once the capacitance of the detector is calculated using the model presented above, the frequency behavior of the whole detector cell can be simulated using a numerical circuit simulator. The product used here is Electronics Workbench (Electronics Workbench Ltd., Toronto, Canada), which is based on the SPICE kernel.

Apart from the wall capacitance, the electrolyte resistance and the combined value of the various sources for stray capacitance have to be estimated (Figure 5-6). For the parameter sweep simulations presented here, electrolyte resistances ranging from 100 to 1350 kΩ are assumed[22]. For this type of simulation, the current flowing through the parallel arrangement of $(R_{el}+C_w)||C_s$ is plotted versus the excitation frequency. To capture the effect of R_{el}, the simulation is repeated for 100, 350, 600, 850, 1100 and 1350 kΩ. The value of the stray capacitance is also varied to illustrate its influence.

---

[22] The value of 700 kΩ corresponds to the resistance of an electrolyte with a conductivity of 150 µS/cm across a 50-µm-wide channel with 12-µm depth over a length of 400 µm.

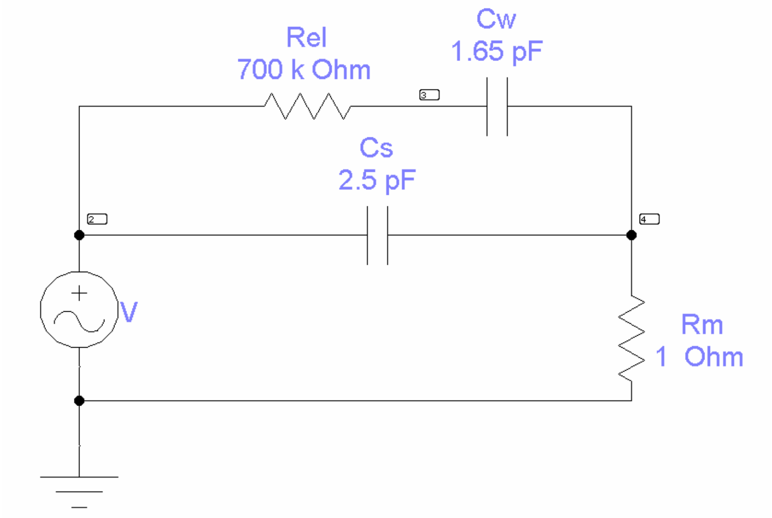

Figure 5-6: *The equivalent circuit of the detector cell used for the simulations. R_{el} represents the electrolyte resistance, C_w the wall capacitance and C_s the stray capacitance. C_s is varied to illustrate its influence. The only purpose of resistor R_m is to deliver a voltage proportional to the current flowing through the parallel arrangement. V is an AC voltage source which is swept over a frequency range from 1 kHz to 5 MHz.*

Figure 5-7 shows the result for the case where the stray capacitance is completely neglected. All results are presented as Bode-plots, with logarithmic axis scales for current and frequency [188]. At low frequencies, the impedance is completely dominated by C_w. The phase shift of the circuit is close to 90°, indicating a purely capacitive behavior. The current increases by one order of magnitude per frequency decade, also related to C_w. At high frequencies, the impedance of C_w is reduced such that the resistance of R_{el} becomes visible until the current saturates and is only dependent on R_{el}.

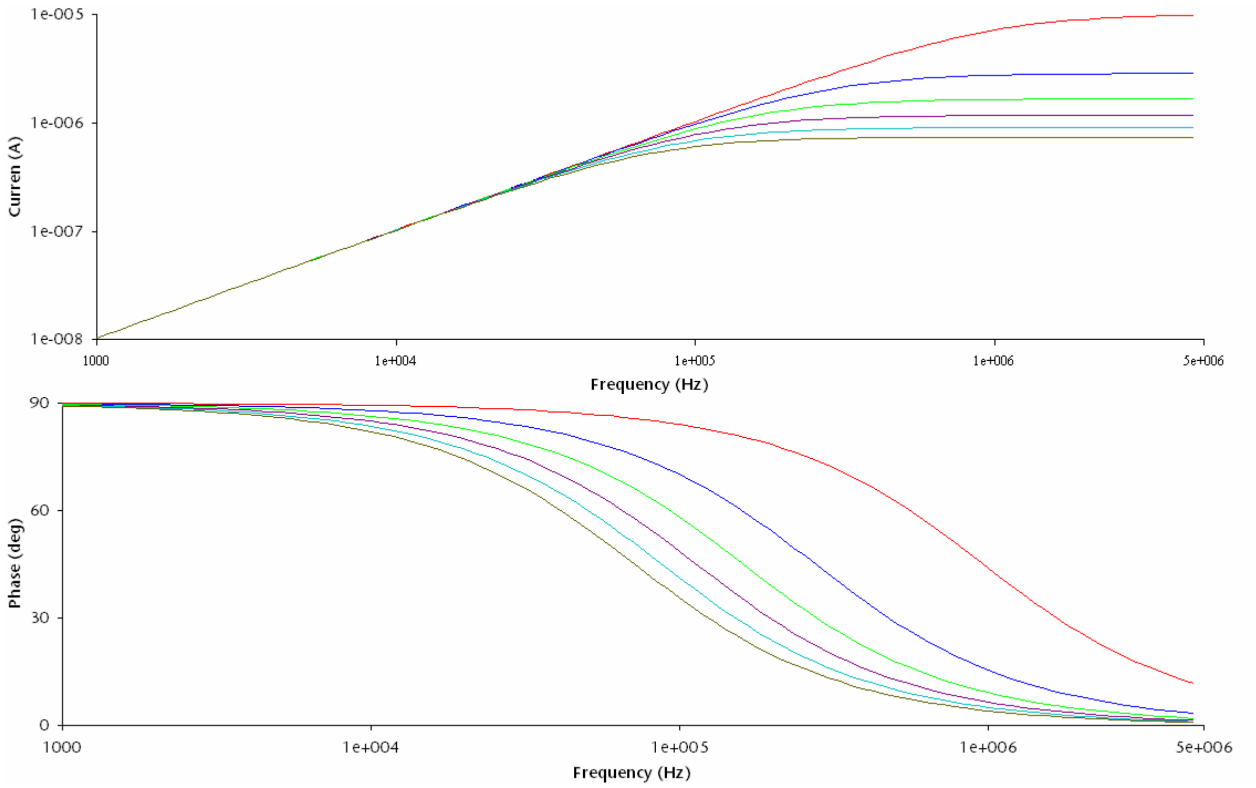

Figure 5-7*: Simulation results for current and phase in the case of* $C_s=0$ *(stray capacitance neglected). At high frequencies, the impedance of* C_w *vanishes and the current reaches a limit as a function of* R_{el}*. Lowest trace corresponds to* $R_{el}=1350\ k\Omega$*, the highest to* $100\ k\Omega$*. The phase indicates the influence of the wall capacitance on the measurement. The closer the phase approaches zero, the less influence has* C_w *on the measurement.*

In Figure 5-8, the stray capacitance is taken into account. Figure 5-8a shows a case of a low stray capacitance of 350 fF (good shielding), while a C_s of 2.5 pF reduces the sensitivity of the detector visibly in Figure 5-8b. The sensitivity of the detector is defined as the derivative of the current i with respect to the electrolyte resistance R_{el} ($\Delta i/\Delta R_{el}$).

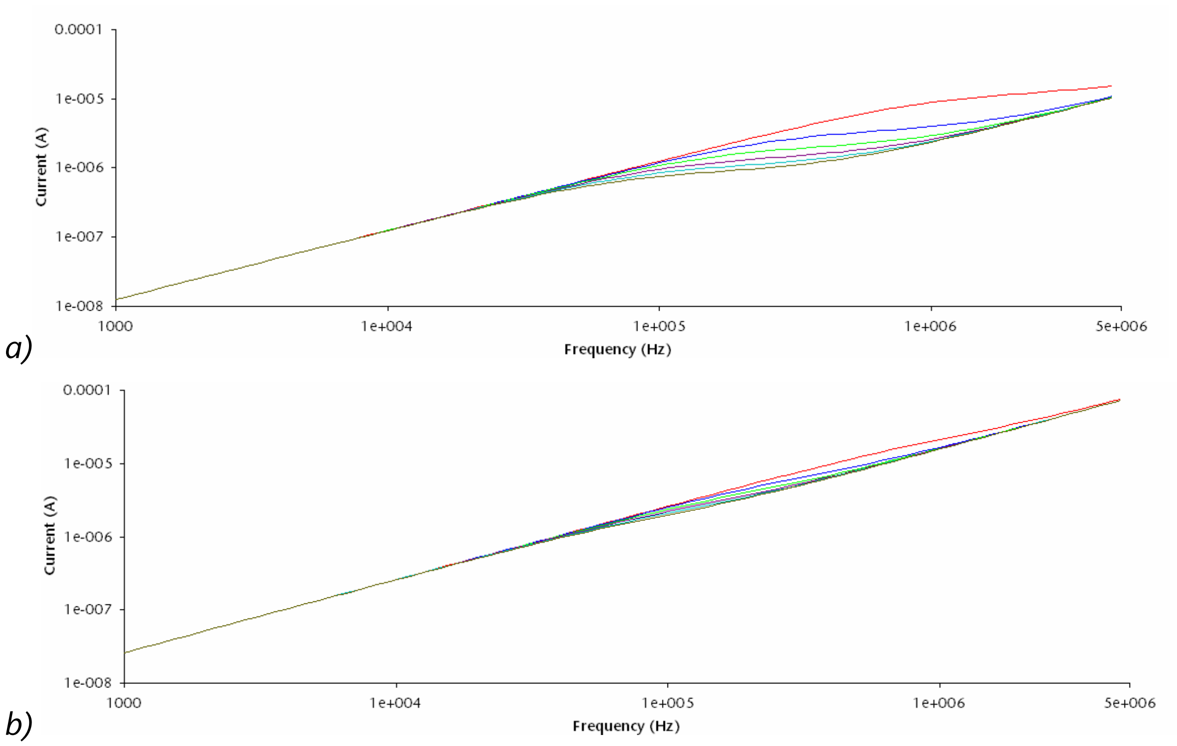

***Figure 5-8**: The two simulations presented here take the stray capacitance C_s into account: a) A low value is assumed for Cs=350 fF. At very high frequencies (>4 MHz) the traces start to reunite as the stray capacitance takes over and short-cuts the AC current.*

b) For C_s=2.5 pF, the influence of the stray capacitance sets in at lower frequencies, thereby reducing the sensitivity ($\Delta i/\Delta R_{el}$) of the detector.

The simulations presented so far are very helpful for gaining a better understanding of the detector cell. However, the approach can be taken one step further by including part of the detector electronics into the simulation as well. This is especially interesting as the first building block of the circuit, the current-to-voltage converter (described in detail in Section 7.2.3), needs to be adapted to the frequency range used. This so-called frequency compensation is achieved by placing a small capacitance, C_c, in parallel to a feedback resistor, R_{fb} (Figure 5-9). Although the operation principle of this circuit might not be completely clear to the reader at this point, the effect of C_c can be easily seen in Figure 5-10. While the circuit becomes unstable if the frequency compensation is not included, the problem is under control if C_c=1.5 pF is placed into the circuit.

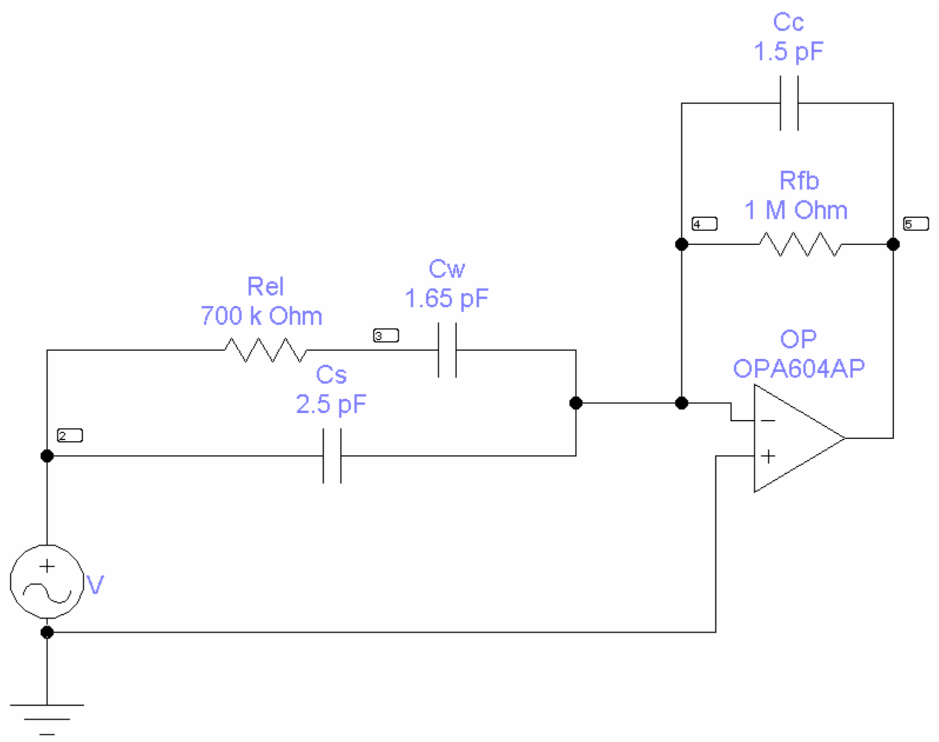

***Figure 5-9**: A 1.5-pF capacitor (C_c) allows phase compensation to improve the frequency response of the I/U-converter and avoid stability problems.*

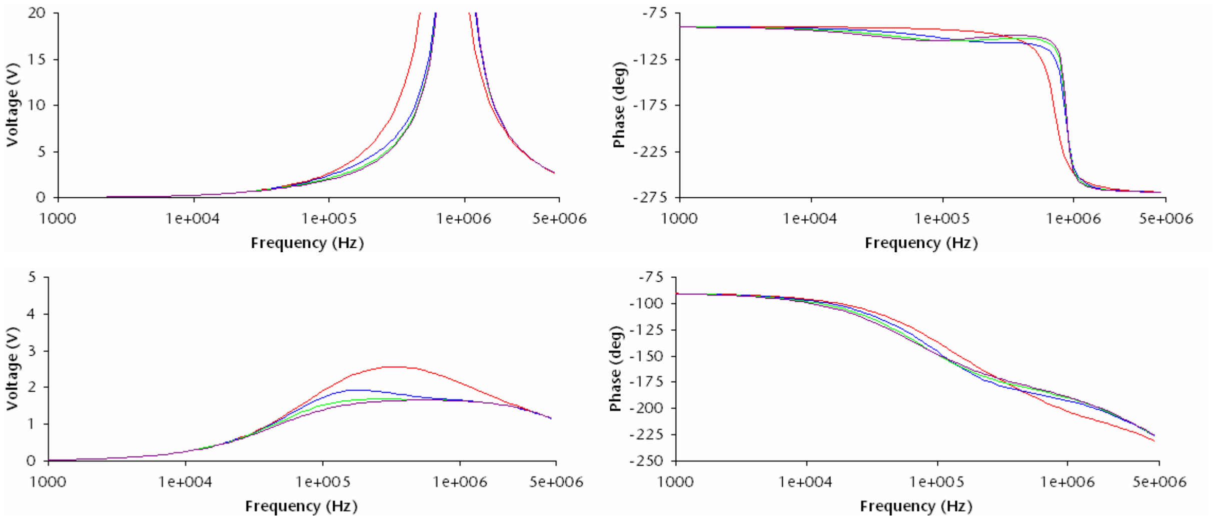

***Figure 5-10**: Simulated frequency response without (upper) and with (lower) phase compensation of the i/V converter. Without compensation, instability occurs for frequencies above 500 kHz. Of course, the output voltage will not be infinitely high as indicated by the upper left graph. This is a flaw in the simulation program.*

5.6 Chip fabrication

The microchip CE system consists of two substrates, one containing interconnecting channels and electrodes, while the other seals the channels and has drilled access holes. The fabrication of the channel-containing substrates involves two major tasks, namely etching of channels and recesses as well as structuring of the platinum electrodes. For a better overview, both processes are presented in separate sections.

5.6.1 Fabrication of channels

The fabrication of the microchannel network by hydrofluoric acid (HF) etching is similar to the standard technique described in Section 3.2, so that only a brief summary is reproduced here.

To start, channels are machined into a 10-cm Pyrex 7740 wafer (Sensorprep Services, Elburn, IL), using a 200-nm-thick layer of polysilicon as etch mask for HF etching (Figure 5-11). After deposition of the polysilicon by low-pressure chemical vapor deposition (LPCVD), wafers are dehydrated at 200°C for 30 min and exposed to hexamethyldisilazane (HMDS) vapor for 15 min to improve photoresist adhesion. A 1.8-µm-thin layer of positive AZ1518 (Clariant AG, Muttenz, Switzerland) photoresist is then spin-coated onto the wafer at 4000 rpm for 40 s and prebaked on a hotplate for 1 min at 100 °C. Laser-plotted films with a dot size of 7 µm (DIP S.A. Repro, Lausanne, Switzerland), mounted on blank 5" glass plates, serve as rapid prototyping photolithography masks. The exposure dose is increased to 60 mJ/cm^2, a value which is 10 % above the recommended value, to compensate for the reduced transparency of the laser-plotted films. Wafers are then developed for 1 min in AZ351 developer (Clariant), which has been diluted 1:4 with de-ionized, 18-MΩ (DI-18M) water. This is followed by a rinse in DI water and postbake at 125 °C for 30 min. Reactive-ion etching (RIE) is used to transfer the pattern into the polysilicon layer. After photoresist removal with acetone, the channel structures are etched into the glass using 49% hydrofluoric acid (HF). Finally, the polysilicon layer is removed in 40% potassium hydroxide (KOH) solution at 60°C for 5 min.

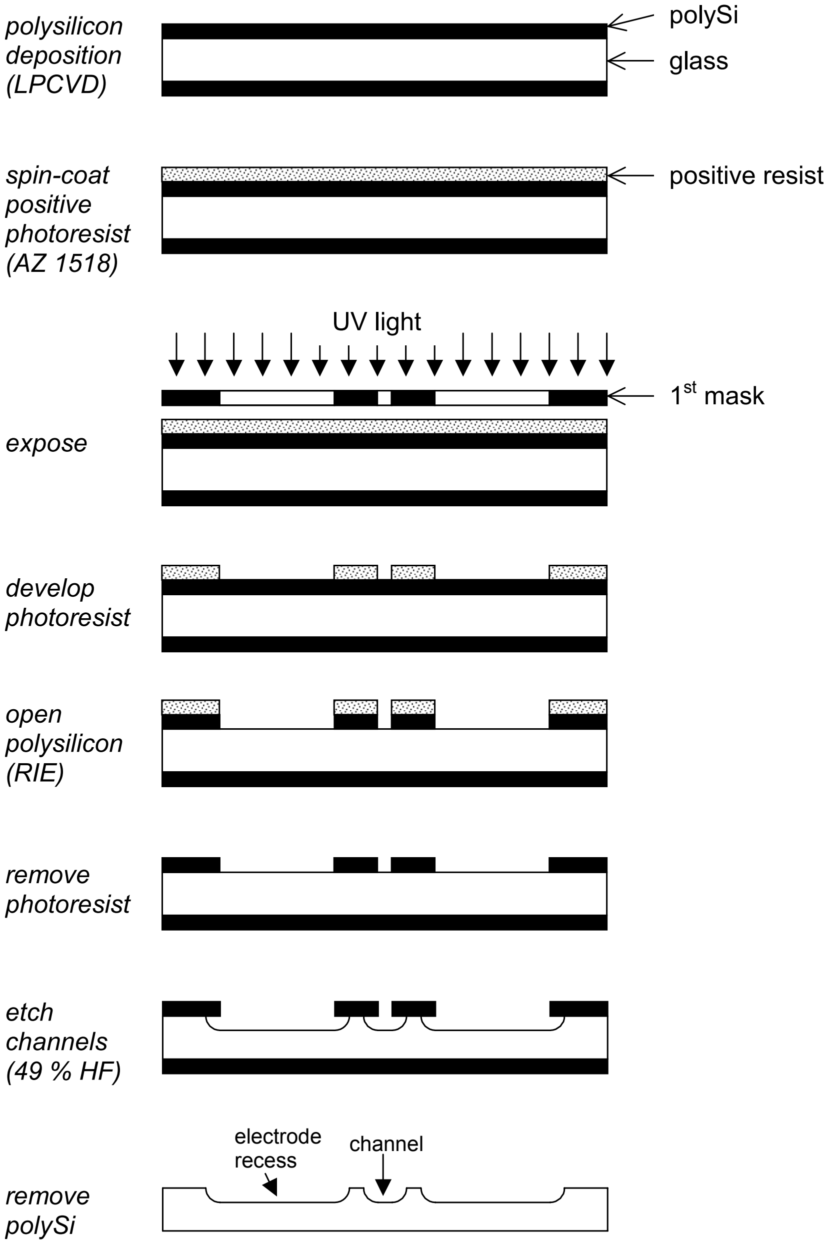

Figure 5-11: *Process flow for channel etching in the lower substrate.*

5.6.2 Fabrication of electrodes

After structuring the substrate by HF etching, the Pt electrodes are formed in the etched recesses using a microfabrication method known as lift-off (Figure 5-12). For lift-off, a layer of photoresist is first deposited and structured on the wafer, followed by metal deposition using either evaporation or sputtering techniques. The photoresist is subsequently removed by organic solvents, which also wash away the metal deposited directly onto the resist. Metal deposited onto the wafer substrate itself will remain, assuming a good adhesive layer was first deposited onto the substrate. In order to achieve well-defined metal lines using lift-off, metal deposition onto the sidewalls of the photoresist structures is best avoided. Therefore, negative resists are often used for this application, as they have the advantage that they can be processed to have negatively inclined sidewalls (i.e. open structures are wider at the bottom than at the top). To achieve this, the photoresist is generally subjected to under-exposure, followed by over-development. Because resulting sidewall surfaces are oriented away from incoming metal species, metal will tend not to deposit there. Though lift-off procedures involve several steps, they remain a good alternative for patterning Pt layers, which do not etch easily.

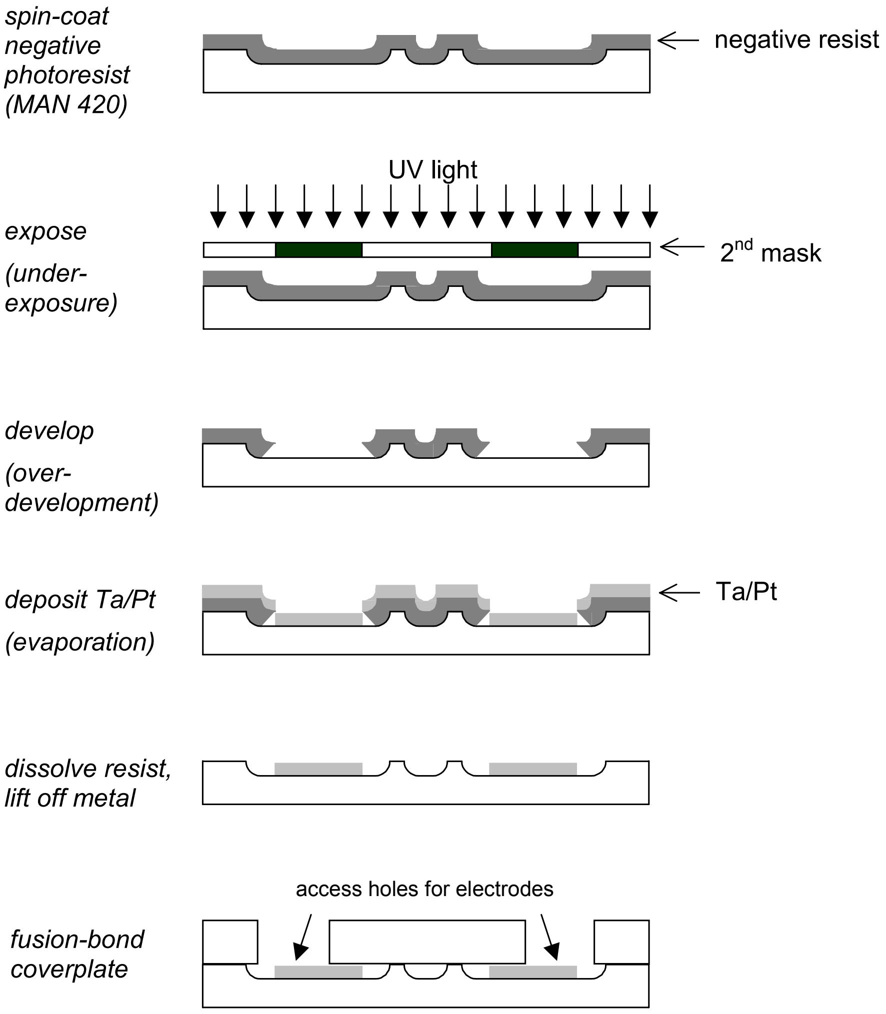

***Figure 5-12**: Platinum electrodes are structured by lift-off. Placement of the electrodes into etched recesses allows fusion-bonding of the lower substrate with a coverplate.*

For the fabrication of the microchip CE devices, a 2.7-µm layer of negative photoresist (MAN 420, Micro Resist Technology GmbH) is used. To achieve good surface and edge coverage on the previously structured wafer, it is spun at a and edge coverage on the previously structured wafer, it is spun at a comparatively low velocity of 2000 rpm for 40 s. The wafer is then immediately transferred onto a hotplate to pre-bake the resist at 100 °C for 2 min, before gravity causes it to flow down the semi-spherical channel walls. Exposure is carried out at a dose of 1050 mJ/cm^2, followed by a 4-min development in MAD-338 developer (Micro Resist Technology GmbH) diluted 1:1 with DI-18M water.

The Pt electrodes were fabricated by first evaporating 20 nm of tantalum as adhesion layer, followed by 150 nm of Pt. The wafer was then immersed in acetone to lift off the metal around the electrodes. If necessary, gentle ultrasonication was used to accelerate the process. The discontinuity of the deposited metal layer around the sidewalls allows metal on the resist to be removed cleanly from the surface without tearing away from the electrodes on the surface. Electrodes with sharp, well-defined edges are thus guaranteed. Figure 5-13 shows two microscope pictures of the detector region after etching of the fluidic features and recesses, and deposition of the metal electrodes.

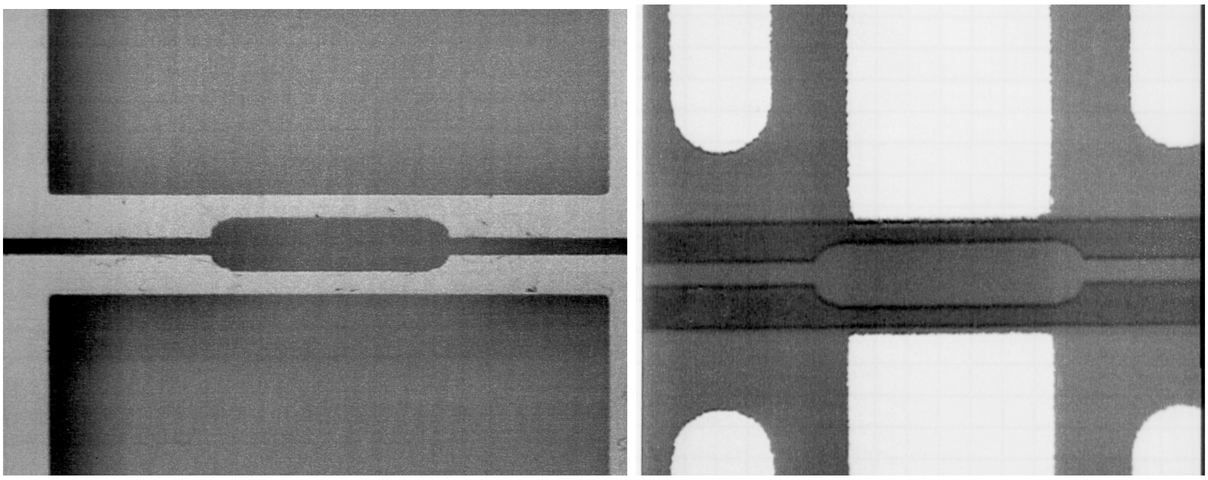

Figure 5-13: *Microscope picture of the detector region after HF etching of channels and recesses (left) and after metal deposition and lift-off (right). The bubble-type detector flow cell is 125 µm wide and 500 µm long; the (wide) measurement electrodes are 400 µm wide. The four additional electrodes serve as electrical shielding lines.*

Excellent lift-off yield could be achieved for recess depths of up to 12 µm, while deeper structures had metal residues at the edges of the etched features (see Figure 5-14). These were caused by inhomogeneous photoresist deposition due to the surface topography, which left parts of the wafer uncovered with resist. Especially the sharp edges around HF-etched features were prone to this, as the resist distribution is difficult around abrupt changes of topography. If deeper channels are required, a different resist for thicker layers (for example AZ 4562 from Clariant AG, Muttenz, Switzerland) or a different deposition method such as spray coating (e.g. the EVG101 system, available from Electronic Vision, Schaerding, Austria) could resolve this problem.

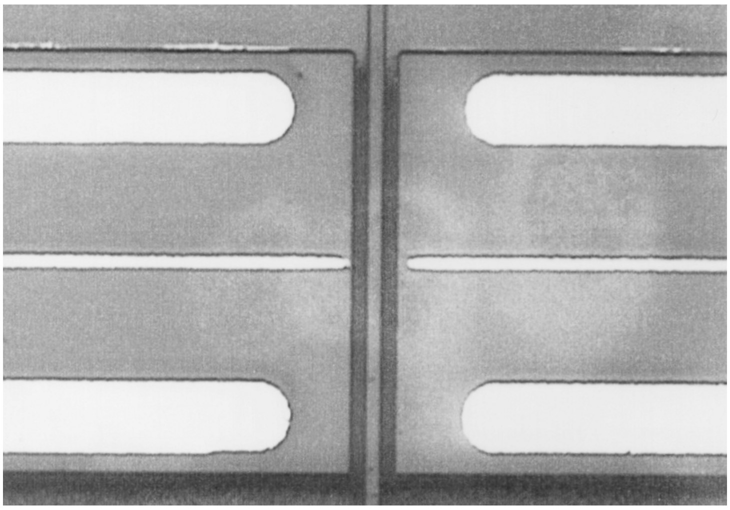

***Figure 5-14**: Metal residue along the edges of HF-etched features appear after lift-off if the surface topography is too deep. This can be seen at the upper edges of the electrode recesses on both sides of the vertical separation channel.*

Finally, the wafer was fusion-bonded to the cover wafer at 650 °C (see Section 3.3). The cover wafer had a grid of ultrasonically drilled holes (Sensorprep Services, Elburn, IL) which serve as inlets to the microfluidic channel system, as well as openings to make electrical contact with the metal electrodes on the chip. Bonding was generally straightforward, as the surfaces of both wafers were flat. However, problems arise if metal structures are displaced and partly deposited on the surface instead of in the recesses, as depicted in Figure 5-15. Small alignment errors, as the one depicted in the figure, often lead to premature dielectric breakdown of the insulation formed by the glass wall. This then causes a fluctuating current flow from the separation channel into the grounded input terminal of the detector instrument. For stronger overlaps, sealing of the fluidic structures was not possible and buffer was drawn into the electrode recesses by capillarity. It should be noted, however, that the alignment precision required is fairly low (~± 5 µm), which can be easily achieved with standard photolithographic equipment.

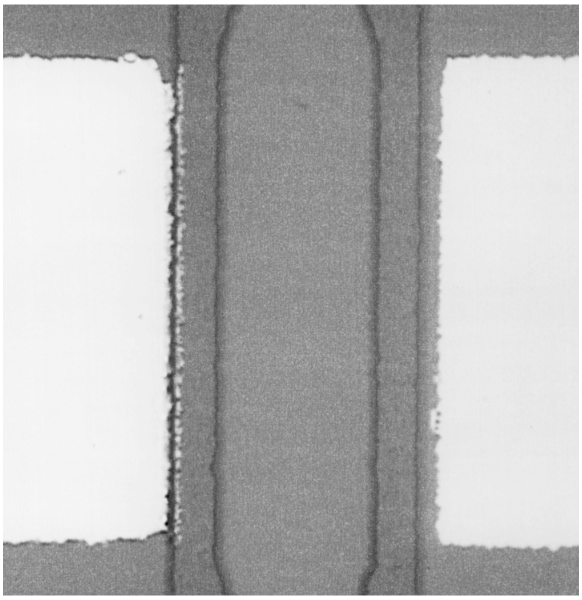

***Figure 5-15**: Imprecise alignment during the photolithography for the electrodes can result in displacement of the metal structures. If they overlap with the glass wall around the fluidic channel, as shown in this figure on the left, problems during the fusion-bonding procedure arise. These lead to imperfect sealing of the chips and premature dielectric breakdown of the insulation formed by the glass wall.*

5.6.3 Device layout and assembly

The layout of the devices employed is shown in Figure 5-16. It includes a double-T injection element with a 150-µm-long intersection for plug formation, and an effective separation length of 34 mm (Figure 5-16, right). The three upstream reservoirs for sample, sample waste and buffer are connected to the double-T structure via 9-mm-long channels. The channels are 12 µm deep, 50 µm wide across the top, and have the typical D-shaped cross-section of isotropically etched structures. The detector consists of two Pt electrodes perpendicular to the channel, positioned directly across from one another. Though close to the electrolyte, they remain separated from it by a glass wall of 10 to 15 µm thickness for contactless operation. To reduce on-chip stray capacitance, the detection electrodes are shielded by two in-plane electrodes positioned alongside. Different detector geometries were fabricated, having electrodes of different widths (40 µm and 400 µm), as well as channels with a bubble-like shape widening up from 50 to 130 µm. The latter geometric variation was included to improve sensitivity by increasing pathlength [159]. However, most results presented in this and in the following chapter were exclusively obtained using the device type with 400-µm-wide electrodes and straight, 50-µm-wide channels, unless stated otherwise. A photograph of the detection system is shown in the inset of Figure 5-16, and Figure 5-17 shows a full photograph of a CCD chip.

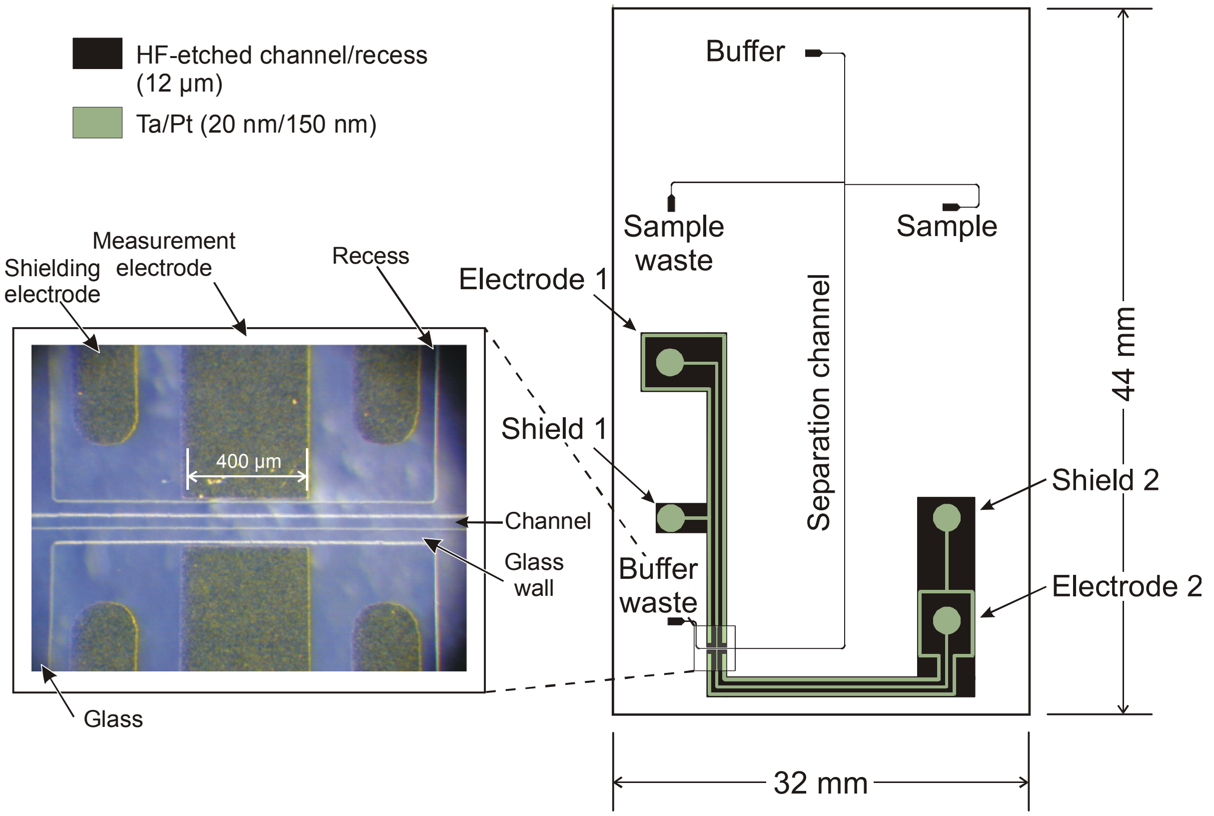

***Figure 5-16**: Layout of the CE chip with contactless detector, which is located at the lower left hand corner of the chip. Electrical connections to the electrodes are made via round contact pads at the end of the metal lines. All metal structures are placed in recesses to prevent topography problems during bonding.*

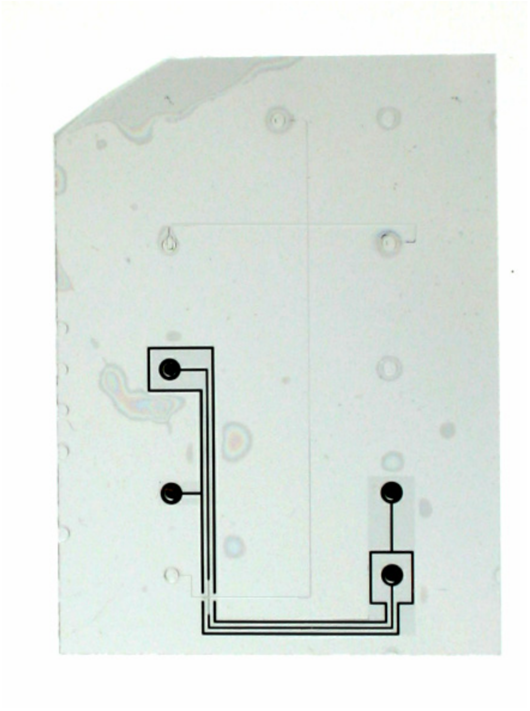

***Figure 5-17**: A photograph of a CCD device with 40-µm-wide detection electrodes. Although sample and separation channels were stained using molybdenum blue solution, they are difficult to spot due to the shallow etch depth (12 µm).*

Once bonded, the wafer was diced into 32 × 44 mm^2 chips, which were mounted in a custom-made, screw-tightened chip holder made from 7-mm-thick PMMA with an aluminum back-plate (see Section 3.4). The entire assembly was then plugged into an electrode holder having short platinum wires to apply high voltage to the reservoirs. Electrical contact to the detector electrodes was made by spring-loaded stainless steel tips (RS Components, Switzerland) in the electrode holder. These pins were inserted through holes in the coverplate to touch the contact pads of the on-chip Pt layer underneath. The electrode holder was designed for small capacitive cross talk between the different contact pins by assuring a maximum distance between wires. Slits cut into the PMMA allowed the insertion of thin aluminum plates for additional electrical shielding.

5.7 Reagents and chip operating procedures

5.7.1 Reagents

The run buffer for all experiments contained 10 mM MES and 7 mM His (short 10 mM MES/His) at pH 6.0. The buffer was 1:1-diluted from a 20 mM stock solution, which was prepared by dissolving 3.9 g of MES (FW: 195.2) and 2.17 g of histidine (FW: 155.2) (obtained from Sigma, Buchs, Switzerland) in DI water (18-MΩ-cm quality).

5.7.2 Cleaning procedures

Chips were rinsed and conditioned prior to each use with the following procedure: DI water for 2 min, 0.1 M NaOH (0.2 µm-filtered, HPCE-grade (Merck, Darmstadt, Germany)) for 5 min, DI water for 2 min, and run buffer for 2 min. Rinsing and conditioning were carried out by filling the three inlet reservoirs with the reagent in question and applying vacuum to the outlet (buffer waste reservoir). The run buffer and water were filtered through 0.2 µm filters as they were introduced to the reservoirs. After filling both sample and sample waste reservoirs with the sample solution, the electrode holder was attached to the chip and run buffer was flushed through the device using a field strength of 200 V/cm until the current stabilized.

At the end of the day, chips were rinsed once more using DI water for 2 min, 0.1 M NaOH for 5 min, DI water for 2 min again, and finally dried using vacuum connected to the buffer waste reservoir.

5.7.3 CE procedure

Separation was generally accomplished using field strengths between 200 and 500 V/cm. Field strengths of 30 V/cm applied in the sample and sample waste side channels during sample injection prevented sample leakage into the separation channel. In terms of absolute voltages, between -1 kV and -3 kV were applied to the buffer waste reservoir during separation, with the sample and sample waste reservoirs being held at 25% of the separation voltage. Sample loading was performed at 385 V/cm, with buffer and buffer waste reservoirs held at ground potential. This was to induce buffer flow from both sides of the separation channel into the sample waste channel to confine and shape the sample plug in the double-T injector [48]. Sample loading was carried out for 20 s before separation to establish stable ion concentrations, independent of their mobilities.

5.8 Brief introduction to the measurement setup

Like the layout of the detector design, the read-out electronics had to be designed carefully, owing to the low intensity signals to be measured. A full, detailed description of the measurement setup is given in Chapter 7. For completeness, a brief overview of the instrumentation involved is given here.

The electronics system consisted of five distinct stages: 1) the signal generator, 2) the input current-to-voltage converter, 3) the synchronous detector, 4) a voltage shifter for baseline compensation and 5) a cascade of low-pass filters (Figure 5-18). To reduce electrical noise pickup, all measurements were carried out in a Faraday cage. The sensitive current-to-voltage converter was also shielded.

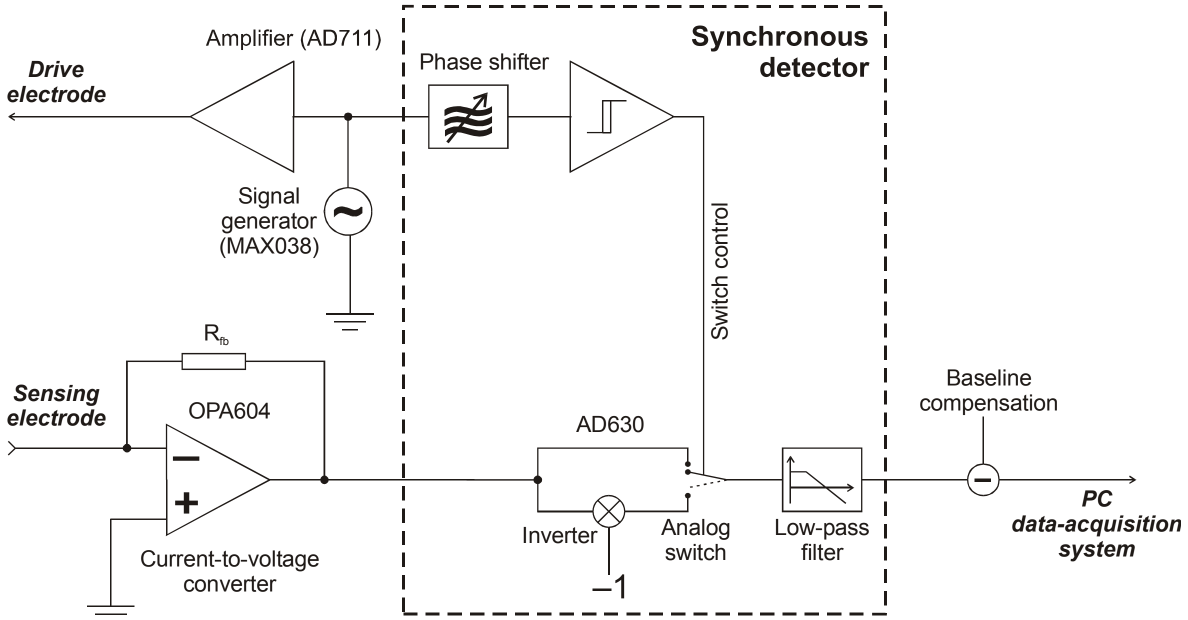

Figure 5-18: Schematic of the read-out circuit consisting of a current-to-voltage converter, synchronous detector, baseline compensation and low-pass filter. Excitation is achieved using a sinus waveform generator followed by a non-inverting amplifier.

A MAX038 integrated frequency generator (Maxim, Sunnyvale, CA, USA) was used to generate the excitation signal for the conductivity detector. The circuit was capable of producing sinus, sawtooth and rectangular signals with frequencies of a few Hertz up to 1 MHz, and could be tuned via a resistor-capacitor network. A non-inverting amplifier based on an AD711 operational amplifier (Analog Devices, Norwood, MA, USA) boosted the signal to a maximum voltage of 15 V peak-to-peak, to provide a sufficient excitation voltage also for small pathlength detector designs. The output of the amplifier was directly connected to the excitation electrode via a shielded coaxial cable.

For the input current-to-voltage converter, an OPA604 single FET-input operational amplifier (Texas Instruments / Burr-Brown, Dallas, TX, USA) was used. This component provided a virtual ground input into the detection system, which was directly connected to a measurement electrode via a coaxial cable. The converter's output voltage, V_{cv}, could be tuned to the measurement current expected for a particular configuration by choosing the appropriate feedback resistance, R_{fb}, as follows:

$$V_{cv} = -i_{in} \cdot R_{fb} \tag{40}$$

with: i_{in}: input current

R_{fb}: feedback resistor

In the configuration depicted in Figure 5-18, a 1-MΩ feedback resistor was used to obtain a conversion factor of 1 V/µA.

The synchronous detector converted the AC output signal of the current-to-voltage converter into a pulsed DC signal by demodulation [189]. To do so, the input signal was multiplied by +1 or –1, depending on the polarity of the reference signal. In this case, the reference signal was derived from the excitation signal via a phase shifter, to allow for compensation of phase shifts in the measurement signal due to the impedance of the detector. The advantage of synchronous detection versus precision rectifier circuits as proposed in [160] is the inherent noise rejection, since the detector excludes frequency components which are not within a narrow range around the reference signal. Analog Devices produces a monolithically integrated synchronous detector (AD630), which performs a complete demodulation step in a single circuit.

As described above, a large part of the current measured by the readout electronics was actually due to parasitic capacitances in the chip and chip holder. Therefore, the measurement signal was dominated by a strong but steady baseline, which was removed using an AD711 subtraction amplifier as proposed in [160]. The baseline compensation allowed further amplification of the signal and assured that optimum use was made of the analog-to-digital conversion capabilities of the data acquisition hardware used.

In a final step, all excitation frequency components of the pulsed DC signal were removed using two higher-order low-pass filters with a final cut-off frequency of 15 Hz. The resulting signal was then acquired by a data acquisition unit (AT-MIO-XE50; National Instruments, Austin, TX, USA) and special software written in-house using National Instruments LabView. The same unit was also used to control a programmable high voltage power supply consisting of two DC-DC converters (PSM 10-103N, Advance Hivolt, Bognor Regis, UK) and a set of high-voltage relays (Günther GmbH, Nürnberg, Germany) as described in Section 2.2.

5.9 Detector characterization

5.9.1 Optimization of operating parameters

As outlined in Section 5.5.2, discrete components of the detector's lumped-element model become dominant at different operating frequencies. As shown in Figure 5-19, three distinct frequency zones can be identified by impedance measurement. At low frequencies, the wall capacitance is dominating and permits current flow through the arrangement. At high frequencies, on the other hand, the stray capacitance takes over and short circuits the current around the actual detector, thereby reducing sensitivity. Finally, in the middle of the frequency range, the electrolyte conductivity becomes dominating, which is indicated by a nearly constant magnitude of *Z*. Additionally, the performance of the detector electronics have to be taken into consideration, as especially the input stage (current-to-voltage converter) has a limited bandwidth.

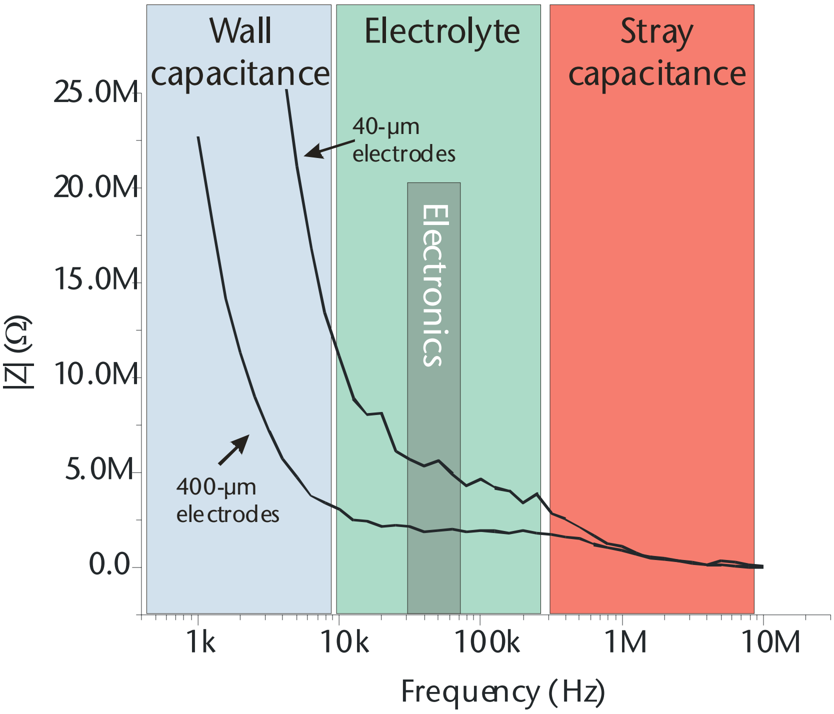

***Figure 5-19**: The impedance spectra of two detectors (one with 40-µm-wide electrodes, the other with 400-µm-wide electrodes) reveal three distinct frequency zones with different dominating elements.*

Successful implementation of the contactless conductivity detector requires finding optimum operating conditions in terms of excitation frequency, waveform and electrode configuration. To do so, plugs of 20 mM MES/His buffer were formed and injected into a 10 mM concentration of the same buffer. Sample plugs were transported through the detector using a field strength of 200 V/cm and other experimental conditions as described above. A sinusoidal excitation signal waveform was used, as the phase shifter in the readout circuit can only handle this type of signal. For the excitation amplitude, the maximum output voltage showed best results in terms of the signal-to-noise ratio and was therefore kept at 15 V peak-to-peak. Experiments were carried out at operating frequencies between 30 kHz and 100 kHz. The heights of the sample peaks were measured on the electropherograms and plotted as a function of frequency.

Figure 5-20 shows results for the frequency optimization procedure for a conductivity detector having 400-µm-wide detector electrodes. At a frequency of 58 kHz, the detector response to the sample plug has a maximum peak height of 300 mV. At lower frequencies, the response falls as the impedance of the channel walls is still fairly high and only a small current passes into the electrolyte. At higher frequencies, two effects influence peak height. Firstly, the impact of the stray capacitance grows, thereby reducing the signal change detected when the sample plug passes. Secondly, the performance of the read-out electronics degenerates with increasing frequency. In the circuit presented here, the latter effect is due mainly to the performance of the current-to-voltage converter.

The effect of the alternating electric field applied across the detector in terms of Joule heating in the detector region is negligible. The power density across a 50-µm channel at 10 $V_{p\text{-}p}$ and 1 µA is only about 140 mW/m. Furthermore, heat is quickly carried away by convection along the channel. Also, for a 100-kHz, square wave form at the same amplitude and a small organic molecule with a μ_{ep} of $-2.5 \cdot 10^{-4}\,\mathrm{cm}^2/\mathrm{Vs}$, the lateral oscillation of the molecule is in the range of 100 nm, assuming instantaneous acceleration.

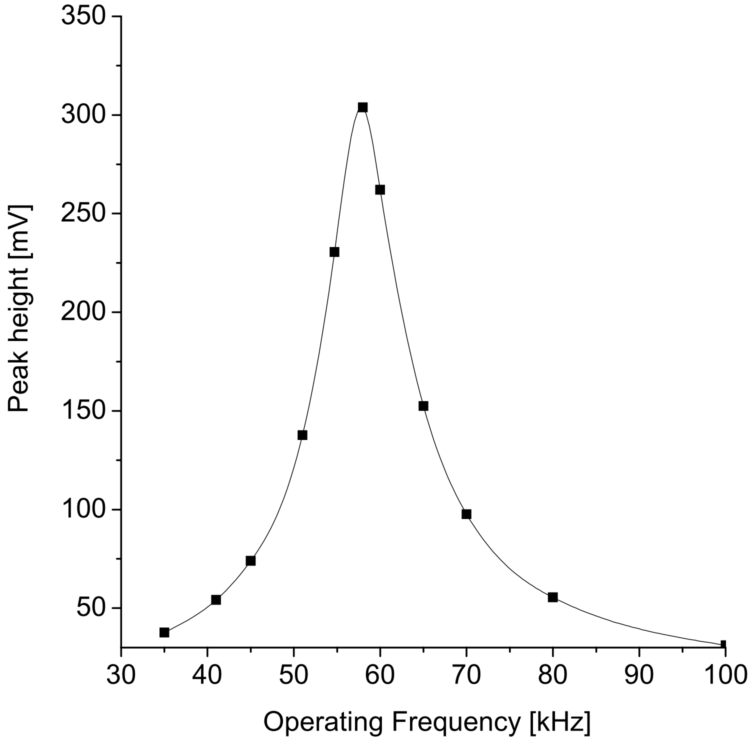

***Figure 5-20**: Determination of the optimum operating frequency. Plugs of 20 mM MES/His were injected at varying excitation frequencies, and the peak height was recorded for each frequency. Curve was drawn for the sake of clarity. In this example for a device with 400-µm-wide electrodes and a 50-µm-wide channel, the optimum operating frequency was found to be 58 kHz. Running buffer: 10 mM MES/His at pH 6.0. Separation conditions: 200 V/cm; effective separation length, 3.4 cm.*

5.9.2 Detector sensitivity

The concentration sensitivity of the detector was studied under the optimum operating parameters determined above (58 kHz, sinusoidal wave, 15 V peak-to-peak). Again, MES/His buffer at various concentrations between 10 and 20 mM served as sample for the experiment, and peak heights were determined from the resulting electropherograms.

As Figure 5-21 shows, a linear regression of the acquired data reveals a sensitivity of 37 mV/mM for different concentrations of MES/His buffer, with a correlation coefficient of 0.99931. This confirms the assumption that the measurement signal is a linear function of the electrical conductivity of the solution.

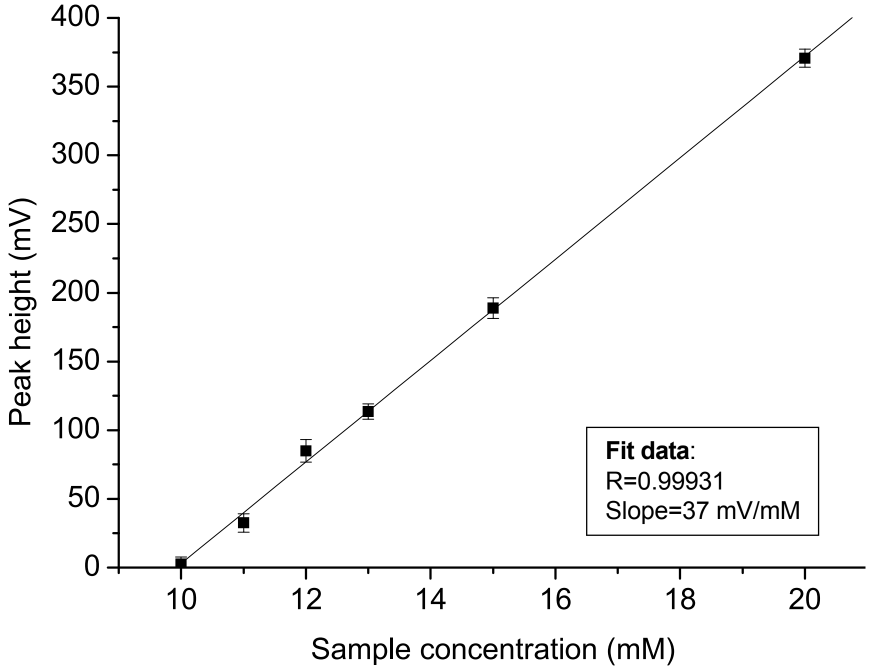

***Figure 5-21**: Detector sensitivity was determined by injecting plugs of running buffer in varying concentrations and measuring the peak height obtained for each sample. The same device as in Figure 5-20 was used. Running buffer: 10 mM MES/His at pH 6.0. Separation conditions: 200 V/cm; effective separation length, 3.4 cm; detection at 58 kHz. Four CE runs were averaged per data point.*

To evaluate the efficiency of the integrated shielding electrodes, the signal-to-noise ratios with and without the shielding electrodes connected were compared using the same procedure as described for the frequency optimization. Although the absolute peak height was reduced due to a slight loss of signal current to the shielding electrodes, the signal-to-noise ratio improved by 30% as the noise was reduced considerably.

5.9.3 Temperature sensitivity

The electrical conductivity of an electrolyte also depends on the temperature. This is due to the temperature-dependence of the viscosity, which is one of the parameters influencing electrophoretic mobility, μ_{ep}. As ions migrate in an electric field at a velocity at which Coulomb forces and viscous drag balance, a decrease in viscosity increases the conductivity of the solution. Over small temperature ranges, it can be assumed that the viscosity, η, decreases exponentially with increasing temperature [131]. Given that a molecule needs a certain energy, E_a, to escape from its surrounding neighbors and to start moving, the probability of a molecule having this energy follows a Boltzmann distribution:

$$\eta \propto \frac{1}{\mathrm{e}^{E_a/kT}} \tag{41}$$

with k: Boltzmann constant ($1.38 \cdot 10^{-23}$ J/K)
T: Temperature (K)

However, other factors, such as the temperature dependence of the fluid density, also influence the viscosity, causing deviations from the relationship above.

The temperature sensitivity of the conductivity detector was determined by filling the separation channel with 32 mM sodium carbonate buffer at a pH of 9.6[23]. The device was placed on an thermostated hotplate at different temperatures and the resulting detector output signal was recorded. To avoid bubble formation due to outgassing at elevated temperatures, the electrolyte was kept flowing by hydrostatic pressure. To do so, the three upstream reservoirs were filled to a higher level than the buffer waste reservoir, which caused a constant flow in the channel. As the solution spent ~45 s in the separation channel before it reached the detector, it can be safely assumed that it was heated to a stable temperature.

It should also be noted that the temperature in the channel was not the same as measured on the hotplate surface due to the thermal gradient across the substrate, which permanently lost heat by convection to the surrounding air. Therefore, absolute measurements are difficult to achieve and require an in-channel calibration, e.g. by using molecular beacons [190]. However, the temperature difference between the heat source and the channel is a linear function of the temperature difference between heat source and the surrounding air temperature. Once the calibration is performed, the obtained measurement data can be corrected assuming identical environmental conditions.

---

[23] The buffer was prepared by dissolving 3.46 g sodium carbonate (Na_2CO_3) and 2.69 g sodium bicarbonate ($NaHCO_3$) in 1 L DI-18M water. The final pH of 9.6 was adjusted using 100 mM HCl.

Figure 5-22 shows the resulting data for the temperature range from 20 to 60 °C. From a linear regression analysis of the data, a temperature sensitivity of 4.4 mV/°C can be calculated for this particular electrolyte.

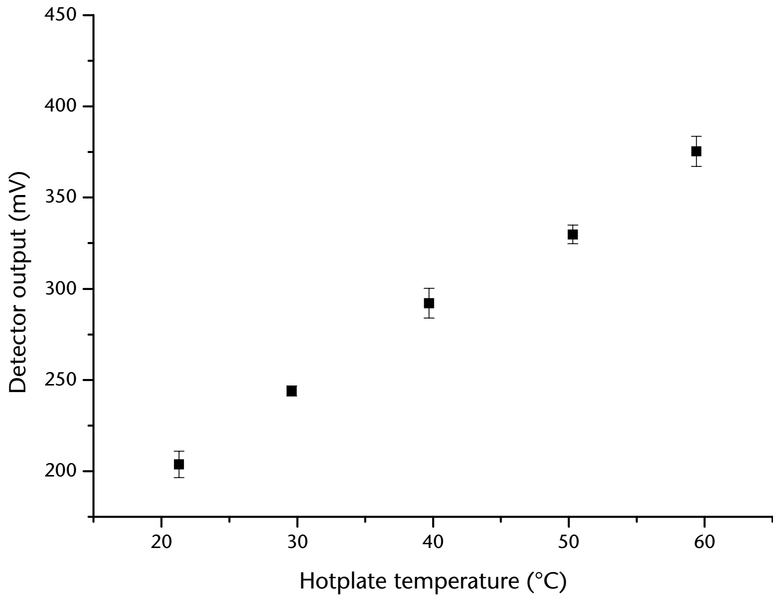

***Figure 5-22**: Temperature dependence of the detector signal for 32 mM sodium carbonate buffer at pH 9.6. The temperature was cycled three times from 20 to 60 °C and data points show the average of these measurements. CCD operation at 58 kHz.*

5.10 Electrode layout

5.10.1 Electrode width

The electrode width directly determines the coupling capacitance, as Equation (39) in this chapter showed earlier. For good detector sensitivity, a large capacitance and therefore wide electrodes are desirable. At the same time, however, the width also affects the size of the detection window, i.e. the volume over which the conductivity is determined. In order to achieve a good separation efficiency, i.e. good resolution of neighboring peaks, small detector windows are desired.

The variance, σ_{det}, caused by the detector can be written as [13]:

$$\sigma_{\mathrm{det}}^2 = \frac{l_{\mathrm{det}}^2}{12} \tag{42}$$

where l_{det}: width of the detector window

The number of theoretical plates, N, is a common figure of merit to describe the efficiency of a separation system, with large numbers being equivalent to better resolutions. The maximum N achievable for a given system with respect to its length is a function of the sum of the variances causing band-broadening:

$$\begin{aligned} N_{\max} &= \frac{L^2}{\sigma^2} \\ &= \frac{L^2}{\sigma_{det}^2 + \sigma_{diff}^2 + \sigma_{inj}^2} \end{aligned} \tag{43}$$

where L: separation length,

σ^2: sum of variances (detector , diffusion, and injection)

For a more detailed analysis, see Ref. [13] and Section 8.1.4.

For the evaluation of the electrode width, two chip designs were compared, one having an electrode width of 40 µm, the other of 400 µm (the latter being the same device as used for the measurements in Figure 5-20). The detector cell was a straight channel 50 µm wide at the top. Again, experiments were carried out at optimum operating parameters, which had to be determined independently for both designs, as the coupling capacitance depends on the electrode width. For the 400-µm-wide electrode, the optimum excitation frequency was 58 kHz, while the smaller electrodes required a higher frequency of 94 kHz (sinusoidal wave, 15 V peak-to-peak). The frequency increase necessary for the smaller electrodes is a consequence of the higher impedance of the coupling capacitance.

For the experiments, plugs of 20 mM MES/His buffer were formed and injected into a 10 mM concentration of the same buffer. They were then electrophoresed at a field strength of 200 V/cm. Figure 5-23 shows the peaks for both structures. From the peak width at half maximum, the number of theoretical plates for this particular separation can be calculated using Equation (54) in Section 8.1.4. Table 7 shows the efficiency data for both detector types.

It becomes evident from Figure 5-23 and Table 7 that the smaller electrode shows better separation efficiency, but lacks sensitivity. In fact, CE separations of samples containing test mixtures of small cations were only possible at comparatively high analyte concentrations (> 800 µM) if the 40-µm electrodes were used. Therefore, a compromise between separation efficiency and device sensitivity has to be made.

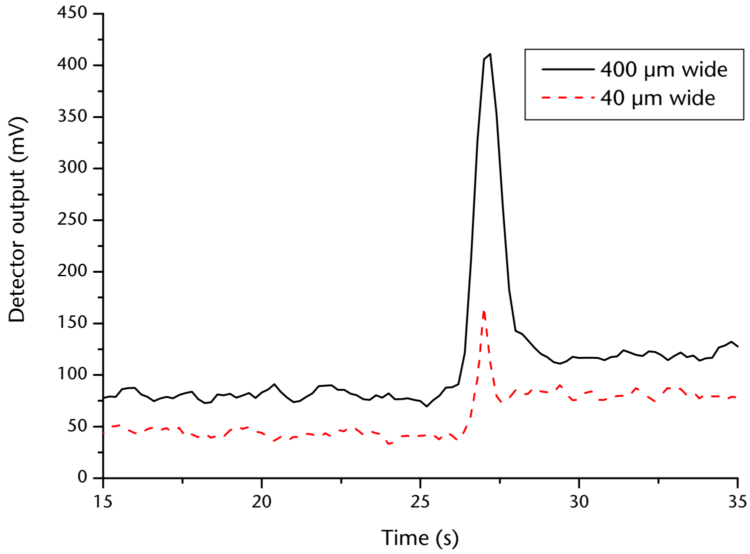

***Figure 5-23**: Comparison of two CCDs with 40- and 400-µm-wide electrodes, respectively. The experiment was carried out at optimum operating frequency (58 kHz for the 400-µm structure and 94 kHz for the 40-µm CCD). Running buffer: 10 mM MES/His at pH 6.0. Separation conditions: 200 V/cm; effective separation length, 3.4 cm.*

Electrode width	***40 µm***	***400 µm***
Migration time (t)	*26.9 s*	*27.2 s*
Peak width at half height ($w_{1/2}$)	*0.6 s*	*0.9 s*
N	*11,100*	*5,100*
Theoretical plates per m	*$330 \cdot 10^3$ m^{-1}*	*$150 \cdot 10^3$ m^{-1}*

***Table 7**: Separation efficiency data for both electrode widths.*

5.10.2 Electrode layout

The electrode layouts presented so far differed in electrode width, but had in common that the radio frequency field was applied across the channel, perpendicular to the buffer flow (Figure 5-24a). In order to improve the sensitivity and to achieve a better spatial confinement of the RF field, a different layout was developed (Figure 5-24b). Here, two pairs of measurement electrodes are used, one pair acting as emitting electrode, the other as receiver. The electrodes forming a pair are electrically interconnected off-chip. Different from the previous layout, the RF field is now mainly applied in parallel with the buffer flow.

This layout has a few advantages compared to the perpendicular scheme. Firstly, the symmetric layout with electrode pairs doubles the coupling capacitance for a given electrode width and thereby improves sensitivity. Secondly, stray fields along the channel, which increase the detector window, are reduced. And finally, the absolute electrolyte resistance to be measured can be adjusted by the distance between the electrode pairs. To improve the signal-to-noise ratio, it is desirable to increase the ratio between electrolyte resistance and coupling impedance. It should be noted, however, that this also increases the detector window.

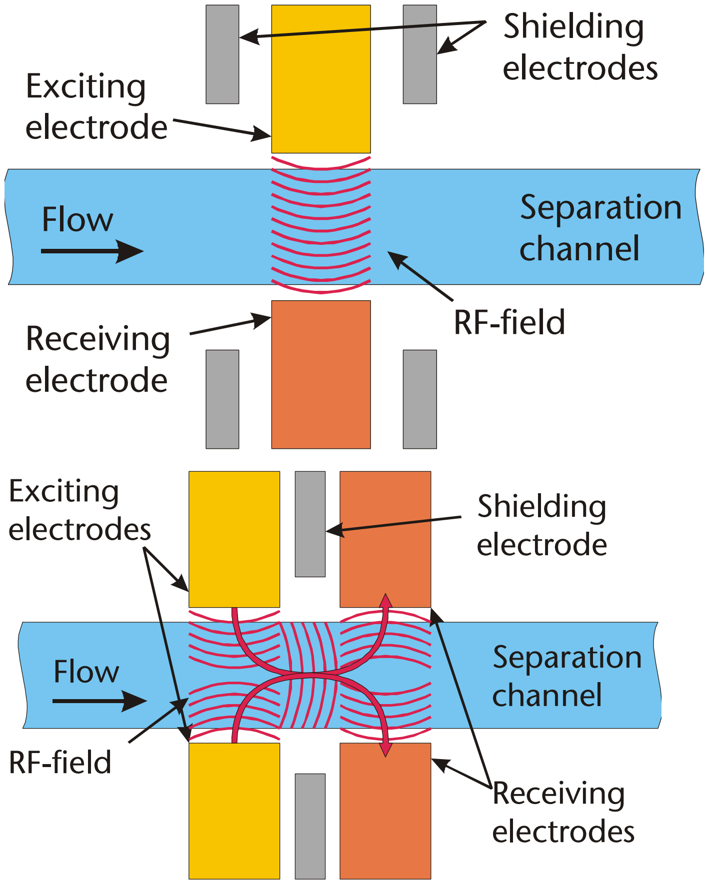

***Figure 5-24**: Comparison between the two detection approaches:*

a) The first layout, already presented in Figure 5-16, detects perpendicular to the flow in the separation channel. Stray fields extending in parallel to the flow may increase the detector window.

b) The second approach detects the local conductivity change mainly along the channel in parallel to the flow. The radio frequency field is better confined spatially, which improves the separation resolution. At the same time, the coupling capacitance is increased by the symmetric layout of the electrodes.

Figure 5-25 shows the schematic layout of the parallel CCD chip. Comparatively large electrodes (350 µm wide) were chosen to assure good capacitive coupling for increased sensitivity, which leads to a total length of 1.07 mm for the detector.

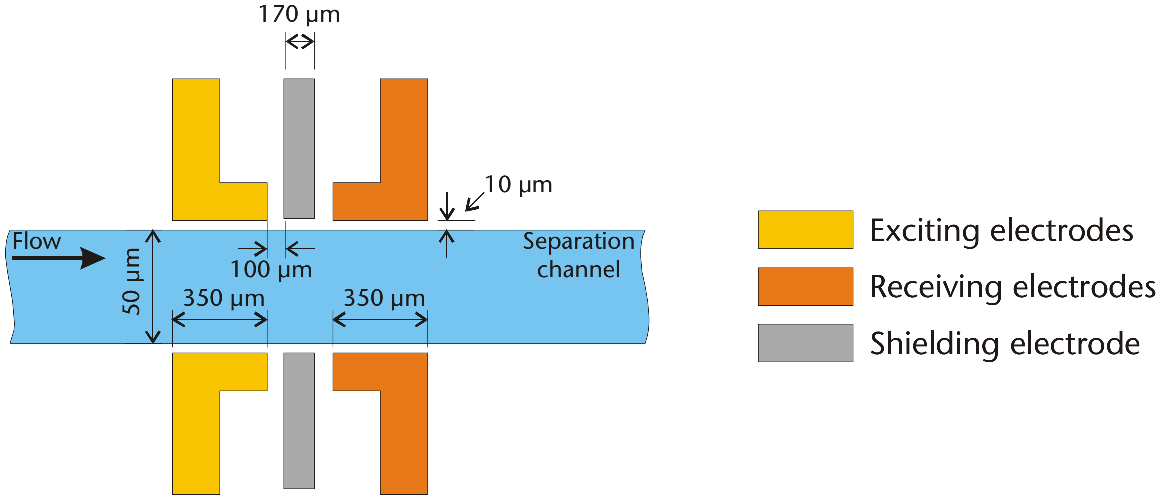

***Figure 5-25**: The layout of the CCD chip with parallel detection approach features two pairs of 350-µm-wide electrodes, which are connected off-chip. The total length of the detector element is 1.07 mm.*

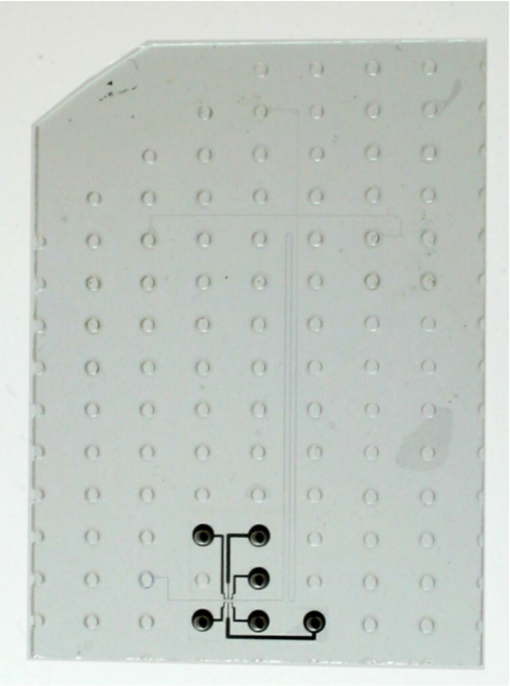

***Figure 5-26**: Photograph of a CCD chip with parallel detection approach. For this particular chip, the separation length between plug formation element and the middle of the detector region is 84.6 mm. This is achieved by a meander-type layout of the separation channel.*

Similar to the experiments carried out in Section 5.10.1, the operating frequency was optimized for the new, parallel structure and buffer plugs were injected to determine the separation efficiency. The resulting data is presented in Figure 5-27 and Table 8, indicating a 60% improvement of the number of theoretical plates for the parallel measurement scheme. This is surprising, given that the total detector length of parallel design is a factor of 2 larger than that of the perpendicular design for 400-µm-wide electrodes. The result backs-up the assumption that the parallel design improves the spatial confinement of the RF field and thereby reduces the detector window. It should also be noted that, apart from the enhanced resolution, the sensitivity is increased by 30% as well, which is a result of the improved capacitive coupling.

The new, parallel detection scheme is a major improvement over the perpendicular device both in terms of separation efficiency and sensitivity. However, in practice it turned out that the close spacing of the contact pads for the external, spring-loaded tips posed problems. The capacitive cross-talk between the contact pins mounted in the PMMA chip holder interfered with the measurement and made device operation difficult. To overcome this, electrical contacts were made using conductive epoxy glue and copper wires. The disadvantage of this comparatively crude approach is the strong influence of the flexible wiring on the measurement results. For the future, either an improved, shielded chip holder or a device layout with larger distances between the contact pads should be used.

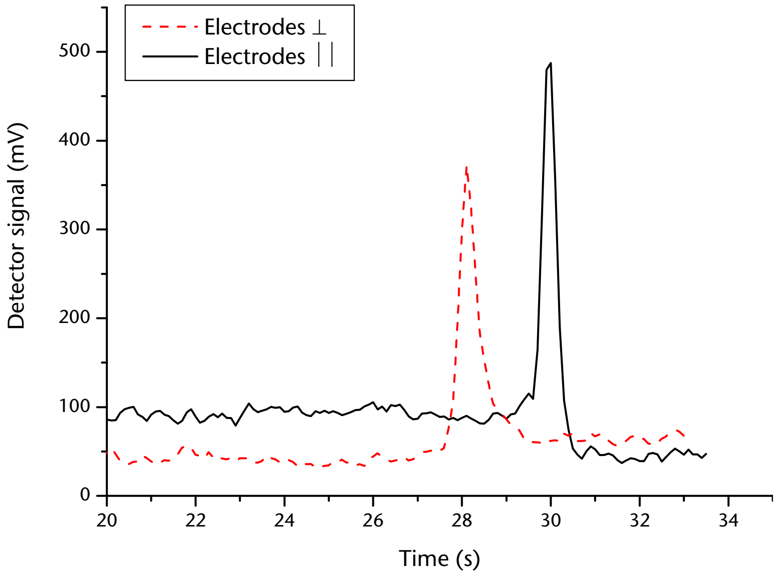

***Figure 5-27**: Comparison of the two CCD-types with perpendicular (⊥) and parallel detection (||). The experiment was carried out at optimum operating frequency (58 kHz for the ⊥–structure and 56 kHz for the ||-CCD). Running buffer: 10 mM MES/His at pH 6.0. Separation conditions: 200 V/cm; effective separation length, 3.4 cm; the same channel layout was used for both separations.*

Electrode width	***Perpendicular ($\perp$)***	***Parallel ($\|$)***
Migration time (t)	*28.0 s*	*29.7 s*
Peak width at half height ($w_{1/2}$)	*0.58 s*	*0.48 s*
N	*12,900*	*21,200*
Theoretical plates per m	$380 \cdot 10^3\ m^{-1}$	$620 \cdot 10^3\ m^{-1}$

***Table 8**: Separation efficiency data for perpendicular and parallel measurement layouts. The perpendicular chip had an electrode width of 400 µm, while the parallel electrodes were 350 µm wide.*

5.11 Conclusion

The contactless conductivity detector presented is a straightforward way to integrate this detection method into glass-based microfluidic systems. It was found that a good characterization of the device is necessary in order to be able to optimize the various operational parameters. The results obtained using the first generation of CCD devices with detection perpendicular to the buffer flow led to the development of a new, parallel detection scheme. The latter improved both separation efficiency and detection sensitivity, even though minor modifications are necessary to the external wiring configuration of the setup.

As expected, the contactless detection approach and the inert glass substrate assured a long device lifetime. Once chips were properly sealed by fusion bonding, they were used for experiments over a period of more than three months without noticeable degradation of detector performance. This is a promising result for the future development of long-term, autonomous analysis systems based on microfluidic components.

Chapter 6

Analytical Applications for Contactless Conductivity Detection

While design, fabrication, and characterization of the contactless conductivity detector were presented in the previous chapter, the focus of Chapter 6 is the evaluation of the device in typical applications. These are primarily the CE separation of small cations and anions, which showed limits of detection down to 9 µM for chloride[24]*. In order to increase the sensitivity of the system further, it has been combined with field-amplification sample stacking (FASS) as described in Chapter 4. This led to a signal gain of up to four-fold at a relative conductivity of 10.*

6.1 Introduction

To evaluate the performance of the new, contactless conductivity detector (CCD), three typical applications were selected: 1) a CE separation of a mixture of three cations, 2) a CE separation of four anions under reversed EOF conditions, and 3) the combination of CE using the CCD with field-amplified sample stacking (FASS), as presented in Chapter 4. Both the cation and the anion separation are typical examples for analysis carried out on a daily basis in the fields of environmental monitoring [42, 43, 191], food analysis [192, 193] or industrial processing [194]. Conductivity detection on microchip-based analysis devices has recently been applied to the measurement of low-explosive ionic components [195], the separation of amino acids, peptides and proteins [172, 173], water analysis [196],

---

[24] Work presented in this chapter was partly published in J. Lichtenberg, N.F. de Rooij, E. Verpoorte, "*A microchip electrophoresis system with integrated in-plane electrodes for contactless conductivity detection*", Electrophoresis 23 (2002) 3769-3780. Previously unpublished is the anion separation.

food analysis [197, 198], urine analysis [199], and monitoring of mixing reactions [174]

For applications where the sensitivity of the CCD is not sufficient, a sample preconcentration step like FASS can be integrated onto the chip to improve limits of detection (LODs). This is especially interesting for contactless conductivity detectors that generally achieve LODs an order of magnitude higher than comparable contact-mode systems [200].

6.2 Experimental

All separations were performed in a buffer containing 10 mM MES and 7 mM His (short 10 mM MES/His) at pH 6.0, prepared as described in Section 5.7.1. Samples were prepared from 10 mM stock solutions of the various ions in 10 mM MES/His. Cation samples were based on their nitrate salts, while sodium salts were used for preparing the anion samples (all purchased from Merck, Darmstadt, Germany).

Microchip cleaning and conditioning was performed as described in Section 5.7.2, and the CE procedure is detailed in Section 5.7.3.

6.3 Cation separation

A mixture of potassium, sodium and lithium cations was used to evaluate the separation performance of the integrated conductivity detector.

Electropherograms for a separation field strength of 280 V/cm and performed on a CCD chip with perpendicular detection scheme are depicted in Figure 6-1. During the first two seconds of the separation, the detector signal is elevated, a phenomenon which is related to the application of the high voltage. This is due to the electrical potential of the electrolyte in the detector volume, which rises rapidly from ground to nearly the negative separation voltage applied to the buffer waste reservoir. The limit of detection for K^+ was estimated to be 18 µM in this experiment. Though the concentrations of K^+, Na^+, and Li^+ are all the same in the sample analyzed, peak intensities decrease in the order $K^+ > Na^+ > Li^+$. This agrees with results obtained for CE separations of these ions both in conventional [160] and chip format [181], and is related to the ionic conductivities of these ions. It would be expected that the more conductive a sample component zone is with respect to the relatively unconductive background electrolyte (MES/His in this case), the greater the sensitivity of the detector is to this component. Not surprisingly, the ionic conductivities of K^+, Na^+, and Li^+ at infinite dilution decrease in the same order as the observed peak intensities.

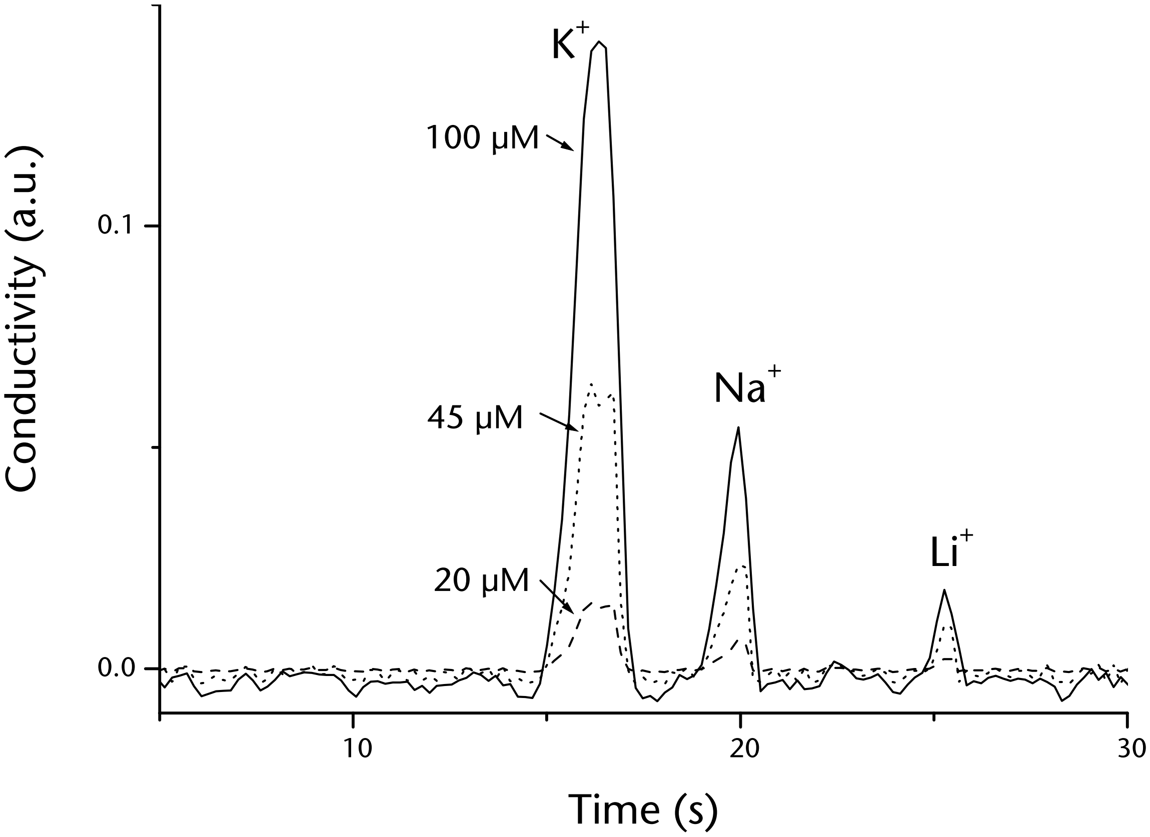

***Figure 6-1**: Three microchip CE separations of samples containing K^+, Li^+ and Na^+ at concentration of 100, 45, and 20 µM in running buffer. The measured plate number for K^+ is 43,200 plates/m, with an estimated limit of detection of 18 µM. In this example for a device with 400-µm-wide electrodes and a 50-µm-wide channel, the optimum operating frequency was found to be 58 kHz. Running buffer: 10 mM MES/His at pH 6.0. Separation conditions: 280 V/cm; effective separation length, 3.4 cm; perpendicular detection scheme.*

If compared to similar chip-based, contactless conductivity detectors, the design presented here has a somewhat lower sensitivity. Pumera *et al.* reported an LOD of 2.8 µM for K^+, for example [181]. Direct comparison of our device with that of Pumera *et al.* is difficult, since electrode layouts differ substantially. However, among the possible causes for the higher LOD in this study is the smaller size of the electrodes (400 µm versus 800 µm in [181]), which leads to less capacitive coupling of the signal into the detection volume. The channel cross-section in [181] was somewhat larger (50 × 50 μm^2, versus 50 × 12 μm^2 in this study), which could contribute to a better measurement signal-to-stray capacitance ratio, and ultimately a lower LOD for K^+. Detector sensitivity is also dependent on electrode spacing, with increased sensitivity achieved over longer distances [159]. In Pumera *et al.* [181], the measurement electrodes were separated by 700 µm, while in our case, the radially positioned electrodes were spaced by 50 µm, the channel width. This could result in a smaller net change in absolute conductance being determined in the detector volume for a given concentration in this study. However, a trade-off between sensitivity and spatial layout of the detector was necessary, in order to retain separation resolution and efficiency over the short (3.4 cm) separation length of the device [159]. Evaluation of the various geometric parameters of importance for achieving enhanced sensitivity is ongoing.

The measured plate number for K^+ is 43,200 plates/m, a rather low value for chip-based separation devices if compared with LIF-based detection on microchips. This result is perhaps attributable to the large width of the measurement electrodes (400 µm) and fringing effects due to stray fields at the end of the electrodes. The length of the detector window can be estimated from the plate number to be 2 mm, taking into account the effects of the injection plug length as well as diffusion during the separation [13]. This value is considerably longer than the detector itself, indicating that there indeed could be effects arising at the detector, due to the electrodes, which degrade detector performance. Investigation of possible causes and solutions for this phenomenon are underway.

Interestingly, however, the results presented in this study compare favorably with microchip cation separations under similar conditions reported by other researchers [173, 181, 201]. The plate numbers obtained by Pumera *et al.* for Na^+ are also on the order of 45,000 to 55,000 for applied field strengths of 100 V/cm to 1000 V/cm [181]. In their experiments, a side-by-side layout of 800-µm-wide electrodes separated by a detection gap of 700 µm probably also resulted in a relatively long detection window (> 700 µm), though this was not discussed.

6.4 Anion separation

For the separation of common anions, a mixture of chloride, nitrite, nitrate, and sulphate was used. The sample contained 100 µM of each anion dissolved in running buffer. However, as small anions have a comparatively high electrophoretic mobility in a direction opposite to the EOF, the latter has to be reversed in order to have the analyte migrating towards the detector. This can be achieved by adding small amounts of long-chain alkyl ammonium salts to the running buffer, which suppress or even invert the polarity of the surface charge on the capillary or microchannel wall and thus also affect the direction and magnitude of the EOF. The EOF modifier used here is cetyl trimethyl ammonium bromide (CTAB, from Sigma, Buchs, Switzerland) added to the running buffer in a concentration of 50 µM.

Figure 6-2 shows the electropherogram for a co-electro-osmotic CE separation performed at a field strength of 370 V/cm. The microchip device used for this separation stems from the second generation, with two pairs of electrodes for detection parallel to the buffer flow (see Section 5.10.2). The improved spatial resolution of this design was necessary to fully separate the chloride and sulphate peaks. Nitrite and nitrate are not fully baseline-resolved here, but this probably would be possible by slightly reducing the EOF modifier concentration to increase the separation time.

It should also be noted that the increased sensitivity of the second generation detector approach led to a lower LOD (9 µM for Cl^-) than that found for cations in the previous section.

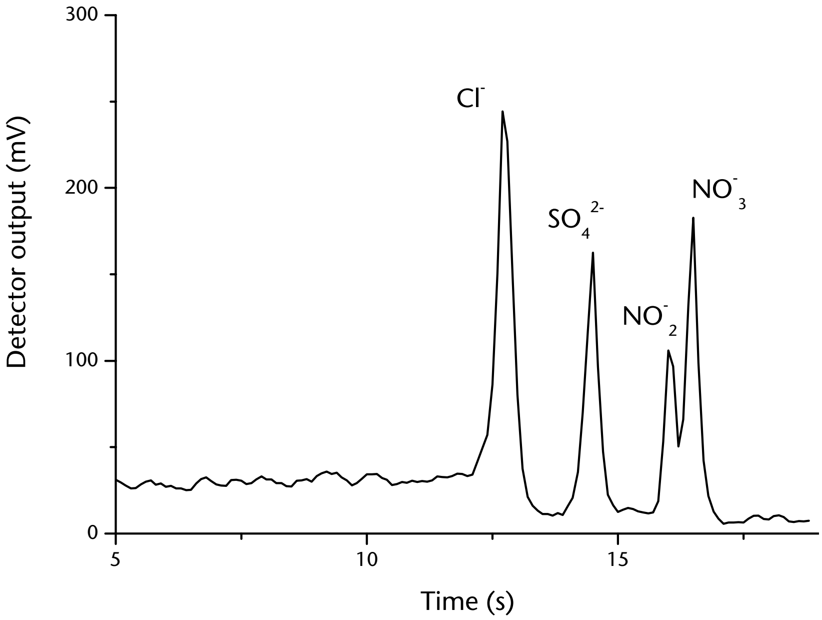

***Figure 6-2**: Microchip CE separation of an anion sample containing 100 µM of Cl^-, SO_4^{2-}, NO_2^-, and NO_3^- each in running buffer. The estimated limit of detection for chloride is 9 µM (background noise ~7 mV_{p-p}). In contrast to the separation depicted in Figure 6-1, the new design based on detection parallel to the buffer flow was used (see Section 5.10.2 for details). Running buffer: 10 mM MES/His at pH 6.0 with 50 µM CTAB as EOF modifier. Separation conditions: 370 V/cm; effective separation length, 3.4 cm; detection at 56 kHz.*

6.5 Field amplified sample stacking

To improve the limit of detection of the microchip CE system further, field-amplified sample stacking (FASS) may be used as a sample preconcentration method prior to CE separation [62]. Sample preconcentration in general allows the collection of sample constituents specifically or non-specifically from a given sample volume, and their confinement in a smaller volume prior to further analysis [49]. Part of the burden of high analysis sensitivity is thus shifted from the detector to earlier stages of the analysis system. A detailed report on FASS in general and research work done on the integration of FASS into microchip-based analysis devices as part of this thesis is given in Chapter 4.

Preconcentration in FASS is achieved by generating a high electrical field within an injected sample plug, that rapidly drives and stacks sample ions at the ends of that plug [83, 87-89]. This field amplification is created when the sample is dissolved in a buffer that has a much lower conductivity than the surrounding running buffer used for separation. Assuming low buffer concentrations, the relative conductivity, γ, is defined as:

$$\gamma = c_r / c_s = \sigma_r / \sigma_s = E_s / E_r \tag{44}$$

where c_r and c_s are buffer concentrations for the running buffer and sample buffer, respectively; σ_r and σ_s are the conductivities of the two buffers, which are in general proportional to c_r and c_s; and E_s and E_r are the electric field strengths in sample and running buffer zones. The electrophoretic velocity of each ionic species in the sample plug is proportional to the field strength, which leads to a rapid migration of anions to the back of the sample plug and cations to the front, assuming electro-osmotic flow towards the cathode. Once they reach the boundary to the high conductivity running buffer, the ions experience a sudden electric field drop, and slow down to form a zone of concentrated sample ions at the end of the sample plug as a result. FASS techniques have been implemented on-chip as a preparation method for mass spectrometry [61] and in combination with CE [62]. Field-amplified injection, a similar application of electrokinetic stacking phenomena, has been reported on chip as well [52, 98].

Figure 6-3 shows three CE separations of a single cation sample containing 100 µM K^+, performed on a CCD chip with perpendicular detection scheme. One experiment was carried out under non-stacking conditions, the sample ion being dissolved in the running buffer (10 mM MES/His at pH 6.0). For the two following runs, the sample ion was dissolved in dilute running buffer at concentrations of 5 and 1 mM, corresponding to γ of 2 and 10, respectively. For γ=10, the peak height of the K^+ peak is four times that recorded under non-stacking conditions. Given that the noise level remains the same, this means an improvement in the detection limit by a factor of four as well. The signal gain achieved by stacking could be higher if larger sample volumes were injected [62]. However, the design of the chips described here was not optimized for FAS.

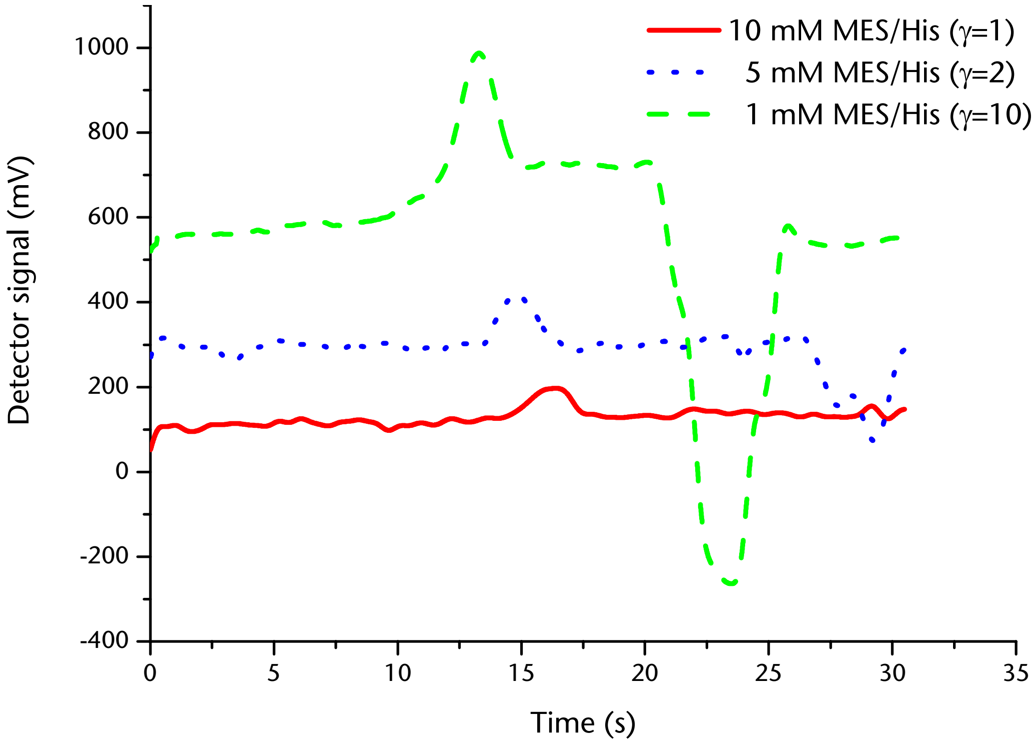

Figure 6-3: *Field-amplified sample stacking combined with conductivity detection yields a four-fold increase in peak height for a relative conductivity of 10. The sample is 100 µM K+ dissolved in 10, 5 and 1 mM MES/His buffer, as indicated in the plot. The same device layout as in* ***Figure 6-1*** *was used. Running buffer: 10 mM MES/His at pH 6.0 with 50 µM CTAB. Separation conditions: 300 V/cm; effective separation length, 3.4 cm; detection at 58 kHz using the perpendicular scheme.*

Under stacking conditions, the electropherogram also reveals the low-conductivity sample buffer plug, which arrives after K^+ at the detector. For higher γ, this negative peak is more pronounced and migrates faster, because the electroosmotic flow velocity within the plug increases with decreasing ionic strength as well as increasing electric field.

6.6 Conclusion

Detector performance was quite good in terms of sensitivity, with an LOD of 18 µM determined for K^+ using the perpendicular detection approach, 9 µM for Cl^- for the parallel electrode layout. Since LODs as low as 1.2 µM for the same ions have been reported using contactless conductivity detection on chip [181], we are confident that this type of result should be possible on our devices as well. This will require some further work on electrode layout and the external wiring to minimize capacitive cross-talk and other undesirable effects. Clearly, though, the fabrication approach chosen has an inherent flexibility with respect to detector configuration that other published methods do not possess. Hence, it should be possible to produce improved chip designs for more sensitive detection and better separation resolution. It should be pointed out as well that this on-column approach already circumvents the band-broadening generally observed for end-column configurations.

Chapter 7

Signal Processing for Contactless Conductivity Detection

The discussion in previous chapters has implied that signal processing for contactless conductivity detection for capillary electrophoresis is a challenging task. This is due to the small coupling capacitances between electrodes and electrolyte, which are additionally overlaid by parasitic stray capacitances in the same order of magnitude. These boundary conditions require sensitive electronics, sophisticated filtering of the signals obtained and thorough shielding of the whole setup. This chapter discusses the different building blocks of the signal processing circuitry and related subjects. Two different techniques to extract the conductivity information from the measurement signal, namely rectified and synchronous detection, will also be presented in detail.

7.1 Introduction

Conductivity detection in capillary electrophoresis [130] detects the separated analyte zones of the initial sample plug by monitoring the local change in conductivity at the end of the separation capillary or channel as described in Chapter 5. The key element of such a detector device is therefore a set of electrodes either in direct electrical contact with the electrolyte (for contact-mode detection) or in close vicinity to the electrolyte, but electrically insulated (for contactless operation). No less important, the signal processing circuitry has to be adapted to the special requirements in CE, especially miniaturization of electrodes, high-voltage compatibility and low noise.

Conductivity is determined by the measurement of the *conductance*, which requires a probing current flowing through the resistor being tested while the resistive voltage drop is measured or vice versa [82]. In both cases, the conductance (in S) is determined by Ohm's law as:

$$G = \frac{1}{R} = \frac{i}{V} \tag{45}$$

with i: current through the resistor (A)

V: voltage across the resistor (V)

While conductance is related to the resistance to electrical current for a volume of given dimension, a specific material property, independent of the volume dimensions, can be derived. For a block of the material with length L (in m) and cross-section A in (m^2) with the measurement current flowing in parallel to L, the *conductivity* σ (in S/m) is defined as:

$$\sigma = G\frac{A}{L} \tag{46}$$

In general laboratory practice, the factor A/L is also known as the *cell constant* for rectangular configurations and conductivity may also be denoted as *specific conductance*.

A straightforward implementation for conductivity determination uses a precise, constant direct-current (DC) source to provide a fixed i, combined with a high-impedance instrumentation amplifier which measures V without considerably loading the current source (Figure 7-1). More advanced techniques employ four-probe schemes to avoid voltage drops across the leads [82].

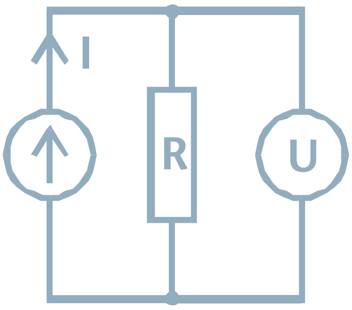

***Figure 7-1**: DC-conductivity measurement setup based on a constant current source and a voltmeter.*

However, due to interferences between the separation and measurement currents, no published implementation of this technique for detection in capillary electrophoresis is known. Other problems include electrolysis at electrodes and electrode polarization as described in Section 5.2.3. Still, DC-mode conductivity detection can be turned into an interesting, straightforward detection technique as described in the next chapter.

7.2 Instrumentation for contactless conductivity detection

For the time being, instrumentation for contactless conductivity detection for CE is not commercially available on the market. Part of the research work involved in this thesis project was the development of a suitable detector read-out, which could also be deployed in a portable instrument design.

Electronic components were obtained from Farnell AG, Zürich, Switzerland (general semiconductors) and Distrelec AG, Nänikon, Switzerland (passive components). Integrated circuits from Analog Devices were obtained from Spoerle Electronic, Rümlang, Switzerland. Printed circuit boards were designed in-house using the Ultiboard software (Electronics Workbench Europe, Naarden, The Netherlands) and fabricated by Beta-Layout (Aarbergen, Germany). Transient data in most figures of this section was acquired by a Gould Digital Oscilloscope Series 400 (Gould Instrument Systems, Valley View, OH, USA) via a serial interface using a transfer software written in-house.

7.2.1 Detector system

As outlined in Chapter 5, contactless conductivity detection requires measurements in the radio frequency range (10 to 600 kHz) to overcome the impedance barrier of the dielectric insulation layer [159, 160, 165]. For excitation of the measurement current, a sinusoidal signal source is directly connected to one of the two measurement electrodes (see Figure 7-2, which is reprinted from Chapter 5 for convenience). The other electrode is connected to a current-to-voltage converter (i/V-converter), which registers the current through the detector arrangement induced by the applied voltage. The following stage isolates and demodulates the sinusoidal output signal obtained from the i/V-converter into a DC signal by synchronous detection. Finally, the demodulated signal is low-pass filtered to remove the excitation frequency components and noise.

Prior to the following discussion of the electronic building blocks of the instrument, it should be noted that most sub-circuits used in this thesis are analyzed in detail in [188, 202], which also give a general introduction into analog electronics. A good discussion of capacitive read-out circuits, shielding and related issues is given by Baxter in [162].

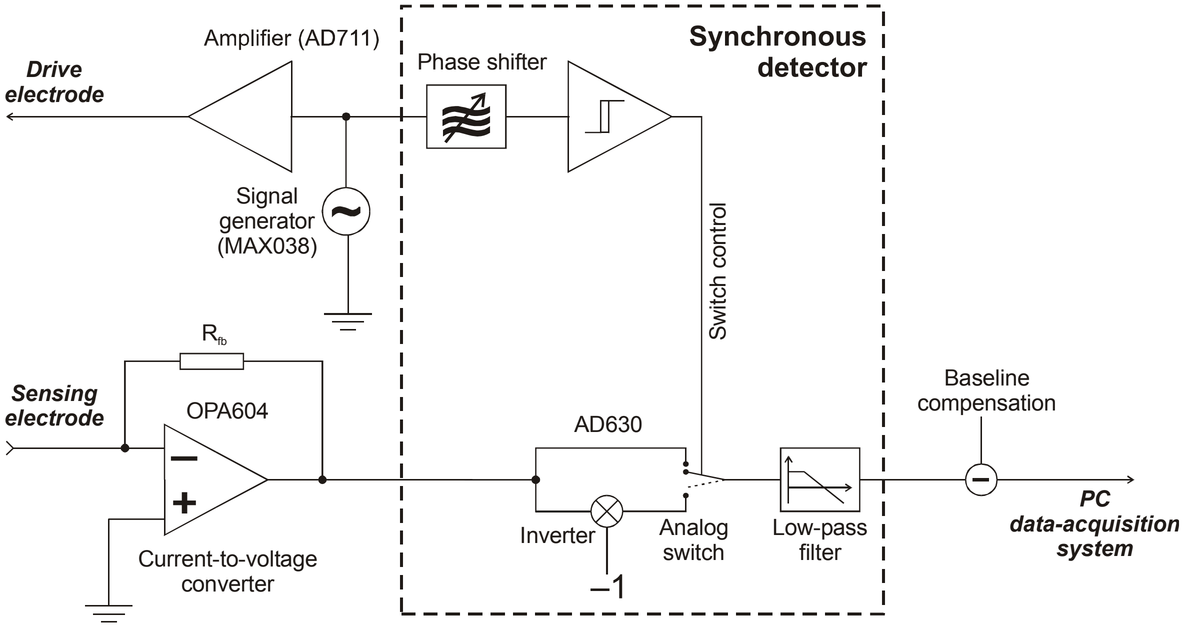

Figure 7-2: *Schematic of the read-out circuit consisting of a current-to-voltage converter, synchronous detector, baseline compensation and low-pass filter. Excitation is achieved using a sinusoidal waveform generator followed by a non-inverting amplifier. Figure reprinted from Chapter 5 for convenience.*

7.2.2 Excitation circuit

The central element of the excitation circuit is the extremely versatile, integrated function or signal generator, MAX038[25] (Maxim, Sunnyvale, CA, USA), which produces sinusoidal, square, and saw-tooth waveforms in a frequency range from 0.1 Hz to 20 MHz (depicted at the upper left in Figure 7-3). The oscillator fre-

---

[25] The datasheet for the MAX038 is available at www.maxim-ic.com.

quency, f_0, is adjusted by a resistor-capacitor combination connected to pins 1/10 (R_{in}=R7+P1) and 5/6 (C_f=C18) according to the formula:

$$f_0 = \frac{2.5}{R_{in} \cdot C_f} \tag{47}$$

For the detector application, a frequency range from 10 to 360 kHz was selected, corresponding to component values of 1 nF for C_f and a (variable) resistor combination with a value between 6.8 and 256.8 kΩ for R_{in}.

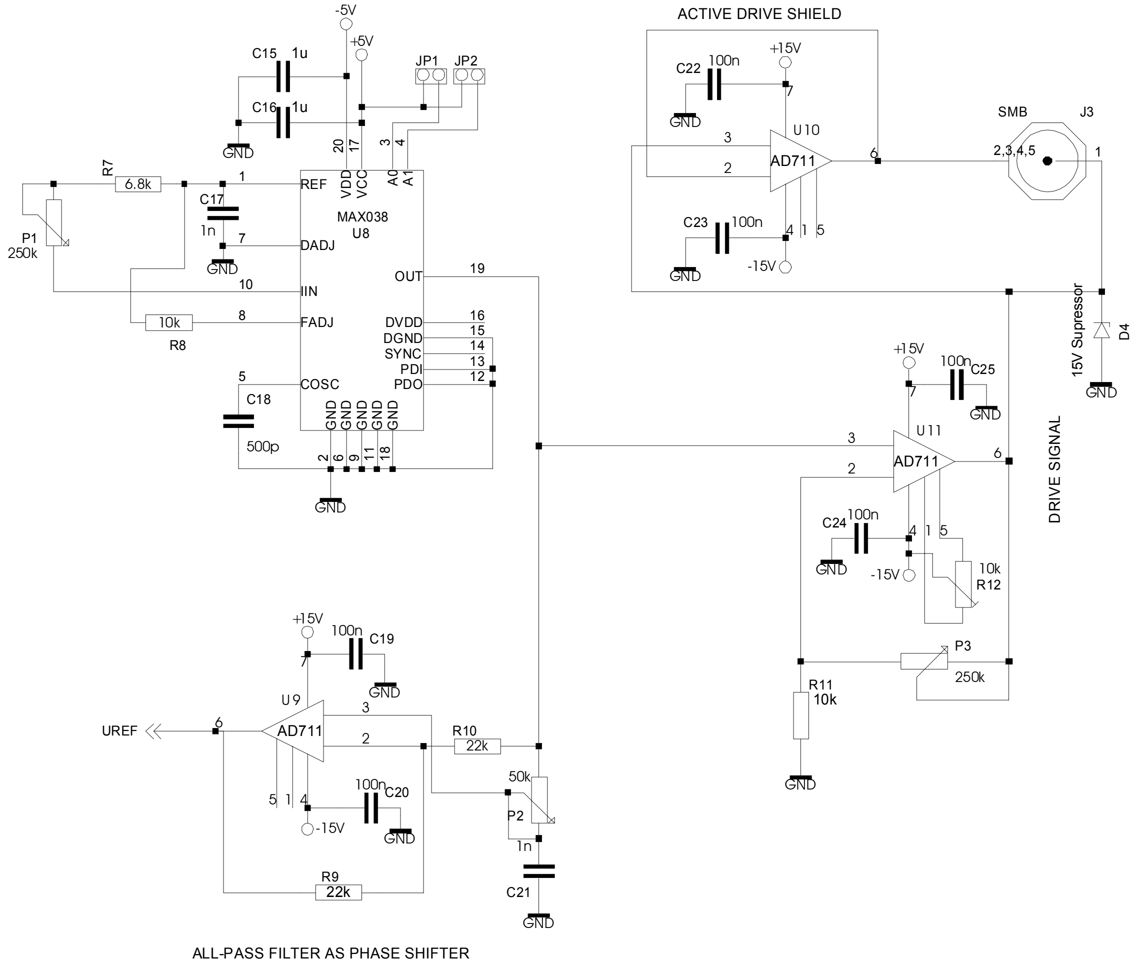

Figure 7-3: *Schematic of the oscillator circuit (top left) with amplifier (lower right). A shield drive for tri-axial cables is included (upper right) as well as a phase shifter for sinusoidal signals for synchronous detection (lower left).*

The waveform type is selected by two digital configuration lines A0 and A1, according to the settings in Table 9, which are implemented as configurable switches in the actual instrument.

A0	**A1**	**Wave form**
X	1	Sine wave
0	0	Square wave
1	0	Saw-tooth wave

***Table 9**: Wave form selection for oscillator (0: pin left open, 1: pin connected to +5V, X: don't care).*

As the maximum output voltage swing of the oscillator is limited to ±2 V_{p-p}, an additional amplifier stage is added to drive the exciting electrode. This driver is based on an AD711 operational amplifier (U11) in a non-inverting configuration with an amplification factor G=1+P3/R11. The maximum G for the component values in Figure 7-3 is 26; however, the maximum output voltage is of course limited by the supply voltage (±15 V) minus the op-amp saturation voltage (1.2 V), which proved to be sufficient for the application envisaged. It should be noted, though, that Tanyanyiwa *et al.* recently presented an excitation circuit for contactless conductivity detection in conventional capillary electrophoresis capable of producing output voltages in the range of ±200 V [166].

One measurement electrode is connected to the output of U9 via a high-frequency-compatible SMB connector on the printed circuit board. Although a regular coaxial cable can be used to connect the amplifier output with the corresponding electrode on the chip, a better signal transmission is achieved by using a tri-axial cable with the intermediate layer connected to the shield driver, U10. This low-impedance voltage follower drives the shield around the actual signal conductor at the same potential, thereby virtually eliminating the coupling capacitance between the conductor and the external ground shield.

An oscilloscope picture of the waveform output at 100 kHz is depicted in Figure 7-4.

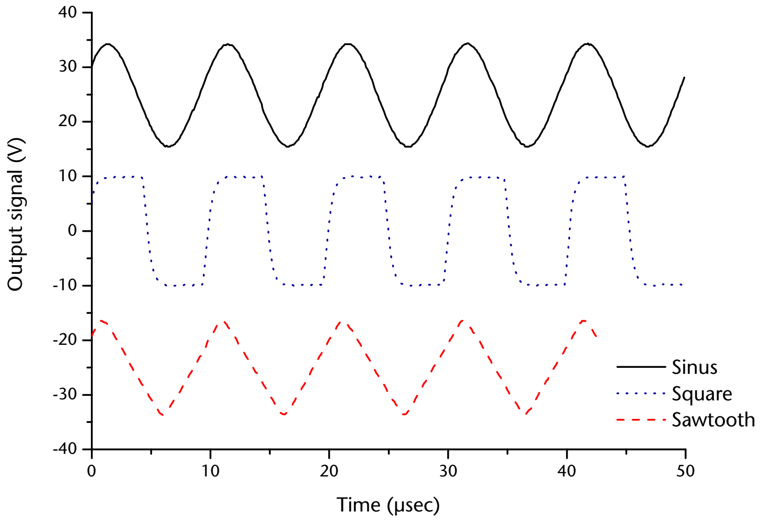

Figure 7-4: *Three different wave forms generated by the oscillator circuit of the detector instrument for 100 kHz and a 20-*$V_{p\text{-}p}$ *output voltage.*

7.2.3 Current-to-voltage converter

The current-to-voltage converter is the first building block on the input side of the detector system, converting the AC current passing through the measurement electrodes into a corresponding AC voltage (see Figure 7-5). The electrode is connected via a short, shielded coaxial cable to the input SMB connector on the printed circuit board. For precise operation, a fast high-impedance op-amp like the OPA604 (Burr-Brown, now part of Texas Instruments, Dallas, TX, USA) has to be used to limit errors due to leakage currents into the amplifier input. The output voltage of the standard current-to-voltage converter circuit for a given input current, i_{in}, and feedback resistor, R_{fb}, can be calculated as:

$$V_{out} = i_{in} \cdot R_{fb} \tag{48}$$

With R_{fb} = 1 MΩ (R_1 in Figure 7-5), an input current of 1 μA produces an output voltage of 1 V. In order to decouple the output of the converter from the following detection and filter stages, a voltage follower (non-inverting, unity gain) buffers the output signal.

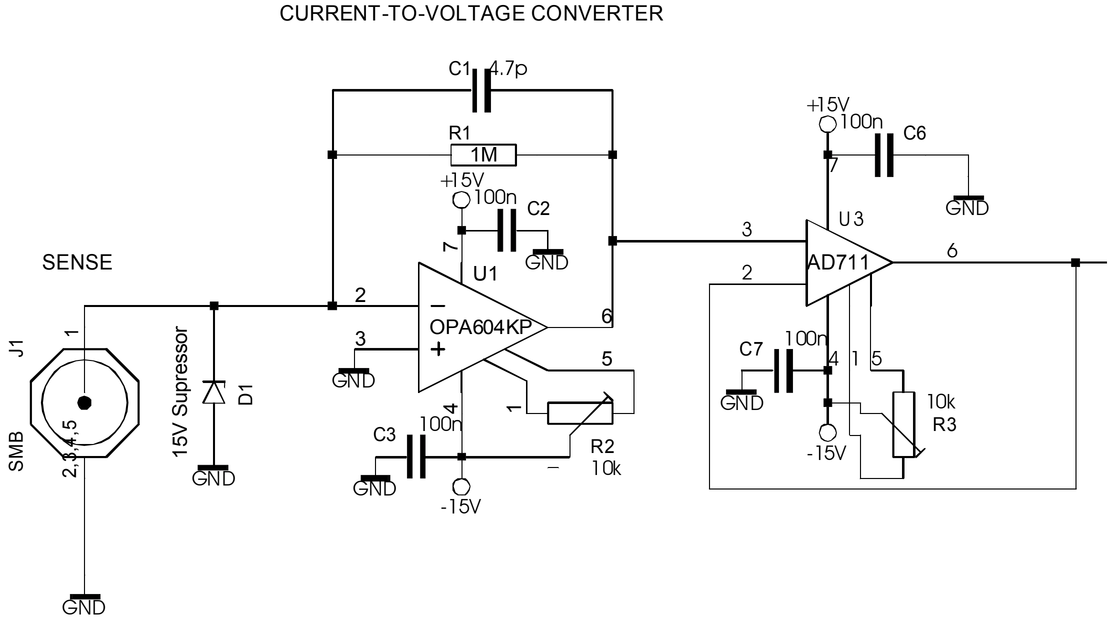

Figure 7-5: Schematic of the input current-to-voltage converter with additional voltage follower on the right side.

Figure 7-6 shows the output signal at pin 6 of U3 for the sinusoidal excitation signal depicted in Figure 7-4. As test device for this and the following oscillograms a contactless conductivity detector on a glass chip as described in Section 5.6.3 was used. The channel was filled with 10 mM MES/His buffer (prepared as described in Section 5.7.1) and the excitation voltage amplitude was 20 V_{p-p}.

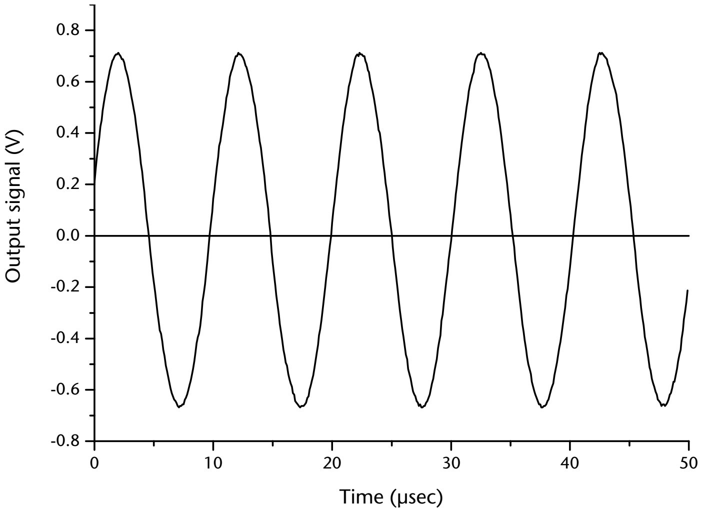

Figure 7-6: Oscillogram taken at the output of the current-to-voltage converter block (pin 6 of U3) for a sinusoidal input of 100 kHz and 20-V_{p-p} amplitude. Note that the output wave form is practically undistorted.

7.2.4 Signal detection by rectification

The actual information about the local electrolyte conductivity in the detector volume is contained in the root-mean-square (RMS) of the output signal of the current-to-voltage converter. The RMS value of a signal $V(t)$ with period τ is defined as:

$$RMS = \sqrt{\frac{1}{\tau}\int_{\tau}\left(v(t)\right)^2 dt} \tag{49}$$

Basically, two straight-forward measurement techniques are available for RMS-to-DC conversion: 1) precision rectification and 2) synchronous detection, both followed by a low-pass filter. Both techniques are presented in this and the following section in theory and practice. For comparison, both approaches were integrated into the electronics for the contactless conductivity detector for parallel evaluation (one of the two detector modes could be selected at a time using a switch).

Rectification generally either removes or inverts the negative half-waves of an AC signal into the positive quadrant by diode elements, as shown in Figure 7-7 for a half-wave rectifier. While the peak output voltage is reduced by passive rectifying circuits due to the forward voltage drop of the diodes involved, an active precision rectifier based on an op-amp as depicted in Figure 7-8 does not have this disadvantage. The configuration presented in the figure is an active, half-wave rectifier with inversion, i.e. always delivering a negative output signal, which is depicted in Figure 7-9.

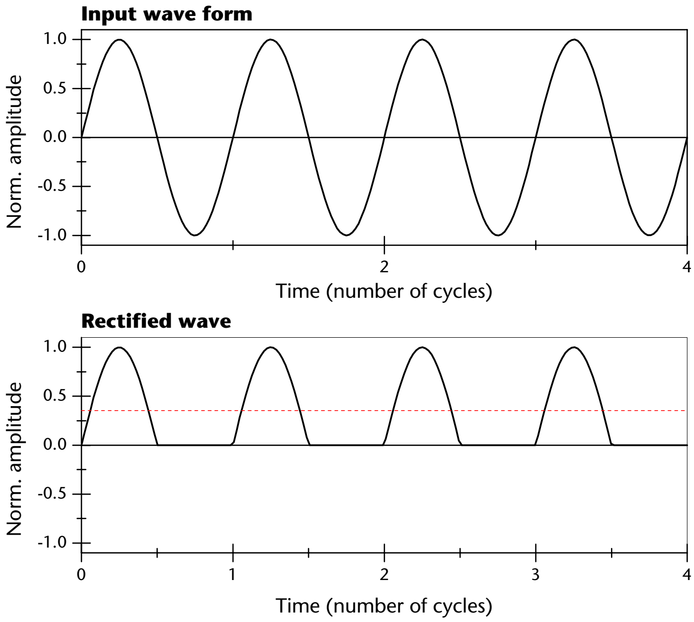

***Figure 7-7**: During rectification, negative portions of the input wave form are removed. The dashed line in the lower graph shows the RMS or effective value of the signal, which is $0.5\sqrt{2}$ in this case.*

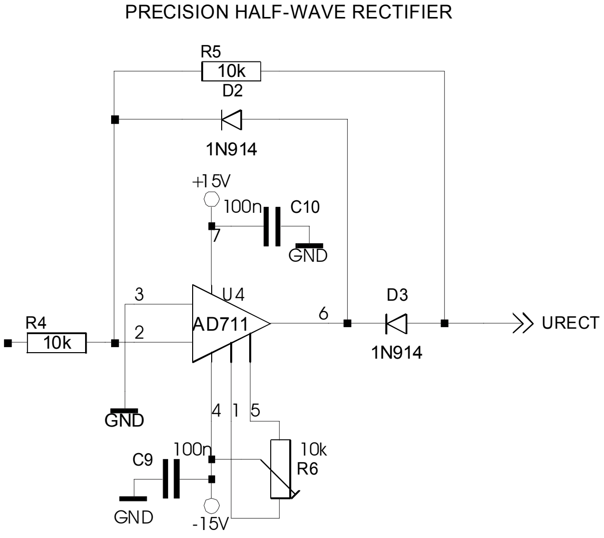

***Figure 7-8**: Schematic of the inverting, full-wave, precision rectifier circuit used for RMS measurement. Due to the feedback loop, pin 2 remains permanently on virtual ground. For positive input voltages, diode 3 (D3) renders the circuit a unity-gain inverter, thus producing a negative mirror of the input voltage. For negative inputs, diode 2 (D2) holds the output of op-amp AD711 at one diode voltage drop (~0.7 V) above ground, so that the output voltage becomes zero.*

As this rectifier is inverting, the resulting signal resembles the inverted signal of Figure 7-7, as depicted in Figure 7-9.

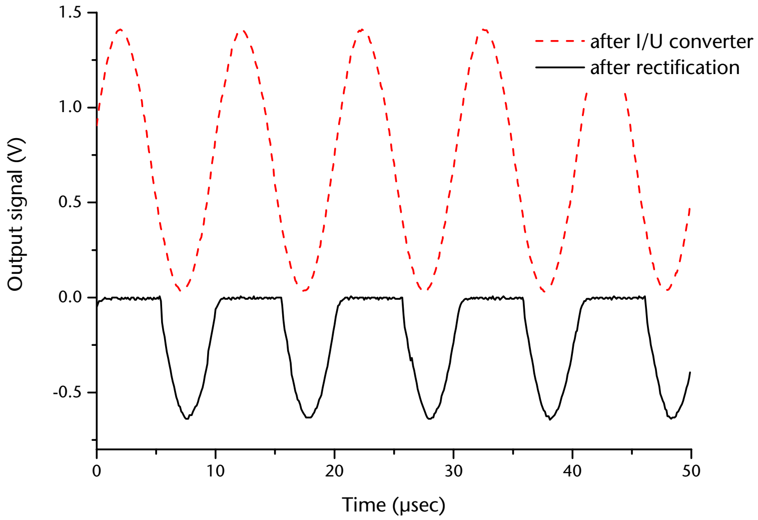

***Figure 7-9**: Oscilloscope scans of the input voltage delivered by the I/U-converter (dotted) and the resulting rectified and inverted signal.*

7.2.5 Signal processing by synchronous detection

Although the rectifier circuit is perfectly adapted for RMS measurements in general, there exist more advanced concepts especially adapted to low signal levels. One desirable feature for the given application is frequency selectivity, i.e. only the excitation frequency is taken into account for the measurement, while all others are disregarded. This drastically improves the signal-to-noise ratio (SNR) after the detector, since the signal itself passes unattenuated while the noise, which is distributed over the whole spectrum, is suppressed. Although improved SNR could also be achieved by including bandpass filters in the measurement circuit, this solution is often not suitable both in terms of selectivity and speed. Synchronous detection, on the other hand, is an ingenious alternative with excellent performance characteristics. This allows isolation of information from signals with 1000 times more noise superimposed on them [189]. Although the SNR ratio for contactless conductivity detection is by far not this low, measurement noise directly affects the obtainable detection limits and should therefore be reduced as much as possible.

In brief, synchronous detection extracts information from an input source, which is contained in a very narrow frequency range around a reference signal. Furthermore, the measurement signal has to be the same as the reference, with respect not just to frequency but also phase; this detection method is therefore also called phase-sensitive detection. If a DC signal is to be measured, it is necessary to convert it into an AC signal first. For instance, in absorbance detection the incident light beam would be chopped or periodically blocked, using a rotating element with a slit placed in front of the beam. In the case of contactless conductivity detection, the measurement signal is already in AC mode due to the capacitive coupling technique used.

Originally, synchronous detection was performed by analogically multiplying input and reference wave forms, followed by low-pass filtering. However, precise analog multiplication is not easily achieved, and two alternative implementations have been conceived. A few years ago, synchronous detectors and lock-in amplifiers based on digital signal processing were introduced on the market. These precision instruments have two disadvantages, namely their price (very expensive) and the fact that they cannot be easily used in electrically floating configurations. The latter is often necessary for detection in capillary electrophoresis to avoid interference on the detection signal by the high electric field applied for separation (100's V/cm). Therefore, a second option was chosen here, based on a monolithic, switching detector in the form of the AD630 integrated circuit (Analog Devices, Norwood, MA, USA). This IC actually multiplies the input signal with a rectangular reference switching between the values of +1 and –1 as depicted in Figure 7-10.

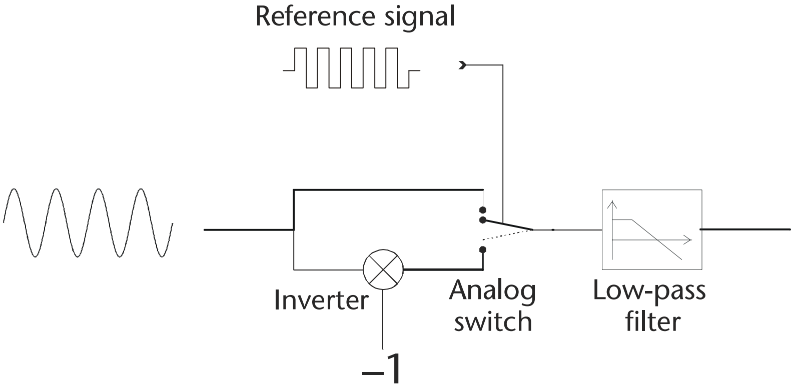

***Figure 7-10**: Schematic diagram of a synchronous detector using an AD630 IC. The input signal is alternating inverted (multiplication with -1) or fed through directly (multiplication with +1) based on the reference signal. Switching is achieved by an analog FET switch.*

To briefly describe the operation of the circuit, a sinusoidal input signal $V(t)$ is considered:

$$V(t) = V_0 \sin(\omega t + \phi) \tag{50}$$

The reference signal is a square wave with transitions at t=0, π/ω, 2π/ω, etc. It is also assumed that the output after the switch in Figure 7-10 is a low-pass filter with a time constant that is much larger than one period (τ=2π/ω) of the reference signal. The low-pass filter output $\langle V_{out} \rangle$ is the average of the signal over one period:

$$\begin{aligned}\left\langle V_{out} \right\rangle &= \frac{1}{\tau}\left(\int_{0}^{\pi/\omega} V_0 \sin(\omega t + \phi) - \int_{\pi/\omega}^{2\pi/\omega} V_0 \sin(\omega t + \phi) \right) \\ &= V_0 \frac{\omega}{2\pi}\left(\left| 2\frac{\cos\phi}{\omega} \right| - \left| -2\frac{\cos\phi}{\omega} \right| \right) \\ &= \frac{2V_0}{\pi}\cos\phi \end{aligned} \tag{51}$$

The final result indicates that the output voltage reflects the peak voltage of the input signal as well as the phase difference between input and reference: at zero difference, the signal is maximum. Therefore, the phase of both signals have to be adjusted, which is normally done by delaying the reference wave by using the phase shifter in Figure 7-3.

To understand how the frequency selectivity of this circuit comes about, consider what happens when a second input signal $V'(t)$ having slightly different frequency is introduced to the circuit:

$$\begin{aligned} V'(t) &= V_0' \sin([\omega + \Delta\omega]t) \\ &= V_0' \sin(\omega t + \phi) \\ &\quad \text{where } \phi \text{ is } t\Delta\omega \end{aligned} \tag{52}$$

Now, the time-average of the signal, V'_{out}, becomes:

$$\left\langle V'_{out} \right\rangle = \frac{2V_0'}{\pi}\cos(\Delta\omega \cdot t) \tag{53}$$

This signal is a sinusoidal wave at a difference frequency Δω, which is generally much lower than ω itself. If 1/Δω is much smaller than the time constant of the low-pass filter – which is generally the case – the off-frequency component V'_{out} will be attenuated and largely removed from the measurement signal. Figure 7-11 illustrates both cases over a larger time frame.

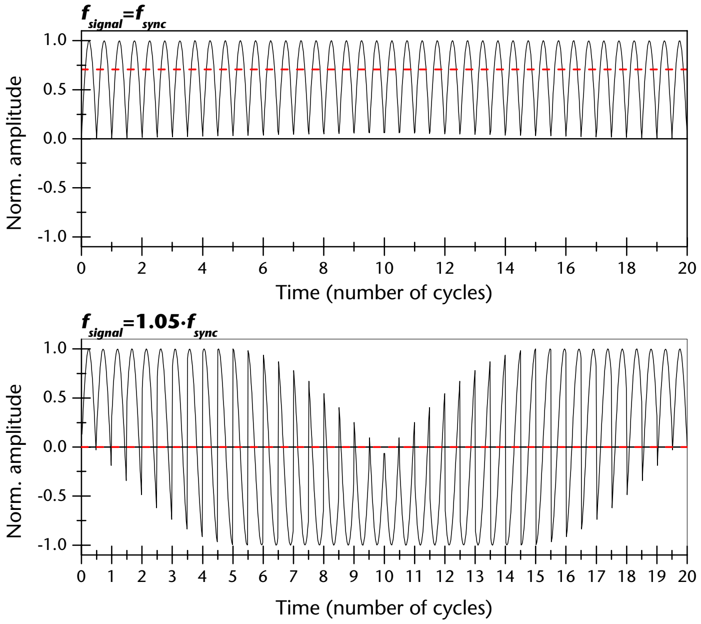

Figure 7-11*: Illustration of the frequency selection in synchronous detection.*

(above) Frequency and phase of the signal and the reference are the same. A full-wave rectification results with a time-average equal to the RMS value.

(below) A slight difference in frequency of 5% also gives rise to a phase variable difference. If the resulting signal is averaged over a longer period of time (in this case 1/0.05=20 cycles), the overall result becomes zero and the off-frequency signal is cancelled out.

7.2.6 Implementation of the synchronous detector

As mentioned above, the integrated circuit AD630 offers a complete synchronous detection system in a monolithic device (Figure 7-12). The signal provided by the current-to-voltage converter is fed into the detector input, pin 1. The reference signal input (pin 10) is followed internally by a Schmitt trigger which converts the sinusoidal wave form into a square wave, which in turn controls the analog switch. The output signal can finally be collected at pin 13. The upper part of Figure 7-13 shows the output signal in the case where input and reference signal are nearly perfectly in phase, the resulting wave being basically the absolute value of the sinusoidal input. The RMS value of this signal can be obtained by time-averaging (i.e. low-pass filtering) and will be $V_{peak}/\sqrt{2}$. However, if the two signals are out of phase a picture like the lower one in this figure is obtained, with a time-average of zero.

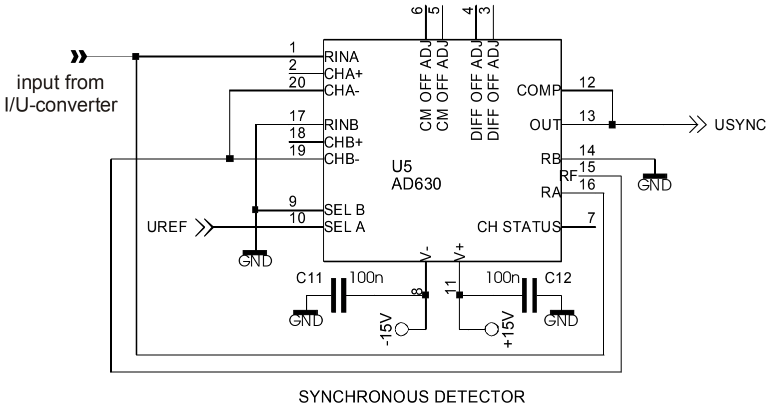

Figure 7-12: Only a few external components are necessary to build a synchronous detector based on the AD630 circuit.

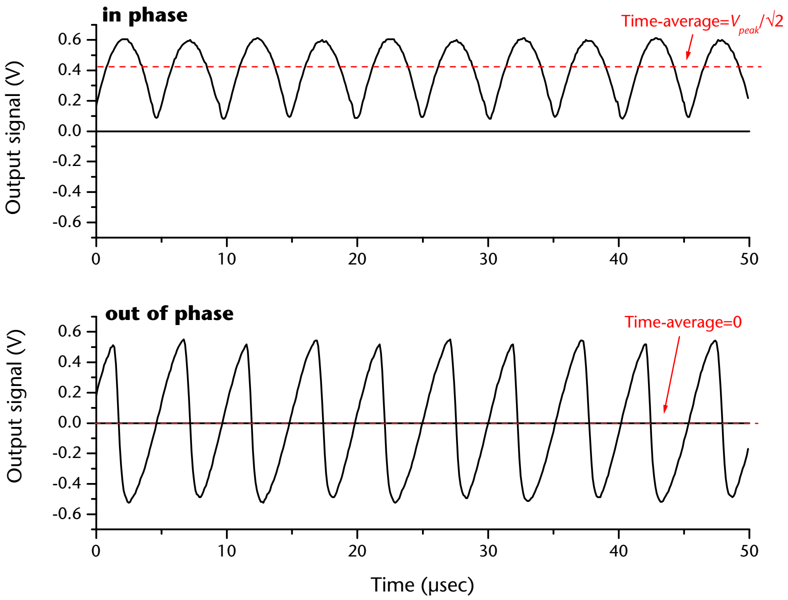

Figure 7-13: Two extreme cases in synchronous detection:

Above, nearly perfect synchronization; the-time average is equal to the RMS value.

Below, signal and reference are 90° out of phase, the resulting time-average is zero.

7.2.7 Filter stages

Independent of whether rectification or synchronous detection is chosen, the demodulated signal has to be low-pass filtered to extract the near-DC portion of the signal while removing the radio-frequency part. For the contactless conductivity detector, this is achieved by a cascade of two active, analog low-pass filters based on the op-amps U12 and U14 in Figure 7-14. The first stage around U12 forms a second-order low-pass filter (25 Hz cut-off frequency) with integrated baseline compensation. This is achieved by an adjustable voltage divider network (P5) at the non-inverting input pin 3 similar to the design in [160]. The potential at this pin is subtracted during the filtering process and can therefore be used to remove the DC background from the measurement signal. In practice, once a new chip is put into the chip holder and connected, the output voltage of the detector is adjusted to ~200 mV by turning P5 before the first CE run is started.

The following stage around U13 is a non-inverting amplifier: once the signal is stripped from its baseline, it can be amplified again (between 10- and 50-fold for the values in Figure 7-14) to reduce noise sensitivity. Finally, before delivering the signal to the data acquisition module in the computer, a last low-pass filter (17 Hz cut-off) removes noise components, which appeared or became amplified during in the previous stage. Figure 7-15 shows the output signal of the filter stage.

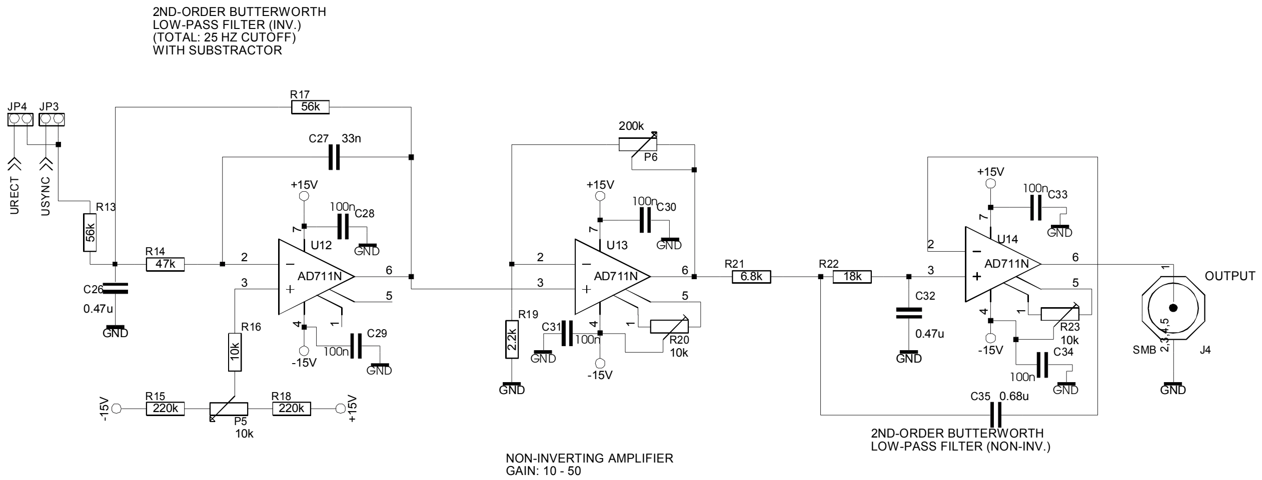

Figure 7-14: *Circuit schematic for a cascade of two low-pass filters, separated by a stage for baseline subtraction and amplification, for final conditioning of the measurement signal.*

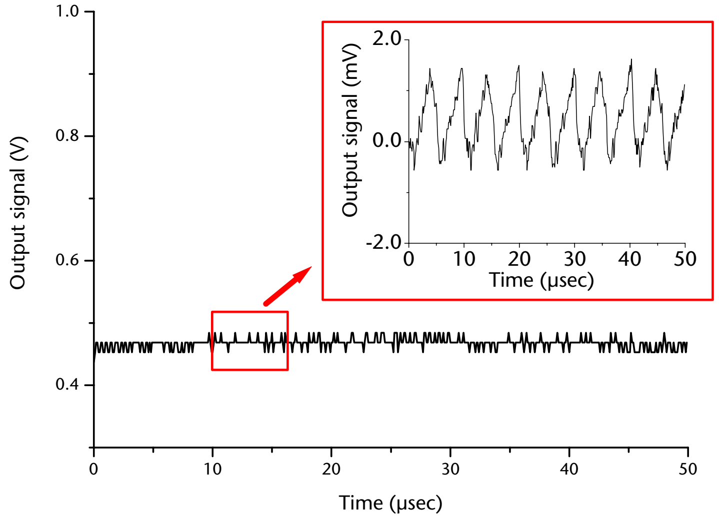

Figure 7-15: *DC output signal after the last low-pass filter of the detector electronics for synchronous detection. The signal fluctuations in the main graph are due to the limited vertical resolution of the storage oscilloscope (8 bit). The inset shows the actual noise overlaying the measurement signal with a peak-to-peak voltage of 2 mV. It is obvious that the noise is largely due to 50-Hz interference from the environment.*

7.2.8 Synchronous versus rectifying detection

As mentioned before, synchronous detection removes noise power from the signal due to its frequency selectivity. Figure 7-16 compares background noise data obtained from the output of the last low-pass filter stage for both detection methods over a time-frame of two seconds. The data was obtained by switching from rectifying to synchronous mode without changing the setup, including the glass chip under test. It becomes obvious that the background noise is roughly one order of magnitude lower for the synchronous configuration. As the sensitivity to conductivity changes is independent of the detection mode, the sensitivity of the detector should therefore improve by the same factor (see Chapter 5).

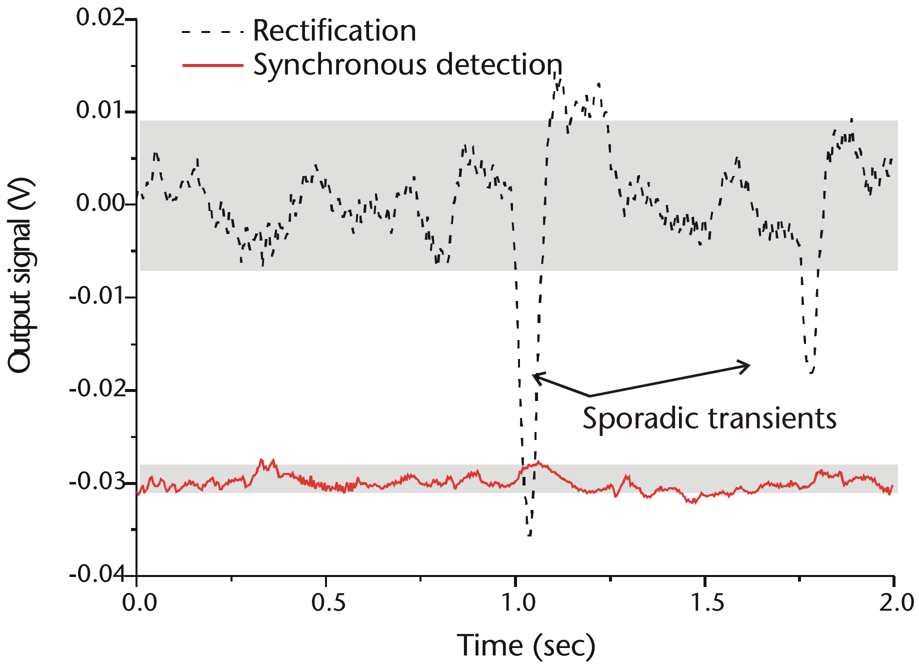

Figure 7-16: *Comparison of noise levels for rectification and synchronous detection. The latter achieves a ~10-fold lower noise floor, thus improving the limit of detection of the overall system accordingly. The gray bars indicate approximately the noise level for each trace.*

7.3 Conclusion

This section described the major building blocks necessary for an instrument for contactless conductivity detection for capillary electrophoresis and related separation techniques. Although conceived for operation in conjunction with microchip-based analysis systems, it should also work well with conductivity detectors developed for conventional capillary systems [159, 160].

It should be noted that the electronic circuits presented here comprise the complete set of modules necessary for performing contactless conductivity detection. No further instruments are required. This means that the detector electronics can be run on a floating, battery-driven power supply. This is especially interesting if very thin dielectric layers are used for electrode insulation [176, 177], since the risk of electrical breakdown is high when grounded measurement equipment is used in these instances. In this case, an optically decoupled data acquisition system as presented in the next chapter might be used to transfer the electropherogram data to a computer.

Furthermore, a new synchronous detection mode similar to lock-in detection has been applied to the demodulation of the AC-signal. The sensitivity in terms of signal-to-noise ratio of this demodulation technique was found to be ~10-fold higher than simple rectification as proposed in [159, 160]. Though probably inferior to commercial lock-in amplifiers, this technique allows the use of wider frequency ranges than most lock-in amplifiers provide at a considerably lower cost.

Chapter 8

Potential-Gradient Detection on Microchips

Potential-gradient detection is an interesting detection technique that combines the simplicity of direct-current, contact-mode methods with the stability of its alternating-current counter part. Briefly, two point electrodes inserted into the separation channel at its downstream end probe the voltage drop over the distance between the electrodes. This voltage is proportional to the electrolyte conductivity in the detector volume. Given that only a minute (<10^{-10} A) leakage current flows over the electrodes into the instrument, electrochemical reactions are largely prevented.

A glass-based microchip with integrated platinum electrodes (spacing of 30 µm) was developed to perform capillary electrophoresis with potential-gradient detection for amino acid samples using an indirect detection scheme. To improve the device sensitivity, modern low-bias current operational amplifiers and the possibility to perform analog-to-digital conversion within a single, electrically floating detector circuit were exploited. Data was continuously transferred to a computer via an optical, high-voltage compatible link. The limit of detection for arginine was determined to be 55 µM when a 32 mM sodium carbonate buffer was used as background electrolyte. This is in good agreement with similar results obtained for indirect fluorescence detection of amino acids on microchips.

8.1 Potential gradient detection

In contrast to the methods described in Chapters 5 and 7, potential-gradient detection (PGD) for capillary electrophoresis does not require an external source to provide the current for resistance measurement. Instead, the voltage drop caused by the separation current between two point-like metal electrodes in the capillary is monitored, as depicted in Figure 8-1. If the separation current remains constant, this voltage drop is proportional to the conductivity of the electrolyte in the detector volume between the two electrodes.

Assuming separation field strengths of 300 to 1000 V/cm and an electrode spacing of 30 µm, baseline voltages in the range of 0.9 to 3 V can be measured at the detector electrodes. However, as these voltage drops are superimposed on the high potential in the separation channel, a means of transforming the information into a low voltage for further processing and recording has to be conceived. The instrumentation for a potential-gradient detector therefore requires a high-impedance instrumentation amplifier to detect the voltage drop and a high-voltage isolation stage for further processing. For increased baseline stability it is advised to perform the CE separation in constant current mode. This is somewhat unusual, although it does not make a difference to the separation process itself.

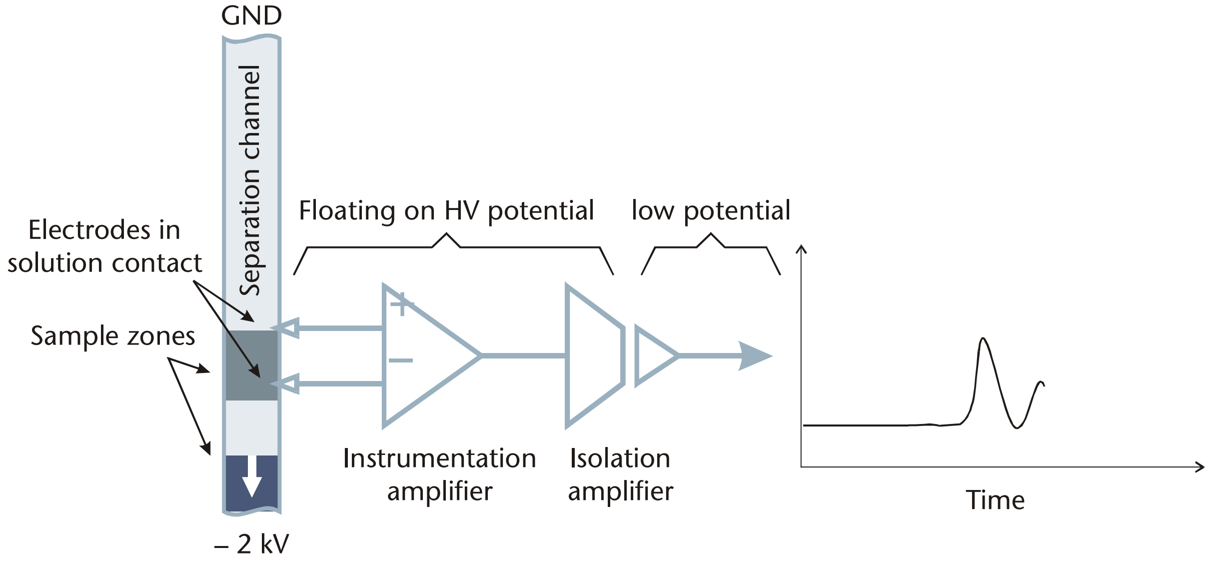

***Figure 8-1**: Potential gradient detection requires a high-impedance instrumentation amplifier to avoid electrode reactions and an isolation stage to deliver the measurement signal to the grounded data acquisition equipment.*

When PGD was introduced in the 70s [152, 203-205], circuits based on junction field-effect transistors, connected to behave like voltage dividers, were used to obtain a low-voltage signal. A different implementation used early, hybrid isolation amplifiers [152] based on analog optical links for HV decoupling. Commercial PGD systems are still frequently used, especially in isotachophoresis. For instance, Fukushi *et al.* reported on direct determination of tributyltin and triphenyltin cations by capillary isotachophoresis [206]. Prest *et al.* developed a single-electrode conductivity detector for microchip-based isotachophoresis, which is in the end a PG detector with the first electrode in the channel and the second placed in the buffer waste reservoir [182]. The disadvantage of this setup is the fairly large distance between the electrodes (5 mm for a separation channel length of 120 mm in total), which reduces the separation efficiency drastically.

In the framework of the research presented in this thesis, a new PG detector concept was developed for microchip-based CE devices. Compared to previous work published about the technique, advantage could be taken of recent developments in the field of analog and digital semiconductor devices. For example, new, high-impedance operational amplifiers allow operation at leakage currents equal to a few thousand electrons per second, thus reducing electrochemical transfer processes to a minimum. Also, electrically floating instruments with digital, optical data links do not compromise device accuracy and are comparatively easy to build.

8.1.1 High-impedance input stage for potential gradient detection

To avoid the adverse effects of electrode reactions described in Section 5.2.3, only a small leakage current in the range of a few hundred pA is allowed [152]. The input impedance of the instrumentation amplifier stage has thus to be greater than 10 GΩ. Although this was difficult to achieve when the technique was invented, today's operational amplifiers with field-effect-transistor input stages generally fulfill the requirement.

In the design presented here, an INA116 amplifier (Burr-Brown, now part of Texas Instruments, Dallas, TX, USA) was chosen, which performs a 1 to 1000-fold amplification and has an extremely low input bias current of typically 3 fA (corresponding to more than $300 \cdot 10^{12}$ Ω)[26]. These low currents can be achieved by advanced geometry, dielectrically-isolated field-effect transistor input stages as commercialized by Burr-Brown. An additional advantage of the INA116 is its high tolerance

---

[26] The datasheet is available at www.burr-brown.com.

to overvoltages at the input (± 40 V are permitted), which make the system more robust and capable of withstanding transient voltage spikes due to gas bubbles and the like. Figure 8-2 shows the input stage of the potential gradient detector on the left side.

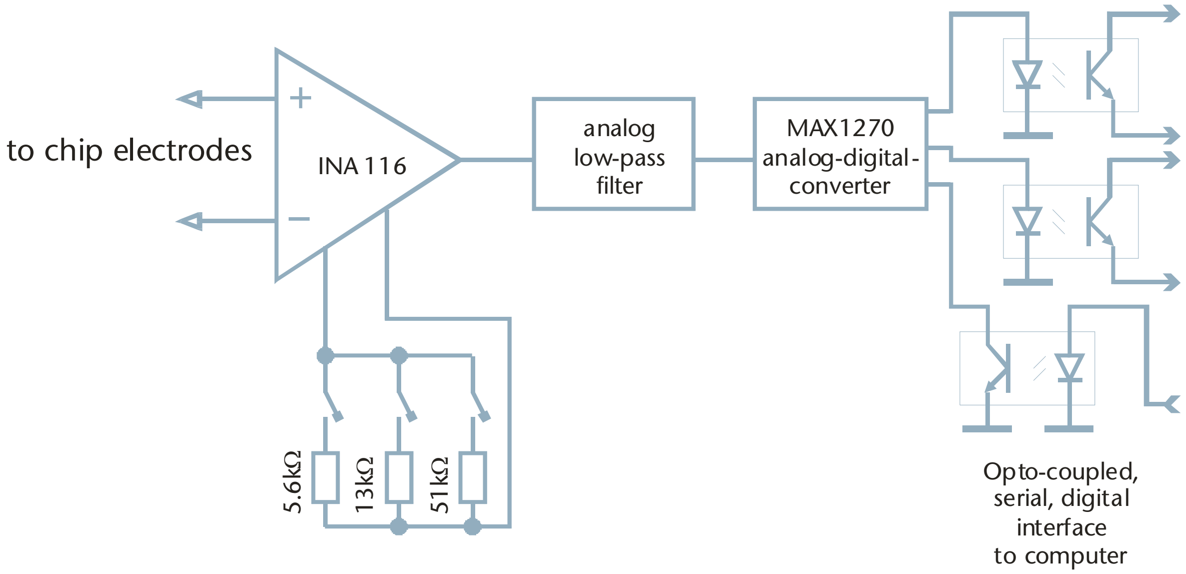

Figure 8-2: Schematic diagram of the floating potential gradient detector. The three resistors and corresponding switches determine the amplification factor of the instrumentation amplifier (1-fold, if all switches are open, 2-fold for the right switch closed, 5-fold for the middle switch, and 10-fold for the left one).

8.1.2 High-voltage isolation interface

The original implementations of this detection mode used either analog isolation amplifiers or buffered voltage dividers. In both cases, linearity and precision are low and the leakage currents over the probe electrodes fairly high. In the design presented here, the analog signal obtained from the instrumentation amplifier is directly converted into digital information by a 12-bit accuracy analog-to-digital converter (ADC) (MAX1270, Maxim, Sunnyvale, CA, USA)[27]. Both the instrumentation amplifier as well as the ADC are connected to a floating power supply, in this case a set of four 9V batteries with a voltage regulator to obtain a dual ±15 V output. This way, the detector electronics are not affected by the high potential in the separation channel as no external ground connection exists. **Note: As the instrument is electrically floating, all parts of the circuit before the optical link**

---

[27] The datasheet is available at www.maxim-ic.com

might be at a potential of several thousand volts and <u>must therefore never be exposed</u>.

Now, to be able to record the electropherograms using a computer, the digitized version of the detector signal has to be transmitted to a PC without a galvanic connection. To this end, an optocoupled interface was developed, which allows bi-directional digital data transfer between the detector electronics and a PC[28]. As the ADC MAX1270 delivers the digital information as a serial stream of bits, only four optical links had to be implemented for a full computer interface. The serial interface protocol is described schematically in Figure 8-3. The full schematic of the detector is included in the annex of this thesis.

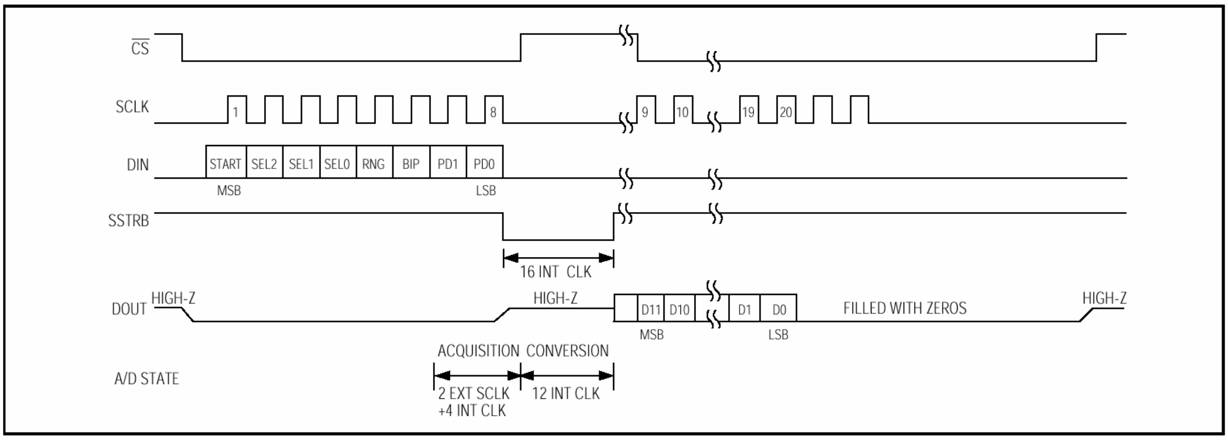

***Figure 8-3**: Serial communication protocol between computer and potential gradient detector. In the left half of the diagram, the computer sends a configuration byte to select the input channel and conversion mode of the ADC. Each bit is put sequentially onto the DIN line and validated by a pulse on the SCLK line. Once the byte is transmitted, a pulse on SSTRB initiates the AD conversion. 16 internal clock cycles later, the resulting 12-bit word can be sequentially read from the DOUT line.*

8.1.3 Chip fabrication

Microchips for CE with potential gradient detection were fabricated in a hybrid polymer/glass technology. The lower glass wafer contained 200-nm-thick platinum electrodes, which were deposited in recesses of the same depth to maintain

---

[28] The interface and the corresponding data acquisition software were developed by Stephan Beer (Masters student at IMT) during a semester project at IMT. His enthusiastic work is greatly appreciated.

an even surface profile. The detector electrodes are 30 µm wide, and are positioned perpendicular to the flow with a spacing of 30 µm. Microfluidic channels (50 µm wide and 20 µm deep) for sample plug formation and separation were formed in the poly(dimethylsiloxane) (PDMS) top wafer by casting onto a silicon master [31, 207]. The separation distance was 34 mm, side arms to the reservoirs were 9 mm long and the double-T type plug formation element [13, 47] had a length of 150 µm (Figure 8-4).

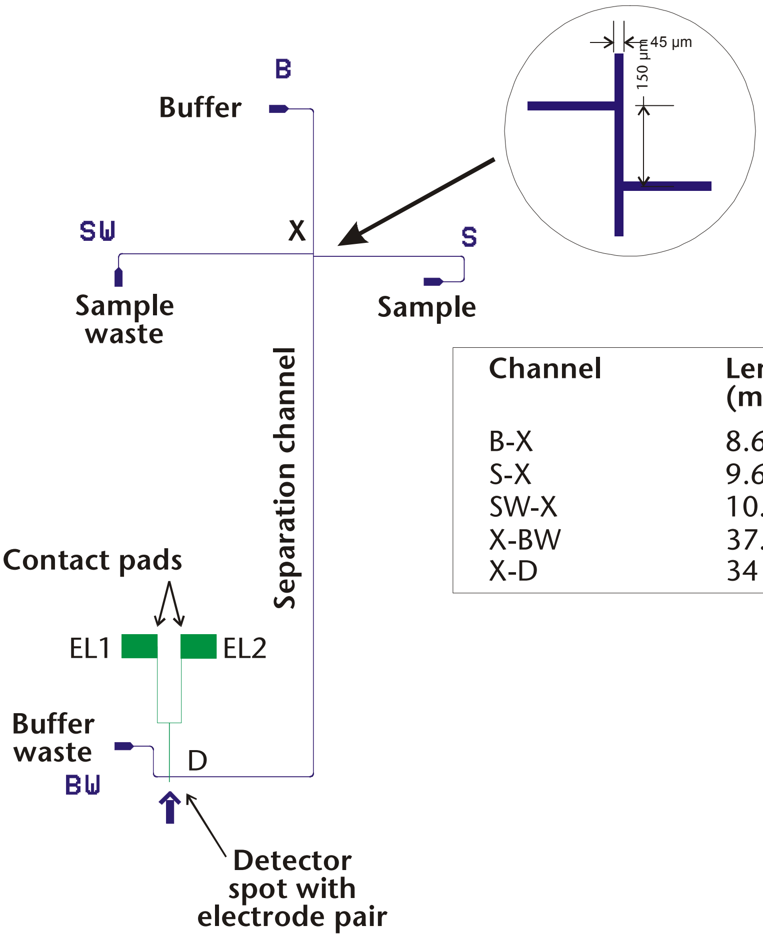

Channel	Length (mm)
B-X	8.6
S-X	9.6
SW-X	10.1
X-BW	37.5
X-D	34

Figure 8-4*: Layout of the PGD device. The detector is placed at a distance of 34 mm from the end of the double-T plug formation element. Copper wires were glued to the two metal pads by conductive glue to establish the connection with the read-out electronics.*

Platinum electrodes were fabricated on double-side polished 100-mm-diameter Pyrex 7740 glass wafers (SensorPrep Services, Elburn, IL, USA) in lift-off technology (see Figure 8-5). After cleaning, a 1.8-µm-thick layer of positive photoresist AZ1518 (Clariant AG, Muttenz, CH) was patterned as sacrificial layer. The lithography details are basically the same as those presented in Section 3.1, but after exposure the photoresist is specially conditioned for easy lift-off in organic solvents. To improve the solubility of the resist, no postbake is carried out in order

To improve the solubility of the resist, no postbake is carried out in order to keep the polymer from hardening. Furthermore, the photoresist surface was hardened chemically between exposure and development to create negative sidewall profiles preventing metal deposition on the walls. To do so, the wafers were immersed in chlorobenzene for 10 min before development [208].

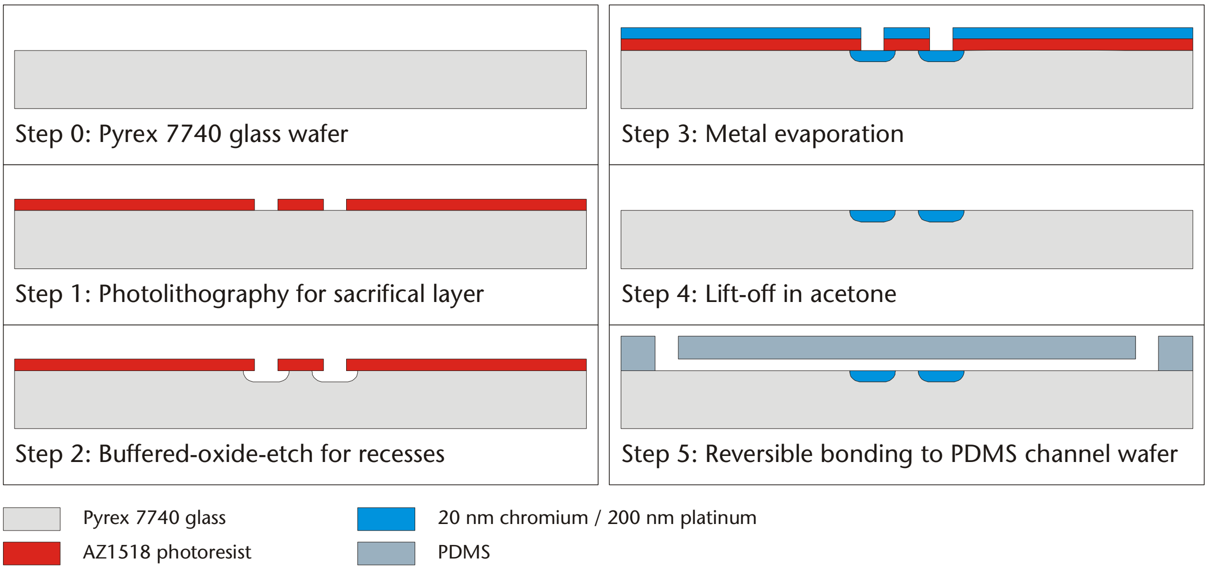

***Figure 8-5**: Process sequence for the fabrication of PDMS/glass hybrids with integrated electrodes for potential gradient detection.*

Once the photoresist was patterned, 220-nm-deep recesses were etched into the glass using a buffered-oxide-etch (BOE) solution (1 part 49% hydrofluoric acid and 7 parts 40% NH_4F, etch rate for Pyrex 7740 is ~40 nm/min). Here, the photoresist lift-off mask serves simultaneously as etching mask for the BOE etching step, thus avoiding an additional lithography process. Subsequently, a 20-nm-thick chromium adhesion layer was evaporated onto the wafers, followed by 200 nm of platinum. Finally, the metal layer was patterned by removing the photoresist in MOS-grade acetone under gentle agitation, thereby lifting off the metal on top. If necessary, a 1-min treatment in an ultrasonic bath was performed to remove residual metal particles.

For the fabrication of the microfluidic network, the negative profile of the channel structure was etched into a polished, 100-mm-diameter silicon wafer by deep reactive-ion etching (DRIE) [207]. A PDMS replica of this master wafer was fabricated by filling the mold to 5 mm height with the liquid Sylgard 184 monomer solution (Dow Corning, Midland, MI, USA) in its recommended mixing ratio. Curing was performed at 65 °C in a convection furnace for four hours. Finally, the PDMS replica was carefully peeled off the mold and could be reversibly bonded to the glass wafer containing the electrodes. Fluidic reservoirs for the microchannels and access holes to the measurement electrodes were made by punching holes into the elastomer wafer prior to bonding. Bonding was performed at room temperature, with no surface pretreatment on the glass or on the PDMS wafer to obtain a reversible seal. The PDMS wafer containing the channel network was aligned with the electrode wafer such that the electrode pairs crossed the channel at the detector site in a perpendicular fashion. A close-up of the detector electrodes is presented in Figure 8-6.

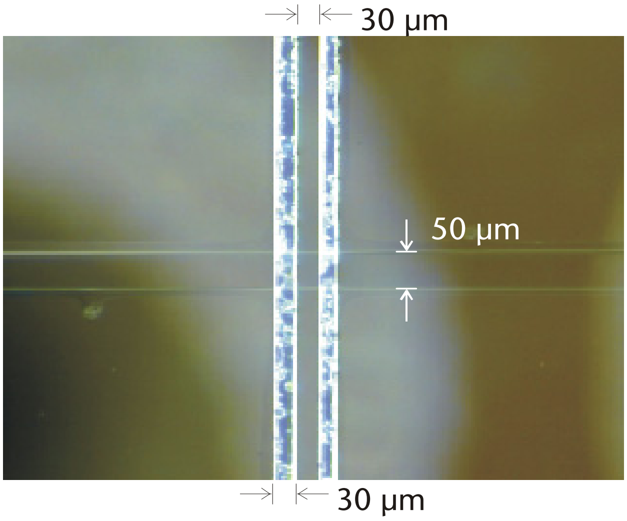

***Figure 8-6**: Two detector electrodes (vertical) intersect with the separation channel (horizontal).*

8.1.4 Experimental results

Figure 8-7 shows the electropherogram of a CE separation of sample containing 150 µM fluorescein-isothiocyanate-(FITC)-labeled arginine using the instrumentation described above (fluorescent labeling was performed for dual laser-induced fluorescence (LIF) and potential gradient detection). In this case, an indirect conductivity detection approach was chosen [139, 168, 209]: Instead of using a low-conductivity background electrolyte for the detection of highly mobile analytes, a high-conductivity buffer (32 mM carbonate, pH 9.6) was used to detect the less conductive amino acid. Therefore, the analytes appear as negative peaks on the electropherogram.

The limit of detection for arginine can be calculated from Figure 8-7 as 55 µM, which corresponds to three times the background noise. This is high compared to LIF but in the same range as chip-based, indirect LIF detection schemes (e.g. average detection limit of 32.9 µM for standard amino acids [125]). To further improve the sensitivity of the detector, different types of modification like shielding and filtering should be implemented. Also, the high-voltage power supply providing the separation voltage should be operated in constant current mode instead of constant voltage mode to increase the baseline stability of the detector.

As a second performance indicator for the PG detector, the separation efficiency can be deduced from the electropherogram in Figure 8-7. Assuming Gaussian peaks, the number of theoretical plates is [40]:

$$N = 5.54 \cdot \left(\frac{t}{w_{1/2}} \right)^2 \tag{54}$$

where t: migration time

$w_{1/2}$: temporal peak width at half height

The results for both peaks are represented in Table 10.

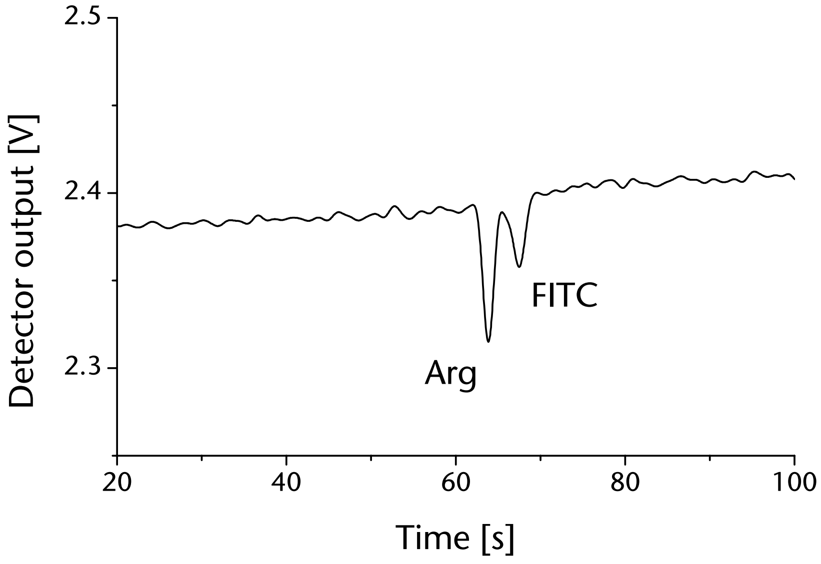

***Figure 8-7**: CE with potential gradient detection of a 150-µM sample of FITC-labeled arginine and residual FITC in 32 mM carbonate buffer, pH 9.6. The separation length was 34 mm, the separation field strength was 240 V/cm. The signal was additionally low-pass filtered by numeric averaging.*

Value	*Arginine*	*FITC*
Migration time (t)	*63.85 s*	*67.5 s*
Peak width at half height ($w_{1/2}$)	*1.25 s*	*1.45 s*
N	*14,500*	*12,000*
Theoretical plates per m	$430 \cdot 10^3$ m^{-1}	$350 \cdot 10^3$ m^{-1}

***Table 10**: Separation efficiency data for the PG detector.*

To estimate the spatial resolution of the detector, the theoretical maximum of *N* can be written as sum of the different band broadening sources involved during the separation [13]:

$$N_{\max} = \frac{L^2}{\sigma^2} \tag{55}$$

where L: separation length,

σ^2: sum of variances causing band broadening

Taking diffusion and the effects of both plug formation (injection) and detection into account, σ^2 becomes:

$$\begin{aligned} \sigma^2 &= \sigma^2_{diff} + \sigma^2_{inj} + \sigma^2_{det} \\ &= 2D_i t + \left(l^2_{inj}/12 + 2D_i t_{dl}\right) + \left(l^2_{det}/12\right) \end{aligned} \tag{56}$$

where D_i: diffusion coefficient of species i,

l_{inj}: plug length upon plug formation,

t_{dl}: delay time between start of the plug formation and start of the separation,

l_{det}: length of the detection window

Effects due to delayed detector response (caused for instance by low-pass filtering) are generally about two orders of magnitude lower than the other sources, and are therefore neglected in this discussion. Based on the diffusion data for FITC-labeled arginine in [13] ($D_{Arg}=3.9 \cdot 10^{-6}$ cm^2/s), σ^2_{diff} becomes $4.98 \cdot 10^{-4}$ cm^2 and σ^2_{inj} becomes $1.95 \cdot 10^{-4}$ cm^2 for a plug length of 150 µm and a delay time of 25 s. Solving Equation 55 for σ^2 assuming the number of theoretical plates for arginine in Table 10, an total variance of σ^2=8·10^{-4} cm^2 is obtained. The variance due to the detector is therefore:

$$\sigma_{det}^2 = \sigma^2 - \sigma_{diff}^2 - \sigma_{inj}^2 \tag{57}$$

For the values calculated above, σ^2_{det} becomes 1.07·10^{-4} cm^2. Now, l_{det} can be calculated by:

$$l_{det} = \sqrt{12\sigma_{det}^2} \tag{58}$$

Combining these results, a value for l_{det} of 350 µm can be calculated. This, however, differs by nearly a factor of 4 from the expected value of 90 µm, which is equal to the distance between the two outer edges of the detection electrodes. Then again, it has to be noted that the calculation in general is approximate as many factors have been left out, e. g. the increased plug dispersion due a 90° turn prior to the detection point.

8.2 Conclusion

A new microchip-based capillary electrophoresis device with an integrated potential-gradient detector has been presented and preliminarily characterized. Both the microfabrication of the integrated platinum electrode pairs as well as the hybrid construction of the microfluidic system are standard techniques widely used in the field. Furthermore, the use of platinum as electrode material and the buried fabrication of the metal structures allow the base substrate to be sealed with a microfluidic network etched into a glass wafer, using high-temperature fusion bonding. Recent literature [210, 211] indicates that such a device made entirely from glass will have an increased stability and reagent compatibility.

Within the short time frame available for evaluation and testing of the detector, both the chips and the detector electronics worked very reliably. The input protection of the high-impedance operational amplifier withstood even small bubbles which passed the detector after insufficient priming of the separation channel and caused voltage spikes.

The limit of detection obtained for the indirect conductivity detection of amino acids is comparable to competing label-free techniques such as indirect fluorescence detection, with the added advantage that no external optics and excitation sources are necessary. Furthermore, the background buffer was not optimized for a high displacement ratio (also called transfer ratio) during the initial experiments; it is this ratio that determines how many background buffer molecules (or added fluorophore molecules in the case of indirect fluorescence detection) are replaced by an analyte molecule [140]. High displacement ratios and a high difference in molar conductivity between buffer and analyte result in low detection limits. For this particular case, improved results are expected once optimization of these parameters has been carried out.

Compared to other conductivity detection techniques, PGD has the disadvantage of a direct electrolyte contact, which ultimately limits the device lifetime. At the same time, however, the fabrication of the microfluidic device is more inexpensive than for instance that of the device presented in Chapter 4. PGD could therefore be an especially interesting solution for disposable µTAS with integrated conductivity detection. Finally, focusing on the instrumentation side, the fact that PGD works in DC mode facilitates the construction of the whole analysis system in terms of shielding and protection against external interferences.

Chapter 9

Conclusion and Outlook

With the goal of small ion analysis in mind, a prototype of a microchip capillary electrophoresis (CE) device has been developed based on a new, integrated, in-plane, contactless conductivity detector (CCD). The device allows fast separation of inorganic anions and cations in the range of 20 s with a total analysis time, including injection, of around one minute. The microfabrication process developed in the context of this thesis makes it possible to easily integrate CCDs with standard glass and polymer micromachining. It also allows the placement of the electrodes close to the separation channel independent of the substrate type, which is a requirement for good detector sensitivity and spatial (i.e. separation) resolution.

To increase the sensitivity of the device, field-amplified sample stacking (FASS) was studied as a technique for sample preconcentration. In order to visualize the microfluidic phenomena involved in stacking, the technique was performed using fluorescently labeled amino acids as analyte. These studies gave important insight into the effect of induced pressure flows in electrokinetically driven devices, in particular those generated during the stacking process. It was also possible for the first time to capture a stacking experiment on video. Signal enhancement due to the preconcentration of up to 95-fold could be obtained by a new on-chip, coupled-column technique. The (technically less complex) stacking of 400-µm-long sample plugs showed a 20-fold increase in peak height. FASS was then deployed in a microchip containing a CCD. A 4-fold signal enhancement for K^+ was achieved by stacking of a 150-µm-long sample plug. It is assumed that longer sample plugs containing a larger amount of the analyte would increase the enhancement factor further.

As an alternative to CCD, a new potential-gradient detector (PGD) was developed. Though this device also distinguishes between analyte zones based on their conductivity, it requires direct electrolyte contact to detect the potential difference between two closely spaced platinum electrodes. Although the detector lifetime will be shorter than that of a CCD, due to electrochemical degradation of the electrodes, preliminary results indicated a very high sensitivity of the device. For the indirect conductivity detection, the microchip CE-PGD device can even compete with more complex methods such as indirect laser-induced fluorescence detection.

Finally, this thesis presented the technical aspects involved in designing mechanical hardware and electronic instruments for microfluidic device operation. Two designs for specially adapted, multi-electrode high-voltage power supplies, electronics for current and voltage monitoring, a laser-induced fluorescence setup as well as analog filters for noise reduction during detection were developed.

While working on this thesis, a number of directions interesting for further investigation became apparent. For instance, in order to further increase the sample loading capability of the FASS technique based on sweeping, one could take advantage of the freedom that the column-coupling approach offers. While keeping the CE separation channel short and its cross-section small in order to achieve a good separation performance, the stacking channel could be etched deeper to increase its volume. A number of multi-level etching techniques for glass and silicon have been developed at IMT for different applications, and could be employed here. These techniques use two different, structured mask layer materials (e.g. polysilicon and photoresist or polysilicon and chrome/gold), which allow etching to two depths without the obligation of performing a photolithography on an already structured substrate.

For the CCD, a thorough numerical analysis based on the finite element method should be performed for a better understanding of the underlying principles and for design optimization. Once this has been achieved, the device has promising prospects not only for conductivity detection per se, but also for other applications. Amongst those are, for instance, temperature measurements based on the temperature dependence of the electrical conductivity. While it is probably difficult to measure the conductivity as an absolute value (due to the influence of a number of additional parameters), relative measurements are possible as described in Section 5.9.3.

Contactless flowrate measurement of a liquid is one interesting application of this relative conductivity measurement. The idea proposed here is based on the "time-of-flight" measurement of a heated plug of liquid between the up-stream heater and a down-stream temperature sensor (Figure 9-1). If heater and sensor are placed in close proximity to each other, the heated plug will not have transferred all its heat to the surrounding capillary walls by the time it arrives at the sensor. The resulting, transient temperature change at the sensor when the plug passes can then be recorded. The time elapsed since the short heating pulse was applied is an absolute measure of linear flow velocity v (in m/s):

$$v = \frac{d_{el}}{t_{of}} \tag{59}$$

where d_{el}: distance between heater and temperature (i.e. σ) sensor (m)

t_{of}: time between application of the heating pulse and arrival of the heated plug at the sensor

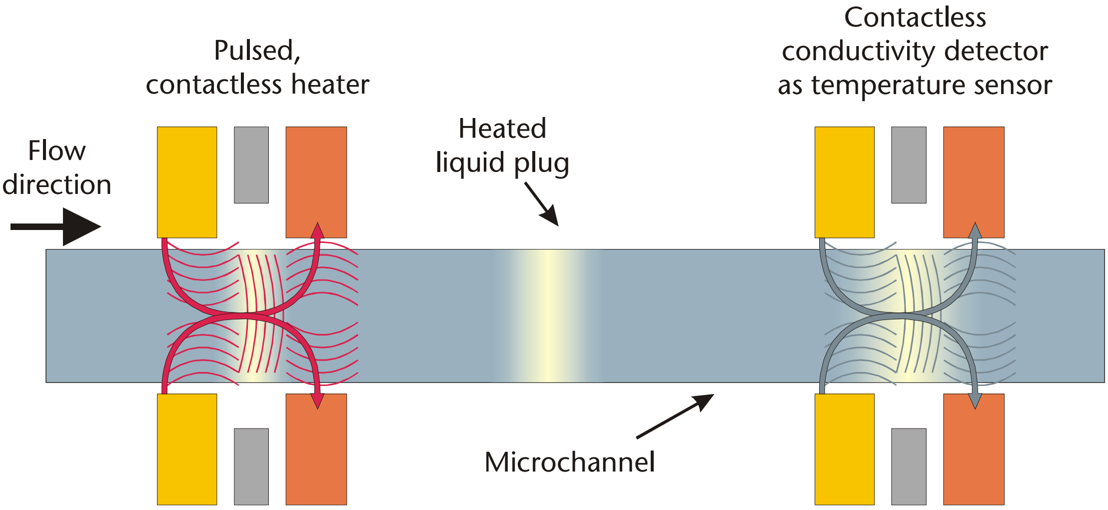

***Figure 9-1**: Schematic of the proposed thermal time-of-flight flow sensor with a pulsed heater on the upstream side (left) and a temperature sensor downstream.*

The striking feature of this design is the fact that the flowrate measurement works precisely and independent of the physical properties of the liquid. Therefore, the device does not need to be calibrated for the liquids used, as it is the case for differential pressure flowrate sensors (dependent on liquid viscosity and temperature) or hot filament sensors (dependent on thermal conductivity and capacitance of the liquid). It is also interesting to note that the CCD device presented in this thesis could also fulfill the role of the heater, by inducing a relatively high AC current pulse perpendicular to the channel. This might require fairly high voltages (a few 100 volt), which can, however, be easily achieved keeping in mind the miniaturized high-voltage source described in Chapter 2. This contactless heating procedure also assures short heating pulses as the Joule energy is deployed directly in the electrolyte. As an alternative application, contactless Joule heating might also be of interest for other temperature control problems, such as miniaturized polymerase chain reactors or the like.

The subjects touched in this theses cover a range of aspects including separation science, microfabrication, and electronic instrumentation. Combined, they build the basis of a miniaturized system for chemical ion analysis, targeted chiefly at water analysis. It is my sincere hope that the research presented in this thesis is of value for the future development of the microfluidics field.

Chapter 10

Glossary

Latin Symbols	Description
A	Surface (m^2)
A_v	Transfer function (for electronic filters)
c	Concentration (M)
C	Capacitance (F)
D	Diffusion constant (cm^2/s)
E	Electric field strength (V/cm)
E_a	Activation energy (J)
f	Frequency (Hz)
f_c	Cut-off frequency of a filter (Hz)
F	Faraday's constant (92,495 C/mol)
G	Conductance (S)
i	Current (A)
I	Ionic strength (mol/kg)
k	Boltzmann constant ($1.38 \cdot 10^{-23}$ J/K)
L	Length (m)
N	Number of theoretical plates
P	Pressure (Pa)
q	Charge (C)
r	Radius (m)
R	Universal gas constant (8.31 J/kmol)
R	Electrical resistance (Ω)
t	Time (s)
T	Temperature (K)
v	Velocity (cm/s)
V	Voltage (V)
X	Impedance (Ω)
z	Valence

Greek Symbols	Description
ϕ	Phase (°)
Λ	Molar (equivalent) conductivity ($S \cdot m^2/mol$)
ε	Dielectric constant (permittivity) ($C^2/N\text{-}m^2$)
γ	Relative conductivity and relative field strength
η	Viscosity (poise)
κ	Debye-Hückel parameter (m^{-1})
μ_{eo}	Electro-osmotic mobility ($cm^2/V\text{-}s$)
μ_{ep}	Electrophoretic mobility ($cm^2/V\text{-}s$)
μ_i	Observed mobility ($=\mu_{eo}+\mu_{ep}$) ($cm^2/V\text{-}s$)
ρ	Electrical resistivity (Ω-cm)
ρ	Mass density (g/cm^3)
σ	Specific volume conductivity (S/m)
σ_s	Surface charge (C/m^2)
σ^2	Variance of separation peaks (cm^2)
τ	Period
ω	Angular frequency (Hz)
ζ	Zeta potential (V)

Subscripts	Description
H	High-field strength zone
i, j	Species type
L	Low-field strength zone

Abbreviation	**Description**
AC	Alternating current
BGE	Background electrolyte
BOE	Buffer oxide etch
CCD	Contactless conductivity detection
CE	Capillary electrophoresis
CEC	Capillary electrochromatography
CTAB	Cetyl trimethyl ammonium bromide
DC	Direct current
DRIE	Deep reactive-ion etching
EK	Electrokinetic
EOF	Electro-osmotic flow
FAI	Field-amplification injection
FASS	Field-amplification sample stacking
His	L-histidine
HV	High voltage
ITP	Isotachophoresis
LIF	Laser-induced fluorescence
LOD	Limit of detection
LPCVD	Low-pressure vapor deposition
MES	2-(N-morpholino)-ethane sulphonic acid
PGD	Potential-gradient detection
PDMS	Poly(dimethyl)siloxane
RIE	Reactive-ion etching
RMS	Root-mean-square
SC	Switched-capacitor
TAS	Total analysis system

Chapter 11

References

[1] G. E. Moore, "Cramming more components onto integrated circuits", *Electronics*, vol. 38, pp. 114-117, 1965.

[2] M. J. Madou, "Beyond moore's law" in *Fundamentals of microfabrication : The science of miniaturization*, 2nd ed. Boca Raton, Florida: CRC Press, 2002, pp. 44-47.

[3] S. C. Jacobson, C. T. Culbertson, J. E. Daler, and J. M. Ramsey, "Microchip structures for submillisecond electrophoresis", *Analytical Chemistry*, vol. 70, pp. 3476-3480, 1998.

[4] A. Manz, D. J. Harrison, E. M. J. Verpoorte, J. C. Fettinger, A. Paulus, H. Ludi, and H. M. Widmer, "Planar chips technology for miniaturization and integration of separation techniques into monitoring systems - capillary electrophoresis on a chip", *Journal of Chromatography*, vol. 593, pp. 253-258, 1992.

[5] A. T. Woolley, G. F. Sensabaugh, and R. A. Mathies, "High-speed DNA genotyping using microfabricated capillary array electrophoresis chips", *Analytical Chemistry*, vol. 69, pp. 2181-2186, 1997.

[6] P. C. Simpson, D. Roach, A. T. Woolley, T. Thorsen, R. Johnston, G. F. Sensabaugh, and R. A. Mathies, "High-throughput genetic analysis using microfabricated 96-sample capillary array electrophoresis microplates", *Proceedings of the National Academy of Sciences of the United States of America*, vol. 95, pp. 2256-2261, 1998.

[7] C. A. Emrich, H. Tian, I. L. Medintz, and R. A. Mathies, "Microfabricated 384-lane capillary array electrophoresis bioanalyzer for ultra high-throughput genetic analysis", *Analytical Chemistry*, vol. 74, pp. 5076-5083, 2002.

[8] H. M. Widmer, "Trends in industrial analytical chemistry", *Trends Anal. Chem.*, vol. 2, pp. VIII-X, 1983.

[9] A. Manz, N. Graber, and H. M. Widmer, "Miniaturized total chemical-analysis systems - a novel concept for chemical sensing", *Sensors and Actuators B*, vol. 1, pp. 244-248, 1990.

[10] K. Seiler, D. J. Harrison, and A. Manz, "Planar glass chips for capillary electrophoresis - repetitive sample injection, quantitation, and separation efficiency", *Analytical Chemistry*, vol. 65, pp. 1481-1488, 1993.

[11] D. J. Harrison, K. Fluri, K. Seiler, Z. H. Fan, C. S. Effenhauser, and A. Manz, "Micromachining a miniaturized capillary electrophoresis-based chemical analysis system on a chip", *Science*, vol. 261, pp. 895-897, 1993.

[12] D. J. Harrison, A. Manz, Z. H. Fan, H. Ludi, and H. M. Widmer, "Capillary electrophoresis and sample injection systems integrated on a planar glass chip", *Analytical Chemistry*, vol. 64, pp. 1926-1932, 1992.

[13] C. S. Effenhauser, A. Manz, and H. M. Widmer, "Glass chips for high-speed capillary electrophoresis separations with submicrometer plate heights", *Analytical Chemistry*, vol. 65, pp. 2637-2642, 1993.

[14] S. C. Jacobson, R. Hergenröder, L. B. Koutny, and J. M. Ramsey, "High-speed separations on a microchip", *Analytical Chemistry*, vol. 66, pp. 1114-1118, 1994.

[15] G. T. A. Kovacs, *Micromachined transducers sourcebook*. New York: McGraw-Hill, 1998.

[16] Z. H. Fan and D. J. Harrison, "Micromachining of capillary electrophoresis injectors and separators on glass chips and evaluation of flow at capillary intersections", *Analytical Chemistry*, vol. 66, pp. 177-184, 1994.

[17] E. Verpoorte, "Microfluidic chips for clinical and forensic analysis", *Electrophoresis*, vol. 23, pp. 677-712, 2002.

[18] S. C. Terry, J. H. Jerman, and J. B. Angel, "A gas chromatographic air analyzer fabricated on a silicon wafer", *IEEE Trans. Electron. Devices*, vol. 26, pp. 1880-1887, 1979.

[19] A. Manz, Y. Miyahara, J. Miura, Y. Watanabe, H. Miyagi, and K. Sato, "Design of an open-tubular column liquid chromatograph using silicon chip technology", *Sensors and Actuators B*, vol. 1, pp. 249-255, 1990.

[20] D. J. Harrison, P. G. Glavina, and A. Manz, "Towards miniaturized electrophoresis and chemical-analysis systems on silicon - an alternative to chemical sensors", *Sensors and Actuators B*, vol. 10, pp. 107-116, 1993.

[21] E. M. J. Verpoorte, B. H. van der Schoot, S. Jeanneret, A. Manz, H. M. Widmer, and N. F. de Rooij, "Three-dimensional micro flow manifolds for minaturized chemical analysis systems", *Journal of Micromechanics and Microengineering*, vol. 4, pp. 246-256, 1994.

[22] D. E. Raymond, A. Manz, and H. M. Widmer, "Continuous sample pretreatment using a free-flow electrophoresis device integrated onto a silicon chip", *Analytical Chemistry*, vol. 66, pp. 2858-2865, 1994.

[23] G. Ocvirk, E. Verpoorte, A. Manz, M. Grasserbauer, and H. M. Widmer, "High performance liquid chromatography partially integrated onto a silicon chip", *Analytical Methods and Instrumentation*, vol. 2, pp. 74-82, 1995.

[24] S. C. Jacobson, A. W. Moore, and J. M. Ramsey, "Fused quartz substrates for microchip electrophoresis", *Analytical Chemistry*, vol. 67, pp. 2059-2063, 1995.

[25] K. Fluri, G. Fitzpatrick, N. Chiem, and D. J. Harrison, "Integrated capillary electrophoresis devices with an efficient postcolumn reactor in planar quartz and glass chips", *Analytical Chemistry*, vol. 68, pp. 4285-4290, 1996.

[26] H. Becker, K. Lowack, and A. Manz, "Planar quartz chips with submicron channels for two-dimensional capillary electrophoresis applications", *Journal of Micromechanics & Microengineering*, pp. 24-28, 1998.

[27] P. C. Simpson, A. T. Wooley, and R. A. Mathies, "Microfabrication technology for the production of capillary array electrophoresis chips", *Biomedical Microdevices*, vol. 1, pp. 7-26, 1998.

[28] K. E. Petersen, "Silicon as a mechanical material", *Proceedings of the IEEE*, vol. 70, pp. 420-457, 1982.

[29] H. Becker and C. Gärtner, "Polymer microfabrication methods for microfluidic analytical applications", *Electrophoresis*, vol. 21, pp. 12-26, 2000.

[30] D. C. Duffy, J. C. McDonald, O. J. A. Schueller, and G. M. Whitesides, "Rapid prototyping of microfluidic systems in poly(dimethylsiloxane)", *Analytical Chemistry*, vol. 70, pp. 4974-4984, 1998.

[31] J. C. McDonald, D. C. Duffy, J. R. Anderson, D. T. Chiu, H. Wu, O. J. A. Schueller, and G. M. Whitesides, "Fabrication of microfluidic systems in poly(dimethylsiloxane) [review]", *Electrophoresis*, vol. 21, pp. 27-40, 2000.

[32] F. Kohlrausch, *Wiedemanns Ann.*, vol. 62, pp. 209, 1897.

[33] J. W. Jorgenson and K. D. Lukacs, "Zone electrophoresis in open tubular glass capillaries", *Analytical Chemistry*, vol. 53, pp. 1298-1302, 1981.

[34] J. W. Jorgenson and K. D. Lukacs, "Free-zone electrophoresis in glass capillaries", *Clinical Chemistry*, vol. 27, pp. 1551-3, 1981.

[35] J. W. Jorgenson and K. D. Lukacs, "Capillary zone electrophoresis", *Science*, vol. 222, pp. 266-272, 1983.

[36] S. Hjertén, "Free zone electrophoresis", *Chromatographic Reviews*, vol. 9, pp. 122-219, 1967.

[37] R. Virtanen, "Zone electrophoresis in a narrow-bore tube employing potentiometric detection - theoretical and experimental study", *Acta Polytechnica Scandinavica - Chemical Technology Series*, vol. 123, pp. 1-67, 1974.

[38] F. E. P. Mikkers, F. M. Everearts, and T. P. E. M. Verheggen, "High-performance zone electrophoresis", *Journal of Chromatography*, vol. 169, pp. 11-20, 1979.

[39] P. D. Grossman and J. C. Colburn, *Capillary electrophoresis : Theory & practice*. San Diego: Academic Press, 1992.

[40] D. R. Baker, *Capillary electrophoresis*. New York: John Wiley & Sons, Inc., 1995.

[41] J. P. Landers, *Handbook of capillary electrophoresis*, 2nd ed. Boca Raton: CRC Press, 1997.

[42] S. Valsecchi, G. Tartari, and S. Polesello, "Determination of anions in rainwater by capillary electrophoresis with conductivity detection", *Journal of Chromatography A*, vol. 760, pp. 326-332, 1997.

[43] S. M. Valsecchi and S. Polesello, "Analysis of inorganic species in environmental samples by capillary electrophoresis", *Journal of Chromatography, A*, vol. 834, pp. 363-385, 1999.

[44] J. Farre, F. Borrull, and M. Calull, "Application of capillary electrophoresis in the quality control of osmotically treated water", *Chromatographia*, vol. 44, pp. 235-239, 1997.

[45] A. R. Timerbaev, "Metal-ion analysis by capillary electrophoresis - new possibilities in separation and detection", *Journal of Capillary Electrophoresis*, vol. 2, pp. 14-23, 1995.

[46] C. Haber, R. J. VanSaun, and W. R. Jones, "Quantitative analysis of anions at ppb/ppt levels with capillary electrophoresis and conductivity detection: Enhancement of system linearity and precision using an internal standard", *Analytical Chemistry*, vol. 70, pp. 2261-2267, 1998.

[47] S. C. Jacobson, R. Hergenröder, L. B. Koutny, R. J. Warmack, and J. M. Ramsey, "Effects of injection schemes and column geometry on the performance of microchip electrophoresis devices", *Analytical Chemistry*, vol. 66, pp. 1107-1113, 1994.

[48] L. L. Shultz-Lockyear, C. L. Colyer, Z. H. Fan, K. I. Roy, and D. J. Harrison, "Effects of injector geometry and sample matrix on injection and sample loading in integrated capillary electrophoresis devices", *Electrophoresis*, vol. 20, pp. 529-538, 1999.

[49] J. Lichtenberg, N. F. de Rooij, and E. Verpoorte, "Sample pretreatment on microfabricated devices", *Talanta*, vol. 56, pp. 233-266, 2002.

[50] S. C. Jacobson, R. Hergenröder, A. W. Moore, and J. M. Ramsey, "Precolumn reactions with electrophoretic analysis integrated on a microchip", *Analytical Chemistry*, vol. 66, pp. 4127-4132, 1994.

[51] S. C. Jacobson, L. B. Koutny, R. Hergenröder, A. W. Moore, and J. M. Ramsey, "Microchip capillary electrophoresis with an integrated postcolumn reactor", *Analytical Chemistry*, vol. 66, pp. 3472-3476, 1994.

[52] J. P. Kutter, R. S. Ramsey, S. C. Jacobson, and J. M. Ramsey, "Determination of metal cations in microchip electrophoresis using on-chip complexation and sample stacking", *Journal of Microcolumn Separations*, vol. 10, pp. 313–319, 1998.

[53] Y. Liu, R. S. Foote, S. C. Jacobson, R. S. Ramsey, and J. M. Ramsey, "Electrophoretic separation of proteins on a microchip with noncovalent, postcolumn labeling", *Analytical Chemistry*, vol. 72, pp. 4608-4613, 2000.

[54] B. He, L. Tan, and F. E. Regnier, "Microfabricated filters for microfluidic analytical systems", *Analytical Chemistry*, vol. 71, pp. 1464-1468, 1999.

[55] J. P. Brody and P. Yager, "Diffusion-based extraction in a microfabricated device", *Sensors and Actuators A*, vol. 58, pp. 13-18, 1997.

[56] A. T. Woolley, D. Hadley, P. Landre, A. J. Demello, R. A. Mathies, and M. A. Northrup, "Functional integration of pcr amplification and capillary electrophoresis in a microfabricated DNA analysis device", *Analytical Chemistry*, vol. 68, pp. 4081-4086, 1996.

[57] E. T. Lagally, I. Medintz, and R. A. Mathies, "Single-molecule DNA amplification and analysis in an integrated microfluidic device", *Analytical Chemistry*, vol. 73, pp. 565-570, 2001.

[58] L. C. Waters, S. C. Jacobson, N. Kroutchinina, J. Khandurina, R. S. Foote, and J. M. Ramsey, "Microchip device for cell lysis, multiplex pcr amplification, and electrophoretic sizing", *Analytical Chemistry*, vol. 70, pp. 158-162, 1998.

[59] L. C. Waters, S. C. Jacobson, N. Kroutchinina, J. Khandurina, R. S. Foote, and J. M. Ramsey, "Multiple sample pcr amplification and electrophoretic analysis on a microchip", *Analytical Chemistry*, vol. 70, pp. 5172-5176, 1998.

[60] S. C. Jacobson and J. M. Ramsey, "Integrated microdevice for DNA restriction fragment analysis", *Analytical Chemistry*, vol. 68, pp. 720-723, 1996.

[61] J. Li, C. Wang, J. F. Kelly, D. J. Harrison, and P. Thibault, "Rapid and sensitive separation of trace level protein digests using microfabricated devices coupled to a quadrupole-time-of- flight mass spectrometer", *Electrophoresis*, vol. 21, pp. 198-210, 2000.

[62] J. Lichtenberg, E. Verpoorte, and N. F. de Rooij, "Sample preconcentration by field amplification stacking for microchip-based capillary electrophoresis", *Electrophoresis*, vol. 22, pp. 258-271, 2001.

[63] H. Yang and R.-L. Chien, "Sample stacking in laboratory-on-a-chip devices", *Journal of Chromatography A*, vol. 924, pp. 155–163, 2001.

[64] J. Palmer, D. S. Burgi, N. J. Munro, and J. P. Landers, "Electrokinetic injection for stacking neutral analytes in capillary and microchip electrophoresis", *Analytical Chemistry*, vol. 73, pp. 725-731, 2001.

[65] A. Daridon, M. Sequeira, G. Pennarun-Thomas, H. Dirac, J. P. Krog, P. Gravesen, J. Lichtenberg, D. Diamond, E. Verpoorte, and N. F. de Rooij, "Chemical sensing using an integrated microfluidic system based on the berthelot reaction", *Sensors and Actuators B*, vol. 76, pp. 235-243, 2001.

[66] A. Daridon, V. Fascio, J. Lichtenberg, R. Wütrich, H. Langen, E. Verpoorte, and N. F. de Rooij, "Multi-layer microfluidic glass chips for microanalytical applications", *Fresenius Journal of Analytical Chemistry*, vol. 371, pp. 261-269, 2001.

[67] J.-C. Roulet, R. Völkel, H. P. Herzig, E. Verpoorte, N. F. de Rooij, and R. Dändliker, "Performance of an integrated micro-optical system for fluorescence detection in microfluidic systems", *Analytical Chemistry*, vol. 74, pp. 3400-3407, 2002.

[68] J. R. Webster, M. A. Burns, D. T. Burke, and C. H. Mastrangelo, "Monolithic capillary electrophoresis device with integrated fluorescence detector", *Analytical Chemistry*, vol. 73, pp. 1622-1626, 2001.

[69] M. L. Chabinyc, D. T. Chiu, J. C. McDonald, A. D. Stroock, J. F. Christian, A. M. Karger, and G. M. Whitesides, "An integrated fluorescence detection system in poly(dimethylsiloxane) for microfluidic applications", *Analytical Chemistry*, vol. 73, pp. 4491-4498, 2001.

[70] S. C. Jacobson, S. V. Ermakov, and J. M. Ramsey, "Minimizing the number of voltage sources and fluid reservoirs for electrokinetic valving in microfluidic devices", *Analytical Chemistry*, vol. 71, pp. 3273-3276, 1999.

[71] X. H. Huang, M. J. Gordon, and R. N. Zare, "Current-monitoring method for measuring the electroosmotic flow rate in capillary zone electrophoresis", *Analytical Chemistry*, vol. 60, pp. 1837-1838, 1988.

[72] J.-C. Roulet, R. Völkel, H. P. Herzig, E. Verpoorte, N. F. de Rooij, and R. Dändliker, "Fabrication of multilayer systems combining microfluidic and microoptical elements for fluorescence detection", *Journal of Microelectromechanical Systems*, vol. 10, pp. 482-491, 2001.

[73] H. Whatley, "Making ce work - points to consider", *LC-GC*, vol. 17, pp. 426-432, 1999.

[74] B. X. Mayer and M. Muller, "Long-term analyses with capillary electrophoresis", *LC-GC*, vol. 18, pp. 694-700, 2000.

[75] Y. Liu, J. C. Fanguy, J. M. Bledsoe, and C. S. Henry, "Dynamic coating using polyelectrolyte multilayers for chemical control of electroosmotic flow in capillary electrophoresis microchips", *Analytical Chemistry*, vol. 72, pp. 5939-5944, 2000.

[76] B. C. Giordano, E. R. Copeland, and J. P. Landers, "Towards dynamic coating of glass microchip chambers for amplifying DNA via the polymerase chain reaction", *Electrophoresis*, vol. 22, pp. 334-340, 2001.

[77] J. E. Melanson, N. E. Baryla, and C. A. Lucy, "Dynamic capillary coatings for electroosmotic flow control in capillary electrophoresis", *Trends in Analytical Chemistry*, vol. 20, pp. 365-374, 2001.

[78] J. Horvath and V. Dolnik, "Polymer wall coatings for capillary electrophoresis", *Electrophoresis*, vol. 22, pp. 644-655, 2001.

[79] P. G. Righetti, C. Gelfi, B. Verzola, and L. Castelletti, "The state-of-the-art of dynamic coatings", *Electrophoresis*, vol. 22, pp. 603-611, 2001.

[80] M. A. Gretillat, F. Paoletti, P. Thiebaud, S. Roth, M. Koudelka-Hep, and N. F. de Rooij, "A new fabrication method for borosilicate glass capillary tubes with lateral inlets and outlets", *Sensors and Actuators A*, vol. 60, pp. 219-222, 1997.

[81] A. J. Ji, M. F. Nunez, D. Machacek, J. E. Ferguson, M. F. Iossi, P. C. Kao, and J. P. Landers, "Separation of urinary estrogens by micellar electrokinetc chromatography", *Journal of Chromatography B*, vol. 669, pp. 15-26, 1995.

[82] P. T. Kissinger and W. R. Heineman, *Laboratory techniques in electroanalytical chemistry*, 2nd , rev. and expanded, ed. New York: Marcel Dekker Inc., 1996.

[83] R. L. Chien and D. S. Burgi, "On-column sample concentration using field amplification in cze", *Analytical Chemistry*, vol. 64, pp. A489-A496, 1992.

[84] D. Ross and L. E. Locascio, "Microfluidic temperature gradient focusing", *Analytical Chemistry*, vol. 74, pp. 2556-2564, 2002.

[85] A. E. Herr, J. I. Molho, J. G. Santiago, M. G. Mungal, T. W. Kenny, and M. G. Garguilo, "Electroosmotic capillary flow with nonuniform zeta potential", *Analytical Chemistry*, vol. 72, pp. 1053-1057, 2000.

[86] M. A. Hayes and A. G. Ewing, "Electroosmotic flow control and monitoring with an applied radial voltage for capillary zone electrophoresis", *Analytical Chemistry*, vol. 64, pp. 512-516, 1992.

[87] R.-L. Chien and J. C. Helmer, "Electroosmotic properties and peak broadening in field-amplified capillary electrophoresis", *Analytical Chemistry*, vol. 63, pp. 1354–1361, 1991.

[88] D. S. Burgi and R.-L. Chien, "Optimization of sample stacking for high-performance capillary electrophoresis", *Analytical Chemistry*, vol. 63, pp. 2042–2047, 1991.

[89] D. S. Burgi and R.-L. Chien, "Application of sample stacking to gravity injection in capillary electrophoresis", *Journal of Microcolumn Separations*, vol. 3, pp. 199–202, 1991.

[90] C. X. Zhang and W. Thormann, "Head-column field-amplified sample stacking in binary system capillary electrophoresis: A robust approach providing over 1000-fold sensitivity enhancement", *Analytical Chemistry*, vol. 68, pp. 2523-2532, 1996.

[91] C. X. Zhang and W. Thormann, "Head-column field-amplified sample stacking in binary system capillary electrophoresis. 2. Optimization with a preinjection plug and application to micellar electrokinetic chromatography", *Analytical Chemistry*, vol. 70, pp. 540-548, 1998.

[92] A. B. Wey and W. Thormann, "Head-column field-amplified sample stacking in binary-system capillary electrophoresis. The need for the water plug", *Chromatographia*, vol. 49, pp. S12-S20, 1999.

[93] R.-L. Chien and D. S. Burgi, "Sample stacking of an extremely large injection volume in high-performance capillary electrophoresis", *Analytical Chemistry*, vol. 64, pp. 1046–1050, 1992.

[94] M. Albert, L. Debusschere, C. Demesmay, and J. L. Rocca, "Large-volume stacking for quantitative analysis of anions in capillary electrophoresis. I. Large-volume stacking with polarity switching", *Journal of Chromatography A*, vol. 757, pp. 281-289, 1997.

[95] S. Pálmarsdóttir and L.-E. Edholm, "Enhancement of selectivity and concentration sensitivity in capillary zone electrophoresis by online coupling with column liquid-chromatography and utilizing a double stacking procedure allowing for microliter injections", *Journal of Chromatography*, vol. 693, pp. 131–143, 1995.

[96] D. S. Burgi, "Large volume stacking of anions in capillary electrophoresis using an electroosmotic flow modifier as pump", *Analytical Chemistry*, vol. 65, pp. 3726–3729, 1993.

[97] M. Albert, L. Debusschere, C. Demesmay, and J. L. Rocca, "Large-volume stacking for quantitative analysis of anions in capillary electrophoresis. Ii. Large-volume stacking without polarity switching", *Journal of Chromatography A*, vol. 757, pp. 291-296, 1997.

[98] S. C. Jacobson and J. M. Ramsey, "Microchip electrophoresis with sample stacking", *Electrophoresis*, vol. 16, pp. 481-486, 1995.

[99] A. Wainright, S. J. Williams, G. Ciambrone, Q. Xue, J. Wei, and D. Harris, "Sample pre-concentration by isotachophoresis in microfluidic devices", *Journal of Chromatography A*, vol. 979, pp. 69-80, 2002.

[100] D. Kaniansky, M. Masar, J. Bielcikova, F. Ivanyi, F. Eisenbeiss, B. Stanislawski, B. Grass, A. Neyer, and M. Johnck, "Capillary electrophoresis separations on a planar chip with the column-coupling configuration of the separation channels", *Analytical Chemistry*, vol. 72, pp. 3596-3604, 2000.

[101] J. Khandurina, S. C. Jacobson, L. C. Waters, R. S. Foote, and J. M. Ramsey, "Microfabricated porous membrane structure for sample concentration and electrophoretic analysis", *Analytical Chemistry*, vol. 71, pp. 1815-1819, 1999.

[102] J. Khandurina, T. E. McKnight, S. C. Jacobson, L. C. Waters, R. S. Foote, and J. M. Ramsey, "Integrated system for rapid pcr-based DNA analysis in microfluidic devices", *Analytical Chemistry*, vol. 72, pp. 2995-3000, 2000.

[103] A. T. Conlisk, J. McFerran, Z. Zheng, and D. Hansford, "Mass transfer and flow in electrically charged micro- and nanochannels", *Analytical Chemistry*, vol. 74, pp. 2139-2150, 2002.

[104] J. M. Ramsey, J. P. Alarie, S. C. Jacobson, and N. J. Peterson, "Molecular transport through nanometer confined channels", *Proceedings of the μTAS 2002 Symposium*, Nara, Japan 2001; Kluwer Academic Publishers; pp. 314-316.

[105] Y.-C. Lin, H.-C. Ho, C.-K. Tseng, and S.-Q. Hou, "A poly-methylmethacrylate electrophoresis microchip with sample preconcentrator", *Journal of Micromechanics and Microengineering*, vol. 11, pp. 189–194, 2001.

[106] J. P. Kutter, S. C. Jacobson, and J. M. Ramsey, "Solid phase extraction on microfluidic devices", *Journal of Microcolumn Separations*, vol. 12, pp. 93-97, 2000.

[107] R. D. Oleschuk, L. L. Shultz-Lockyear, Y. Ning, and D. J. Harrison, "Trapping of bead-based reagents within microfluidic systems: On-chip solid-phase extraction and electrochromatography", *Analytical Chemistry*, vol. 72, pp. 585-590, 2000.

[108] D. Figeys and R. Aebersold, "Nanoflow solvent gradient delivery from a microfabricated device for protein identifications by electrospray ionization mass spectrometry", *Analytical Chemistry*, vol. 70, pp. 3721-3727, 1998.

[109] B. M. Paegel, L. D. Hutt, P. C. Simpson, and R. A. Mathies, "Turn geometry for minimizing band broadening in microfabricated capillary electrophoresis channels", *Analytical Chemistry*, vol. 72, pp. 3030-3037, 2000.

[110] J. I. Molho, A. E. Herr, B. P. Mosier, J. G. Santiago, T. W. Kenny, R. A. Brennen, G. B. Gordon, and B. Mohammadi, "Optimization of turn geometries for microchip electrophoresis", *Analytical Chemistry*, vol. 73, pp. 1350-1360, 2001.

[111] B. B. VanOrman, G. G. Liversidge, G. L. McIntire, T. M. Olefirowicz, and A. G. Ewing, "Effects of buffer composition on electroosmotic flow in capillary electrophoresis", *Journal of Microcolumn Separations*, vol. 2, pp. 176–180, 1990.

[112] G. J. M. Bruin, J. P. Chang, R. H. Kuhlman, K. Zegers, J. C. Kraak, and H. Poppe, "Capillary zone electrophoretic separations of proteins in polyethylene glycol-modified capillaries", *Journal of Chromatography*, vol. 471, pp. 429-436, 1989.

[113] D. J. Harrison, C. Wang, P. Thibault, F. Ouchen, and S. B. Cheng, "The decade's search for the killer ap in µtas", Enschede 2000; Kluwer Academic Publishers; pp. 195–204.

[114] A. Dodge, K. Fluri, E. Verpoorte, and N. F. de Rooij, "Electrokinetically driven microfluidic chips with surface modified chambers for heterogeneous immunoassays", *Analytical Chemistry*, vol. 73, pp. 3400-3409, 2001.

[115] L.-M. Fu, R.-J. Yang, G.-B. Lee, and H.-H. Liu, "Electrokinetic injection techniques in microfluidic chips", *Analytical Chemistry*, vol. 74, pp. 5084-5091, 2002.

[116] A. Manz, D. J. Harrison, E. M. J. Verpoorte, and H. M. Widmer, "Planar chips technology for miniaturization of separation systems: A developing perspective in chemical monitoring," in *Advances in chromatography*, vol. 33, P. R. Brown and E. Grushka, Eds. New York, Basel, Hong Kong: Marcel Dekker, Inc., 1993, pp. 1-65.

[117] G. J. M. Bruin, "Recent developments in electrokinetically driven analysis on microfabricated devices", *Electrophoresis*, vol. 21, pp. 3931-3951, 2000.

[118] D. R. Reyes, D. Iossifidis, P. A. Auroux, and A. Manz, "Micro total analysis systems. 1. Introduction, theory, and technology", *Analytical Chemistry*, vol. 74, pp. 2623-2636, 2002.

[119] P. A. Auroux, D. Iossifidis, D. R. Reyes, and A. Manz, "Micro total analysis systems. 2. Analytical standard operations and applications", *Analytical Chemistry*, vol. 74, pp. 2637-2652, 2002.

[120] G. Ocvirk, T. Tang, and D. J. Harrison, "Optimization of confocal epifluorescence microscopy for microchip-based miniaturized total analysis systems", *Analyst*, vol. 123, pp. 1429-1434, 1998.

[121] G. F. Jiang, S. Attiya, G. Ocvirk, W. E. Lee, and D. J. Harrison, "Red diode laser induced fluorescence detection with a confocal microscope on a microchip for capillary electrophoresis", *Biosensors & Bioelectronics*, vol. 14, pp. 861-869, 2000.

[122] J. C. Fister, S. C. Jacobson, L. M. Davis, and J. M. Ramsey, "Counting single chromophore molecules for ultrasensitive analysis and separations on microchip devices", *Analytical Chemistry*, vol. 70, pp. 431-437, 1998.

[123] B. B. Haab and R. A. Mathies, "Single-molecule detection of DNA separations in microfabricated capillary electrophoresis chips employing focused molecular streams", *Analytical Chemistry*, vol. 71, pp. 5137-5145, 1999.

[124] B. L. Hogan and E. S. Yeung, "Determination of intracellular species at the level of a single erythrocyte via capillary electrophoresis with direct and indirect fluorescence detection", *Analytical Chemistry*, vol. 64, pp. 2841-2845, 1992.

[125] N. J. Munro, Z. Huang, D. N. Finegold, and J. P. Landers, "Indirect fluorescence detection of amino acids on electrophoretic microchips", *Analytical Chemistry*, vol. 72, pp. 2765-2773, 2000.

[126] S. Sirichai and A. J. de Mello, "A capillary electrophoresis chip for the analysis of print and film photographic developing agents in commercial processing solutions using indirect fluorescence detection", *Electrophoresis*, vol. 22, pp. 348-354, 2001.

[127] N. Burggraf, B. Krattiger, A. J. de Mello, N. F. de Rooij, and A. Manz, "Holographic refractive index detector for application in microchip-based separation systems", *Analyst*, vol. 123, pp. 1443-1447, 1998.

[128] N. A. Lacher, K. E. Garrison, R. S. Martin, and S. M. Lunte, "Microchip capillary electrophoresis/electrochemistry", *Electrophoresis*, vol. 22, pp. 2526-2536, 2001.

[129] M. A. Schwarz and P. C. Hauser, "Recent developments in detection methods for microfabricated analytical devices", *Lab on a Chip*, vol. 1, pp. 1–6, 2001.

[130] A. J. Zemann, "Conductivity detection in capillary electrophoresis", *Trends in Analytical Chemistry*, vol. 20, pp. 346-354, 2001.

[131] P. W. Atkins, *Physical chemistry*, 6th ed. New York: Freeman, 1998.

[132] R. A. Robinson and R. H. Stokes, *Electrolyte solutions : The measurement and interpretation of conductance, chemical potential and diffusion in solutions of simple electrolytes*, 2nd ed ed. London, England: Butterworths Scientific Publications, 1959.

[133] H. Small, T. S. Stevens, and W. C. Bauman, "Novel ion exchange chromatographic method using conductimetric detection", *Analytical Chemistry*, vol. 47, pp. 1801–1809, 1975.

[134] X. Huang and R. N. Zare, "Improved end-column detector for capillary zone electrophoresis", *Analytical Chemistry*, vol. 63, pp. 2193–2196, 1991.

[135] X. Huang, T.-K. J. Pang, M. J. Gordon, and R. N. Zare, "On-column conductivity detector for capillary zone electrophoresis", *Analytical Chemistry*, vol. 59, pp. 2747–2749, 1987.

[136] X. Huang, J. A. Luckey, M. J. Gordon, and R. N. Zare, "Quantitative analysis of low molecular weight carboxylic acids by capillary zone electrophoresis / conductivity detection", *Analytical Chemistry*, vol. 59, pp. 2747–2749, 1989.

[137] X. Huang, R. N. Zare, S. Sloss, and A. G. Ewing, "End-column detection for capillary zone electrophoresis", *Analytical Chemistry*, vol. 63, pp. 189–192, 1991.

[138] C. A. Lucy and Q. Wu, "Characteristics and calibration of conductivity detection in capillary electrophoresis", *Journal of Chromatography Science*, vol. 36, pp. 33-36, 1998.

[139] P. A. Gallagher and N. D. Danielson, "Capillary electrophoresis of cationic and anionic surfactants with indirect conductivity detection", *Journal of Chromatography A*, vol. 781, pp. 533–540, 1997.

[140] E. S. Yeung and W. G. Kuhr, "Indirect detection methods for capillary electrophoresis", *Analytical Chemistry*, vol. 63, pp. 275A-282A, 1991.

[141] X. Huang, M. J. Gordon, and R. N. Zare, *Journal of Chromatography*, vol. 480, pp. 285–288, 1989.

[142] P. Jandik and G. Bonn, *Capillary electrophoresis of small molecules and ions*. New York, NY: Vch, 1993.

[143] N. E. Good, G. D. Winget, W. Winter, T. N. Connolly, S. Izawa, and R. M. M. Singh, "Hydrogen buffer for biological research", *Biochemistry*, vol. 5, pp. 467–477, 1966.

[144] W. J. Ferguson, K. I. Braunschweiger, W. R. Braunschweiger, J. R. Smith, J. J. McCormick, C. C. Wasmann, N. P. Jarvis, D. H. Bell, and N. E. Good, "Hydrogen-ion buffers for biological research", *Analytical Biochemistry*, vol. 104, pp. 300–310, 1980.

[145] M. Horká and K. Šlais, "Low-conductivity background electrolytes in capillary zone electrophoresis - myth or reality?" *Electrophoresis*, vol. 21, pp. 2814-2827, 2000.

[146] S. Blanco, M. J. Clifton, J. L. Joly, and G. Peltre, "Protein separation by electrophoresis in a nonsieving amphoteric medium", *Electrophoresis*, vol. 17, pp. 1126-1133, 1996.

[147] S. Hjertén, L. Valtcheva, K. Elenbring, and J. L. Liao, "Fast, high-resolution (capillary) electrophoresis in buffers designed for high field strengths", *Electrophoresis*, vol. 16, pp. 584-594, 1995.

[148] P. K. Dasgupta and L. Bao, *Analytical Chemistry*, vol. 65, pp. 1003, 1993.

[149] N. Avdalovic, C. A. Pohl, R. D. Rocklin, and J. R. Stillian, "Determination of cations and anions by capillary electrophoresis combined with suppressed conductivity detection", *Analytical Chemistry*, vol. 65, pp. 1470-1475, 1993.

[150] J. J. Carr, *Sensors and circuits : Sensors, transducers, and supporting circuits for electronic instrumentation, measurement, and control*. Englewood Cliffs, N.J.: PTR Prentice Hall, 1993.

[151] R. Pallás-Areny and J. G. Webster, *Sensors and signal conditioning*, 2nd ed. New York: J. Wiley, 2001.

[152] F. M. Everaerts, J. L. Beckers, and T. P. E. M. Verheggen, *Isotachophoresis : Theory, instrumentation, and applications*. Amsterdam ; New York: Elsevier Scientific Pub. Co., 1976.

[153] D. Kaniansky, M. Koval', and S. Stankoviansky, "Simple cell for conductimetric detection in capillary isotachophoresis", *Journal of Chromatography A*, vol. 267, pp. 67-73, 1983.

[154] H. Zhao, R. Dadoo, R. J. Reay, G. T. A. Kovacs, and R. N. Zare, "Electrically floating conductivity detection system for capillary electrophoresis", *Journal of Chromatography A*, vol. 813, pp. 205-208, 1998.

[155] P. Bocek, *Analytical isotachophoresis*. Weinheim, Federal Republic of Germany ; New York, NY, USA: Vch, 1988.

[156] B. Gaš, M. Demjanenko, and J. Vacik, "High-frequency contactless conductivity detection in isotachophoresis", *Journal of Chromatography*, vol. 192, pp. 253-257, 1980.

[157] J. C. Reijenga, H. J. Slaats, and F. M. Everaerts, "Determination of conjugated bile acids in human bile by isotachophoresis in a non-aqueous solvent using a.C. Conductivity and uv detection", *Journal of Chromatography*, vol. 267, pp. 85-89, 1983.

[158] J. Vacik, J. Zuska, and I. Muselasova, "Improvement of the performance of a high-frequency contactless conductivity detector for isotachophoresis", *Journal of Chromatography*, vol. 320, pp. 233-240, 1985.

[159] A. J. Zemann, E. Schnell, D. Volgger, and G. K. Bonn, "Contactless conductivity detection for capillary electrophoresis", *Analytical Chemistry*, vol. 70, pp. 563-567, 1998.

[160] J. A. F. da Silva and C. L. do Lago, "An oscillometric detector for capillary electrophoresis", *Analytical Chemistry*, vol. 70, pp. 4339-4343, 1998.

[161] H. V. Malmstadt, C. G. Enke, and S. R. Crouch, *Electronics and instrumentation for scientists*. Menlo Park, California: The Benjamin/Cummings Publishing Company, Inc., 1981.

[162] L. K. Baxter, *Capacitive sensors : Design and applications*. New York: IEEE Press, 1997.

[163] K. Mayrhofer, A. J. Zemann, E. Schnell, and G. K. Bonn, "Capillary electrophoresis and contactless conductivity detection of ions in narrow inner diameter capillaries", *Analytical Chemistry*, vol. 71, pp. 3828-3833, 1999.

[164] J. A. F. da Silva and C. L. do Lago, "Conductivity detection of aliphatic alcohols in micellar electrokinetic chromatography using an oscillometric detector", *Electrophoresis*, vol. 21, pp. 1405–1408, 2000.

[165] J. A. da Silva, N. Guzman, and C. L. do Lago, "Contactless conductivity detection for capillary electrophoresis. Hardware improvements and optimization of the input-signal amplitude and frequency", *Journal of Chromatography A*, vol. 942, pp. 249-58, 2002.

[166] J. Tanyanyiwa, B. Galliker, M. A. Schwarz, and P. C. Hauser, "Improved capacitively conductivity detector for capillary electrophoresis", *The Analyst*, vol. 127, pp. 214-218, 2002.

[167] E. Baltussen, R. M. Guijt, G. van der Steen, F. Laugere, S. Baltussen, and G. W. K. van Dedem, "Considerations on contactless conductivity detection in capillary electrophoresis", *Electrophoresis*, vol. 23, pp. 2888-2893, 2002.

[168] P. Kuban, B. Karlberg, and V. Kuban, "Application of a contactless conductometric detector for the simultaneous determination of small anions and cations by capillary electrophoresis with dual-opposite end injection", *Journal of Chromatography A*, vol. 964, pp. 227-41, 2002.

[169] V. Unterholzner, M. Macka, P. R. Haddad, and A. Zemann, "Simultaneous separation of inorganic anions and cations using capillary electrophoresis with a movable contactless conductivity detector", *Analyst*, vol. 127, pp. 715-8, 2002.

[170] B. Graß, A. Neyer, M. Jöhnck, D. Siepe, F. Eisenbeiß, G. Weber, and R. Hergenröder, "A new pmma-microchip device for isotachophoresis with integrated conductivity detector", *Sensors and Actuators B*, vol. 72, pp. 249-258, 2001.

[171] J. E. Prest, S. J. Baldock, P. R. Fielden, and B. J. Brown, "Determination of metal cations on miniaturised planar polymeric separation devices using isotachophoresis with integrated conductivity detection", *Analyst*, vol. 126, pp. 433-437, 2001.

[172] M. Galloway, W. Stryjewski, A. Henry, S. M. Ford, S. Llopis, R. L. McCarley, and S. A. Soper, "Contact conductivity detection in poly(methyl methacrylate)-based microfluidic devices for analysis of mono- and polyanionic molecules", *Analytical Chemistry*, vol. 74, pp. 2407-15, 2002.

[173] R. M. Guijt, E. Baltussen, G. van der Steen, H. Frank, H. Billiet, T. Schalkhammer, F. Laugere, M. Vellekoop, A. Berthold, L. Sarro, and G. W. van Dedem, "Capillary electrophoresis with on-chip four-electrode capacitively coupled conductivity detection for application in bioanalysis", *Electrophoresis*, vol. 22, pp. 2537-2541, 2001.

[174] Y. Liu, D. O. Wipf, and C. S. Henry, "Conductivity detection for monitoring mixing reactions in microfluidic devices", *Analyst*, vol. 126, pp. 1248-51, 2001.

[175] H. E. Ayliffe, A. B. Frazier, and R. D. Rabbitt, "Electric impedance spectroscopy using microchannels with integrated metal electrodes", *Journal of Microelectromechanical Systems*, vol. 8, pp. 50-57, 1999.

[176] F. Laugere, G. W. Lubking, J. Bastemeijer, and M. J. Vellekoop, "Design of an electronic interface for capacitively coupled four-electrode conductivity detection in capillary electrophoresis microchip", *Sensors and Actuators B*, vol. 83, pp. 104–108, 2002.

[177] J. Bastemeijer, W. Lubking, F. Laugere, and M. Vellekoop, "Electronic protection methods for conductivity detectors in micro capillary electrophoresis devices", *Sensors and Actuators B*, vol. 83, pp. 98–103, 2002.

[178] J. Lichtenberg, E. Verpoorte, and N. F. de Rooij, "Operating parameters for an in-plane, contactless conductivity detector for microchip-based separation methods", *Proceedings of the µTAS 2001 Symposium*, Monterey 2001; Kluwer Academic Publishers; pp. 323-324.

[179] J. Lichtenberg, E. Verpoorte, and N. F. de Rooij, "A miniaturized analysis system based on capillary electrophoresis and contactless conductivity detection", *Proceedings of the Transducers '01*, Munich 2001; pp. 408-411.

[180] J. Lichtenberg, N. F. de Rooij, and E. Verpoorte, "A microchip electrophoresis system with integrated in-plane electrodes for contactless conductivity detection", *Electrophoresis*, vol. 23, pp. 3769-3780, 2002.

[181] M. Pumera, J. Wang, F. Opekar, I. Jelinek, J. Feldman, H. Löwe, and S. Hardt, "Contactless conductivity detector for microchip capillary electrophoresis", *Analytical Chemistry*, vol. 74, pp. 1968-71, 2002.

[182] J. E. Prest, S. J. Baldock, N. Bektas, P. R. Fielden, and B. J. T. Brown, "Single electrode conductivity detection for electrophoretic separation systems", *Journal of Chromatography A*, vol. 836, pp. 59-65, 1999.

[183] R. S. Martin, A. J. Gawron, S. M. Lunte, and C. S. Henry, "Dual-electrode electrochemical detection for poly(dimethylsiloxane)-fabricated capillary electrophoresis microchips", *Analytical Chemistry*, vol. 72, pp. 3196-3202, 2000.

[184] J. C. Fanguy and C. S. Henry, "The analysis of uric acid in urine using microchip capillary electrophoresis with electrochemical detection", *Electrophoresis*, vol. 23, pp. 767-773, 2002.

[185] D. E. Johnson, *Electric circuit analysis*, 3rd ed. Upper Saddle River, N.J.: Prentice Hall, 1997.

[186] L. T. Pillage, R. A. Rohrer, and C. Visweswariah, *Electronic circuit and system simulation methods*. New York: McGraw-Hill, 1995.

[187] A. J. Bard and L. R. Faulkner, *Electrochemical methods–fundamentals and applications*, 2nd ed. New York: John Wiley & Sons, 2000.

[188] P. Horowitz and W. Hill, *The art of electronics*, 2nd ed. New York: Cambridge University Press, 1989.

[189] M. L. Meade, *Lock-in amplifiers : Principles and applications*. Stevenage: Peregrinus, 1983.

[190] A. Dodge, G. Turcatti, I. Lawrence, N. F. d. Rooij, and E. Verpoorte, "Thermal dehybridization of surface-bound DNA in a microfluidic device for nucleic acid analysis", *submitted.*

[191] K. Fukushi, S. Takeda, K. Chayama, and S. Wakida, "Application of capillary electrophoresis to the analysis of inorganic ions in environmental samples", *Journal of Chromatography A*, vol. 834, pp. 349–362, 1999.

[192] J. Sadecka and J. Polonsky, "Determination of inorganic ions in food and beverages by capillary electrophoresis", *Journal of Chromatography, A*, vol. 834, pp. 401-417, 1999.

[193] J. Sadecka and J. Polonsky, "Electrophoretic methods in the analysis of beverages", *Journal of Chromatography, A*, vol. 880, pp. 243-279, 2000.

[194] R. G. Kelly, J. Yuan, C. M. Weyant, and K. S. Lewis, "Applications of capillary electrophoresis in corrosion science and engineering", *Journal of Chromatography, A*, vol. 834, pp. 433-444, 1999.

[195] J. Wang, M. Pumera, G. Collins, F. Opekar, and I. Jelinek, "A chip-based capillary electrophoresis-contactless conductivity microsystem for fast measurements of low-explosive ionic components", *Analyst*, vol. 127, pp. 719-23., 2002.

[196] R. Bodor, V. Madajova, D. Kaniansky, M. Masar, M. Jöhnck, and B. Stanislawski, "Isotachophoresis and isotachophoresis-zone electrophoresis separations of inorganic anions present in water samples on a planar chip with column-coupling separation channels and conductivity detection", *Journal of Chromatography A*, vol. 916, pp. 155-65., 2001.

[197] M. Masar, D. Kaniansky, R. Bodor, M. Jöhnck, and B. Stanislawski, "Determination of organic acids and inorganic anions in wine by isotachophoresis on a planar chip", *Journal of Chromatography A*, vol. 916, pp. 167-74., 2001.

[198] R. Bodor, M. Zuborova, E. Olvecka, V. Madajova, M. Masar, D. Kaniansky, and B. Stanislawski, "Isotachophoresis and isotachophoresis-zone electrophoresis of food additives on a chip with column-coupling separation channels", *Journal of Separation Science*, vol. 24, pp. 802-809, 2001.

[199] M. Zuborova, M. Masar, D. Kaniansky, M. Jöhnck, and B. Stanislawski, "Determination of oxalate in urine by zone electrophoresis on a chip with conductivity detection", *Electrophoresis*, vol. 23, pp. 774-781, 2002.

[200] A. R. Timerbaev and W. Buchberger, "Prospects for detection and sensitivity enhancement of inorganic ions in capillary electrophoresis", *Journal of Chromatography, A*, vol. 834, pp. 117-132, 1999.

[201] R. M. Guijt, E. Baltussen, G. van der Steen, R. B. Schasfoort, S. Schlautmann, H. A. Billiet, J. Frank, G. W. van Dedem, and A. van den Berg, "New approaches for fabrication of microfluidic capillary electrophoresis devices with on-chip conductivity detection", *Electrophoresis*, vol. 22, pp. 235-41, 2001.

[202] J. M. Jacob, *Applications and design with analog integrated circuits*, 2nd ed. Englewood Cliffs, N.J.: Regents/Prentice Hall, 1993.

[203] F. M. Everaerts and T. P. E. M. Verheggen, "High-resolution isotachophoresis by means of direct conductivity measurements with miniature sensing electrodes", *Journal of Chromatography*, vol. 73, pp. 193, 1972.

[204] F. M. Everaerts and T. P. E. M. Verheggen, "Isotachophoresis - applications in biochemical field", *Journal of Chromatography*, vol. 91, pp. 837-851, 1974.

[205] J. Akiyama and T. Mizuno, "Sensitivity of a newly designed potential gradient detector for isotachophoresis", *Journal of Chromatography A*, vol. 119, pp. 605–608, 1976.

[206] K. Fukushi, K. Sagishima, K. Saito, S. Takeda, S.-i. Wakida, and K. Hiiro, "Simultaneous determination of tributyltin and triphenyltin cations by capillary isotachophoresis with potential-gradient detector for direct detection", *Analytica Chimica Acta*, vol. 383, pp. 205–211, 1999.

[207] L. Ceriotti, N. F. de Rooij, and E. Verpoorte, "An integrated fritless column for on-chip capillary electrochromatography with conventional stationary phases", *Analytical Chemistry*, vol. 74, pp. 639-647, 2002.

[208] M. Hatzakis, B. J. Canavello, and J. M. Shaw, "Single-step optical lift-off process", *IBM Jounal of Research and Development*, vol. 24, pp. 452-460, 1980.

[209] G. Schill and J. Crommen, "Indirect detection in high-performance liquid chromatography", *Trends in Analytical Chemistry*, vol. 6, pp. 111–116, 1987.

[210] V. Linder, E. Verpoorte, W. Thormann, N. F. de Rooij, and H. Sigrist, "Surface biopassivation of replicated poly(dimethylsiloxane) microfluidic channels and application to heterogeneous immunoreaction with on-chip fluorescence detection", *Analytical Chemistry*, vol. 73, pp. 4181-4189, 2001.

[211] G. Ocvirk, M. Munroe, T. Tang, R. Oleschuk, K. Westra, and D. J. Harrison, "Electrokinetic control of fluid flow in native poly(dimethylsiloxane) capillary electrophoresis devices", *Electrophoresis*, vol. 21, pp. 107-115, 2000.

Chapter 12

Acknowledgements

When I arrived in Neuchâtel on a cold Wednesday morning in October 1998, I started a new diary, whose pages filled quickly with recollections of marvelous moments and new friendships. It was not an easy decision to leave my home in the north of Germany and to move to a location quite far from old friends and family, but it was a very good one. Living in Neuchâtel, this lively city between the lake and the mountains, was a great experience that I will never want to miss.

Working in Prof. Nico de Rooij's group at the Institute of Microtechnology was surely the best time of my professional life. The atmosphere in his team is a perfect mixture of motivation and friendship seasoned with an excellent infrastructure, which makes working at IMT a pleasure. Thanks so much, Nico, for giving me the opportunity of being part of the Samlab team and to pursue my PhD under your direction.

What I have learned about microfluidics, I have learned from my supervisor Dr. Elisabeth Verpoorte, who accepted me as one of her first PhD students. Sabeth, for your dedication to our team, your guidance of my research work, the many hours you spent on my papers and abstracts, and for your friendship I am deeply indebted. Thanks for everything, including the great barbecues we had in your place overlooking the lake from your porch.

I also gratefully acknowledge Prof. Andreas Manz, of the Centre of Analytical Chemistry at the Imperial College in London, and Prof. Pierre-André Farine, of the Institute of Microtechnology at the University of Neuchâtel, for kindly agreeing to be the co-examiners of my PhD thesis.

Even a PhD student can not live on science alone. Therefore, the financial support provided by the Swiss Ministry for Education and Science (OFES) and by Norchip AS, Klokkarstua, Norway is greatly appreciated.

In an interdisciplinary field of science like microfluidics, it is especially true that a team values more than the sum of its individuals. I definitely subscribe to this point of view and I'd therefore address special thanks to my fellow µTAS-colleagues Alexandra Homsy, Laura Ceriotti, Roos Guijt, Arash Dodge, Gian-Luca Lettieri, Nathan Lacher, Sander Koster, and Vincent Linder. I am especially grateful to the first member of the µTAS team, Antoine Daridon, for being a great colleague and one of my best friends.

My office mates Jean-Charles Fiaccabrino, Marc Boillat (15%) and Bart van der Schoot (15%) are gratefully acknowledged for the nice atmosphere around and for overlooking my messy desk (which is, as I would like to emphasize, a token of creativity).

The microfabrication of the devices presented in this thesis would not have been possible without the help of IMT's highly skilled technical staff: Pierre-André Clerc, Nicole Hegelbach-Guye, Sylvain Jeanneret, Sabina Jenny, Pierre-André Kuenzi, Edith Millotte, Gianni Mondin, Sylviane Pochon, and Jose Vaquera. Their invaluable help and advice is greatly appreciated. Thanks also to Claudio Novelli, who kept our IT running perfectly and to Margrit Rüegg and Florence Rohrbach for their secretarial work. Mireille Leboef and Massoud Dadras have contributed great electron microscope images.

Finally, thanks to all members of Nico's group and of IMT at large for helping me out when necessary and being always there, both at work and outside!

I'd also like to acknowledge a few people, who are not connected to this thesis directly. My family was always there to support my fascination for science and technology (I remember my mum going crazy when preparing litmus pH paper in the kitchen based on red cabbage). It was essentially your help, support, and love that took me to where I am now.

For the end, I saved the most important. I'd like to address my special thanks to Frauke Greve, the one special person in my life, for her love and her endless support. You are my star.

Chapter 13

List of Publications

Refereed articles

Jan Lichtenberg, Nico F. de Rooij, Elisabeth Verpoorte, " A microchip electrophoresis system with integrated in-plane electrodes for contactless conductivity detection ", **Electrophoresis** 23 (2002), 3769-3780.

Jan Lichtenberg, Nico F. de Rooij, Elisabeth Verpoorte, "Sample pretreatment on microfabricated devices", **Talanta** 56 (2002) 233–266.

Jan Lichtenberg, Elisabeth Verpoorte, Nico F. de Rooij, "Sample preconcentration by field amplification stacking for microchip-based capillary electrophoresis", **Electrophoresis** 22 (2001) 258–271.

Margaret Sequeira, Dermot Diamond, Antoine Daridon, Jan Lichtenberg, Sabeth Verpoorte, and Nico F. de Rooij, " Progress in the realisation of an autonomous environmental monitoring device for ammonia", **Trac-Trends in Analytical** Chemistry 21 (2002) 816-827.

Bruce H. Weiller, Laura Ceriotti, Takayuki Shibata, Dietrich Rein, Matthew A. Roberts, Jan Lichtenberg, J. Bruce German, Nico F. de Rooij, and Elisabeth Verpoorte, "Analysis of Lipoproteins by Capillary Zone Electrophoresis in Microfluidic Devices: Assay Development and Surface Roughness Measurements", **Analytical Chemistry** 74 (2002), 1702–1711.

Rosanne M. Guijt, Jan Lichtenberg, Nico F. de Rooij, Elisabeth Verpoorte, Erik Baltussen, and Gijs W. K. van Dedem, "Indirect electro-osmotic pumping", **Journal of the Association for Laboratory Automation** 7 (2002) 62-64.

Antoine Daridon, Valia Fascio, Jan Lichtenberg, Rolf Wütrich, Hans Langen, Elisabeth Verpoorte, Nico F. de Rooij, "Multi-layer microfluidic glass chips for microanalytical applications, **Fresenius Journal of Analytical Chemistry** 371 (2001) 261–269.

Antoine Daridon, Margaret Sequeira, Gaëlle Pennarun-Thomas, Holger Dirac, Jens Peter Krog, Peter Gravesen, Jan Lichtenberg, Dermot Diamond, Elisabeth Verpoorte, Nico F. de Rooij, "Chemical sensing using an integrated microfluidic system based on the Berthelot reaction", **Sensors and Actuators** B 76 (2001) 235–243.

Elisabeth Verpoorte, Jan Lichtenberg, "Mikrofluidik-Chips", **MedizinischeGenetik** 3(12) (2000) 291–295. ISSN 0936-5931.

Oral presentations at conferences and workshops

Jan Lichtenberg, Elisabeth Verpoorte, Nico F. de Rooij, "A miniaturized analysis system based on capillary electrophoresis and contactless conductivity detection", **Transducers '01**, June 10-14, 2001, Munich, Germany (see Proceedings of the Transducers '01, p. 408-411).

Jan Lichtenberg, Elisabeth Verpoorte, Laura Ceriotti, Antoine Daridon, Gian-Luca Lettieri, Vincent Linder, Takayuki Shibata, Bruce Weiller, Nico F. de Rooij, "Microfluidics: Rethinking the Chemical Lab", **ANAKON 2001**, April 4-7, 2001, Konstanz, Germany

Jan Lichtenberg, Elisabeth Verpoorte, Nico F. de Rooij, "Coupled-column devices for sample preconcentration on-chip", 14th International Symposium on Microscale Separations and Analysis (**HPCE 2001**), January 13-18, 2001, Boston.

Rosanne M. Guijt, Jan Lichtenberg, Erik Baltussen, Elisabeth Verpoorte, Nico F. de Rooij, Gijs W.K. van Dedem, "Indirect Electro-Osmotically Induced Hydraulic Pumping", **LabAutomation 2002**, January 26–30, 2002, Palm Springs, USA.

Elisabeth Verpoorte, Laura Ceriotti, Jan Lichtenberg, Nico F. de Rooij, "Achieving Greater Flexibility in Chip-Based Separation", **SmallTalk 2001**, August 27-31, 2001, San Diego, USA

Antoine Daridon, Jan Lichtenberg, Elisabeth Verpoorte, Nico F. de Rooij et al, "Chemical sensing using an integrated μfluidic system based on colorimetrics", 8th International Meeting on Chemical Sensors (**IMCS**), 3 - 5 July 2000 Basel, Switzerland.

Poster presentations at conferences and workshops

Jan Lichtenberg, Laura Ceriotti, Nathan A. Lacher, Susan M. Lunte, Nico F. de Rooij, Elisabeth Verpoorte, "Microfluidic device for nucleic acid fragmentation by shear force", **μTAS 2002** Symposium, Nara, Japan (see Proceedings of the μTAS 2002 Symposium, p. 172–174) (poster award).

Jan Lichtenberg, Nico F. de Rooij, Elisabeth Verpoorte, "Different electrode geometries for on-chip conductivity detection", **SmallTalk 2002**, July 28 – 30 2002, San Diego; USA (poster award).

Jan Lichtenberg, Elisabeth Verpoorte, Nico F. de Rooij, "Operating parameters for an in-plane, contactless conductivity detector for microchip-based separation methods", **μTAS 2001** Symposium, Monterey (see Proceedings of the μTAS 2001 Symposium, p. 323–324).

Jan Lichtenberg, Gerhard Lammel, Mathieu Ouveley, Philippe Renaud, Nico F. de Roij, "Electrically insulated microchannels in silicon", **Eurosensors XIV**, August 27-30 2000, Copenhagen, Denmark (see Proceedings of the Eurosensors XIV conference, p. 259–261).

Jan Lichtenberg, Antoine Daridon, Elisabeth Verpoorte, Nico F. de Rooij, "Combination of Sample Pre-Concentration and Capillary Electrophoresis On-Chip", **μTAS 2000** Symposium, Enschede, The Netherlands (see Proceedings of the μTAS 2000 Symposium, p. 307–310).

Jan Lichtenberg, Antoine Daridon, Elisabeth Verpoorte, Nico F. de Rooij, "Sample Pre-Concentration by Field-Amplification Stacking on a CE-Chip", 13th International Symposium on High Performance Capillary Electrophoresis and Related Microscale Techniques (**HPCE 2000**), February 20-24, 2000, Saarbrücken, Germany.

A. Homsy, J. Lichtenberg, C. Massin, F. Vincent, P. -A. Besse, R. S. Popovic, N. F. de Rooij, and E. Verpoorte, "Fabrication of microfluidic channels with symmetric cross-sections for integrated NMR analysis", **μTAS 2002** Symposium, Nara, Japan.

Laura Ceriotti, Jan Lichtenberg , Arash Dodge, Nico F. de Rooij, Elisabeth Verpoorte, "Combined nucleic acid extraction and enrichment in bead-packed plastic beds", **μTAS 2002** Symposium, Nara, Japan.

Laura Ceriotti, Jan Lichtenberg, Stephanie Clément, Philippe Nussbaum, Elisabeth Verpoorte, René Dändliker, Nico F. de Rooij, " Visible and UV detection through square, deep PDM channels", **μTAS 2001** Symposium, Monterey (see Proceedings of the μTAS 2001 Symposium, p. 339–340).

Rosanne M. Guijt, Jan Lichtenberg, Erik Baltussen, Elisabeth Verpoorte, Nico F. de Rooij, Gijs W. K. van Dedem, "Indirect electro-osmotic pumping for direct sampling from bioreactors", **μTAS 2001** Symposium, Monterey (see Proceedings of the μTAS 2001 Symposium, p. 399–401).

Bruce H. Weiller, Takayuki Shibata, Laura Ceriotti, Mathew A. Roberts, Dietrich Rein, J. Bruce German, Jan Lichtenberg, Elisabeth Verpoorte, Nico F. de Rooij, "Development of a new, chip-based method for lipoprotein analysis by capillary electrophoresis", **µTAS 2001** Symposium, Monterey (see Proceedings of the µTAS 2001 Symposium, p. 426–428).

Antoine Daridon, Gaëlle Pennarun-Thomas, Margaret Sequeira, Jan Lichtenberg, Elisabeth Verpoorte, Dermot Diamond, Nico F. de Rooij, "Comparative kinetic studies of the Berthelot reaction for ammonia determination in microfluidic and spectrophotometric systems", **Eurosensors XIV**, August 27-30 2000, Copenhagen, Denmark (see Proceedings of the Eurosensors XIV conference, p. 451–452).

Gian-Luca Lettieri, Arash Dodge, Gerben Boer, Jan Lichtenberg, Elisabeth Verpoorte, Nico F. de Rooij, "Consequences of Opposing Electrokinetically and Pressure-Induced Flows in Microchannels of Varying Geometries ", **µTAS 2000** Symposium, Enschede, The Netherlands (see Proceedings of the µTAS 2000 Symposium, p. 351–354).

Arash Dodge, Karl Fluri, Vincent Linder, Gian-Luca Lettieri, Jan Lichtenberg, Elisabeth Verpoorte, Nico F. de Rooij, "Valveless, Sealed Microfluidic Device for Automated Heterogeneous Immunoassay: Design and Operational Considerations ", **µTAS 2000** Symposium, Enschede, The Netherlands (see Proceedings of the TAS 2000 Symposium, p. 407–410).

Jens Peter Krog, Holger Dirac, Birgit Fabius, Peter Gravesen, Antoine Daridon, Jan Lichtenberg, Elisabeth Verpoorte, Nico F. de Rooij, Gaëlle Pennarun-Thomas, Margaret Sequeira, Dermot Diamond, Steffen Howitz, Cyril Strec, Philippe Charles, Louis Cognet, "Realization of a Prototype Industrial On-Line Sensing System for Ammonium Based on Micro System Technology: Results and Perspectives", **µTAS 2000** Symposium, Enschede, The Netherlands (see Proceedings of the TAS 2000 Symposium, p. 419–422).

Margaret Sequeira, Gaelle Pennarun, Dermot Diamond, Birgit Fabius, Peter Gravesen, Jens Peter Krog, Theiss Stenstrøm, Ivan Ring Nielsen',Sabeth Verpoorte, Antoine Daridon, Jan Lichtenberg, Louis Cognet, Pieter Telleman, Holger Dirac, Oliver Geschke, Mark Denninger, Steffen Howitz, Thomas Gehring, Thomas Wegener, "Microsensor for ammonia", 12th International Symposium by the Society for Analytical Chemistry (**SAC**) 99, July 1999, Dublin, Ireland.

Chapter 14

Biography

Jan Hendrik Lichtenberg, born on June 19, 1972 in Munich, Germany, received his M. S. degree in electrical and microengineering in 1998 from the University of Bremen, Germany, and was research assistant at the Institute of Microsensors, -actuators and -systems (IMSAS). He was visiting student at the Talent Identification Program of Duke University, Durham, North Carolina, USA, in the summer of 1992, exchange student at the Ecole Polytechnique Fédérale de Lausanne, Switzerland in 1994/95 and held a scholarship of the "Studienstiftung des deutschen Volkes" during his studies. In 1995, he spent four months as an intern at the Institute of Microelectronics (IME) in Singapore working on new etching techniques for CMOS-integrated pressure sensors. For his research project “Unilyser – a universal computer system for chemical analysis" (1990), he received the nation-wide first price at the “Young Scientists” competition in Germany, an innovation award, donated by the former German chancellor Dr. Helmut Kohl, and a second price at the “European Union Contest for Young Scientists” in Copenhagen, Denmark. In 1997, Jan founded “Advanced Micromachining Tools AMMT GmbH” together with his partner Robert Nitzschmann, with whom he also shares the CEO position. AMMT GmbH is a technology company, which holds the worldwide market leader position for specialized wet etching and porous silicon equipment for microfabrication.

In November 1998, Jan Lichtenberg joined the Sensors, Actuators and Microsystems Laboratory (SAMLAB), headed by Prof. Nico F. de Rooij, at the Institute of Microtechnology (University of Neuchâtel, Switzerland). His research activities in the microfluidics group of Dr. Elisabeth Verpoorte focus on the development of miniaturized systems for chemical and biochemical analysis.

Abstract

With the goal of small ion analysis in mind, a prototype of a microchip capillary electrophoresis (CE) device has been developed based on a new, integrated, inplane, contactless conductivity detector (CCD). The device allows fast separation of inorganic anions and cations in the range of 20 s. The microfabrication process developed in the context of this thesis makes it possible to easily integrate CCDs with standard glass and polymer micromachining. It also allows to place the electrodes close to the separation channel independent of the substrate type, which is a requirement for good detector sensitivity and spatial (i.e. separation) resolution. The performance of the detector is further enhanced by an integrated sample preconcentration step based on field-amplified sample stacking.